technische universität
dortmund

Dissertation
zur Erlangung des Grades
Dr. rer. nat.
im Fach Physik

$|\Delta c| = |\Delta u| = 1$ transitions in and beyond the Standard Model

Marcel Golz
geboren in Duisburg

Dortmund, April 2022

Lehrstuhl für theoretische Physik IV
Fakultät Physik
Technische Universität Dortmund

Gutachter der Dissertation:
Prof. Dr. Gudrun Hiller
Jun.-Prof. Dr. Emmanuel Stamou
Prof. Dr. Alexander Lenz

Datum der Abgabe:
20.04.2022

Vorsitzender des Promotionsausschusses:
Prof. Dr. Johannes Albrecht

Datum der mündlichen Prüfung:
21.06.2022

For Lotta

Kurzfassung

In dieser Arbeit werden seltene semileptonische $|\Delta c| = |\Delta u| = 1$ Übergänge im Standardmodell und jenseits davon studiert. Die Standardmodellphenomenologie von Dreikörper-Mesonzerfällen $D \to P\ell\ell$, sowie von Drei- und Vierkörperzerfällen von Charmbaryonen, $B_0 \to B_1(\to B_2\pi)\ell\ell$, wird analysiert und die Dominanz von Resonanzbeiträgen zu den Verzweigungsverhältnissen wird herausgestellt. Effekte von Physik jenseits des Standardmodells werden modellunabhängig und im Rahmen von Leptoquark– und flavorvollen, Anomalie-freien Z'–Modellen untersucht. Die Dominanz der Resonanzbeiträge wird in Analysen sauberer Nulltestobservablen, wo jegliches Signal auf neue Physik hinweist, überwunden oder sogar als Katalysator genutzt. Nulltests basieren auf Winkelobservablen, CP–Erhaltung, Leptonflavoruniversalität und der Erhaltung von geladenem Leptonflavor. Bereits eine Teilmenge von vier Winkelobservablen in seltenen Drei- und Vierkörperzerfällen von Charmbaryonen genügt, um Beiträge jenseits des Standardmodells von Dipol- und (Axial-)Vektor-Wilsonkoeffizienten vollständig voneinander zu unterscheiden, wohingegen seltene, (semi-)leptonische Mesonzerfälle $D \to (P)\ell\ell$ auf (pseudo-)skalare und (pseudo-)tensorielle Effekte hindeuten. Eine globale Sichtweise auf Verbindungen zwischen verschiedenen Flavorsektoren wird im Kontext von flavoraufsummierten Verzweigungsverhältnissen mit einem Neutrino-Antineutrino-Paar im Endzustand dargelegt. Indirekte Tests von Leptonflavoruniversalität und der Erhaltung von geladenem Leptonflavor werden für den Charmsektor präsentiert, wo Dineutrinomoden ohnehin Nulltests des Standardmodells darstellen. In $|\Delta b| = |\Delta s| = 1$ Übergängen ist der erste Nachweis für die Verletzung von Leptonflavoruniversalität im Verhältnis von Myon über Elektron B–Mesonverzweigungsverhältnissen gefunden. Ergänzend zu den direkten Herangehensweisen wird gezeigt, dass Dineutrinomoden die Struktur von geladenem Leptonflavor in der Korrelation zwischen $B \to P\nu\bar{\nu}$ und $B \to V\nu\bar{\nu}$ testen. Ähnliche indirekte Tests von Leptonflavor in anderen Quarksektoren werden ebenfalls besprochen.

Abstract

This thesis comprises a study of rare semileptonic $|\Delta c| = |\Delta u| = 1$ transitions in the Standard Model and beyond. The Standard Model phenomenology of three-body meson decays $D \to P\ell\ell$, as well as three- and four-body charmed baryon decays $B_0 \to B_1(\to B_2\pi)\ell\ell$, is analyzed and branching ratios are found to be dominated by resonances. Physics effects beyond the Standard Model are studied model-independently as well as in the framework of leptoquark– and flavorful, anomaly-free Z'–models. Resonance dominance is shown to be overcome or even used as a catalyst in analyses of clean null-test observables, where any signal indicates new physics. Null tests are based on angular observables, CP–conservation, lepton flavor universality and charged lepton flavor conservation. Already a subset of four angular observables in three- and four-body rare charm baryon decays are sufficient to disentangle beyond Standard Model effects in dipole and (axial) vector Wilson coefficients, whereas (semi-)leptonic rare meson decays $D \to (P)\ell\ell$ are shown to control (pseudo-)scalar and (pseudo-)tensor effects. A global view on connections between different flavor sectors is put forward in the context of flavor summed dineutrino branching ratios. Indirect tests of lepton flavor universality and charged lepton flavor conservation are presented for the charm sector, where dineutrino modes already pose null tests of the Standard Model. In $|\Delta b| = |\Delta s| = 1$ transitions, the first evidence for the violation of lepton flavor universality is found in muon over electron ratios of B–meson branching fractions. Complementing the direct probes, dineutrino modes are shown to test charged lepton flavor indirectly in the correlation of $B \to P\nu\bar{\nu}$ and $B \to V\nu\bar{\nu}$. Similarly, indirect flavor probes in other quark sectors are also commented on.

Acknowledgments

The last few years have been the most fascinating, amazing and eventful time of my life so far and I would like to thank all people, who have accompanied my journey.

I am thankful for the financial and idealistic continuous support from the German Academic Scholarship Foundation *(Studienstiftung des deutschen Volkes)* throughout my studies and PhD. I was lucky to participate in many inspiring and intellectually stimulating events organized by the German Academic Scholarship Foundation. Also, my participation in some international conferences would not have been possible without their financial support.

I would like to thank my advisor, Gudrun Hiller, for the opportunity to live and work as a PhD candidate in the high-energy physics department at TU Dortmund. For her guidance and the development of research projects, which I was able to participate in. For being introduced into the world of the international, highly motivated high-energy physics community. For many meetings and extensive physics discussions. For her inspiring, seamlessly endless motivation that also helped to stay productive during the corona pandemic. For her support and understanding regarding my "family project". For the opportunities to be send to many trips to conferences, schools and workshops.

My special gratitude to all further collaborators of the research works this thesis is based on. To Dominik Mitzel for his expertise and very useful discussions on experimental issues and for his curiosity and many useful questions. To Tom Magorsch, who learned a lot fast and without whom the rare charm baryon projects would not have been possible. And finally, to Rigo Bause and Hector Gisbert. It has been a pleasure to work and discuss with you guys, and I have strongly profited from your expertise and impressive work performances.

I also thank all the (former) members of the department and beyond: Kevin, Janina, Jonathan, Björn, Stefan, Dennis, Clara, Peter, Maggi, Andrey, Mathias, Sinan, Philipp, Tim, Tim, Tom, Dominik, Dominik and Lara for all the climbing and bouldering sessions, post climbing beers, endless coffee breaks, coffee room discussions; for creating a motivating, exciting and sociable work environment and simply making this an incredibly joyful time.

A special praise for everybody, who has proofread (parts) of this thesis and the many useful comments that improved this work.

I am grateful to my parents, brother, sister-in-law and parents-in-law for their unconditional and continuous support. This work is only possible due to you guys, a myriad of childcare time slots covered and numerous compensation days, bike trips, holidays and many other things, that helped me to recharge my batteries countless times.

Finally, I am not able to express in a few lines how much I owe my wife, Linda. Thank you for being my reliable partner, believing in me, supporting my plans and even pushing them forward. This thesis would not have been possible without your encouragement.

Publications

This thesis is based on the following publications by the author, Refs. [1–8]:

- Rigo Bause, Marcel Golz, Gudrun Hiller and Andrey Tayduganov,
  "The New Physics Reach of Null Tests with $D \to \pi\ell\ell$ and $D_s \to K\ell\ell$ Decays",
  In: *Eur. Phys. J. C* ***80*** *(2020) no.1, 65, Eur. Phys. J. C* ***81*** *(2021) no.3, 219 (erratum)*,
  DOI:10.1140/epjc/s10052-020-7621-7, 10.1140/epjc/s10052-021-08998-w (erratum),
  e-Print: 1909.11108 [hep-ph].

- Rigo Bause, Hector Gisbert, Marcel Golz and Gudrun Hiller,
  "Exploiting CP–asymmetries in rare charm decays",
  In: *Phys. Rev. D 101 (2020) 11, 115006*,
  DOI:10.1103/PhysRevD.101.115006,
  e-Print: 2004.01206 [hep-ph].

- Rigo Bause, Hector Gisbert, Marcel Golz and Gudrun Hiller,
  "Lepton universality and lepton flavor conservation tests with dineutrino modes",
  In: *Eur. Phys. J. C* ***82*** *(2022) no.2, 164*,
  DOI:10.1140/epjc/s10052-022-10113-6,
  e-Print: 2007.05001 [hep-ph].

- Rigo Bause, Hector Gisbert, Marcel Golz and Gudrun Hiller,
  "Rare charm $c \to u\,\nu\bar{\nu}$ dineutrino null tests for e^+e^- machines",
  In: *Phys. Rev. D 103 (2021) 1, 015033*,
  DOI:10.1103/PhysRevD.103.015033,
  e-Print: 2010.02225 [hep-ph].

- Hector Gisbert, Marcel Golz and Dominik Stefan Mitzel,
  "Theoretical and experimental status of rare charm decays",
  In: *Mod. Phys. Lett. A 36 (2021) 04, 2130002*,
  DOI:10.1142/S0217732321300020,
  e-Print: 2011.09478 [hep-ph].

- Marcel Golz, Gudrun Hiller and Tom Magorsch,
  "Probing for New Physics with Rare Charm Baryon (Λ_c, Ξ_c, Ω_c) Decays",
  In: *J. High Energ. Phys. 09 (2021), 208*,
  DOI:10.1007/JHEP09(2021)208,
  e-Print: 2107.13010 [hep-ph].

- Rigo Bause, Hector Gisbert, Marcel Golz and Gudrun Hiller,
  "Interplay of dineutrino modes with semileptonic B–decays",
  In: *J. High Energ. Phys. 12 (2021), 061*,
  DOI:10.1007/JHEP12(2021)061,
  e-Print: 2109.01675 [hep-ph].

- Marcel Golz, Gudrun Hiller and Tom Magorsch,
  "Pinning down $c \to u\ell^+\ell^-$ couplings with rare charm baryon decays",
  In: *Eur. Phys. J. C* ***82*** *(2022) no.4, 357*,
  DOI:10.1140/epjc/s10052-022-10302-3,
  e-Print: 2202.02331 [hep-ph].

and the conference proceedings, Refs. [9–12]:

- Marcel Golz,
  "Physics reach of $D_{(s)} \to \pi(K)\ell\ell$ and other charming null test opportunities",
  Contribution to: 55th Rencontres de Moriond on Electroweak Interactions and Unified Theories (Moriond EW 2021),
  e-Print: 2105.03453 [hep-ph],
  Speaker: Marcel Golz.

- Marcel Golz,
  "Null test searches for BSM physics with rare charm decays",
  Contribution to: 10th International Workshop on Charm Physics (CHARM 2020),
  e-Print: 2109.07155 [hep-ph],
  Speaker: Marcel Golz.

- Rigo Bause, Hector Gisbert, Marcel Golz and Gudrun Hiller,
  "Dineutrino modes probing lepton flavor violation",
  Contribution to: European Physical Society Conference on High Energy Physics 2021 (EPS-HEP2021),
  e-Print: 2110.08795 [hep-ph],
  Speaker: Hector Gisbert.

- Marcel Golz, Gudrun Hiller and Tom Magorsch,
  "Null test BSM searches with rare charm baryon decays",
  Contribution to: 11th International Workshop on the CKM Unitarity Triangle (CKM 2021),
  e-Print: 2203.01965 [hep-ph],
  Speaker: Marcel Golz.

Contents

1 Introduction

The field of elementary particle physics aims at describing nature at the most fundamental level, both in terms of the building blocks and interactions. During the last decades, our knowledge has rapidly increased through concurrent developments in theory and experiment. In particular, the field of quark flavor physics had its starting point in the 1960s with the prediction of the strange quark and the development of the eightfold way to classify experimentally observed hadrons [13]. Further experimental developments implied the need for a charm quark [14] to avoid flavor changing neutral currents (FCNCs) via a generalized Glashow-Iliopolus-Maiani (GIM) mechanism [15]. The charm quarks actual discovery took place in the *November Revolution* in 1974 [16, 17]. The discoveries of the heavy electroweak gauge bosons followed in 1983, see [18] for a review, and were the starting point of still ongoing electroweak precision measurements. Finally, after the prediction of the Higgs boson in the 1960s [19–22], the Standard Model of particle physics (SM) was completed with the discovery of a heavy boson in 2012 [23, 24], which later was confirmed to share the SM Higgs properties [25, 26]. The overwhelming majority of subsequent analyses corroborate the predictions of the SM, thus forging the most frequently tested and most successful fundamental theory to date.

Despite its success, the SM is known to be an insufficient description of nature for several reasons. One being the prediction [27–29] and discovery [30, 31] of neutrino oscillations, implying non-vanishing neutrino masses, which are, however, vanishing according to predictions of the SM. Another problem stems from cosmological observations which imply the existence of dark matter [32], as well as the lack of sufficient CP–violation as proposed by the Sakharov conditions [33] for the emergence of a baryon–asymmetry in the universe. In addition, the SM describes only three of the four known fundamental interactions and a quantum theory of gravity is yet to be found.

The modern route towards the discovery of physics beyond the Standard Model (BSM) utilizes two complementary methods. The high-energy frontier pushes the largest tested center-of-mass energy in single-particle collisions in order to directly produce heavy BSM particles, which is the only way to unambiguously claim the discovery of heavy new physics (NP) particles beyond the SM. On the other hand, the main idea at the precision frontier is to indirectly test much larger energy ranges through BSM contributions to loop processes by pushing the theoretical and experimental precision of a given process into a regime in which deviations from SM predictions become apparent. These deviations then indicate a certain energy scale and, therefore, provide guidance for direct searches where the lack of direct detection of any BSM particle calls for a prediction of a new energy scale, at which NP is expected to show up.

Indeed, hints for deviations from the SM have emerged at the precision frontier. These include the first evidence for the violation of lepton flavor universality (LFU) in decays of B–mesons [34], which fit into similar deviations of less significance [35–37], along with systematically suppressed branching ratio measurements [38–41], as well as deviations in angular asymmetries [42–47] in $b \to s\mu^+\mu^-$ induced modes, commonly referred to as the B–anomalies. A second example is the muon anomalous magnetic moment, where Run 1 of the Fermilab $g-2$ experiment [48–51] confirms an earlier BNL measurement [52] and both measurements globally point towards a 4.2σ tension with respect to the SM prediction [53], see also Ref. [54] for a recent White Paper.

In order to reconcile the observed discrepancies while being in line with constraints in other sectors, which are in agreement with SM expectations, a global picture is needed. Several strategies are at hand. The model-dependent route is to construct a specific ultraviolet (UV)–complete BSM model, which is able to reconcile as many discrepancies and problems of the SM as possible and make verifiable

predictions in other observables. The alternative is the model-independent study of BSM physics in an Effective Field Theory (EFT) framework. Here, we distinguish two cases. On the one hand, we apply the Weak Effective Theory (WET), which for example can be used for $b \to s\mu^+\mu^-$ processes, where global fits with increasing significance are performed, *e.g.* Ref. [55]. On the other hand, the Standard Model Effective Field Theory (SMEFT) framework is utilized and allows to systematically probe heavy NP simultaneously in various different sectors, which comes at the prize of 2499 parameters at leading order. Therefore, it is crucial to follow the "leave-no-stone-unturned-guideline" and study as many different sectors of the SM as possible. SMEFT analyses involving top quarks are of recent interest, *e.g.* Refs. [56–59]. This is because the top, being the third generation up-type cousin of the b–quark and the heaviest SM particle, is likely to couple to NP. However, FCNCs of top quarks [60] have only very recently been tested in searches for $t \to c\gamma$ and $t \to u\gamma$, and are only poorly constrained [61]. At the same time the tree-level contributions to single-top-quark production in association with a photon, $tq\gamma$ with light down-type quarks q, were also only recently discovered [62]. More analyses with top quarks are needed, but lack sufficient statistics to probe rare processes and are only probed directly, as the top-quark decays before hadronization.

Therefore, the natural and unique place to look for up-type FCNCs is in rare charm decays. The charm quark is the first (semi-)heavy candidate that allows for flavor physics probes with hadrons and rare decays are suitable for a variety of flavor facilities such as the Large Hadron Collider beauty (LHCb) experiment [63], Belle II [64], BESIII [65] and possible future machines, such as the super charm-tau factory [66] and the Future Circular Collider (FCC) [67, 68]. As of today, only very few rare charm decays have been observed, including the radiative mode $D \to \rho\gamma$ seen at Belle [69] and the observation and first angular analysis of $D^0 \to \pi^+\pi^-\mu^+\mu^-$ and $D^0 \to K^+K^-\mu^+\mu^-$ [70, 71], with a very recent update available in Ref. [72]. For other modes, upper limits exist on the purely leptonic decays $D^0 \to \mu^+\mu^-$ [73] and $D^0 \to \mu^\pm e^\mp$ [74], various semileptonic $D \to P\ell\ell^{(\prime)}$ modes [75, 76], $\Lambda_c \to p\mu^+\mu^-$ [77] and $D^0 \to \pi^0\nu\bar{\nu}$ [78], all of which will be discussed in more detail in the remainder of this thesis.

Experimentally, charm physics rapidly evolved ever since the first evidence for $D^0 - \bar{D}^0$ mixing in 2007 by the Belle [79], BaBar [80] and CDF [81] collaborations. Nowadays, more and more precise information on mixing is available from LHCb [82–84] and tests for CP–violation in mixing seem to be within reach. The first observation of direct CP–violation in the charm sector was performed in an analysis by LHCb in 2019 [85].

Although $|\Delta c| = |\Delta u| = 1$ transitions are the up-type counterparts of down-type FCNCs, naïve applications of known methods fail in charm. Nature seems to accidentally have laid the mass of the charm quark in an unpleasant region, where it is too heavy to apply flavor symmetries and relate it to the light quarks u, d, s, however too light to employ a fast converging heavy quark expansion. Despite these theoretical challenges, research interest in $c \to u\ell\ell$, $c \to u\nu\bar{\nu}$ and $c \to u\gamma$ induced modes is ongoing and ever increasing and clean probes of the SM can be performed and complement the flavor physics programs in the down-type sectors. For instance, (semi-)leptonic rare charm decays with charged leptons are studied in Refs. [86–104], with missing energy in Refs. [105–107] and rare radiative charm decays in Refs. [108–112].

While the main focus of this work is on rare semileptonic charm decays, the overall goal is a broader

view on the quark flavor sector of the SM and to fully exploit correlations between sectors in order to unravel the origin of flavor.

This thesis is based on Refs. [1–12] by the author and structured as follows. Five main chapters are followed by a conclusion and outlook in Chapter 7. The main chapters contain the following topics:

- In Chapter 2 we review flavor physics within the SM and introduce the EFT framework, which is extensively used throughout this thesis and based on an Operator Product Expansion (OPE) [113]. We distinguish the WET and SMEFT and discuss SM values for so-called Wilson coefficients contributing to semileptonic rare charm decays in both EFT frameworks.

- Chapter 3 presents the SM phenomenology of the rare charm three-body decays $D^+ \to \pi^+\ell^+\ell^-$, $D^0 \to \pi^0\ell^+\ell^-$ and $D_s^+ \to K^+\ell^+\ell^-$ and baryon three- and four-body decays $\Lambda_c \to p\ell^+\ell^-$, $\Xi_c^0 \to \Sigma^0\ell^+\ell^-$, $\Xi_c^0 \to \Lambda^0(\to p\pi^0)\ell^+\ell^-$, $\Xi_c^+ \to \Sigma^+(p\pi^0)\ell^+\ell^-$ and $\Omega_c^0 \to \Xi^0(\to \Lambda^0\pi^0)\ell^+\ell^-$, where the latter three are discussed as three- and four-body final state decays. We also give a brief introduction to CP–asymmetries in hadronic decays of D–mesons.

- In Chapter 4 we discuss BSM physics in rare charm decays. We work out the model-independent available parameter space, *i.e.* we obtain upper limits on BSM Wilson coefficients by collecting available experimental constraints. We further introduce effects induced in leptoquark (LQ)–and flavorful anomaly-free Z'–models and investigate bounds on the model parameters.

- Chapter 5 is dedicated to an extensive study of null-test possibilities in rare charm decays. We discuss angular observables in three-body meson, three- and four-body baryon decays and beyond and comment on the viability of a future global fit. We further discuss CP–asymmetries in semileptonic modes, comment on CP–asymmetric angular observables and investigate correlations between semileptonic and hadronic CP–violation in the context of anomaly-free Z'–models. Finally, direct probes of (accidental) charged lepton flavor symmetries are discussed. Violation of LFU is probed in ratios of branching fractions of semileptonic modes into muons over electrons and charged lepton flavor conservation (cLFC) is tested via branching ratios of lepton flavor violating (LFV) decay modes.

- Indirect tests of charged lepton flavor are presented in Chapter 6. Due to the flavor inclusiveness of dineutrino branching ratios and a SMEFT–based $SU(2)_L$–link, upper limits on rare charm dineutrino branching ratios are proportional to charged lepton couplings and depend on assumptions on charged lepton flavor. The same link can be exploited in both directions and other quark flavor sectors. We investigate implications for $b \to s$ and $b \to d$ induced modes and comment on further possibilities with rare kaon and top decays.

More details on SM Wilson coefficients, Z'–models, the helicity formalism and $SU(2)_L$–links in SMEFT can be found in the appendix. For self-containment the appendix also comprises parameters, experimental input and explicit expressions for angular distributions and helicity amplitudes, as well as utilized form factors and decay constants. The presented research works are performed using the computer software packages in Refs. [114–119].

2 The Standard Model and effective field theories

This chapter is split into three parts. In Sec. 2.1 we give an overview of the SM following standard literature, see Refs. [120–124]. First, we turn to the gauge symmetry, particle content, and symmetry breaking mechanism of the SM with a special emphasis on the flavor sector and the charm quark, which will be the main object of study in this thesis. We also discuss shortcomings of the SM that motivate the search for BSM physics.

The second part deals with EFTs. Here, the main objects of interest are Wilson coefficients. EFTs are only valid up to a certain scale, at which heavy degrees of freedom are integrated out and encoded in Wilson coefficients, whereas the remaining light degrees of freedom are included in the form of effective operators. We discuss two different implementations of EFTs. First, we focus on the so-called WET at the charm mass scale and discuss SM contributions to Wilson coefficients of operators involving leptons and neutrinos, respectively. Afterwards, we introduce the SMEFT, where all SM particles are kept as light degrees of freedom, *i.e.* they are contained in SMEFT operators, such that only heavy BSM physics enters the associated Wilson coefficients.

The last part summarizes the short-distance contributions to SM Wilson coefficients relevant for this work within the different EFTs.

2.1 The Standard Model of particle physics

The SM is a renormalizable quantum field theory (QFT) with a local gauge symmetry $SU(3)_C \otimes SU(2)_L \otimes U(1)_Y$. Here, $SU(3)_C$ refers to the theory of quantum chromodynamics (QCD) [125–129], whereas the electroweak interactions are encoded in the $SU(2)_L \otimes U(1)_Y \to U(1)_{\text{QED}}$, see Refs. [130–132]. The field content of the SM is divided into two classes, fermions with spin $\frac{1}{2}$ and bosons with spin 0 or 1. The SM Lagrangian is then compactly written as

$$\begin{aligned}\mathcal{L}_{\text{SM}} = &-\frac{1}{4}\left(B_{\mu\nu}B^{\mu\nu} + W^a_{\mu\nu}W^{\mu\nu}_a + G^a_{\mu\nu}G^{\mu\nu}_a\right)\\ &+ \mathrm{i}\overline{Q}_i \not{D} Q_i + \mathrm{i}\overline{D}_i \not{D} D_i + \mathrm{i}\overline{U}_i \not{D} U_i + \mathrm{i}\overline{L}_i \not{D} L_i + \mathrm{i}\overline{E}_i \not{D} E_i\\ &- \overline{Q}_i H Y_D^{ij} D_j - \overline{Q}_i \tilde{H} Y_U^{ij} U_j - \overline{L}_i H Y_E^{ij} E_j + \text{h.c.}\\ &+ |D_\mu H|^2 + \mu^2 |H|^2 - \lambda |H|^4 \,.\end{aligned} \tag{2.1}$$

The first line encodes the kinetic terms of the gauge fields with

$$F^a_{\mu\nu} = \partial_\mu F^a_\nu - \partial_\nu F^a_\mu + \mathrm{i} g_{(\mathcal{G})}\, f^{abc}_{(\mathcal{G})} F^b_\mu F^c_\nu \,, \tag{2.2}$$

where $g_{(\mathcal{G})}$ is the gauge coupling associated with the gauge group $\mathcal{G}$ and $f^{abc}_{(\mathcal{G})}$ are structure constants. For $B^{\mu\nu}$ the structure constants vanish as the gauge interaction is abelian, $f^{abc}_{U(1)_Y} = 0$. Bosons mediating the gauge interactions have spin 1 and are referred to as gauge bosons, including gluons G^a_μ for QCD and the electroweak gauge bosons $W^\pm_\mu$, Z^0_μ, $\gamma\,(A_\mu)$, which are linear combinations of the W^a_μ and B_μ

and the W^3_μ-B_μ mixing is parametrized by the weak mixing angle θ_W

$$\begin{aligned} W^\pm_\mu &= \frac{1}{2}\left(W^1_\mu \mp \mathrm{i}\, W^2_\mu\right) , \\ Z^0_\mu &= \cos\theta_W W^3_\mu - \sin\theta_W B_\mu , \\ A_\mu &= \sin\theta_W W^3_\mu + \cos\theta_W B_\mu . \end{aligned} \tag{2.3}$$

The second line in Eq. (2.1) contains the gauge interactions to SM fermions induced by the covariant derivative, in compact notation $\not{D} = D^\mu \gamma_\mu$ with the Dirac gamma matrices γ_μ and

$$D_\mu = \partial_\mu + \mathrm{i} g_s G^a_\mu T^a_{SU(3)} + \mathrm{i} g_w W^a_\mu T^a_{SU(2)} + \mathrm{i} g' Y B_\mu . \tag{2.4}$$

Here, the gauge couplings g_s, g_w and g' refer to $SU(3)_C$, $SU(2)_L$ and $U(1)_Y$, respectively, and the T^a are generators of the non-abelian gauge factors in the representation of the field the derivative is acting on, whereas Y is the hypercharge.

The only fundamental spin 0 boson in the SM is the Higgs H, an $SU(2)_L$–doublet and QCD singlet responsible for spontaneously breaking the electroweak sector down to quantumelectro dynamics (QED) due to acquiring a non-trivial vacuum expectation value (vev) $v = \frac{2\, m_W}{g_w} \simeq 246\,\mathrm{GeV}$ with the W–boson mass m_W. The remaining massive physical degree of freedom contained in the Higgs doublet is generally referred to as the Higgs boson h^0. Interactions between the Higgs and all other particles are possible via Yukawa interactions, which are given in the third line of Eq. (2.1) and with the help of the vev are responsible for the generation of masses. The experimentally measured values of these masses are collected in App. A. The fourth line in Eq. (2.1) contains the kinetic term and potential of the Higgs doublet. For all SM fermions the respective group representations for both left-handed (LH) and right-handed (RH) field components are given in Tab. 2.1.

Fermions in the SM are classified according to their gauge interactions. The $SU(2)_L$ gauge symmetry acts on the LH field component, hence one distinguishes LH $SU(2)_L$–doublets and RH singlets. Fermions charged under $SU(3)_C$ are called quarks, $SU(3)_C$–singlets are called leptons. In the quark sector, up-type and down-type quarks are distinguished. We use Q for the $SU(2)_L$–doublet containing LH up- and down-type field components and U, D for the RH up- and down-type components, respectively. For the charged leptons we use E for the RH field components and L for the doublet, which also includes LH neutrinos. In the SM, neutrinos remain massless and no RH field component exists, whereas all other fermion fields acquire their masses due to Yukawa terms involving both LH and RH field components and a Higgs.

Most importantly, both quarks and leptons come in three *families*, *generations* or *flavors* (used synonymously) as indicated by flavor indices i, j in Eq. (2.1). The first generation makes up everyday matter, the other two generations are heavier, but otherwise identical copies of the first generation. The study of transitions between these three families and the search for a deeper reason for the three identical copies define the field of *flavor physics*.

Table 2.1: SM fermion fields and their group representations and charges under the SM gauge groups. The convention $q = Y + T_3$, with q the electrical charge in units of the proton charge is used. T_3 refers to the third component of the weak isospin and Y denotes the hypercharge. The indices L and R indicate LH and RH particle fields. The bold numbers **1**, **2**, **3** denote a singlet, doublet and triplet representation, respectively.

Particle field	$SU(3)_C$	$SU(2)_L$	Y	T_3	q
$\begin{pmatrix} u \\ d \end{pmatrix}_L, \begin{pmatrix} c \\ s \end{pmatrix}_L, \begin{pmatrix} t \\ b \end{pmatrix}_L$	**3**	**2**	1/6	1/2 −1/2	2/3 −1/3
u_R, c_R, t_R	**3**	**1**	2/3	0	2/3
d_R, s_R, b_R	**3**	**1**	−1/3	0	−1/3
$\begin{pmatrix} \nu_e \\ e \end{pmatrix}_L, \begin{pmatrix} \nu_\mu \\ \mu \end{pmatrix}_L, \begin{pmatrix} \nu_\tau \\ \tau \end{pmatrix}_L$	**1**	**2**	−1/2	1/2 −1/2	0 −1
e_R, μ_R, τ_R	**1**	**1**	−1	0	−1

2.1.1 Flavor physics and the charm quark

In the SM, fermion masses are induced due to the Yukawa terms, *i.e.* the third line in Eq. (2.1),

$$-\mathcal{L}_{\text{Yukawa}} = \overline{Q}_i H Y_D^{ij} D_j + \overline{Q}_i \tilde{H} Y_U^{ij} U_j + \overline{L}_i H Y_E^{ij} E_j + \text{h.c.}\,, \tag{2.5}$$

where $\tilde{H} = i\tau_2 H^*$ is the $SU(2)_L$ conjugate of the Higgs doublet H with the Pauli matrix τ_2. The Yukawa matrices Y_D, Y_U, Y_E explicitly carry flavor indices i, j. After spontaneous symmetry breaking, the Higgs acquires its vev and Dirac masses are induced

$$M_\Psi^{ij} = \frac{v}{\sqrt{2}} Y_\Psi^{ij}\,. \tag{2.6}$$

These mass matrices are in general non-diagonal and chiral, unitary field rotations need to be applied for the diagonalization and switch from the gauge basis to the mass basis

$$\Psi_{L,R}^i \to V_{\Psi_{L,R}}^{ij} \Psi_{L,R}^j\,. \tag{2.7}$$

In the quark sector, four of these rotations exist, one for each up- and down-type and each LH and RH field component. For the leptons there are three such rotations, since no RH neutrinos exist in the SM. However, most of these rotations are unphysical. QCD, QED, as well as the neutral currents mediated by the Z–boson are not sensitive to these rotations. For QCD and QED only vector interactions exist and $\overline{\Psi}\gamma_\mu\Psi = \overline{\Psi}_L\gamma_\mu\Psi_L + \overline{\Psi}_R\gamma_\mu\Psi_R$, such that the individual rotations drop out. In the case of the Z boson, the W_μ^3 part of the interaction only couples to LH fermions, such that the rotation directly cancels, whereas the B_μ part is again a vector interaction. For all of these interactions, the cancellation only occurs because the gauge interaction is flavor blind, *i.e.* the gauge interaction obeys lepton and

quark flavor universality as charges and representations are identical for all three generations.

Flavor changing interactions are, however, induced in the SM via charged currents interacting with the $W^{\pm}$–bosons

$$\mathcal{L}_{\text{SM}} \supset \frac{e}{\sqrt{2}\sin\theta_W}\left(W_\mu^+ V_{ij}\overline{u}_L^i\gamma^\mu d_L^j + W_\mu^- V_{ij}^\dagger\overline{d}_L^i\gamma^\mu u_L^j\right), \tag{2.8}$$

where e refers to the $U(1)_{\text{QED}}$ gauge coupling and the misalignment of the gauge and mass basis for LH up- and down-type quarks becomes physical. The unitary matrix quantifying this misalignment is the Cabibbo-Kobayashi-Maskawa (CKM) matrix [133, 134]

$$V = V_{\text{CKM}} = V_L^{u\dagger}V_L^d = \begin{pmatrix} V_{ud} & V_{us} & V_{ub} \\ V_{cd} & V_{cs} & V_{cb} \\ V_{td} & V_{ts} & V_{tb} \end{pmatrix}. \tag{2.9}$$

The CKM matrix has four independent parameters, three mixing angles and one CP–violating phase. Experimentally, one finds a strong hierarchy between the elements of the CKM matrix and it is convenient to express in terms of the Wolfenstein parametrization

$$V_{\text{CKM}} = \begin{pmatrix} 1-\frac{\lambda^2}{2} & \lambda & A\lambda^3(\rho-\mathrm{i}\eta) \\ -\lambda & 1-\frac{\lambda^2}{2} & A\lambda^2 \\ A\lambda^3(1-\rho-\mathrm{i}\eta) & -A\lambda^2 & 1 \end{pmatrix} + \mathcal{O}(\lambda^4), \tag{2.10}$$

with expansion parameter $\lambda \sim 0.2$. Numerical values for CKM parameters and $\sin\theta_W$ are given in App. A. From a theoretical point of view, neither the CKM hierarchy nor the hierarchy between the measured quark masses with $m_u < m_d \ll m_s \ll m_c < m_b \ll m_t$ is understood, and therefore this issue is referred to as the *flavor puzzle* of the SM, see *e.g.* Ref. [135].

While parameters of the CKM matrix can be extracted from measurements of flavor changing charged currents (FCCCs), mediated by tree-level $W^{\pm}$ exchange, we learn that FCNCs are not induced at tree level in the SM. Studies of FCNCs are therefore interesting for BSM physics searches, as they test the quantum structure of the SM and are sensitive to scales much higher than the available center-of-mass energies at current colliders. FCNC-induced decays are the main objective in this thesis. In the down-type sector there are the $b \to s$, $b \to d$ and the $s \to d$ transitions, whereas in the up-sector $t \to c$ and $t \to u$ transitions cannot easily be probed, as the top quark decays before hadronization. Therefore, our main focus is on rare charm decays, induced by a $c \to u$ transition, see Chapters 3 to 5. These are the unique up-type candidates to probe flavor in the SM and beyond. Ultimately, all of the aforementioned FCNCs need to be analyzed to fully explore the quantum structure of quark flavor physics. We will therefore globally investigate FCNCs with dineutrinos in Chapter 6.

In Fig. 2.1 we illustrate typical one-loop contributions to $b \to s$ (left) and $c \to u$ (right) FCNCs in the SM. Differences between the up- and the down-sector loop only occur due to the internal quarks. This has, however, a significant impact on the size of the contribution. Neglecting quark masses, the sum over internal quarks leads to a sum of CKM factors that vanishes due to unitarity. This cancellation is

Figure 2.1: FCNCs in the SM for $b \to s$ (left) and $c \to u$ (right) transitions. Insertions of CKM factors at every dot are understood.

referred to as the GIM mechanism [15]. The otherwise exact GIM cancellation of the amplitude is broken by the differences in the quark masses. Therefore, down-type FCNCs are driven by the heavy top-quark mass, whereas for up-type FCNCs the GIM mechanism is more efficient. For rare charm transitions in particular, a generic $c \to u$ amplitude can be written as

$$\mathcal{A}(c \to u) \sim \frac{1}{16\pi^2} V_{cs}^* V_{us} \cdot \left(\frac{m_s^2}{m_W^2} - \frac{m_d^2}{m_W^2} \right) + \frac{1}{16\pi^2} V_{cb}^* V_{ub} \cdot \left(\frac{m_b^2}{m_W^2} - \frac{m_d^2}{m_W^2} \right) . \tag{2.11}$$

In Eq. (2.11) the first term is GIM suppressed due to small differences between the strange and the down quark mass. The second term suffers from a strong CKM suppression of order $V_{cb}^* V_{ub} \sim \mathcal{O}(\lambda^5)$ and also includes the only involved CP–violating phase. Using masses from App. A, we obtain $\mathrm{Re}[\mathcal{A}(c \to u)] \sim 5 \cdot 10^{-9}$. In $b \to s$ a similar estimate yields $\mathrm{Re}[\mathcal{A}(b \to s)] \sim 10^{-3}$. We learn that FCNCs are tiny in rare charm decays, however enhanced by QCD effects, discussed in the next sections. In the down-type sector the GIM cancellation is lifted by the heavy top quark mass and therefore the weak SM amplitude is significantly larger than in rare charm decays. BSM physics on the other hand is not necessarily suffering from CKM and GIM suppression, and therefore searches in rare FCNC decays are encouraged.

2.1.2 Motivation for physics beyond the Standard Model

Despite its success and the lack of direct discoveries of NP particles, the SM is not the fundamental theory of nature. The first clear indication of BSM physics is the experimental observation of neutrino oscillations [27] by the Sudbury Neutrino Observatory [31] and the Super-Kamiokande experiment [30]. Although not directly measured, the evidence for neutrino oscillations implies non-vanishing neutrino masses, which is not possible within the SM, due to the lack of RH neutrinos. The mixing mechanism of the different neutrino flavors can again be described by a mismatch of gauge and mass bases and is encoded in the so-called Pontecorvo-Maki-Nakagawa-Sakata (PMNS) matrix [27–29] in analogy to the CKM matrix in the quark sector.

There are several more shortcomings of the SM from cosmological observations. First of all, the visible matter only amounts to 5 % of the energy budget of the universe. Larger amounts of this budget are taken by dark matter and dark energy, both of which are unexplained within the SM. On top of that, the Sakharov conditions [33] imply that the observed baryon asymmetry in the universe, *i.e.* the fact

that we observe galaxies formed from matter and none from antimatter, is only achieved via processes in the early universe that fulfill three conditions. The first is the violation of baryon number B, the second is the violation of C- and CP–symmetry, and the last one are so-called out-of-thermal-equilibrium processes. In order to achieve the observed baryon asymmetry of the universe, new sources of baryon- or lepton-number violating processes as well as new sources of CP–violation are needed. Also cosmology deals with effects of gravity at large scales, an interaction not included in the SM as a quantum theory.

A more phenomenological argument for BSM physics is connected to the flavor puzzle. Most of the free parameters of the SM are part of the flavor sector. As such, a fundamental theory should be able to explain the observed hierarchies between masses and CKM entries, rather than having them as free and accidental parameters. Several BSM models are proposed, which incorporate these hierarchies as flavor symmetries. Those BSM scenarios include minimal supersymmetric models [136], $U(1)_{\text{FN}}$ Frogatt-Nielson extensions [137], discrete symmetries [138] and LQ–models [90, 139, 140].

The last motivation to further study BSM effects in flavor physics is the emergence of first hints for NP in several B–decay observables and measurements of the muon anomalous magnetic moment.

B–decays have served as standard candles for the field of flavor physics ever since the planning and operation of the B–factories Belle at KEKB in Tsukuba and BaBar at SLAC, see Ref. [141] for an extensive overview. In recent years, the flavor physics program at the Large Hadron Collider (LHC) in Geneva, mostly carried out by the LHCb experiment, as well as results from Babar and Belle lead to the emergence of deviations in $b \to s\ell^+\ell^-$ and $b \to c\ell^-\bar{\nu}_\ell$ induced observables and motivates future flavor physics programs, see Ref. [63]. For the FCNC $b \to s\ell^+\ell^-$, suppressed branching ratio measurements [38–41], as well as deviations in angular asymmetries [42–47] make up a first class of observables which show deviations from the SM predictions. These measurements are, however, subject to potentially sizable hadronic uncertainties, as discussed in Refs. [142–146]. Deviations in optimized observables [147, 148] testing LFU are therefore even more intriguing [34–37]. Similarly, ratios of FCCC $b \to c\ell^-\bar{\nu}_\ell$ branching ratios are put to test and also yield signs of LFU violation [149–155]. All of these anomalies globally do not exceed a deviation at the level of $\sim 2-3\sigma$, see for instance Ref. [55].

Looking at the SM prediction of the muon anomalous magnetic moment [53, 54] an even larger deviation from the experimental average is observed, currently at the level of 4.2σ. The experimental world average includes Run 1 of the Fermilab $g-2$ experiment [48–51], as well as the earlier BNL measurement [52], which are in agreement with each other.

Until future clarification, either due to theory improvements or due to upcoming updated measurements with a higher statistical significance, these hints will stay and provide guidance for model building. Cross-checks with other flavor sectors will help to disentangle the nature of possible BSM physics.

One necessity is to investigate FCNC decays in the up-type sector. Here, rare charm decays are the ideal candidate to perform SM tests, which is demonstrated in later chapters of this work. We also refer to Ref. [5] for a recent review.

2.2 Effective field theories

Due to the absence of direct evidence for BSM physics in high-energy measurements as of today and the remarkable success of the SM, most models introducing NP particles are already tightly constrained. This fact leads to a splitting of active research into two frontiers. One possibility is to introduce weakly interacting massive particles (WIMPs) or even feebly interacting massive particles (FIMPs) with light masses but tiny couplings, *e.g.* as dark matter candidates as in Refs. [156, 157] and references therein. The second possibility is to introduce massive NP particles with masses well separated from the electroweak scale ($\sim m_W$, m_Z, m_h, m_t). In the second scenario, indirect searches become crucial as the energy to directly produce these particles might not be available at the LHC. Since ambiguities with several models explaining the same signatures in data cannot be avoided, a global and model-independent framework is needed to interpret data and identify deviations from the SM. This framework is represented by an EFT and allows to systematically decouple heavy degrees of freedom from a description at lower energies given a sufficient separation of these scales, which is known as the Appelquist-Carazzone decoupling theorem [158]. Within an EFT a large class of models are tested simultaneously in a *bottom-up* approach. Instead of calculating contributions to several observables within one model (*top-down*), deviations of large sets of experimental data from the SM are tested model-independently and provide guidance for model-building. However, the bottom-up approach requires to add all possible terms, while top-down requires only those that are induced at a certain scale by the model.

As a historic example, Fermi's theory for β–rays [159] can be understood as an EFT. In this theory, the massive W– and Z–bosons are integrated out and not present as dynamical degrees of freedom. Instead, their effect is encoded in a coupling constant. The corresponding Hamiltonian for nuclear β decay is $d \to u e \bar{\nu}_e$ induced and given by

$$\mathcal{H}_{\text{Fermi}} = -\frac{4G_F}{\sqrt{2}} V_{ud}\, C\, (\bar{u}\gamma_\mu P_L d)(\bar{e}\gamma_\mu P_L \nu_e) + \mathcal{O}\left(\frac{q^2}{m_W^2}\right), \tag{2.12}$$

with $P_L = \frac{1}{2}(1-\gamma_5)$ being the LH projector, C the Wilson coefficient and $G_F = \frac{\sqrt{2}g_w^2}{8m_W^2}$ the Fermi constant with the numerical value given in App. A. Since the full theory is known, C is determined by matching the full theory onto the EFT at the mass scale of the particle integrated out, here m_W. Due to the normalization, $C = 1$ at leading order (LO). The process of integrating out the W–boson is shown diagramatically in Fig. 2.2.

The approach of writing down interactions as a sum of products of Wilson coefficients and effective vertices as in Eq. (2.12) is formally referred to as the OPE and allows to systematically study all possible interactions [124, 160]. Note that operators with higher mass dimension, *i.e.* involving more particle fields, are suppressed by higher powers of the heavy mass scale, given by m_W in Fermi's theory.

Since EFTs are often used for decays of hadrons, the energy scale is set by the hadron mass, whereas the Wilson coefficients are evaluated at the electroweak scale. Therefore, QCD corrections need to be

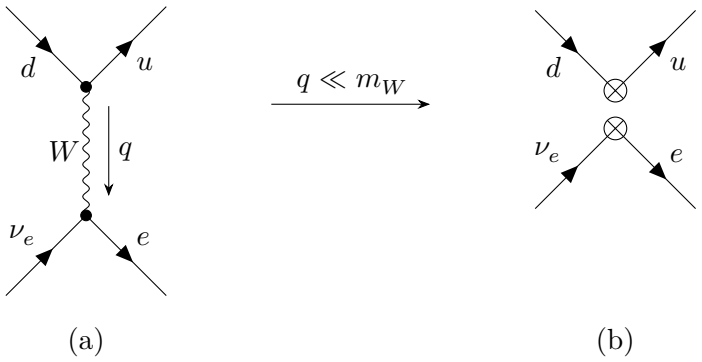

Figure 2.2: Feynman diagrams for nuclear β decay in (a) the full theory, *i.e.* the LO SM and (b) Fermi's theory.

accounted for. Consider the general effective Hamiltonian at dimension six

$$\mathcal{H}_{\text{eff}} = \frac{1}{\Lambda^2} \sum C_i(\mu) O_i(\mu) \,, \tag{2.13}$$

where we introduced the renormalization scale μ. We require our theory to be independent of this scale, and therefore

$$\frac{\mathrm{d}(C_i(\mu)O_i(\mu))}{\mathrm{d}\log\mu} = 0 = \left(\frac{\mathrm{d}C_i(\mu)}{\mathrm{d}\log\mu}\right) O_i(\mu) + C_i(\mu)\,\frac{\mathrm{d}O_i(\mu)}{\mathrm{d}\log\mu}\,. \tag{2.14}$$

Due to this requirement and the renormalization of operators

$$\frac{\mathrm{d}O_i(\mu)}{\mathrm{d}\log\mu} = -\gamma_{ij} O_j \,, \tag{2.15}$$

which defines the anomalous dimension matrix (ADM) γ_{ij}, we find for the running of the Wilson coefficients

$$\frac{\mathrm{d}C_i(\mu)}{\mathrm{d}\log\mu} = \gamma_{ji} C_j = (\gamma^T)_{ij} C_j \,. \tag{2.16}$$

The ADM can be systematically calculated order by order in $\alpha_s = g_s^2/(4\pi)$ as $\gamma_{ij}(\alpha_s) = \sum_k \gamma_{ij}^{(k)} \left(\frac{\alpha_s}{4\pi}\right)^k$, yielding for the Wilson coefficients at LO

$$\vec{C}(\mu) = \vec{C}(\Lambda)\, \exp\left(\frac{\gamma^{(0)T}}{2\beta_0^{(n_f)}} \cdot \log\frac{\alpha_s(\Lambda)}{\alpha_s(\mu)}\right) = \vec{C}(\Lambda)\, \left(\frac{\alpha_s(\Lambda)}{\alpha_s(\mu)}\right)^{\frac{\gamma^{(0)T}}{2\beta_0^{(n_f)}}} \,, \tag{2.17}$$

with $\beta_0^{(n_f)} = 11 - \frac{2}{3}n_f$ the LO beta function for the running of α_s and n_f the number of active quarks, *i.e.* $n_f = 5$ for scales between the b–quark and the t-quark mass. The numerical value of α_s at the scale of the Z–boson mass is given App. A. The solution in Eq. (2.17) is the leading logarithmic order (LLO) and resums contributions of the form $\left(\alpha_s \log \frac{\Lambda}{\mu}\right)^n$ to all orders ($n \in \mathbb{N}_0$). At next-to-leading logarithmic order (NLLO), contributions of the form $\alpha_s \cdot \left(\alpha_s \log \frac{\Lambda}{\mu}\right)^n$ are resummed and likewise for higher orders.

For further details on the general concept of EFTs we refer to Refs. [124, 160–165].

2.2.1 Wilson coefficients at the charm mass scale

In this section, the calculation of SM Wilson coefficients for semileptonic $c \to u\ell^+\ell^-$ transitions at the charm mass scale $\mu_c \sim m_c$ is outlined. The presented results are based on Refs. [86, 87, 90] and the PhD thesis [166], which is why we only give a brief outline and refer to the aforementioned references for details on the calculation. The relevant effective Hamiltonian reads

$$\mathcal{H}_{\text{eff}}^{\text{weak}}\Big|_{m_W \geq \mu > m_b} = -\frac{4\,G_F}{\sqrt{2}} \sum_{q \in \{d,\,s,\,b\}} V_{cq}^* V_{uq} \left(\widetilde{C}_1(\mu) P_1^{(q)} + \widetilde{C}_2(\mu) P_2^{(q)}\right) , \tag{2.18}$$

$$\mathcal{H}_{\text{eff}}^{\text{weak}}\Big|_{m_b > \mu \geq m_c} = -\frac{4\,G_F}{\sqrt{2}} \sum_{q \in \{d,\,s\}} V_{cq}^* V_{uq} \left(\widetilde{C}_1(\mu) P_1^{(q)} + \widetilde{C}_2(\mu) P_2^{(q)} + \sum_{i=3}^{10} \widetilde{C}_i(\mu) P_i\right) , \tag{2.19}$$

with a sum over light down-type fields. Above the b–quark mass scale, only the operators $P_{1,\,2}^{(q)}$ contribute

$$P_1^{(q)} = (\bar{u}_L \gamma_\mu T^a q_L)(\bar{q}_L \gamma^\mu T^a c_L) , \qquad P_2^{(q)} = (\bar{u}_L \gamma_\mu q_L)(\bar{q}_L \gamma^\mu c_L) . \tag{2.20}$$

At m_b further operators P_i with $i = 3, \ldots 10$ are also induced and are defined as

$$\begin{aligned}
P_3 &= (\bar{u}_L \gamma_\alpha c_L) \sum_{\{q:m_q<\mu\}} (\bar{q}\gamma^\alpha q) , & P_4 &= (\bar{u}_L \gamma_\alpha T^a c_L) \sum_{\{q:m_q<\mu\}} (\bar{q}\gamma^\alpha T^a q) , \\
P_5 &= (\bar{u}_L \gamma_\alpha \gamma_\beta \gamma_\rho c_L) \sum_{\{q:m_q<\mu\}} (\bar{q}\gamma^\alpha \gamma^\beta \gamma^\rho q) , & P_6 &= (\bar{u}_L \gamma_\alpha \gamma_\beta \gamma_\rho T^a c_L) \sum_{\{q:m_q<\mu\}} (\bar{q}\gamma^\alpha \gamma^\beta \gamma^\rho T^a q) , \\
P_7 &= \frac{e}{g_s^2} m_c \,(\bar{u}_L \sigma^{\mu\nu} c_R)\, F_{\mu\nu} , & P_8 &= \frac{1}{g_s} m_c \,(\bar{u}_L \sigma^{\mu\nu} T^a c_R)\, G^a_{\mu\nu} , \\
P_9 &= \frac{e^2}{g_s^2} (\bar{u}_L \gamma_\mu c_L) \left(\bar{\ell}\gamma^\mu \ell\right) , & P_{10} &= \frac{e^2}{g_s^2} (\bar{u}_L \gamma_\mu c_L) \left(\bar{\ell}\gamma^\mu \gamma_5 \ell\right) .
\end{aligned} \tag{2.21}$$

In Eqs. (2.20) and (2.21) the generators T^a correspond to $SU(3)_C$, $q_{L/R} = \frac{1}{2}(1 \mp \gamma_5)q$ are chiral quark fields, $\sigma^{\mu\nu} = \frac{\mathrm{i}}{2}[\gamma^\mu, \gamma^\nu]$, and the electromagnetic and chromomagnetic field strength tensors $F_{\mu\nu}$ and $G^a_{\mu\nu}$ are defined as in Eq. (2.2).

Contributions to the operators in Eq. (2.21) are not induced at the matching scale $\mu \sim m_W$ because they are driven by penguin-type diagrams involving down-type quarks in the loop. For consistency,

light quark fields form the operators but do not contribute to Wilson coefficients, which is why effects of down-type quark masses are set to zero and the GIM cancellation becomes exact. When masses are kept finite, large logarithms of ratios involving light quark masses are induced [166, 167]. We also neglect contributions from primed operators, obtained from Eqs. (2.20) and (2.21) by $L \leftrightarrow R$, as the chirality flip yields an $\frac{m_u}{m_c}$ suppression.

The calculation of SM Wilson coefficients is performed at (partly) next-to-next-to-leading logarithmic order (NNLLO) in QCD,

$$\widetilde{C}_i(\mu) = \widetilde{C}_i^{(0)}(\mu) + \frac{\alpha_s(\mu)}{4\pi}\,\widetilde{C}_i^{(1)}(\mu) + \left(\frac{\alpha_s(\mu)}{4\pi}\right)^2 \widetilde{C}_i^{(2)}(\mu) + \mathcal{O}(\alpha_s^3(\mu))\,. \tag{2.22}$$

The procedure is as follows. The Wilson coefficients $\widetilde{C}_1$ and $\widetilde{C}_2$ are calculated at the matching scale μ_W at next-to-next-to-leading order (NNLO). As a second step, the renormalization group (RG)–evolution down to m_b is performed at NNLLO in the RG-improved perturbation theory. A five-to-four flavor matching is applied at next-to-leading order (NLO) at μ_b, where the b–quark is integrated out. Parts of the NNLO contributions are included as well. In this step, Wilson coefficients corresponding to operators in Eq. (2.21) are induced. Finally, the RG–evolution of all Wilson coefficients is performed again at NNLLO. In principle, the use of different orders in the individual steps is inconsistent, however, missing NNLO calculations for the matching at μ_b are expected to be small [166].

Following these steps and implementing them in a *Python* script yields the Wilson coefficients presented in Tab. 2.2, where $\mu_c \in \left[\frac{m_c}{\sqrt{2}}, \sqrt{2}\,m_c\right]$ is taken as an scale uncertainty. In addition, we explicitly checked that further scale uncertainties induced by the variations $\mu_W = \left[\frac{m_W}{2}, 2\,m_W\right]$ and $\mu_b = \left[\frac{m_b}{2}, 2\,m_b\right]$ have negligible effect compared to the charm scale variation. In Tab. 2.2, the first three columns show the NNLLO result for three different choices of the charm scale. The last column shows the central value and symmetrized uncertainty of the respective Wilson coefficient. The obtained values are in agreement with Refs. [86, 87, 90, 166][1]. We provide the results of Tab. 2.2 split into LO, NLO and NNLO contributions as in Eq. (2.22) in App. B.

For the phenomenological analysis of semileptonic $c \to u\ell^+\ell^-$ processes, it is useful to define a different and extended basis of operators. We use

$$\mathcal{H}_{\text{eff}} \supset -\frac{4G_F}{\sqrt{2}}\frac{\alpha_e}{4\pi}\sum_k (C_k O_k + C'_k O'_k)\,, \tag{2.23}$$

where $\alpha_e = e^2/(4\pi)$ is the electromagnetic fine-structure constant and we refer to App. A for the

[1] There is a sign typo for $\widetilde{C}_6^{(1)}$ in [166].

Table 2.2: SM Wilson coefficients $\widetilde{C}_j(\mu)$ for $j \in [1, 10]$ up to (partly) NNLO accuracy. In the first three columns we display the values obtained for the three different choices of the charm mass scale $\mu = \sqrt{2}\, m_c$, $\mu = m_c$ and $\mu = m_c/\sqrt{2}$. The last column displays the central value and symmetrized uncertainty.

	$\mu = \sqrt{2}\, m_c$	$\mu = m_c$	$\mu = m_c/\sqrt{2}$	$\widetilde{C}_j$	$\pm$	$\Delta\widetilde{C}_j$
$\widetilde{C}_1(\mu)$	−0.5159	−0.6402	−0.7902	−0.64	$\pm$	0.14
$\widetilde{C}_2(\mu)$	1.0257	1.0349	1.0431	1.035	$\pm$	0.009
$\widetilde{C}_3(\mu)$	−0.0037	−0.0084	−0.0184	−0.008	$\pm$	0.007
$\widetilde{C}_4(\mu)$	−0.0583	−0.0953	−0.1649	0.095	$\pm$	0.05
$\widetilde{C}_5(\mu)$	0.0002	0.0005	0.0011	0.0005	$\pm$	0.0005
$\widetilde{C}_6(\mu)$	0.0002	0.0009	0.0031	0.0009	$\pm$	0.0015
$\widetilde{C}_7(\mu)$	0.0020	0.0038	0.0071	0.004	$\pm$	0.003
$\widetilde{C}_8(\mu)$	0.0013	−0.0024	−0.0046	−0.002	$\pm$	0.002
$\widetilde{C}_9(\mu)$	−0.0083	−0.0133	−0.0214	−0.013	$\pm$	0.006
$\widetilde{C}_{10}(\mu)$	0.0000	0.0000	0.0000	0	$\pm$	0

numerical value. The operators O_k are given as follows

$$\begin{aligned}
O_7 &= \frac{m_c}{e}(\overline{u}_L\sigma_{\mu\nu}c_R)F^{\mu\nu}\,, & O_7' &= \frac{m_c}{e}(\overline{u}_R\sigma_{\mu\nu}c_L)F^{\mu\nu}\,,\\
O_9 &= (\overline{u}_L\gamma_\mu c_L)(\bar{\ell}\gamma^\mu\ell)\,, & O_9' &= (\overline{u}_R\gamma_\mu c_R)(\bar{\ell}\gamma^\mu\ell)\,,\\
O_{10} &= (\overline{u}_L\gamma_\mu c_L)(\bar{\ell}\gamma^\mu\gamma_5\ell)\,, & O_{10}' &= (\overline{u}_R\gamma_\mu c_R)(\bar{\ell}\gamma^\mu\gamma_5\ell)\,,\\
O_S &= (\overline{u}_L c_R)(\bar{\ell}\ell)\,, & O_S' &= (\overline{u}_R c_L)(\bar{\ell}\ell)\,,\\
O_P &= (\overline{u}_L c_R)(\bar{\ell}\gamma_5\ell)\,, & O_P' &= (\overline{u}_R c_L)(\bar{\ell}\gamma_5\ell)\,,\\
O_T &= \frac{1}{2}(\overline{u}\sigma_{\mu\nu}c)(\bar{\ell}\sigma^{\mu\nu}\ell)\,, & O_{T5} &= \frac{1}{2}(\overline{u}\sigma_{\mu\nu}c)(\bar{\ell}\sigma^{\mu\nu}\gamma_5\ell)\,.
\end{aligned} \tag{2.24}$$

We have added (pseudo-)scalar operators $O_{S,P}$, tensor operators $O_{T,T5}$ and primed operators, as while they do not receive contributions within the SM, they might be induced in BSM models. Again, the primed operators are obtained by $L \leftrightarrow R$. The connection of the results presented in Tab. 2.2 and the basis in Eq. (2.24) reads

$$C_{7,9}^{\text{eff}} = \frac{4\pi}{\alpha_s}\left[V_{cd}^* V_{ud}\, C_{7,9}^{\text{eff}(d)}(q^2) + V_{cs}^* V_{us}\, C_{7,9}^{\text{eff}(s)}(q^2)\right]\,, \tag{2.25}$$

where $C_{7,9}^{\text{eff}(q)}(q^2)$ for $q = d$, s are q^2 dependent effective coefficients containing all contributions of the operators in Eqs. (2.20) and (2.21) as well as two-loop virtual corrections from Ref. [86]. q^2 denotes

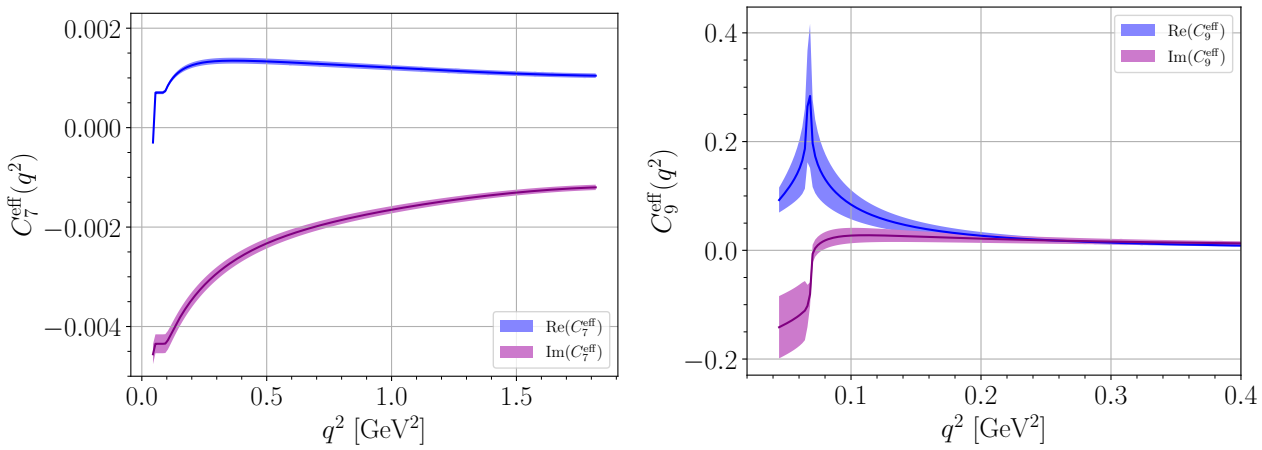

Figure 2.3: Real and imaginary parts of perturbative contributions to C_7^{eff} (left), C_9^{eff} (right) in the SM as functions of q^2 in blue and lilac, respectively. $C_9^{\text{eff}}(q^2)$ is not shown above $q^2 \gtrsim 0.4\,\text{GeV}^2$ as it remains essentially constant. The uncertainty bands are mainly due to the scale uncertainty μ_c.

the dilepton invariant mass, *i.e.* the momentum transfer to the lepton pair in the $c \to u\ell^+\ell^-$ process. We give explicit expressions for $C_{7,9}^{\text{eff}(q)}(q^2)$ in App. B, however, we display the real and imaginary parts of Eq. (2.25) here in Fig. 2.3.

No further perturbative contributions exist in the SM for rare charm decays at this level of precision. NP contributions can be studied model-independently as additional contributions to Wilson coefficients of the operators in Eq. (2.24). Fig. 2.3 demonstrates the effects of the severe GIM cancellation in rare charm decays. Perturbative contributions to C_7 do not exceed $\sim 10^{-3}$, and C_9 is below $\mathcal{O}(0.01)$ for most of the kinematic region and only reaches $\mathcal{O}(0.4)$ at a narrow peak in the very low q^2 region. Note that QED corrections at two-loop order affect the SM values of C_9 and C_{10}, however, naïve estimates of these effects amount to $\mathcal{O}(3\,\%)$ changes for C_9, while for C_{10} they imply the upper limit $C_{10}^{\text{eff}} < 0.01 \cdot C_9^{\text{eff}}$ [166], which is at least one order below C_7^{eff}.

2.2.2 Dineutrino Wilson coefficients

The situation further simplifies in the case of rare charm dineutrino transitions $c \to u\nu\bar{\nu}$. In the SM, no light RH neutrinos exist and therefore only two operators contribute for each neutrino flavor combination ij. Thus, the Hamiltonian is given by

$$\mathcal{H}_{\text{eff}}^{\nu_i\bar{\nu}_j} = -\frac{4\,G_{\text{F}}}{\sqrt{2}}\frac{\alpha_e}{4\pi}\left(\mathcal{C}_L^{ij}Q_L^{ij} + \mathcal{C}_R^{ij}Q_R^{ij}\right) + \text{h.c.}\,, \tag{2.26}$$

with the four-fermion operators

$$\begin{aligned} Q_L^{ij} &= (\bar{u}_L \gamma_\mu c_L)\,(\bar{\nu}_{jL} \gamma^\mu \nu_{iL})\,, \\ Q_R^{ij} &= (\bar{u}_R \gamma_\mu c_R)\,(\bar{\nu}_{jL} \gamma^\mu \nu_{iL})\,, \end{aligned} \tag{2.27}$$

and where i, j sum the neutrino flavors in the mass basis. No further dimension-six operators exist in $\mathcal{H}_{\text{eff}}^{\nu_i \bar{\nu}_j}$. In Eq. (2.26) the normalization with $\frac{\alpha_e}{4\pi}$ is used in order to easily compare to

$$\mathcal{H}_{\text{eff}}^{\ell_i \bar{\ell}_j} = -\frac{4\,G_{\text{F}}}{\sqrt{2}} \frac{\alpha_e}{4\pi} \left(\mathcal{K}_L^{ij} O_L^{ij} + \mathcal{K}_R^{ij} O_R^{ij} \right) + \text{h.c.}\,, \tag{2.28}$$

where the dilepton operators are then given by

$$O_L^{ij} = (\bar{u}_L \gamma_\mu c_L)\,(\bar{\ell}_{jL} \gamma^\mu \ell_{iL})\,, \tag{2.29}$$

$$O_R^{ij} = (\bar{u}_R \gamma_\mu c_R)\,(\bar{\ell}_{jL} \gamma^\mu \ell_{iL})\,, \tag{2.30}$$

and finally to connect with Eq. (2.23), we find the matching conditions

$$\mathcal{K}_L^{ii} = C_9 - C_{10}\,, \tag{2.31}$$

$$\mathcal{K}_R^{ii} = C_9' - C_{10}'\,, \tag{2.32}$$

which holds for all $i = e,\, \mu,\, \tau$. With these connections we see that $\mathcal{K}_L^{ii}$ is tiny in the SM and all other contributions ($i \neq j$) vanish. Especially, contributions to $\mathcal{C}_{L,\,R}^{ij}$ are absent, as they can only be induced via Z penguins, which are GIM canceled for up-type FCNCs and no electromagnetic corrections exist, due to the neutrinos in the final state. For the purpose of our analysis in Chapter 6, we will completely neglect SM effects. The reason is that NP effects can be sizable and interference effects with the SM contributions in $\mathcal{K}_L^{ii}$ are numerically small.

Of course the basis in Eq. (2.26) is enlarged if light RH neutrinos are taken into account. They form the following additional operators

$$\begin{aligned} Q_{LR}^{ij} &= (\bar{u}_L \gamma_\mu c_L)\,(\bar{\nu}_{jR} \gamma^\mu \nu_{iR})\,, & Q_{RR}^{ij} &= (\bar{u}_R \gamma_\mu c_R)\,(\bar{\nu}_{jR} \gamma^\mu \nu_{iR})\,, \\ Q_S^{ij} &= (\bar{u}_L c_R)\,(\bar{\nu}_j \nu_i)\,, & Q_S'^{ij} &= (\bar{u}_R c_L)\,(\bar{\nu}_j \nu_i)\,, \\ Q_P^{ij} &= (\bar{u}_L c_R)\,(\bar{\nu}_j \gamma_5 \nu_i)\,, & Q_P'^{ij} &= (\bar{u}_R c_L)\,(\bar{\nu}_j \gamma_5 \nu_i)\,, \\ Q_T^{ij} &= (\bar{u} \sigma_{\mu\nu} c)\,(\bar{\nu}_j \sigma^{\mu\nu} \nu_i)\,, & Q_{T5}^{ij} &= (\bar{u} \sigma_{\mu\nu} c)\,(\bar{\nu}_j \sigma^{\mu\nu} \gamma_5 \nu_i)\,. \end{aligned} \tag{2.33}$$

Clearly, the situation simplifies drastically in the SM, where only LH neutrinos build the operators. We will investigate in Chapter 6 which implications can be drawn from the two-operator-scenario, and how one can probe for the existence of the further operators in Eq. (2.33).

2.2.3 Standard model effective field theory and connections to other sectors

In this section, we briefly introduce the SMEFT. Here, all SM particles are kept as light particles and appear in the operators. Assuming BSM physics to be sufficiently separated from the electroweak scale, one is led to an EFT which is the formal model-independent generalization of the SM[2]. Consequently, only NP contributions enter the Wilson coefficients in SMEFT and higher dimensional operators are added to the SM Lagrangian

$$\mathcal{L}_{\text{SMEFT}} = \mathcal{L}_{\text{SM}} + \sum_{d=5}^{\infty} \sum_{i}^{n_d} \frac{C_i^{(d)}}{\Lambda^{d-4}} Q_i^{(d)} \,, \tag{2.34}$$

where d denotes the dimension of the effective operator and n_d is the number of independent operators at dimension d. For each dimension d the higher dimensional operators are suppressed by $d-4$ powers of the NP scale Λ, such that it is sufficient to only consider the first appearing terms in the infinite sum. A very clear distinction from the WET is that operators are required to be invariant under the full SM gauge group. At dimension five, only a single operator exists [169], which can generate Majorana masses for neutrinos and is lepton-number violating. Even-dimensional operators on the other hand conserve both lepton and baryon number [170, 171]. The foundations of SMEFT dimension-six operators were given in Ref. [172], however, an overcomplete set is given. The first basis without redundancies, now referred to as the Warsaw basis, was given in Ref. [173]. Operators at higher dimensions are also known and can be obtained by an algorithm known in the literature, see the recent review Ref. [174] and references therein. The main argument to utilize the SMEFT framework is that it is model-independent (assuming NP to be sufficiently heavy) and therefore able to test the SM in all sectors simultaneously by performing a global fit of SMEFT Wilson coefficients. However, the prize to pay is the huge number of free parameters. Although only 59 independent operators exist at dimension six, there are flavor indices to be taken into account. In the most general case, operators with different flavor indices are not connected, such that the number of free parameters at dimension six increases to 2499. In order to make progress with limited data at hand, it is therefore necessary to investigate parts of the full SMEFT parameter set. That is why we refrain from listing the full set of 59 operators at dimension six. Instead, we quote operators relevant for this work, which are the four-fermion operators

$$\mathcal{L}_{\text{SMEFT}} \supset \frac{C_{\ell q}^{(1)}}{v^2} \bar{Q}\gamma_\mu Q\, \bar{L}\gamma^\mu L + \frac{C_{\ell q}^{(3)}}{v^2} \bar{Q}\gamma_\mu \tau^a Q\, \bar{L}\gamma^\mu \tau^a L + \frac{C_{\ell u}}{v^2} \bar{U}\gamma_\mu U\, \bar{L}\gamma^\mu L + \frac{C_{\ell d}}{v^2} \bar{D}\gamma_\mu D\, \bar{L}\gamma^\mu L \,. \tag{2.35}$$

Here, τ^a are the Pauli-matrices. We have dropped four flavor indices in each operator and Wilson coefficient for readability, but note that these are crucial when effects of these operators are studied.

Although the ultimate goal would be a global fit to SMEFT Wilson coefficients including all 2499 free parameters (at dimension six), the SMEFT framework allows for fundamental and consistent

[2] A second implicit assumption in SMEFT is that the discovered Higgs boson is indeed a fundamental $SU(2)_L$ particle. An even more general ansatz relaxing this assumption is given by the so-called Higgs Effective Field Theory (HEFT), see for example Ref. [168].

analyses already with a limited amount of available data. Furthermore, the SMEFT helps to correlate different sectors and provides guidance for NP searches in flavor physics. As discussed in detail in Chapter 6, the operators in Eq. (2.35) allow to connect different quark and lepton flavor sectors via dineutrino observables.

2.3 Summary of standard model Wilson coefficients

To summarize the chapter, we collect SM contributions to Wilson coefficients for $c \to u$ FCNCs within the different implementations. In the WET only C_7 and C_9 receive finite contributions. However, these are negligibly small, see Fig. 2.3. We quote again

$$\begin{aligned} C_7^{\text{eff}}(q^2) &\lesssim 5 \times 10^{-3}\,, \\ C_9^{\text{eff}}(q^2 > 0.2\,\text{GeV}^2) &\lesssim 5 \times 10^{-2}\,. \end{aligned} \tag{2.36}$$

For dineutrino modes we work with

$$\mathcal{K}_L^{ij}|_{\text{SM}} = \mathcal{K}_R^{ij}|_{\text{SM}} = 0 \quad \forall i,\, j \in [1,\, 2,\, 3]\,, \tag{2.37}$$

as SM effects are not within reach of current and (foreseeable) future flavor experiments. Lastly, we note again that by construction SMEFT Wilson coefficients vanish in the absence of BSM physics, see Eq. (2.34). As we have seen, this also holds in the WET for $c \to u\ell^+\ell^-$ and $c \to u\nu\bar{\nu}$ induced modes to good approximation, but is different for down-type flavor transitions, see Secs. 6.3 and 6.4.

3 Phenomenology of rare charm decays in the Standard Model

We discuss the SM phenomenology of (differential) branching ratios and CP–asymmetries in rare charm decay channels as well as CP–asymmetries in two-body hadronic D–meson decays. First, we give a general overview of different concepts for the parametrization of hadronic matrix elements available in the literature in Sec. 3.1. In Sec. 3.2 we turn to rare charm decays and discuss $\mathcal{B}(D^0 \to \ell^+\ell^-)$ with $\ell = e, \mu$. Sec. 3.3 contains the SM phenomenology for semileptonic D–meson decays such as $D^+ \to \pi^+\ell^+\ell^-$. Here, we discuss utilized form factors and SM contributions from intermediate resonances, which turn out to dominate the differential branching ratio in the full phase space region in semileptonic rare charm decays. We estimate and discuss (differential) branching ratios in the SM. A similar strategy is utilized to obtain the SM phenomenology in semileptonic three- and four-body decays of charmed baryons in Sec. 3.4. Finally, we discuss generalities as well as the SM phenomenology of CP–asymmetries for the rare charm decay modes as well as for hadronic decays in Sec. 3.5.

3.1 Parametrization of non-perturbative hadronic matrix elements

As introduced in Sec. 2.2 the OPE leads to a factorization in Wilson coefficients and effective operators, where the latter are split into lepton and quark currents. Effects from the lepton currents are calculated perturbatively, whereas the quark currents are sandwiched between matrix elements of either a vacuum state or a physical hadronic state and suffer from non-perturbative QCD dynamics. It is however useful to exploit the Lorentz structure of *hadronic matrix elements* as well as symmetries of QCD such as parity conservation and split contributions accordingly. This leads to a separation of effects into contributions proportional to so-called *decay constants* and *form factors*. More details and numerical values for form factors and decay constants of multiple (semi-)leptonic decay modes discussed throughout this thesis are compiled in App. C. Here, we provide an overview of available approaches for the parametrization and calculation of these hadronic matrix elements.

The easiest case is a matrix element involving a single hadronic state, as for instance appearing in purely leptonic decays. This matrix element is proportional to a single non-perturbative factor, which is referred to as the *decay constant* of the hadronic state. Exemplary, the decay constant of the D^0–meson is defined as

$$\langle 0|\overline{u}\gamma^\mu\gamma_5 c|D^0(p)\rangle = -\mathrm{i}f_D p^\mu \,, \tag{3.1}$$

where p^μ is the D^0–meson's four-momentum and only available kinematic variable. A tensor operator cannot contribute, since no anti-symmetric tensor can be built from a single four-vector. For the scalar contribution Eq. (3.1) can simply be multiplied with p_μ and the equations of motion (EOM) of the involved quarks can be applied. Contributions of operators without γ_5 vanish, as the D^0 is parity-odd. Therefore, Eq. (3.1) applies to any pseudoscalar meson and no further non-perturbative factor is needed. Following similar arguments, hadronic matrix elements involving more than one hadronic state are written as linear combinations of available kinematic variables and *form factors*. For example, for a transition $D \to P$ involving two pseudoscalars, as in $D^+ \to \pi^+\ell^+\ell^-$, three independent

form factors, $f_{+,0,T}(q^2)$, are needed to describe all hadronic matrix elements,

$$\langle P(k)|\bar{u}\gamma^\mu c|D(p)\rangle = \left[(p+k)^\mu - \frac{m_D^2 - m_P^2}{q^2}q^\mu\right] f_+(q^2) + q^\mu \frac{m_D^2 - m_P^2}{q^2} f_0(q^2)\,, \tag{3.2}$$

$$\langle P(k)|\bar{u}\sigma^{\mu\nu}(1\pm\gamma_5)c|D(p)\rangle = -\mathrm{i}\,(p^\mu k^\nu - k^\mu p^\nu \pm \mathrm{i}\,\epsilon^{\mu\nu\rho\sigma}p_\rho k_\sigma)\frac{2f_T(q^2)}{m_D + m_P}\,, \tag{3.3}$$

where p, k are the four-momenta of the D–meson and final state meson P, respectively, and $q = p - k$ is the four-momentum of the dilepton system. The dilepton invariant mass squared q^2 will appear frequently as an important kinematic variable and refers to the fraction of energy carried by the lepton pair.

For a $P_1 \to V$ transition, with a vector meson V, seven independent form factors are sufficient to describe all hadronic matrix elements, whereas the number further increases for baryon transitions $B_1 \to B_2$, where ten independent form factors are needed. We refer to App. C for explicit expressions.

For the estimation of decay constants and form factors three different approaches exist:

1) **Fits to experimental data:** Here, one has to assume that a certain semileptonic transition is SM dominated. Then a direct fit of a form factor parametrization to data can be done. However, we will mostly refuse to make use of this possibility, as we are interested in possible NP effects and do not want to make strong assumptions.

2) **Lattice QCD (LQCD):** A straightforward approach towards the calculation of form factors and decay constants is given by LQCD. Here, QCD is simulated on a discrete lattice and within a finite volume instead of the continuous and infinite space-time. This approach is limited by computing power due to discretization uncertainties. As a general feature, the simulation works better if the participating quarks are slow and do not leave the finite volume of the simulation. LQCD is therefore expected to work best at high q^2, or synonymously at low hadronic recoil.

3) **Light-cone sum rules (LCSR):** LCSR are obtained by considering the correlator of the time-ordered product of two quark currents evaluated between the final state on-shell meson and the vacuum [142]. This method is complementary to the LQCD approach as the convergence of the Light-cone expansion is limited and works below a certain q^2 value, and therefore is expected to be applicable especially at low q^2 values, *i.e.* large hadronic recoil.

Due to the complementarity of the different approaches it is customary to combine input from LQCD and LCSR and perform fits for the form factors, see for instance Ref. [144] for modes induced by $b \to s$ and $b \to d$ quark transitions. Further combinations and averages are provided by the HFLAV collaboration, see Refs. [175, 176] for the last two publications and updates at https://hflav.web.cern.ch/.

Despite the increasing effort, form factors often pose the dominant source of theoretical uncertainty in both SM and BSM predictions of semileptonic baryon and meson decays with a typical uncertainty of $\mathcal{O}(10\,\%)$ originating from the non-perturbative hadronic matrix elements.

In the following sections we explicitly provide information for form factors and decay constants used in our analyses either directly in the main text or in App. C. We also focus on rare charm decays from

now on. However, rare decays in other flavor sectors, including form factors and decay constants for $b \to s$, $b \to d$, $s \to d$ transitions, will become relevant in Chapter 6 and are therefore also contained in App. C.

3.2 Leptonic decay $D^0 \to \ell^+\ell^-$

The simplest rare charm decay is the purely leptonic decay of a D^0–meson $D^0 \to \ell^+\ell^-$. In agreement with Ref. [177] and for vanishing up-quark mass we obtain for the branching ratio in terms of Wilson coefficients

$$\begin{aligned}\mathcal{B}(D^0 \to \ell^+\ell^-) = \tau_D \frac{G_F^2 \alpha_e^2 m_D^5 f_D^2}{64\pi^3 m_c^2} \sqrt{1-\frac{4m_\ell^2}{m_D^2}} \Bigg[\left(1-\frac{4m_\ell^2}{m_D^2}\right) |C_S - C_S'|^2 \\ + \left| C_P - C_P' + \frac{2m_\ell m_c}{m_D^2}(C_{10} - C_{10}') \right|^2 \Bigg] ,\end{aligned} \tag{3.4}$$

where τ_D is the lifetime of the D^0–meson and f_D its decay constant defined in Eq. (3.1).

Here, the lepton currents of the respective operators factorize. Due to the helicity suppression, the axial vector contributions from $C_{10}^{(\prime)}$ are m_ℓ^2 suppressed with respect to contributions from (pseudo-)scalar coefficients. Sec. 2.3 implies $C_P^{(\prime)} \sim C_S^{(\prime)} \sim C_{10}^{(\prime)} \sim 0$, so that SM contributions to the leptonic decay are strongly suppressed. In fact, the dominant SM effect for the muon final state is estimated to stem from an intermediate two-photon contribution and scales as [98]

$$\mathcal{B}(D^0 \to \mu^+\mu^-) \sim 2.7 \cdot 10^{-5} \cdot \mathcal{B}(D^0 \to \gamma\gamma) \,. \tag{3.5}$$

Using the current upper limit $\mathcal{B}(D^0 \to \gamma\gamma) < 8.5 \cdot 10^{-7}$ at 90 % confidence level (C.L.) from the Belle collaboration [178], SM effects are not expected above $\mathcal{O}(10^{-11})$. On the other hand the direct search by LHCb [73] resulted in an upper limit of $\mathcal{B}(D^0 \to \mu^+\mu^-) < 6.2 \cdot 10^{-9}$ at 90 % C.L., which already constrains the involved Wilson coefficients in Eq. (3.4). An in-depth discussion of all available bounds on BSM Wilson coefficients is given in Sec. 4.1.

3.3 Semileptonic meson decays $D \to P\ell^+\ell^-$

The first rare charm decays without helicity suppression of (axial) vector operators are the semileptonic decays $D \to \pi\ell^+\ell^-$ and $D_s^+ \to K^+\ell^+\ell^+$ where for the $D \to \pi$ transition both charged and neutral modes are possible. In this section, we study SM contributions to these three decay modes. First we discuss external input for the form factors in Sec. 3.3.1, then we model long-range QCD resonance contributions from intermediate vector and pseudoscalar states, which turn out to dominate the short-distance effects discussed in Sec. 2.2. In Sec. 3.3.3 the resulting phenomenology of both short- and long-distance SM contributions are discussed.

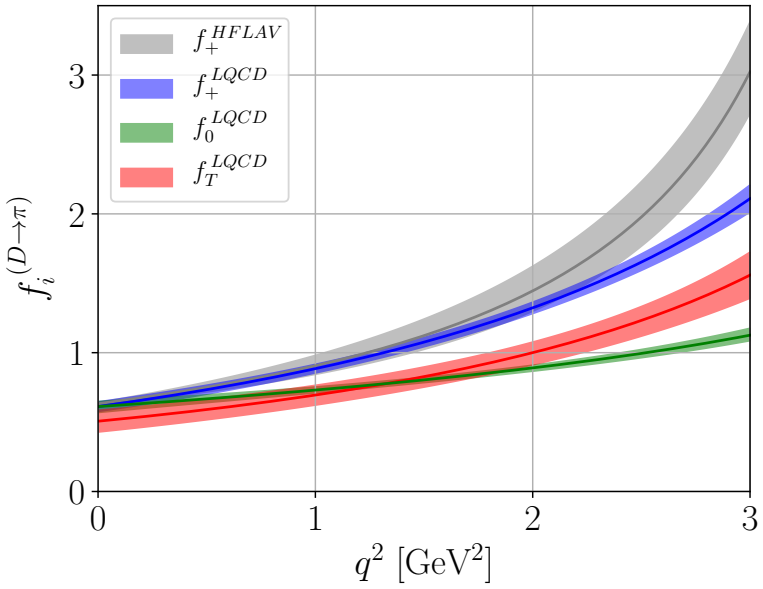

Figure 3.1: The $D \to \pi$ form factors f_+, f_0, f_T from LQCD [179, 180] in blue, red and green, respectively, and f_+ from HFLAV 2017 [175] in gray, solid lines are wrapped by their 1σ uncertainty bands.

3.3.1 Form factors

For the form factors we follow Refs. [179, 180], where LQCD results are reported for $D \to \pi$ transition, the three relevant form factors, $f_{+,0,T}(q^2)$, are defined in Eq. (3.2) and Eq. (3.3). The authors in Refs. [179, 180] make use of the so-called z–expansion, for $i = +, 0, T$,

$$f_i(q^2) = \frac{1}{1 - P_i\, q^2}\left[f_i(0) + c_i\,(z(q^2) - z(0))\left(1 + \frac{z(q^2) + z(0)}{2}\right)\right], \tag{3.6}$$

where

$$z(q^2) = \frac{\sqrt{t_+ - q^2} - \sqrt{t_+ - t_0}}{\sqrt{t_+ - q^2} + \sqrt{t_+ - t_0}}, \quad t_\pm = (m_D \pm m_P)^2\,, \quad t_0 = (m_D + m_P)(\sqrt{m_D} - \sqrt{m_P})^2\,. \tag{3.7}$$

The numerical values of the parameters $f_i(0)$, c_i and P_i along with their uncertainties and covariance matrices are given in [179, 180] and collected for completeness in App. C. Taking into account these correlations, Fig. 3.1 shows the $D \to \pi$ form factors within their 1σ uncertainties. Also shown in gray is f_+ obtained from the HFLAV collaboration as of 2017 [175], where fit parameters are extracted from data on semileptonic $D \to \pi\ell\overline{\nu}$ decays from several experiments. Fig. 3.1 clearly shows the improvements in form factor extractions in the past few years. In the most recent HFLAV update

several lattice calculations are presented and an average can even improve the uncertainty, see Table 280 in Ref. [176] and proves good agreement between the lattice collaborations and between lattice values and results extracted from experimental data. However, since as of today the updated results are only available at $q^2 = 0$, we stick to the results from Refs. [179, 180]. Furthermore, we assume the $D_s \to K$ and $D \to \pi$ form factors to be the same, which is motivated by U- and V-spin symmetry and supported by the lattice study [181]. The $D^0 \to \pi^0$ form factors receive an additional isospin factor $f_i \to f_i/\sqrt{2}$. Here and in the remainder of this thesis we use flavor symmetries of light quarks such as isospin ($u \leftrightarrow d$), U–spin ($s \leftrightarrow u$) and V–spin ($s \leftrightarrow d$) to relate form factors. They are $SU(2)$ subgroups of the larger $SU(3)_F$ symmetry, which holds in the limit of degenerate masses for the light quarks u, d, s. At LO this symmetry holds, as effects of the spectator quarks are neglected in naïve factorization. We remark that isospin and U–, V–spin breaking effects are induced by mass differences and $U(1)_{\text{EM}}$ effects and can amount to few % and $\mathcal{O}(20\,\%)$, respectively.

3.3.2 Modeling QCD resonances

The results of the previous sections include perturbative short-distance SM contributions in naïve factorization. Here, contributions are expressed as products of Wilson coefficients and form factors. BSM effects can also be probed within this framework via additional contributions to Wilson coefficients. However, further SM contributions need to be taken into account, which are then labeled as *non-factorizable* contributions. These include in general annihilation, spectator scattering and form-factor correcting contributions. It is not possible to calculate these contributions from first principles as the rather light charm quark mass close to the scale of QCD confinement $\frac{m_c}{\Lambda_{\text{QCD}}} \sim 1$ prohibits a systematic expansion within the QCD Factorization (QCDF) approach [102]. There are two different possibilities to deal with this obstacle, both of which are discussed in the remainder of this subsection.

The first approach is taking into account vector meson dominance (VMD), where only contributions of intermediate (vector) resonances are modeled as they are expected to dominate the non-perturbative effects. This approach follows the lines of Refs. [91–94, 96] and is also applied in Ref. [90]. Schematically, these contributions proceed via $D \to PM(\to \gamma^* \to \ell^+\ell^-)$ with M being one of the light vector resonances $M = \rho$, ω, ϕ or pseudoscalar resonances $M = \eta$, η'. Such a cascade factorizes in the narrow width approximation $\Gamma_M \ll m_M$ as [91, 182]

$$\mathcal{B}(D \to PM \to P\ell^+\ell^-) = \mathcal{B}(D \to PM) \cdot \mathcal{B}(M \to \ell^+\ell^-)\,. \tag{3.8}$$

Eq. (3.8) is reproduced by a simple phenomenological ansatz in terms of a Breit-Wigner contribution to the decay amplitude for vector resonances

$$-\mathrm{i}\mathcal{A}|_M = \frac{G_F\,\alpha_e}{2\sqrt{2}\pi}\,\frac{a_M \exp(\mathrm{i}\delta_M)}{q^2 - m_M^2 + \mathrm{i}m_M\Gamma_M}\,\bar{\ell}(p_+)\not{p}_D\ell(p_-)\,, \tag{3.9}$$

and for pseudoscalar resonances

$$-\mathrm{i}\mathcal{A}|_M = \frac{G_F\,\alpha_e}{2\sqrt{2}\pi}\,\frac{a_M \exp(\mathrm{i}\delta_M)}{q^2 - m_M^2 + \mathrm{i}m_M\Gamma_M}\,\bar{\ell}(p_+)\gamma_5\ell(p_-)\,, \tag{3.10}$$

where a_M is a positive real fit parameter fixed by experimental input and Eq. (3.8). p_+ and p_- are the four-momenta of the two leptons implying $p_+ + p_- = q$ and δ_M is an unknown strong phase. Now, since these amplitudes enter on top of the perturbative contributions it is *convenient* to include all effects according to the lepton currents compactly as

$$\begin{aligned} C_9^R(q^2) &= a_\rho e^{\mathrm{i}\,\delta_\rho}\left(\frac{1}{q^2 - m_\rho^2 + \mathrm{i}\,m_\rho\Gamma_\rho} - \frac{1}{3}\frac{1}{q^2 - m_\omega^2 + \mathrm{i}\,m_\omega\Gamma_\omega}\right) + \frac{a_\phi e^{\mathrm{i}\,\delta_\phi}}{q^2 - m_\phi^2 + \mathrm{i}\,m_\phi\Gamma_\phi}\,, \\ C_P^R(q^2) &= \frac{a_\eta e^{\mathrm{i}\,\delta_\eta}}{q^2 - m_\eta^2 + \mathrm{i}\,m_\eta\Gamma_\eta} + \frac{a_{\eta'}}{q^2 - m_{\eta'}^2 + \mathrm{i}\,m_{\eta'}\Gamma_{\eta'}}\,. \end{aligned} \tag{3.11}$$

By doing so, effects from Eqs. (3.9) and (3.10) are explicitly scaled with the form factors entering C_9 and C_P contributions and therefore further increase the associated uncertainties[1]. This procedure is conservative as the a_M factors are fixed only at a single q^2 point ($q^2 = m_\phi^2$ for a_ϕ) and the q^2 dependence is unknown, whereas the q^2 behavior induced by the form factors is modest, as apparent from Fig. 3.1. In Eq. (3.11) the ρ and the ω contributions are related via isospin $3\,a_\omega = a_\rho$ to reduce the number of parameters in accordance with Refs. [90, 93, 96]. $SU(3)_F$ further relates the strong phases, which implies the minus sign between the ρ and the ω contributions and predicts $|\delta_\rho - \delta_\phi| = \pi$, see Ref. [96]. Although very naïve and data-driven, this approach reproduces the anticipated VMD and properties of the involved resonances. Most importantly, long-distance effects are induced by QCD×QED and included as effective contributions to the Wilson coefficients C_9 and C_P. Using experimental input for the involved masses, widths, and branching ratios in Eqs. (3.8), (3.11), which are collected in App. A, and the differential decay distribution from App. E.1 we can extract the a_M parameters for all resonances and all $D \to P\ell^+\ell^-$ modes for the muon final state $\ell = \mu$. This is done by separately including one resonance at a time. The results are compiled in Tab. 3.1. For $a_{\eta'}$ we only quote an estimate, since $\mathcal{B}(\eta' \to \mu^+\mu^-)$ is not measured, see App. A.

Since the last update of Ref. [1] experimental results for $\mathcal{B}(D^+ \to \pi^+\phi)$, $\mathcal{B}(D_s^+ \to K^+\eta)$, $\mathcal{B}(D_s^+ \to K^+\eta')$ and $\mathcal{B}(D_s^+ \to K\omega)$ were updated in Ref. [184]. Except for negligibly small changes, the values in Tab. 3.1 are unchanged with respect to results presented in Ref. [1]. With these updates direct calculations of a_ω yield ratios $a_\rho/a_\omega = 0.05$, 0.17 and 0.17 for $D^0 \to \pi^0$, $D^+ \to \pi^+$ and $D_s^+ \to K^+$, respectively, which is below the expected isospin limit $a_\rho/a_\omega = \frac{1}{3}$. Uncertainties on a_M parameters can further be reduced in the future with improved measurements of hadronic branching ratios $\mathcal{B}(D \to \pi M)$ and $\mathcal{B}(D_s \to KM)$, but their numerical impact is small as long as the strong phases δ_M remain unknown

[1] One has to be careful when comparing the obtained a_M factors with the literature. For instance in Ref. [183] the resonances are also scaled with the form factors, however a_M parameters are used from Refs. [91, 92], where the parameters are fitted without the additional form factor scaling.

Table 3.1: Resulting phenomenological resonance parameters a_M (in GeV^2) for $D^+ \to \pi^+\mu^+\mu^-$, $D^0 \to \pi^0\mu^+\mu^-$ and $D_s^+ \to K^+\mu^+\mu^-$. They are extracted from experimental measurements of $\mathcal{B}(D \to \pi M)$, $\mathcal{B}(D_s \to KM)$ and $\mathcal{B}(M \to \mu^+\mu^-)$ where M denotes one of the resonances ρ, ϕ, η, η'.

	a_ρ	a_ϕ	a_η	$a_{\eta'}$
$D^+ \to \pi^+$	0.18 ± 0.02	0.23 ± 0.01	$(5.7 \pm 0.4) \times 10^{-4}$	$\sim 8 \times 10^{-4}$
$D^0 \to \pi^0$	0.86 ± 0.04	0.25 ± 0.01	$(5.3 \pm 0.4) \times 10^{-4}$	$\sim 8 \times 10^{-4}$
$D_s^+ \to K^+$	0.49 ± 0.04	0.07 ± 0.01	$(5.6 \pm 0.4) \times 10^{-4}$	$\sim 9 \times 10^{-4}$

and need to be varied within $-\pi < \delta_M \leq \pi$.

A second approach for modeling the long-range dynamics in rare charm decays is taken in Ref. [104] for $D \to \pi\ell^+\ell^-$, which further improves the results of Ref. [102] for $D \to \rho\ell^+\ell^-$. Here, the authors obtain the resonance contributions via a dispersion relation, based on Ref. [185]. The parameters of their model are extracted from $e^+e^- \to$ (hadrons) data and similar branching ratios as in Eq. (3.8). Although this approach might be more advanced than the first one from a theoretical perspective, it also relies on experimental input, even introduces more model parameters and does not include effects of the pseudoscalar resonances η, η' [104]. In the end both approaches result in similar branching ratio predictions, which is discussed in the next section. In agreement with Ref. [104], we conclude that none of the aforementioned resonance models needed for the description of $D \to \pi\ell^+\ell^-$ and other rare charm decays is completely sound from a theoretical perspective. Later sections of this thesis, however, demonstrate that this resonance pollution does not hamper the possibility to test NP in rare charm decays.

3.3.3 Phenomenology

With relevant form factors as well as short- and long-distance contributions at hand, we are able to discuss the (differential) branching ratio of $D \to P\ell^+\ell^-$ decays in the SM. The decay is described by a double differential distribution [177]

$$\frac{\mathrm{d}^2\Gamma}{\mathrm{d}q^2 \mathrm{d}\cos\theta_\ell} = a(q^2) + b(q^2)\cos\theta_\ell + c(q^2)\cos^2\theta_\ell\,, \tag{3.12}$$

where θ_ℓ is the angle between the momenta of the ℓ^- and the final state meson P in the dilepton rest frame. Angular observables are built from the q^2 depending factors $a(q^2)$, $b(q^2)$, $c(q^2)$ and will be discussed in the SM and beyond in Sec. 5.1.1. Here, we discuss the q^2 differential decay distribution, obtained via $\cos\theta_\ell$ integration within the allowed range $-1 \leq \cos\theta_\ell \leq 1$

$$\int_{-1}^{1} \frac{\mathrm{d}^2\Gamma}{\mathrm{d}q^2 \mathrm{d}\cos\theta_\ell} \mathrm{d}\cos\theta_\ell = \frac{\mathrm{d}\Gamma}{\mathrm{d}q^2} = 2 \cdot \left(a(q^2) + \frac{c(q^2)}{3} \right)\,. \tag{3.13}$$

Including only SM contributions, we obtain in agreement with Refs. [90, 166, 177]

$$\frac{\mathrm{d}\Gamma}{\mathrm{d}q^2} = \frac{G_F^2\alpha_e^2\beta_\ell}{1024\pi^5 m_D^3}\sqrt{\lambda_{DP}}\cdot\left\{\frac{2}{3}\lambda_{DP}\left(1+\frac{2m_\ell^2}{q^2}\right)f_+^2\left|C_9^{\text{eff}}+C_9^R+C_7^{\text{eff}}\frac{2m_c}{m_D+m_P}\frac{f_T}{f_+}\right|^2 + \frac{q^2}{m_c^2}(m_D^2-m_P^2)^2 f_0^2|C_P^R|^2\right\}, \tag{3.14}$$

with $\lambda_{DP} = \lambda(m_D^2, m_P^2, q^2) = m_D^4 + m_P^4 + q^4 - 2m_D^2\, m_P^2 - 2m_D^2\, q^2 - 2m_P^2 q^2$, $\lambda(a, b, c)$ the usual Källén function and $\beta_\ell = \sqrt{1-\frac{4m_\ell^2}{q^2}}$. The full distribution in terms of all Wilson coefficients can be found in App. E.1. The only difference between the three different modes $D^+ \to \pi^+\ell^+\ell^-$, $D^0 \to \pi^0\ell^+\ell^-$ and $D_s^+ \to K^+\ell^+\ell^-$ is the values for m_D, m_P and the form factors. To obtain the differential branching ratio, also the different lifetimes τ_D need to be taken into account.

In Fig. 3.2 we show the differential branching ratios $\frac{\mathrm{d}\mathcal{B}}{\mathrm{d}q^2} = \tau_D \cdot \frac{\mathrm{d}\Gamma}{\mathrm{d}q^2}$ for $D^+ \to \pi^+\mu^+\mu^-$ (left plot) and $D_s^+ \to K^+\mu^+\mu^-$ (right plot). We use Eq. (3.14) with the resonance contributions from Eq. (3.11) and a_M parameters collected in Tab. 3.1, shown in orange, as well as the perturbative contributions $C_{7,9}^{\text{eff}}$ as discussed in Sec. 2.3, shown in blue. Main sources of uncertainties are shown as bands and stem from form factors as well as strong phases $-\pi < \delta_M \leq \pi$ for the resonant contributions and μ_c scale variation for the non-resonant contributions. For the resonant contribution, the solid line shows the evaluation at central values and for fixed strong phases $\delta_\rho = 0$ and $\delta_\phi = \pi$ consistent with the $SU(3)_F$ limit $|\delta_\rho - \delta_\phi| = \pi$. The dashed solid line shows the scenario with $\delta_\rho = \delta_\phi = 0$ for comparison. Clearly, the resonances yield contributions several orders above the perturbative SM calculation in the whole allowed kinematic region. Perturbative contributions are therefore negligible for the estimation of the SM branching ratios and hence branching ratio measurements do not probe perturbative effects. This situation is in stark contrast to similar rare decays in the beauty sector. Here, perturbative contributions dominate for most of the available phase space and resonance effects are avoided by appropriate selection criteria, however are also blocking the road to ultimate precision [63]. The fundamental difference between the up- and down-sectors in this respect is the GIM mechanism, which is lifted by the heavy top quark mass in down-type processes, however highly effective for up-type FCNCs such as rare charm decays.

We also learn from Fig. 3.2 that uncertainties in the modeling of resonances, mainly driven by the unknown strong phases δ_M, are huge and very sensitive to interference effects, as apparent from different behavior in low and high q^2 regions for $D \to \pi$ and $D_s \to K$ transitions. The different hierarchy between a_ρ and a_ϕ from Tab. 3.1 leads to larger uncertainties for the low q^2 region up to the ρ/ω peak for $D \to \pi$ and a rather stable behavior for $q^2 > m_\phi^2$, whereas the situation is the opposite for $D_s \to K$. This sensitivity to interference effects can only be reduced with better knowledge of the resonance model parameters, which can only be achieved via improved data in the future. Effects from the pseudoscalar resonances η, η' on the other hand are negligible for the calculation of the branching ratio due to their small widths and only have an influence exactly at $q^2 = m_\eta^2$ and $q^2 = m_{\eta'}^2$.

Due to the sizable uncertainties, the branching ratio cannot be reliably predicted. In order to compare the predictions in Ref. [104] with the resonance model in Eq. (3.11) and with limits from

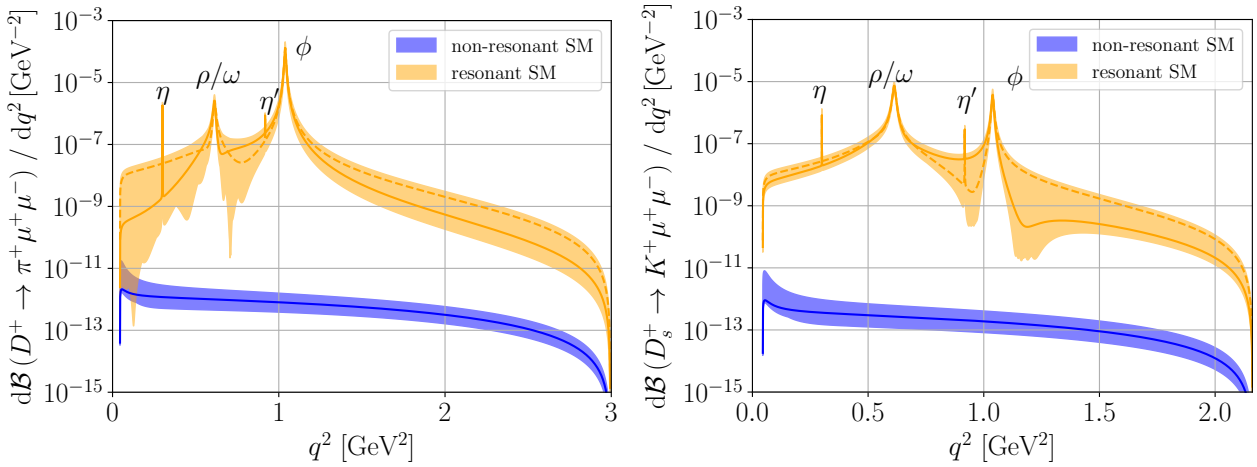

Figure 3.2: Resonant (orange) and non-resonant (blue) contributions to the differential branching ratios of the rare charm decays $D^+ \to \pi^+\mu^+\mu^-$ (left plot) and $D_s^+ \to K^+\mu^+\mu^-$ (right plot) in the SM. The band widths show theoretical uncertainties of resonance parameters, μ_c variation and hadronic form factors and solid (dashed) lines show the evaluation for central values of input and fixed strong phases, see main text.

experimental searches, we integrate the orange band from Fig. 3.2 to give a rough estimate. However, since the model is data-driven we do not claim a central value with uncertainties and only provide the order of magnitude. We exemplary compare numbers for all three decay modes for the experimentally defined regions

- high q^2 region: $\quad (1.25\,\mathrm{GeV})^2 \leq q^2 \leq (m_D - m_P)^2\,,$
- low q^2 region: $\quad (0.25\,\mathrm{GeV})^2 \leq q^2 \leq (0.525\,\mathrm{GeV})^2\,,$

and collect our estimate, the prediction from Ref. [104] and the 90 % C.L. upper limits in Tab. 3.2.

From Tab. 3.2 we learn the following

- Although only available for $D^+ \to \pi^+\mu^+\mu^-$ we conclude that the simple resonance model is in agreement with the approach followed in Ref. [104] within uncertainties and only experimental input will help to disentangle and improve the resonance behavior.
- For $D^+ \to \pi^+\mu^+\mu^-$ the experimental upper limits are one order of magnitude away from the predictions in this work and Ref. [104], and therefore close to observation. In Ref. [76] an improved upper limit $\mathcal{B}(D^+ \to \pi^+\mu^+\mu^-) < 6.7 \times 10^{-8}$ at 90 % C.L. for the full q^2 region is already reported, however not used here, see next point.
- Experimental upper limits are reported for the full q^2 region, although the resonance region, roughly from the η mass up to the ϕ, is cut out in the analyses. The signal events in the low q^2

Table 3.2: Comparison of integrated branching ratio predictions for the resonant SM in this work and Ref. [104] with the 90 % C.L. upper limits for the high and low q^2 regions $q^2 > (1.25\,\text{GeV})^2$ and $(0.25\,\text{GeV})^2 \leq q^2 \leq (0.525\,\text{GeV})^2$. † marked upper limits are only available for the full q^2 region, see main text.

mode and q^2 bin	This work	Ref. [104]	90 % C.L. upper limit
$\mathcal{B}(D^+ \to \pi^+\mu^+\mu^-) \times 10^9$			
high q^2	0.3 ... 3	$2.7^{+4.0}_{-2.6}$	26 [75]
low q^2	0.1 ... 3	$8.1^{+5.9}_{-6.1}$	20 [75]
$\mathcal{B}(D^0 \to \pi^0\mu^+\mu^-) \times 10^9$			
high q^2	0.1 ... 2	-	$1.8 \cdot 10^5$ † [186]
low q^2	3 ... 6	-	$1.8 \cdot 10^5$ † [186]
$\mathcal{B}(D_s^+ \to K^+\mu^+\mu^-) \times 10^9$			
high q^2	0.03 ... 0.3	-	140 † [76]
low q^2	3 ... 4	-	140 † [76]

and high q^2 regions are extracted and then extrapolated to full q^2. Since the individual upper limits are not available, it is not possible to compare the branching ratio estimates.[2]

Note that instead of same flavor charged leptons in the final state also LFV modes and dineutrino modes can be studied. The former are forbidden in the SM and discussed as SM null tests in Sec. 5.4, the latter are discussed separately in Chapter 6.

3.4 Rare charm baryon decays

In this section, we study semileptonic decays of charmed baryons as an extension of analyses of charmed meson decays in the previous section and Refs. [88, 90]. The motivation to study baryons instead of mesons is complementarity. Due to the enriched spin structure more combinations of Wilson coefficients appear as well as an increased number of angular observables.

The lightest charmed baryon is the Λ_c with a mass of $m_{\Lambda_c} \sim 2.3\,\text{GeV}$ and therefore the easiest semileptonic rare charm baryon decay is $\Lambda_c \to p\ell^+\ell^-$. However, more possibilities to test the $c \to u\ell^+\ell^-$ quark transition in baryon decays exist. In total, we identify five three-body modes [3]

$$\Lambda_c^+ \to p\ell^+\ell^-\,, \quad \Xi_c^+ \to \Sigma^+\ell^+\ell^-\,, \quad \Xi_c^0 \to \Sigma^0\ell^+\ell^- \quad \Xi_c^0 \to \Lambda^0\ell^+\ell^-\,, \quad \Omega_c^0 \to \Xi^0\ell^+\ell^-\,, \tag{3.15}$$

[2] For future analyses we suggest to quote either the extrapolation factor or limits on individual bins as in Ref. [75].

[3] Two further decays are presumably possible $\Xi_c'^+ \to \Sigma^+\ell^+\ell^+$ and $\Xi_c'^0 \to \Lambda^0\ell^+\ell^-$ [112], however neither the quantum numbers nor the lifetimes of $\Xi_c'^+$ and $\Xi_c'^0$ are measured yet.

Table 3.3: Phenomenological resonance parameters a_M (in GeV^2) for rare charm baryon transitions (first column) extracted from measurements of $\mathcal{B}(\Lambda_c \to pM)$ and $\mathcal{B}(M \to \mu^+\mu^-)$ with $M = \omega,\, \phi,\, \eta,\, \eta'$, see text for details.

	a_ω	a_ϕ	a_η	$a_{\eta'}$
$\Lambda_c \to p$	0.062 ± 0.009	0.108 ± 0.008	$(5.8 \pm 0.8) \times 10^{-4}$	$\sim 5 \times 10^{-4}$
$\Xi_c^+ \to \Sigma^+$	~ 0.06	~ 0.1	$\sim 5 \times 10^{-4}$	$\sim 4 \times 10^{-4}$
$\Xi_c^0 \to \Sigma^0$	~ 0.06	~ 0.1	$\sim 5 \times 10^{-4}$	$\sim 4 \times 10^{-4}$
$\Xi_c^0 \to \Lambda^0$	~ 0.06	0.080 ± 0.013	$\sim 5 \times 10^{-4}$	$\sim 4 \times 10^{-4}$
$\Omega_c^0 \to \Xi^0$	~ 0.05	~ 0.09	$\sim 5 \times 10^{-4}$	$\sim 4 \times 10^{-4}$

and three (quasi-)four-body modes

$$\Xi_c^+ \to \Sigma^+(\to p\pi^0)\ell^+\ell^-\,, \quad \Xi_c^0 \to \Lambda^0(\to p\pi^-)\ell^+\ell^-\,, \quad \Omega_c^0 \to \Xi^0(\to \Lambda^0\pi^0)\ell^+\ell^-\,, \tag{3.16}$$

with details given in the next sections. Again, the study of LFV modes and dineutrino modes can be found in Sec. 5.4 and Chapter 6, respectively. Unless otherwise stated we refer to these modes with $B_0 \to B_1\ell^+\ell^-$ and $B_0 \to B_1(\to B_2\pi)\ell^+\ell^-$, *i.e.* B_0 is the initial charmed baryon, B_1 is the final (intermediate) state baryon in the three-body (four-body) case, and B_2 is the final state baryon in the four-body modes.

Besides the short-distance contributions we again model intermediate QCD resonances $B_0 \to B_1 M(\to \ell^+\ell^-)$ by the phenomenological ansatz, *i.e.* we apply Eq. (3.11).

In Sec. 3.3.2 we have learned that $a_\rho/a_\omega = \frac{1}{3}$ from isospin does not necessarily hold for the meson case, however we are forced to apply it also for the baryons as no data on $\mathcal{B}(B_0 \to B_1\rho)$ is available. Results for the baryon a_M parameters are compiled in Tab. 3.3. Again, experimental input from App. A and the distribution from App. E are used. Note, mostly branching ratios of the Λ_c are available, such that these also serve as an input for all other baryon modes. We refer to App. C for details on this procedure.

In Ref. [6, 8] we used $a_{\eta'} = a_\eta$ as the recent result from the Belle collaboration for $\mathcal{B}(\Lambda_c \to p\eta')$ [187] was not available. However, as apparent from Tab. 3.3 the approximation still holds, especially considering the lack of data on $\mathcal{B}(\eta' \to \mu^+\mu^-)$.

3.4.1 Semileptonic three-body decays

For the baryonic three-body modes, the angular distribution reads

$$\frac{\mathrm{d}^2\Gamma}{\mathrm{d}q^2 \mathrm{d}\cos\theta_\ell} = \frac{3}{2} \cdot (K_{1ss}\,\sin^2\theta_\ell + K_{1cc}\,\cos^2\theta_\ell + K_{1c}\,\cos\theta_\ell)\,. \tag{3.17}$$

Here, θ_ℓ is the angle of the ℓ^+ with respect to the negative direction of flight of the Λ_c in the dilepton rest frame.

Form factors are available from LQCD [103], quark models [188] and for $\Xi_c \to \Sigma$ from LCSR [189]. In the baryon case ten independent (axial) vector and tensor form factors exist

$$f_0\,,\ f_+\,,\ f_\perp\,,\ g_0\,,\ g_+\,,\ g_\perp\,,\ h_+\,,\ h_\perp\,,\ \tilde{h}_+\,,\ \tilde{h}_\perp\,. \tag{3.18}$$

Their definitions and further details are compiled in App. C. We use the results from Ref. [103] and apply $SU(3)_F$ relations for the other baryon modes. The same $SU(3)_F$ relations have been employed to relate the $\Lambda_c \to pM$ branching ratios to any other $B_0 \to B_1 M$ branching ratio in the determination of the a_M factors in Tab. 3.3, along with two-body phase space factors. Again we refer to App. C for further details.

The q^2-dependent coefficients K_{1ss}, K_{1cc} and K_{1s} are given in App. E.2 and are obtained using the helicity formalism, see Refs. [190–193], which we introduce and discuss separately in App. F. In the SM the q^2 differential decay distribution is given by

$$\begin{aligned}
\frac{\mathrm{d}\Gamma}{\mathrm{d}q^2} &= \int_{-1}^{1} \frac{\mathrm{d}^2\Gamma}{\mathrm{d}q^2 \mathrm{d}\cos\theta_\ell}\,\mathrm{d}\cos\theta_\ell = 2\,K_{1ss} + K_{1cc} \\
&= \frac{G_F^2 \alpha_e^2 \beta_\ell \sqrt{\lambda_{B_0 B_1}}}{1536 \cdot \pi^5 m_{B_0}^3} \cdot \Bigg[\quad (2q^2 + 4m_\ell^2) \left| C_7^{\text{eff}} \frac{2m_c}{q^2} (m_{B_0} + m_{B_1}) h_\perp + (C_9^{\text{eff}} + C_9^{\text{R}}) f_\perp \right|^2 \cdot s_- \\
&\qquad + (2q^2 + 4m_\ell^2) \left| C_7^{\text{eff}} \frac{2m_c}{q^2} (m_{B_0} - m_{B_1}) \tilde{h}_\perp + (C_9^{\text{eff}} + C_9^{\text{R}}) g_\perp \right|^2 \cdot s_+ \\
&\qquad + \left(1 + \frac{2m_\ell^2}{q^2}\right) \left| C_7^{\text{eff}} 2m_c h_+ + (C_9^{\text{eff}} + C_9^{\text{R}}) \cdot (m_{B_0} + m_{B_1}) f_+ \right|^2 \cdot s_- \\
&\qquad + \left(1 + \frac{2m_\ell^2}{q^2}\right) \left| C_7^{\text{eff}} 2m_c \tilde{h}_+ + (C_9^{\text{eff}} + C_9^{\text{R}}) \cdot (m_{B_0} - m_{B_1}) g_+ \right|^2 \cdot s_+ \\
&\qquad + \frac{3q^2}{2m_c^2} \left((m_{B_0} - m_{B_1})^2 f_0^2\, s_+ (m_{B_0} + m_{B_1})^2 g_0^2\, s_- \right) \left| C_P^{\text{R}} \right|^2 \Bigg]\,,
\end{aligned} \tag{3.19}$$

where, again, $\lambda_{B_0 B_1} = \lambda(m_{B_0}^2, m_{B_1}^2, q^2)$ is the Källén function and we introduce $s_\pm = (m_{B_0} \pm m_{B_1})^2 - q^2$. For the contributions proportional to $|C_P^{\text{R}}|^2$ we neglect the lepton masses, since we are only interested in the size of the contributions of the pseudoscalar resonances. In this limit no interference terms between the scalar and vector contributions exist, which is in agreement with Ref. [194].

Table 3.4: Collection of the branching ratios and weak decay parameters α of the secondary baryonic $B_1 \to B_2\pi$ decays [184] for self-analyzing rare charm four-body decays $B_0 \to B_1(\to B_2\pi)\ell^+\ell^-$.

	$\Xi_c^+ \to \Sigma^+ (\to p\pi^0)\ell^+\ell^-$	$\Xi_c^0 \to \Lambda^0 (\to p\pi^-)\ell^+\ell^-$	$\Omega_c^0 \to \Xi^0 (\to \Lambda^0\pi^0)\ell^+\ell^-$
$\mathcal{B}(B_1 \to B_2\pi)$	$(51.6 \pm 0.3)\%$	$(63.9 \pm 0.5)\%$	$(99.5 \pm 0.0)\%$
α	$(-98.0 \pm 1.0)\%$	$(73.0 \pm 1.0)\%$	$(-36.0 \pm 1.0)\%$

3.4.2 Semileptonic (quasi-)four-body decays

We also study (quasi-)four-body decays, where the secondary baryon decays weakly $B_1 \to B_2\pi$ with sizable branching ratio and polarization parameter α. The total decay chain for the resonance contributions is then given by $B_0 \to B_1 M(\to \ell^+\ell^-) \to B_1\ell^+\ell^- \to B_1(\to B_2\pi)\ell^+\ell^- \to B_2\pi\ell^+\ell^-$, as the lifetime of the resonances $M = \rho, \omega, \phi, \eta, \eta'$ is much shorter than the weak decay of the daughter baryon $B_1 = \Sigma^+, \Lambda^0, \Xi^0$. Hence, we can use the same a_M parameters from Tab. 3.3 and also the same form factors apply. The advantage of the four-body final state is that it offers an increased number of angular observables. The angular distribution now reads

$$\begin{aligned}\frac{\mathrm{d}^4\Gamma}{\mathrm{d}q^2 \mathrm{d}\cos\theta_\ell \mathrm{d}\cos\theta_\pi \mathrm{d}\phi} = \frac{3}{8\pi} \cdot \Big[& K_{1ss} \sin^2\theta_\ell + K_{1cc} \cos^2\theta_\ell + K_{1c} \cos\theta_\ell \\ & + \big(K_{2ss} \sin^2\theta_\ell + K_{2cc} \cos^2\theta_\ell + K_{2c} \cos\theta_\ell\big) \cos\theta_\pi \\ & + (K_{3sc} \sin\theta_\ell \cos\theta_\ell + K_{3s} \sin\theta_\ell) \sin\theta_\pi \sin\phi \\ & + (K_{4sc} \sin\theta_\ell \cos\theta_\ell + K_{4s} \sin\theta_\ell) \sin\theta_\pi \cos\phi \Big] .\end{aligned} \tag{3.20}$$

θ_ℓ is the same angle as in the three-body case, Eq. (3.17). Similarly, θ_π is the angle between the momentum of the final state baryon (B_2) and the negative direction of flight of the B_1 baryon in the B_2-pion center-of-mass frame. The azimuthal angle ϕ describes the angle between the dilepton and the $B_2\pi$ decay planes. The allowed regions for the angles θ_ℓ, θ_π, ϕ are $-1 \leq \cos\theta_\ell \leq +1$, $-1 < \cos\theta_\pi < 1$ and $0 < \phi < 2\pi$. Again the angular coefficients entering in Eq. (3.20) are given in terms of Wilson coefficients and form factors in App. E.3. For the SM contributions to the q^2 differential branching ratio, it is sufficient to multiply Eq. (3.19) with the lifetime of the B_0 and the branching ratio for the secondary weak decay

$$\frac{\mathrm{d}\mathcal{B}(B_0 \to B_1(\to B_2\pi)\ell^+\ell^-)}{\mathrm{d}q^2} = \tau_{B_0} \frac{\mathrm{d}\Gamma(B_0 \to B_1\ell^+\ell^-)}{\mathrm{d}q^2} \cdot \mathcal{B}(B_1 \to B_2\pi) , \tag{3.21}$$

which is discussed in detail in App. F.3 and the relevant branching ratios and decay parameters are collected in Tab. 3.4.

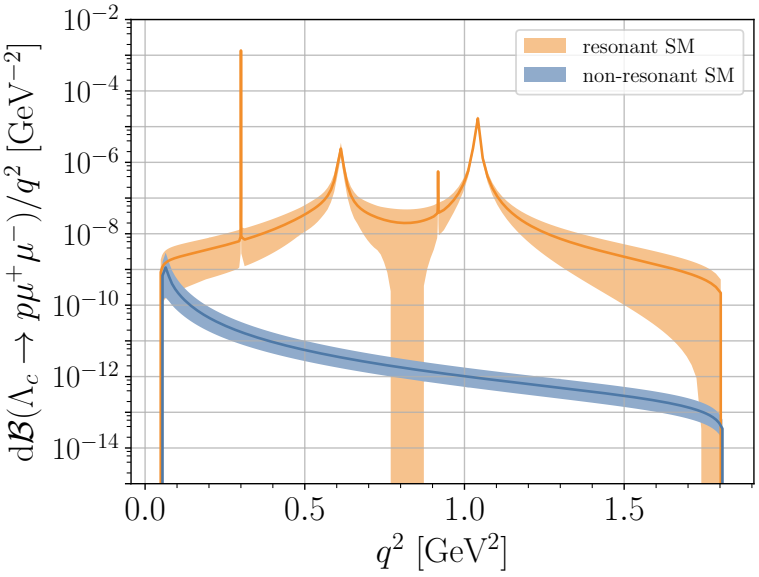

Figure 3.3: Resonant and non-resonant SM contributions to the differential branching ratio of $\Lambda_c \to p\mu^+\mu^-$ in orange and blue, respectively. Uncertainties of the resonant SM are predominantly due to unknown strong phases in Eq. (3.11). The perturbative SM, where uncertainties arise from μ_c scale variation, is negligible in the full kinematic region. Form factor uncertainties are included.

3.4.3 Phenomenology

The q^2 spectrum for the three-body decay $\Lambda_c \to p\mu^+\mu^-$ is shown in Fig. 3.3.

For this mode dedicated lattice results for the form factors are available, whereas for all other modes the branching ratio can only be naïvely estimated. The LHCb collaboration has obtained an upper limit at the 90 % C.L. [77]

$$\mathcal{B}(\Lambda_c \to p\mu^+\mu^-) < 7.7 \times 10^{-8}\,, \tag{3.22}$$

where 40 MeV cuts around the resonance masses of the ω, ϕ are applied and the signal is extrapolated to the full q^2 region $4m_\ell^2 \leq q^2 \leq (m_{\Lambda_c} - m_p)^2$ via a phase space model. Due to the lack of further information, the obtained upper limit cannot be compared accurately to the resonance model in Fig. 3.3.

Nevertheless, we estimate the expected branching ratios for all three- and four-body modes applying exactly the 40 MeV cuts used in [77]. Note that the four-body estimates follow from the respective three-body modes by multiplication with branching ratios of the secondary weak decay from Tab. 3.4 and we use $q^2_{\text{min}} = 4m_\ell^2$ and $q^2_{\text{max}} = (m_{B_0} - m_{B_1})^2$.

$$
\begin{aligned}
&\mathcal{B}(\Lambda_c^+ \to p\mu^+\mu^-) = (1.9^{+1.8}_{-1.5}) \times 10^{-8}\,, \\
&\mathcal{B}(\Xi_c^+ \to \Sigma^+\mu^+\mu^-) \sim 3.4 \times 10^{-8}\,, && \mathcal{B}(\Xi_c^+ \to \Sigma^+(\to p\pi^0)\mu^+\mu^-) \sim 1.8 \times 10^{-8}\,, \\
&\mathcal{B}(\Xi_c^0 \to \Sigma^0\mu^+\mu^-) \sim 7.6 \times 10^{-9}\,, && \\
&\mathcal{B}(\Xi_c^0 \to \Lambda^0\mu^+\mu^-) \sim 3.8 \times 10^{-9}\,, && \mathcal{B}(\Xi_c^0 \to \Lambda^0(\to p\pi^-)\mu^+\mu^-) \sim 2.4 \times 10^{-9}\,, \\
&\mathcal{B}(\Omega_c^0 \to \Xi^0\mu^+\mu^-) \sim 2.5 \times 10^{-8}\,, && \mathcal{B}(\Omega_c^0 \to \Xi^0(\to \Lambda^0\pi^0)\mu^+\mu^-) \sim 2.5 \times 10^{-8}\,.
\end{aligned}
\tag{3.23}
$$

3.5 CP–asymmetries in semileptonic and hadronic charm decays

In this section, we briefly present SM expectations for CP–violation in charm decays. We first discuss generalities and SM predictions for CP–violation in semileptonic decays in Sec. 3.5.1, and further discuss CP–asymmetries in hadronic decays in Sec. 3.5.2.

3.5.1 CP–asymmetry generalities

CP–violation is a key requirement for the successful generation of the observed baryon asymmetry in the early universe. However, the amount of CP–violation in the SM is not sufficient to explain the observed matter-antimatter asymmetry, which is why new sources of CP–violation are expected to show up in particle physics experiments.

Following Ref. [195] we classify CP–violating phenomena in flavor transitions as follows

- **CP–violation in decay (direct CP–violation):** Given the decay of a particle M into a final state f proceeds via two different amplitudes with both CP–even (strong, δ_i) and CP–odd (weak, ϕ_i) phases, the direct CP–asymmetry is induced via the interference of the two amplitudes and observable only in the case of non-vanishing strong and weak phase differences.

- **CP–violation in mixing (indirect CP–violation):** For neutral mesons M^0, $\overline{M}^0$, a difference between flavor and mass eigenstates exists. This is described by the following Hamiltonian

$$
\mathcal{H} = M - \mathrm{i}\frac{\Gamma}{2}\,, \tag{3.24}
$$

  with two by two matrices M and Γ, which due to CPT invariance can be written as

$$
M = \begin{pmatrix} M_{11} & M_{12} \\ M_{12} & M_{11} \end{pmatrix}\,, \quad \Gamma = \begin{pmatrix} \Gamma_{11} & \Gamma_{12} \\ \Gamma_{12} & \Gamma_{11} \end{pmatrix}\,. \tag{3.25}
$$

  The diagonalization of $\mathcal{H}$ results in the mass eigenstates of M^0. The resulting $M^0 - \overline{M}^0$ mixing

is described by the three physical quantities

$$x_{12} = 2\frac{|M_{12}|}{\Gamma}\,, \quad \Gamma_{12} = 2\frac{|\Gamma_{12}|}{\Gamma}\,, \quad \phi_{12} = \arg\left(\frac{M_{12}}{\Gamma_{12}}\right)\,, \tag{3.26}$$

where ϕ_{12} describes the interference between mixing via M and Γ and quantifies CP–violation in mixing.

- **CP–violation in interference between decays with and without mixing:** Here, CP–violation is observed due to the interference of $M \to f$ and $M \to \overline{M} \to f$.

We are interested in CP–violation phenomena of the first class, *i.e.* **direct** CP–violation. In the SM many of the observed CP–violating processes involve the interference of a tree-level amplitude with a *penguin*-type loop diagram. However, in charm decays we have already observed that the GIM cancellation suppresses penguin contributions, and contributions proportional to the CP–violating phase in the CKM matrix are suppressed by five powers of Wolfenstein λ, see Eq. (2.11). Hence, CP–violation in rare semileptonic charm decays is completely negligible in the SM as the dominant contributions are due to CP–conserving $SU(3)_C \times U(1)_{\text{QED}}$ induced resonances. In Sec. 5.2 we investigate the NP potential of CP–asymmetries in charm decays. As it turns out, there is strong benefit in the resonance contributions, as they induce a strong phase and are able to interfere with CP–violating NP contributions. Hence, BSM CP–violation is expected to be enhanced around the resonance masses, where the strong phase is large. These resonance catalyzed CP–asymmetries were first proposed in Ref. [92] and are the ideal place to search for new sources of CP–violation in up-type FCNCs.

3.5.2 Hadronic decays and ΔA_{CP}

The first observation of CP–violation in charm decays was presented by the LHCb collaboration in 2019 in the measurement of ΔA_{CP} [85]

$$\Delta A_{\text{CP}} = A_{\text{CP}}(D^0 \to K^+K^-) - A_{\text{CP}}(D^0 \to \pi^+\pi^-) = (-16.4 \pm 2.8) \times 10^{-4}\,, \tag{3.27}$$

where we quote the world average [176] and

$$A_{\text{CP}}(D^0 \to f) = \frac{\Gamma(D^0 \to f) - \Gamma(\overline{D}^0 \to f)}{\Gamma(D^0 \to f) + \Gamma(\overline{D}^0 \to f)}\,, \quad \text{with } f = K^+K^-,\, \pi^+\pi^-\,. \tag{3.28}$$

For a recent review on CP–violation in hadronic charm decays and $D^0 - \overline{D}^0$ mixing see Ref. [196]. Naïvely, the CKM hierarchy predicts $\text{Im}(V_{cb}^* V_{ub}/(V_{cs}^* V_{us})) \sim 7 \cdot 10^{-4}$, however another order of suppression is expected to arise from the *penguin over tree* ratio of the dominant and sub-dominant amplitudes. Since no reliable SM prediction for this ratio is available, the NP nature of this measurement one order above the naïve expectation is discussed in recent literature, see Refs. [197–208].

For our phenomenological purposes, we write the $D^0(\overline{D}^0)$ decay amplitudes $\mathcal{A}_f$ ($\overline{\mathcal{A}_f}$) to CP–eigenstates

f as

$$\mathcal{A}_f = \mathcal{A}_f^T \, \mathrm{e}^{+\mathrm{i}\,\phi_f^T} \left[1 + r_f \, \mathrm{e}^{\mathrm{i}\,(\delta_f + \phi_f)}\right] \ , \qquad \overline{\mathcal{A}_f} = \eta_{\mathrm{CP}} \, \mathcal{A}_f^T \, \mathrm{e}^{-\mathrm{i}\,\phi_f^T} \left[1 + r_f \, \mathrm{e}^{\mathrm{i}\,(\delta_f - \phi_f)}\right] \ , \tag{3.29}$$

where $\eta_{\mathrm{CP}} = \pm 1$ is the CP–eigenvalue of f. In the SM the dominant amplitude is denoted by $\mathcal{A}_f^T \, \mathrm{e}^{\pm \mathrm{i}\,\phi_f^T}$, and r_f parametrizes the relative magnitude of all sub-leading amplitudes to the dominant amplitude, *i.e.* the *penguin over tree ratio*. In the limit of $r_f \ll 1$, we find for the CP–asymmetry in Eq. (3.28)

$$A_{\mathrm{CP}}(f) = -\,2\, r_f \, \sin\delta_f \, \sin\phi_f \, + \, \mathcal{O}(r_f^2) \ , \tag{3.30}$$

To study NP contributions we expand SM amplitudes and BSM effects as

$$\mathcal{A}_f \, = \, \sum_{q=d,s,b} \lambda_q \, (\mathcal{A}_f^q)_{\mathrm{SM}} \, + \, \mathcal{A}_f^{\mathrm{NP}} \ , \tag{3.31}$$

where the first term contains the SM with CKM–factors $\lambda_q = V_{cq}^* V_{uq}$ made explicit, and the second term accounts for NP. Using CKM unitarity $\lambda_d \, + \, \lambda_s \, + \lambda_b \, = \, 0$ one finds

$$\mathcal{A}_{K(\pi)} = \lambda_{s(d)} \, (\mathcal{A}_{K(\pi)}^{s(d)} - \mathcal{A}_{K(\pi)}^{d(s)})_{\mathrm{SM}} + \lambda_b \, (\mathcal{A}_{K(\pi)}^{b} - \mathcal{A}_{K(\pi)}^{d(s)})_{\mathrm{SM}} + \mathcal{A}_{K(\pi)}^{\mathrm{NP}} \ , \tag{3.32}$$

where the final states K^+K^- and $\pi^+\pi^-$ are denoted by the subscripts $f = K$ and $f = \pi$, respectively. The first term is the dominant tree-level contribution and the second one corresponds to "penguin" contributions with small Wilson coefficients which are strongly CKM–suppressed by $\lambda_b/\lambda_{s,d}$. The last term $\mathcal{A}_{K(\pi)}^{\mathrm{NP}}$ encodes NP contributions. Using Eqs. (3.29), (3.30) and (3.32), we obtain

$$\Delta A_{\mathrm{CP}} = \Delta A_{\mathrm{CP}}^{\mathrm{SM}} - \frac{2}{|\lambda_{s,d}|} \, \Delta r^{\mathrm{NP}} \ . \tag{3.33}$$

Predictions for $\Delta A_{\mathrm{CP}}^{\mathrm{SM}}$ are given in Refs. [205–209] and span a considerable range. Therefore, the implications of large contributions to ΔA_{CP} from NP effects can be tested, which is studied in the framework of anomaly-free, flavorful Z'–models in Sec. 5.2.3.

4 Models extending the Standard Model

In this section, we give a brief overview of possible BSM scenarios. We follow a bottom-up approach and study effects mediated by new heavy particles at tree level unless stated otherwise. In Sec. 4.1 we first discuss the available model-independent parameter space, *i.e.* we discuss bounds on BSM contributions to Wilson coefficients and further constraints. In Sec. 4.2 we summarize features of LQ–models and in Sec. 4.3 we introduce simple Z'–extensions of the SM. Since we are only interested in general features of the respective models that show up in low-energy observables we refrain from conducting a detailed study of UV–complete models.

4.1 Model-independent analysis

To start completely model-independently, we study possible BSM contributions to the Wilson coefficients in Eq. (2.24). We have seen in previous sections that perturbative SM contributions do not exceed ~ 0.01 and only enter in C_7 and C_9, while the SM phenomenology is dominated by long-range effects from intermediate resonances. Here, the dominant contributions from the vector resonances ρ, ω, ϕ are compactly implemented as a resonance shaped contribution to C_9, see Eq. (3.11). BSM contributions are constrained by several different approaches, the most straightforward being the experimental limits on semileptonic rare decays themselves. In the SM, contributions to these decays are LFU, such that contributions to dimuon and dielectron final states are equal. Since this is not necessarily the case in BSM scenarios, we have to distinguish available bounds on muon and electron Wilson coefficients, which is why we make the lepton index explicit in all Wilson coefficients except for C_7, because the photon to lepton coupling is LFU.

An equation bounding (pseudo-)scalar and axial vector muon Wilson coefficients is derived from the upper limit $\mathcal{B}(D^0 \to \mu^+\mu^-) < 6.2 \times 10^{-9}$ at 90 % C.L. [73] and Eq. (3.4) and reads

$$|C_S^{(\mu)} - C_S^{(\mu)\prime}|^2 + |C_P^{(\mu)} - C_P^{(\mu)\prime} + 0.1(C_{10}^{(\mu)} - C_{10}^{(\mu)\prime})|^2 \lesssim 0.007\,. \tag{4.1}$$

Further, we obtain from integrating the differential decay distribution given in Eq. (E.4) in App. E.1, while neglecting SM contributions, and using $\mathcal{B}(D^+ \to \pi^+\mu^+\mu^-) < 6.7 \times 10^{-8}$ at 90 % C.L. for the full q^2 region [76]

$$\begin{aligned} &1.3\,|C_7|^2 + 1.3\left|C_9^{(\mu)}\right|^2 + 1.3\left|C_{10}^{(\mu)}\right|^2 + 2.6\left|C_S^{(\mu)}\right|^2 + 2.7\left|C_P^{(\mu)}\right|^2 + 0.4\left|C_T^{(\mu)}\right|^2 + 0.4\left|C_{T5}^{(\mu)}\right|^2 \\ &+0.3\,\mathrm{Re}\left[C_9^{(\mu)}\,C_T^{(\mu)*}\right] + 1.1\,\mathrm{Re}\left[C_{10}^{(\mu)}\,C_P^{(\mu)*}\right] + 2.6\,\mathrm{Re}\left[C_7\,C_9^{(\mu)*}\right] + 0.6\,\mathrm{Re}\left[C_7\,C_T^{(\mu)*}\right] \lesssim 1\,. \end{aligned} \tag{4.2}$$

As Eq. (4.2) is obtained from $D^+ \to \pi^+\mu^+\mu^-$ all Wilson coefficients except the tensor ones are understood as $C_i^{(\mu)} + C_i^{(\mu)\prime}$. The possibility of cancellations remains, as for instance $C_9 + C_9'$ is constrained, but C_9 is unconstrained as long as $C_9 = -C_9'$. A special case arises for the axial vector contributions. Here, both the sum and the difference of LH and RH quark currents are constrained

from Eqs. (4.1) and (4.2), so that we find without the possibility for large cancellations

$$\begin{aligned} |C_{10}^{(\mu)}| &\lesssim 0.85\,, \\ |C_{10}^{(\mu)\prime}| &\lesssim 0.85\,. \end{aligned} \tag{4.3}$$

Furthermore, $\mathcal{B}(\Lambda_c \to p\mu^+\mu^-) < 7.7 \times 10^{-8}$ at 90 % C.L. [77] implies $|C_9^{(\mu)}| \lesssim 0.93$ and is therefore close to the limit $|C_9^{(\mu)}| \lesssim 0.88$ obtained from Eq. (4.2). Since the branching ratios in baryon decays depends on both combinations $|C_9^{(\mu)} \pm C_9^{(\mu)\prime}|^2$, individual and independent constraints on $C_9^{(\mu)}$ and $C_9^{(\mu)\prime}$ similar to Eq. (4.3) cannot be given yet.

A global fit of muon Wilson coefficients including the recent measurements of the angular distribution of $D^0 \to \pi^+\pi^-\mu^+\mu^-$ and $D^0 \to K^+K^-\mu^+\mu^-$ [72] and possibly fitting Wilson coefficients and resonance parameters simultaneously is beyond the scope of this work. However, with this first measurement and upcoming updates for LHCb searches for $D^0 \to \mu^+\mu^-$, $D \to P\mu^+\mu^-$ and $\Lambda_c \to p\mu^+\mu^-$ experimental searches start to be constraining and interesting physics in rare charm decays can be probed in the near future.

For dielectron modes the situation is different and bounds on Wilson coefficients are weaker. We find with $\mathcal{B}(D^+ \to \pi^+e^+e^-) < 1.1 \times 10^{-6}$ at 90 % C.L. for the full q^2 region [210]

$$\begin{aligned} &0.8\,|C_7|^2 + 0.8\left|C_9^{(e)}\right|^2 + 0.8\left|C_{10}^{(e)}\right|^2 + 1.7\left|C_S^{(e)}\right|^2 + 1.7\left|C_P^{(e)}\right|^2 \\ &+0.2\left|C_T^{(e)}\right|^2 + 0.2\left|C_{T5}^{(e)}\right|^2 + 1.6\,\mathrm{Re}\left[C_7\,C_9^{(e)*}\right] \lesssim 10\,, \end{aligned} \tag{4.4}$$

where again $C_i^{(e)} \to C_i^{(e)} + C_i^{(e)\prime}$ except for the tensor contributions and we skip negligible interference terms. From $\mathcal{B}(D^0 \to e^+e^-) < 7.9 \times 10^{-8}$ [211] we find

$$\left|C_S^{(e)} - C_S^{(e)\prime}\right|^2 + \left|C_P^{(e)} - C_P^{(e)\prime} + 0.0004\left(C_{10}^{(e)} - C_{10}^{(e)\prime}\right)\right|^2 \lesssim 0.08\,. \tag{4.5}$$

Especially the stronger helicity suppression objects a useful bound on axial vector couplings.

Dipole operators are constrained from $\mathcal{B}(D^0 \to \rho\gamma) = (1.77 \pm 0.3 \pm 0.07) \times 10^{-5}$ [212]. Neglecting SM contributions one obtains $|C_7^{(\prime)}| \lesssim 0.5$ [89]. However, SM corrections from hard spectator interactions and weak annihilation contributions are sizable and lead to the following bound on BSM dipole couplings [89]

$$\begin{aligned} |C_7| &\lesssim 0.3\,, \\ |C_7'| &\lesssim 0.3\,, \end{aligned} \tag{4.6}$$

which is slightly stronger than the bound extracted from Eq. (4.2).

Beyond the SM also LFV couplings exist. $c \to u\ell^-\ell'^+$ ($\ell \neq \ell'$) decays are induced by the following

effective Hamiltonian,

$$\mathcal{H}_{\text{eff}}^{\text{LFV}} = -\frac{4G_F}{\sqrt{2}}\frac{\alpha_e}{4\pi}\sum_i \left(K_i^{(\ell\ell')}O_i^{(\ell\ell')} + K_i'^{(\ell\ell')}O_i'^{(\ell\ell')}\right), \tag{4.7}$$

where the $K_i^{(\prime)}$ denote LFV Wilson coefficients and the operators $O_i^{(\prime)}$ read as

$$\begin{aligned}
O_9^{(\ell\ell')} &= (\overline{u}_L\gamma_\mu c_L)(\bar{\ell}\gamma^\mu\ell'), & O_9'^{(\ell\ell')} &= (\overline{u}_R\gamma_\mu c_R)(\bar{\ell}\gamma^\mu\ell'),\\
O_{10}^{(\ell\ell')} &= (\overline{u}_L\gamma_\mu c_L)(\bar{\ell}\gamma^\mu\gamma_5\ell'), & O_{10}'^{(\ell\ell')} &= (\overline{u}_R\gamma_\mu c_R)(\bar{\ell}\gamma^\mu\gamma_5\ell'),\\
O_S^{(\ell\ell')} &= (\overline{u}_L c_R)(\bar{\ell}\ell'), & O_S'^{(\ell\ell')} &= (\overline{u}_R c_L)(\bar{\ell}\ell'),\\
O_P^{(\ell\ell')} &= (\overline{u}_L c_R)(\bar{\ell}\gamma_5\ell'), & O_P'^{(\ell\ell')} &= (\overline{u}_R c_L)(\bar{\ell}\gamma_5\ell'),\\
O_T^{(\ell\ell')} &= \frac{1}{2}(\overline{u}\sigma_{\mu\nu}c)(\bar{\ell}\sigma^{\mu\nu}\ell'), & O_{T5}'^{(\ell\ell')} &= \frac{1}{2}(\overline{u}\sigma_{\mu\nu}c)(\bar{\ell}\sigma^{\mu\nu}\gamma_5\ell').
\end{aligned} \tag{4.8}$$

Note that there is no $O_7^{(\prime)}$ contribution since the photon does not couple to different lepton flavors. The differential distribution for LFV decays $D \to P\ell\ell'$ is given in App. E.1 and for the purely leptonic decays we find

$$\begin{aligned}
\mathcal{B}(D^0 \to e^\pm\mu^\mp) = \tau_{D^0}\frac{G_F^2\alpha_e^2 m_D^5 f_D^2}{64\pi^3 m_c^2}\left(1-\frac{m_\mu^2}{m_D^2}\right)^2 \cdot \Bigg\{ &\left|K_S - K_S' \pm \frac{m_\mu m_c}{m_D^2}(K_9 - K_9')\right|^2\\
&+ \left|K_P - K_P' + \frac{m_\mu m_c}{m_D^2}(K_{10} - K_{10}')\right|^2 \Bigg\},
\end{aligned} \tag{4.9}$$

with $K_i^{(\prime)} = K_i^{(\prime)(\mu e)}$ for $D^0 \to e^+\mu^-$ and $K_i^{(\prime)} = K_i^{(\prime)(e\mu)}$ for $D^0 \to e^-\mu^+$. Using $\mathcal{B}(D^0 \to e^\pm\mu^\mp) < 1.3 \times 10^{-8}$ at 90 % C.L. [74], we obtain

$$\left|K_S - K_S' \pm 0.04\,(K_9 - K_9')\right|^2 + \left|K_P - K_P' + 0.04\,(K_{10} - K_{10}')\right|^2 \lesssim 0.01\,. \tag{4.10}$$

And from $\mathcal{B}(D^+ \to \pi^+e^+\mu^-) < 2.1 \times 10^{-7}$ and $\mathcal{B}(D^+ \to \pi^+\mu^+e^-) < 2.2 \times 10^{-7}$ at 90 % C.L. [76] we obtain

$$\begin{aligned}
&0.4\,|K_9|^2 + 0.4\,|K_{10}|^2 + 0.9\,|K_S|^2 + 0.9\,|K_P|^2 + 0.1\,|K_T|^2 + 0.1\,|K_{T5}|^2 +\\
&0.2\,\text{Re}[K_{10}K_P^* \pm K_9K_S^*] + 0.1\,\text{Re}[K_9K_T^* \pm K_{10}K_{T5}^*] \lesssim 1\,,
\end{aligned} \tag{4.11}$$

where for all coefficients except for the tensor ones $K_i = K_i^{e\mu} + K_i'^{e\mu}$ for $D^+ \to \pi^+e^+\mu^-$ and $K_i = K_i^{\mu e} + K_i'^{\mu e}$ for $D^+ \to \pi^+\mu^+e^-$.

Another possibility to constrain $c \to u\ell^+\ell^{-\prime}$ couplings comes from high–p_T dilepton tails in Drell-Yan searches [213, 214]. In these analyses dilepton spectra in $pp \to \ell^+\ell^{-\prime}$ are utilized and, hence, upper limits on four-fermion couplings can be obtained for any quark flavor combination, *i.e.* FCNCs

Table 4.1: Upper limits on BSM Wilson coefficients for rare charm decays from low energy observables (collected from main text) and high–p_T dilepton searches [213, 214]. The lepton flavor violation (LFV) bound is quoted as flavor-summed, $\sqrt{|C_i^{\ell\ell'}|^2 + |C_i^{\ell'\ell}|^2}$. Entries marked as n.a.† are not available, because no limit on $D^0 \to e^\pm\tau^\mp$ exists, although kinematically accessible. Low energy limits are obtained for a single coefficient at a time and barring cancellations.

		ee	$\mu\mu$	$\tau\tau$	$e\mu$	$e\tau$	$\mu\tau$
$C_{9,10}^{(\prime)}$	high–p_T	2.9	1.6	5.6	1.6	4.7	5.1
	low energy	3.5	0.9	-	2.2	n.a.†	-
$C_{S,P}^{(\prime)}$	high–p_T	7.2	3.8	14	1.2	3.5	3.8
	low energy	0.3	0.1	-	0.1	n.a.†	-
$C_{T,T5}$	high–p_T	1.2	0.63	2.5	6.4	19	20.4
	low energy	7	1.6	-	3.2	n.a.†	-

$b \to s\ell^+\ell^{-\prime}$, $c \to u\ell^+\ell^{-\prime}$, ..., as well as diagonal quark couplings $qq\ell^+\ell^{-\prime}$ for any quark except the top. The extracted limits scale with the quark parton distribution functions (PDFs) of the proton. The main advantage of the high–p_T limits is that they are extracted at high energies, where lepton mass effects are negligible and the partonic cross section factorizes into a sum of absolute values squared of Wilson coefficients with different Lorentz structures and chirality combinations in quark and lepton current. This implies that no cancellations can occur.

We collect upper limits on rare charm Wilson coefficients for each lepton flavor combination from low energy measurements and Drell-Yan searches in Tab. 4.1. Here, we assume no large cancellations are possible for the low energy limits. For high–p_T limits on scalar and tensor Wilson coefficients, running effects down to 2 GeV are taken into account in order to be comparable to the low energy limits. Interestingly, bounds from high–p_T searches are compatible with low energy bounds for rare charm decays for (axial) vector operators and lepton flavors ee, $\mu\mu$ and $e\mu$ and can even provide limits involving τ's. For (pseudo-)scalar operators low energy bounds are better due to their contributions in purely leptonic D^0 meson decays. For (pseudo-)tensor operators low energy limits are better only for $e\mu$ and worse in the other cases.

Recently, another possibility to study NP charm couplings in low-energy (polarized) scattering processes $e^-p \to e^-(\mu^-)\Lambda_c$ was proposed in Refs. [215, 216]. However, no appropriate experimental setup to study these processes exists today, so that we refuse to further discuss possible future bounds in this work.

4.2 Leptoquarks

LQs are hypothetical particles that directly couple leptons to quarks. LQ–models can therefore be classified according to their SM group representations and their spin. Especially, one distinguishes $SU(2)_L$–singlets, –doublets and –triplets [217], whereas all LQs are color-triplets or color-anti-triplets, see [218] for an extensive modern classification. Vector LQs have spin 1 and need to be part of an extended gauge sector, which then necessarily calls for a UV–completion. These vector LQs naturally appear in $SU(4)$ models, where leptons can be seen as the fourth color, originally proposed in the 1970s by Pati and Salam [219–221]. Often these scenarios require the LQ to be very heavy. Scalar LQs with spin 0, on the other hand, can be rather light and are therefore appealing from a model building perspective. Since LQ–models have become very popular as a solution to the current B–anomalies [139, 140, 222–229], it is interesting to study possible effects in rare charm decays as well. A detailed classification of LQ–effects is given in Ref. [140] and their phenomenology in rare charm decays is investigated in Ref. [90].

In agreement with [90, 140], the straightforward strategy to include LQs and bypass constraints from the kaon sector at the same time is to consider only the scalar LQs $S_{1(2)}$ with right(left)-handed couplings to leptons and the vector ones $\tilde{V}_{1,2}$.

The interaction Lagrangian contributing to $c \to u\ell^-\ell'^+$ processes is given by [217]

$$\mathcal{L}_{\text{LQ}} \supset \lambda^{ij}_{S_1}\, \overline{u}^c_{iR} l_{jR}\, S_1 + \lambda^{ij}_{S_2}\, \overline{u}_{iR} L_{jL}\, S_2 + \lambda^{ij}_{\widetilde{V}_1}\, \overline{u}_{iR}\gamma^\mu l_{jR}\, \tilde{V}_{1\mu} + \lambda^{ij}_{\widetilde{V}_2}\, \overline{u}^c_{iR}\gamma^\mu L_{jL}\, \tilde{V}_{2\mu} + \text{c.c.}\,, \tag{4.12}$$

where L_L denotes the lepton doublet, l_R, u_R are lepton and up-type quark singlets and the superscript c indicates a charge conjugation; i, j are the generation indices. Hypercharge assignments of the LQs can be read off from Eq. (4.12).

Signatures of S_2 have been studied for charm decays in [93, 230] and of $\tilde{V}_1$ in [93]. The LQs $S_2^{5/3}$, $\tilde{V}_2^{1/3}$, and $S_1^{1/3}$, $\tilde{V}_1^{5/3}$ (superscripts indicate the electric charge) are the only ones inducing interactions of up-type quarks and charged leptons. Using Fierz identities the Wilson coefficients of the $O_9'^{(\ell\ell')}$ and $O_{10}'^{(\ell\ell')}$ operators can be written as, *e.g.* [90],

$$\begin{aligned} K_9'^{(\ell\ell')} &= \frac{\sqrt{2}\pi}{G_F\alpha_e}\cdot\left[\frac{\lambda^{c\ell'}_{S_1}\lambda^{u\ell *}_{S_1}}{4M^2_{S_1}} - \frac{\lambda^{u\ell'}_{S_2}\lambda^{c\ell *}_{S_2}}{4M^2_{S_2}} - \frac{\lambda^{u\ell'}_{\widetilde{V}_1}\lambda^{c\ell *}_{\widetilde{V}_1}}{2M^2_{\widetilde{V}_1}} + \frac{\lambda^{c\ell'}_{\widetilde{V}_2}\lambda^{u\ell *}_{\widetilde{V}_2}}{2M^2_{\widetilde{V}_2}}\right], \\ K_{10}'^{(\ell\ell')} &= \frac{\sqrt{2}\pi}{G_F\alpha_e}\cdot\left[\frac{\lambda^{c\ell'}_{S_1}\lambda^{u\ell *}_{S_1}}{4M^2_{S_1}} + \frac{\lambda^{u\ell'}_{S_2}\lambda^{c\ell *}_{S_2}}{4M^2_{S_2}} - \frac{\lambda^{u\ell'}_{\widetilde{V}_1}\lambda^{c\ell *}_{\widetilde{V}_1}}{2M^2_{\widetilde{V}_1}} - \frac{\lambda^{c\ell'}_{\widetilde{V}_2}\lambda^{u\ell *}_{\widetilde{V}_2}}{2M^2_{\widetilde{V}_2}}\right], \end{aligned} \tag{4.13}$$

with M_X, $X = S_{1,2}, \tilde{V}_{1,2}$ the LQ–mass. One finds $K_9' = K_{10}'$ in the singlet scenarios (S_1, $\tilde{V}_1$), while for the doublets (S_2, $\tilde{V}_2$) $K_9' = -K_{10}'$. Note that only RH quark currents are induced in these scenarios, therefore no effects are present in the down-type sector. The corresponding lepton flavor conserving contributions to $C_{9,10}'^{(\ell)}$ read exactly like Eq. (4.13) with $\ell' = \ell$.

Using Eqs. (4.2), (4.4), (4.11) and neglecting the SM contribution, the following constraints from the upper limits on $\mathcal{B}(D^+ \to \pi^+\mu^+\mu^-)$ [76], $\mathcal{B}(D^+ \to \pi^+e^+e^-)$ [210] and $\mathcal{B}(D^+ \to \pi^+e^\pm\mu^\mp)$ [76] are obtained,

$$\begin{aligned}
&|\lambda^{c\mu}_{S_{1,2}}\lambda^{u\mu*}_{S_{1,2}}| \lesssim 0.05 \left(\frac{M_{S_{1,2}}}{1\text{ TeV}}\right)^2, \qquad |\lambda^{c\mu}_{\widetilde{V}_{1,2}}\lambda^{u\mu*}_{\widetilde{V}_{1,2}}| \lesssim 0.02 \left(\frac{M_{\widetilde{V}_{1,2}}}{1\text{ TeV}}\right)^2,\\
&|\lambda^{ce}_{S_{1,2}}\lambda^{ue*}_{S_{1,2}}| \lesssim 0.19 \left(\frac{M_{S_{1,2}}}{1\text{ TeV}}\right)^2, \qquad |\lambda^{ce}_{\widetilde{V}_{1,2}}\lambda^{ue*}_{\widetilde{V}_{1,2}}| \lesssim 0.10 \left(\frac{M_{\widetilde{V}_{1,2}}}{1\text{ TeV}}\right)^2,\\
&|\lambda^{ce(c\mu)}_{S_{1,2}}\lambda^{u\mu(ue)*}_{S_{1,2}}| \lesssim 0.09 \left(\frac{M_{S_{1,2}}}{1\text{ TeV}}\right)^2, \quad |\lambda^{ce(c\mu)}_{\widetilde{V}_{1,2}}\lambda^{u\mu(ue)*}_{\widetilde{V}_{1,2}}| \lesssim 0.04 \left(\frac{M_{\widetilde{V}_{1,2}}}{1\text{ TeV}}\right)^2,
\end{aligned} \tag{4.14}$$

slightly improved with respect to results in Ref. [1] due to the recent updates in $\mathcal{B}(D^+ \to \pi^+e^\pm\mu^\mp)$ and $\mathcal{B}(D^+ \to \pi^+\mu^+\mu^-)$ in Ref. [76], which now give the most stringent bounds.

4.3 Flavorful Z'–models

In Z'–models the SM gauge symmetry is augmented with an $U(1)'$ gauge factor. We refer to the associated charges as F_ψ for each field ψ and allow for generation dependent charge assignments. These flavor non-universal charges induce FCNCs at the tree level, however dependent on specific assumptions on the flavor to mass basis rotation for LH and RH up- and down-type quarks. Similarly, LFV couplings are induced depending on the misalignment of flavor and mass basis between charged leptons and neutrinos. Z'–scenarios are also studied extensively as a solution to the B–anomalies [231–243]. Extending the gauge sector entails several challenges for model building. Although a $U(1)'$ extension is very likely, as it is contained at least as a subgroup in most UV–complete models, one has to take into account anomaly cancellation conditions, Ref. [244] and App. D.1, and depending on the UV–setting of the model, a large gauge coupling and possibly additional heavy BSM particles lead to a Landau pole at energies below the Planck scale, hence exposing the model as inconsistent. Since the Z' is a massive gauge particle, the $U(1)'$ gauge group is spontaneously broken at a high NP scale and necessarily yields an extended scalar sector at high energies, which leads to further constraints on the vacuum stability of the Higgs. Again, we follow a bottom-up approach and detailed investigations of the UV–completion are beyond the scope of this work. We include anomaly cancellation conditions and low energy constraints, such as $D^0 - \overline{D}^0$ mixing generated at tree level.

Following this procedure we obtain several candidate models, which are listed in App. D. For this class of models the effective Z'–interaction Hamiltonian part for $c \to u\ell^-\ell'^+$ processes can be written as

$$\mathcal{H}_{Z'} \supset \left(g_L^{uc}\,\overline{u}_L\gamma_\mu c_L + g_R^{uc}\,\overline{u}_R\gamma_\mu c_R + g_L^{\ell\ell'}\,\overline{\ell}_L\gamma_\mu \ell'_L + g_R^{\ell\ell'}\,\overline{\ell}_R\gamma_\mu \ell'_R\right) Z'^\mu + \text{h.c.}\,. \tag{4.15}$$

The following Wilson coefficients are induced at tree level

$$\begin{aligned} C_{9/10}^{(\ell)} &= -\frac{\pi}{\sqrt{2}G_F\alpha_e}\cdot\frac{g_L^{uc}(g_R^{\ell\ell}\pm g_L^{\ell\ell})}{M_{Z'}^2}\,, & C_{9/10}^{\prime\,(\ell)} &= -\frac{\pi}{\sqrt{2}G_F\alpha_e}\cdot\frac{g_R^{uc}(g_R^{\ell\ell}\pm g_L^{\ell\ell})}{M_{Z'}^2}\,, \\ K_{9/10}^{(\ell\ell')} &= -\frac{\pi}{\sqrt{2}G_F\alpha_e}\cdot\frac{g_L^{uc}(g_R^{\ell\ell'}\pm g_L^{\ell\ell'})}{M_{Z'}^2}\,, & K_{9/10}^{\prime\,(\ell\ell')} &= -\frac{\pi}{\sqrt{2}G_F\alpha_e}\cdot\frac{g_R^{uc}(g_R^{\ell\ell'}\pm g_L^{\ell\ell'})}{M_{Z'}^2}\,. \end{aligned} \tag{4.16}$$

Again, Eqs. (4.1), (4.2), (4.4), (4.5), (4.10) and (4.11), yield the following constraints when SM contributions are neglected and where $M_{Z'}$ denotes the mass of the Z'

$$\begin{aligned} \left|(g_L^{uc}-g_R^{uc})(g_L^{\mu\mu}-g_R^{\mu\mu})\right| &\lesssim 0.03\left(\frac{M_{Z'}}{1\text{ TeV}}\right)^2, & \left|g_L^{uc}+g_R^{uc}\right|\sqrt{\left|g_L^{\mu\mu}\right|^2+\left|g_R^{\mu\mu}\right|^2} &\lesssim 0.02\left(\frac{M_{Z'}}{1\text{ TeV}}\right)^2, \\ \left|(g_L^{uc}-g_R^{uc})(g_L^{ee}-g_R^{ee})\right| &\lesssim 27\left(\frac{M_{Z'}}{1\text{ TeV}}\right)^2, & \left|g_L^{uc}+g_R^{uc}\right|\sqrt{\left|g_L^{ee}\right|^2+\left|g_R^{ee}\right|^2} &\lesssim 0.10\left(\frac{M_{Z'}}{1\text{ TeV}}\right)^2, \\ \left|g_L^{uc}-g_R^{uc}\right|\sqrt{\left|g_L^{\mu e}\right|^2+\left|g_R^{\mu e}\right|^2} &\lesssim 0.07\left(\frac{M_{Z'}}{1\text{ TeV}}\right)^2, & \left|g_L^{uc}+g_R^{uc}\right|\sqrt{\left|g_L^{\mu e}\right|^2+\left|g_R^{\mu e}\right|^2} &\lesssim 0.04\left(\frac{M_{Z'}}{1\text{ TeV}}\right)^2. \end{aligned} \tag{4.17}$$

As discussed in App. D stronger bounds arise from tree-level Z'–contributions to $D^0-\overline{D}^0$ mixing. Here, both LH and RH quark couplings contribute and we obtain the following bound, dropping the superscript 'uc' for brevity,

$$|g_L^2+g_R^2-X\,g_L\,g_R| \simeq (4.14\pm 0.31)\times 10^{-7}\left(\frac{M_{Z'}}{1\text{ TeV}}\right)^2, \tag{4.18}$$

with $X\sim 20$ for $1\,\text{TeV}\lesssim M_{Z'}\lesssim 10\,\text{TeV}$. The main sources of uncertainty are the experimental limit on the $D^0-\overline{D}^0$ mixing parameter, the QCD running effects depending on the Z'–mass and hadronic matrix elements, however uncertainties are reduced with respect to a similar bound in Ref. [1]. In the case of only one non-vanishing coupling, *i.e.* $g_L\neq 0$ and $g_R=0$ or $g_R\neq 0$ and $g_L=0$, we obtain $|g_{L/R}|\lesssim 7\times 10^{-4}\,(M_{Z'}/\text{TeV})$. This constraint is severe, as it renders Eq. (4.17) irrelevant and the lepton couplings are instead bounded by perturbativity. Using order one lepton couplings yields $C_{9/10}\lesssim\mathcal{O}(10^{-2})$ and $K_{9/10}\lesssim\mathcal{O}(10^{-2})$ for $M_{Z'}\gtrsim 1\,\text{TeV}$, consistent with [93]. As presented in App. D.2, larger couplings are allowed in scenarios with both couplings present $g_L\neq 0$ and $g_R\neq 0$, then bounded only by Eq. (4.17). To cancel the constraint from $D^0-\overline{D}^0$ mixing, we need

$$g_L\approx X g_R \quad\text{or}\quad g_L\approx\frac{1}{X}g_R\,. \tag{4.19}$$

In the following we present flavorful Z'–models, which satisfy the condition (4.19) without introducing unnatural hierarchies. As discussed in detail in App. D.1, $c\to u$ transitions are induced in these models from non-universal charges F_ψ and flavor mixing. In order to have $g_L\neq 0$ and $g_R\neq 0$ we require non

zero differences between charm and up-quark charges for the doublets and the singlets, respectively, *i.e.* $\Delta F_{L(R)} \neq 0$ and

$$\Delta F_L = F_{Q_2} - F_{Q_1}\,, \quad \Delta F_R = F_{u_2} - F_{u_1}\,. \tag{4.20}$$

For the flavor mixing, four rotations between flavor and mass basis exist, which we refer to as U_u, U_d, V_u and V_d for RH up quarks, RH down quarks and up- and down-type components of the LH quark doublet, respectively. All of these constitute unitary matrices, where the only constraint is $V_u^\dagger V_d = V_{\rm CKM}$. Since effects in the down sector are strongly constrained by rare kaon decays, *e.g.* [245], we consider CKM effects and unknown misalignment for the quark singlets to predominantly stem from up-type rotations, *i.e.* $U_d = 1, V_d = 1$, hence $V_u = V_{\rm CKM}^\dagger$ and U_u unconstrained.

We further assume the third generation to be sufficiently decoupled, such that we can work with two by two orthogonal matrices. These are parametrized by a single angle each, θ_u and Φ_u, for U_u and V_u, respectively.

Then,

$$g_L = g_4\,\Delta F_L \cos\Phi_u \sin\Phi_u\,, \quad g_R = g_4\,\Delta F_R \cos\theta_u \sin\theta_u\,, \tag{4.21}$$

with the $U(1)'$ gauge coupling strength g_4 and, due to $V_u = V_{\rm CKM}^\dagger$, we obtain

$$\frac{g_R}{g_L} \simeq \frac{\Delta F_R \cos\theta_u \sin\theta_u}{\Delta F_L \lambda}\,, \tag{4.22}$$

with Wolfenstein λ. The condition (4.19) can be satisfied for $g_R/g_L = X$

$$\frac{\Delta F_R}{\Delta F_L} \sin 2\theta_u \simeq 8\,, \tag{4.23}$$

and for $g_R/g_L = 1/X$

$$\frac{\Delta F_R}{\Delta F_L} \sin\theta_u \simeq 1/100\,, \tag{4.24}$$

and we refer to Eq. (4.23) as RH dominated and to Eq. (4.24) as LH dominated. The RH dominated case requires a hierarchy between ΔF_L and ΔF_R, whereas the LH dominated scenario can be satisfied with mixing alone $\theta_u = \mathcal{O}(10^{-2})$. In both cases the hierarchy is inherited by the Wilson coefficients

$$\frac{C_{9/10}^{(\ell)}}{C_{9/10}^{\prime(\ell)}}, \frac{K_{9/10}^{(\ell\ell')}}{K_{9/10}^{(\prime)(\ell\ell')}} \sim X\ (\text{LH}) \quad \text{or} \quad \sim 1/X\ (\text{RH})\,. \tag{4.25}$$

Tab. 4.2 contains benchmark models, which are LH dominated or RH dominated (indicated with a prime) along with the associated mixing angle θ_u. The values of ΔF_R and ΔF_L are possible choices for anomaly-free Z'–models presented in Tab. D.1 of App. D.1.

$\Delta F_R/\Delta F_L$ ranges within $\sim [0.9, 35]$ for the presented models and for $\Delta F_R/\Delta F_L \geq 8$ both RH– and LH–dominated scenarios are possible, depending on the value of θ_u.

These concrete Z'–models are now constrained from the $D^+ \to \pi^+\mu^+\mu^-$ branching ratio limit, see

Table 4.2: Benchmark scenarios of anomaly-free Z'–models and the corresponding mixing angle θ_u for different possible charge assignments according to Tab. D.1. Solutions with a prime are RH dominated, all others are LH–dominated.

sol. #	ΔF_R	ΔF_L	g_R/g_L case	θ_u
1	3	2	$1/X$	0.008
2	12	9	$1/X$	0.009
$3'$	35	1	X	0.122
3	35	1	$1/X$	0.0003
4	3	3	$1/X$	0.011
5	3	3	$1/X$	0.011
6	15	16	$1/X$	0.012
7	0	0	-	-
$8'$	18	1	X	0.244
8	18	1	$1/X$	0.0006

Eq. (4.17), using $g_L^{\ell\ell} = g_4 F_{L_\ell}$, $g_R^{\ell\ell} = g_4 F_{e_\ell}$

$$g_4^4 \left(\lambda\, \Delta F_L\right)^2 \left\{1 + \left(\frac{\Delta F_R \sin 2\theta_u}{\Delta F_L 2\lambda}\right)\right\}^2 \left(F_{L_2}^2 + F_{e_2}^2\right) \lesssim 6 \times 10^{-4} \left(\frac{M_{Z'}}{1\ \text{TeV}}\right)^4 , \tag{4.26}$$

where depending on the scenario $\frac{\Delta F_R \sin 2\theta_u}{\Delta F_L 2\lambda} = X, \frac{1}{X}$, such that the maximal $g_4/M_{Z'}$ is fixed in each model as

$$g_4^2 \lesssim \frac{0.12}{\Delta F_L \sqrt{F_{L_2}^2 + F_{e_2}^2}} \left(\frac{M_{Z'}}{1\,\text{TeV}}\right)^2 \times \begin{cases} (1+X)^{-1} & \text{(RH)} \\ (1+1/X)^{-1} & \text{(LH)} \end{cases} . \tag{4.27}$$

We illustrate these bounds in Fig. 4.1, in the plane of the BSM coupling g_4 and the Z'–mass. Each line corresponds to an upper limit of a scenario from Tab. 4.2 with one specific choice for the charges $F_{L_1}\,(F_{L_2})$ and $F_{e_1}\,(F_{e_2})$ for electrons (muons).

Note that due to larger values for the charges, constraints on the gauge coupling for RH cases are stronger than for corresponding LH ones in Eq. (4.27). We indicate a black exclusion region, which is due to resonance searches in dilepton spectra of $M_{Z'} \gtrsim 5\,\text{TeV}$ [184]. The lower mass bound is model dependent because of the different quark and lepton charge assignments and also differs for dielectron and dimuon searches. For that reason the lower mass region in Fig. 4.1 is covered by a fading black band, as the region $g_4 < 0.5$ and $M_{Z'} < 5\,\text{TeV}$ might still be viable, however might be constrained from other searches [246].

LFV couplings can be induced in Z'–models in close analogy to the quark FCNC couplings. LH couplings to charged leptons with LFV are absent if the PMNS matrix is due to rotations in the neutrino sector only. Stringent constraints on a misalignment between flavor and mass bases in the lepton sector arise from $(i)\,\tau \to (\mu, e)\ell\ell$ with $\ell = e, \mu$, as well as $(ii)\,\mu \to eee$ and $\mu \to e\gamma$, as they are induced at tree level. In contrast these decays are only induced at the loop level in LQ–scenarios via

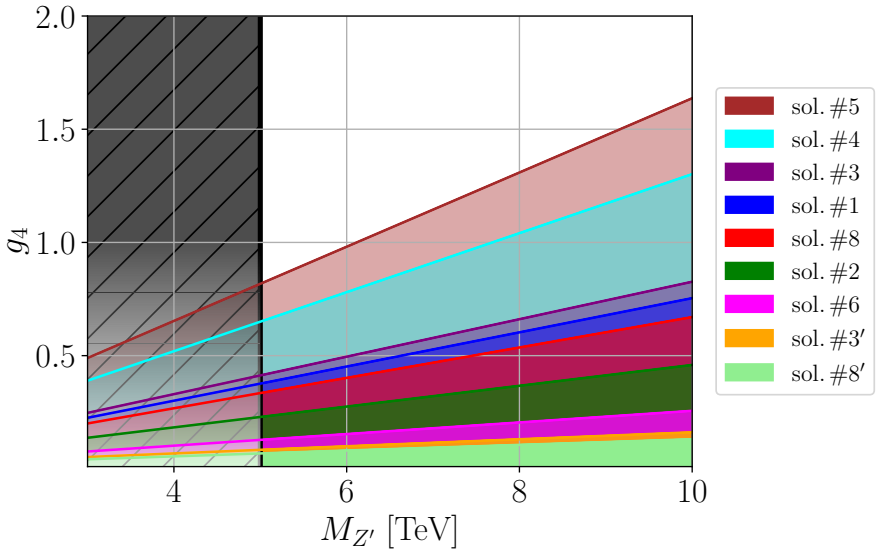

Figure 4.1: Upper limits and allowed parameter region for the $U(1)'$ gauge coupling g_4 as a function of the Z'–mass, see Eq. (4.27), for the models in Tab. 4.2. The black region is excluded by direct searches in dimuon and dielectron spectra [184]. For small gauge coupling values g_4, bounds become model-dependent, which is indicated by the fading black band, see main text.

LQ-quark-loops [184].

Due to the assumption $V_u = V_{\text{CKM}}^\dagger$ FCNCs with LH down-type quarks are avoided. Those exactly address the present discrepancies in semileptonic rare B–decays. Down-type FCNCs can still be generated for RH singlets. Further simultaneous contributions to $|\Delta c| = |\Delta u| = 1$ and $|\Delta b| = |\Delta s| = 1$ can be generated if the CKM rotation stems from both up- and down-type quark sectors, for instance V_{us} from up-sector rotations and V_{cb} from down-sector rotations. A phenomenological analysis of these scenarios would be desirable, but is beyond the scope of this work.

In contradiction to Ref. [205], CP–violating effects are vanishing in these types of Z'–models, as

- g_L is induced by the CKM rotation with a negligibly small CP–violating phase in the sub-matrix of the first two generations.
- $D^0 - \overline{D}^0$ mixing constraints can be evaded with $g_L \neq 0$ and $g_R \neq 0$, however then the CP–phases need to be aligned to be able to cancel in Eq. (4.18). Then the first point restricts CP–violating effects to be small for both LH and RH quark coupling.

Maximal CP–violation can be achieved in scenarios of $g_L = 0$ and g_R maximal with CP–violating phase around $\phi_R = \frac{\pi}{2}$ (or $\phi_R = \frac{3\pi}{2}$), because it enters twice in the mixing amplitude and drops out, whereas it only enters once in amplitudes of direct CP–violation. In this scenario kaon constraints are naturally avoided. We study implications in detail in Sec. 5.2.3.

5 Null-test strategies and New Physics sensitivity in rare charm decays

In this section, we discuss in detail how the SM can be probed and NP can be identified with rare charm decays. Significant uncertainties due to resonance contributions block the access to BSM physics in simple observables. We demonstrate how the resonance dominance can be made irrelevant or even used as a catalyst in so-called *null-test* observables. Here, observables are designed to have a vanishing SM expectation, such that any observation implies NP to be present. Further, we quantitatively demonstrate opportunities to disentangle contributions to different BSM Wilson coefficients and comment on future global fits. The structure of this section is as follows. We start with opportunities in angular observables in Sec. 5.1, where angular observables with SM background and null tests are discussed for $D \to P\ell^+\ell^-$ as well as rare charm baryon decays. CP–asymmetries are discussed in Sec. 5.2. Here, resonance enhancement can be used in semileptonic modes, CP–violation in angular observables can provide further insight into the nature of BSM couplings and we investigate correlations between CP–violating effects in semileptonic and hadronic decays within flavorful Z'–models. Sec. 5.3 discusses possibilities to test LFU in ratios of branching ratios in close analogy to similar ratios known from the B–anomalies. Finally, we discuss opportunities and distributions for LFV decay modes in Sec. 5.4. Sec. 5.5 summarizes the NP reach of null-test observables in rare charm decays.

5.1 Angular observables

The first opportunity to test the SM, despite the significant resonance induced uncertainties on the branching ratio, is to fully exploit the angular distribution of the respective decay modes. In this section we perform a sensitivity study of angular observables for $D \to P\ell^+\ell^-$ and rare charm baryon decays.

5.1.1 $D \to P\ell^+\ell^-$

From the double differential decay distribution for $D \to P\ell^+\ell^-$, given in Eq. (3.12), we identify three q^2 dependent functions $a(q^2), b(q^2)$ and $c(q^2)$. The first combination is the q^2 differential decay distribution $2 \cdot (a(q^2) + c(q^2)/3)$ and is given in App. E.1. The two remaining combinations are the lepton forward-backward asymmetry $\tilde{A}_{\rm FB}^{\ell} \sim b(q^2)$ and the *flat term* $F_H \sim a(q^2) + c(q^2)$. Their full dependence on BSM Wilson coefficients reads

$$\begin{aligned}\tilde{A}_{\rm FB}^{\ell}(q^2) &= \frac{1}{\Gamma}\left[\int_0^1 - \int_{-1}^0\right]\frac{\mathrm{d}^2\Gamma}{\mathrm{d}q^2\mathrm{d}\cos\theta}\mathrm{d}\cos\theta = \frac{b(q^2)}{\Gamma} \\ &= \frac{1}{\Gamma}\frac{G_F^2\alpha_e^2\, v^2}{512\pi^5 m_D^3}\lambda_{DP}\,(m_D^2 - m_P^2)\, f_0 \left\{\mathrm{Re}\left[\left(C_9 + C_7\frac{2m_c}{m_D+m_P}\frac{f_T}{f_+}\right)C_S^*\right]\frac{m_\ell}{m_c}f_+ \right. \\ &\quad \left. + 2\mathrm{Re}\left[C_{10}C_{T5}^*\right]\frac{m_\ell}{m_D+m_P}f_T + \mathrm{Re}\left[C_S C_T^* + C_P C_{T5}^*\right]\frac{q^2}{m_c(m_D+m_P)}f_T\right\},\end{aligned} \tag{5.1}$$

$$
\begin{aligned}
F_H(q^2) &= \frac{2}{\Gamma}\left[a(q^2)+c(q^2)\right] \\
&= \frac{1}{\Gamma}\frac{G_F^2\alpha_e^2\, v}{1024\pi^5 m_D^3}\sqrt{\lambda_{DP}}\left\{\left|C_9 + C_7\frac{2m_c}{m_D+m_P}\frac{f_T}{f_+}\right|^2\frac{4m_\ell^2}{q^2}\lambda_{DP}f_+^2\right. \\
&\quad + |C_{10}|^2\frac{4m_\ell^2}{q^2}(m_D^2-m_P^2)^2 f_0^2 + \left[|C_S|^2\left(1-\frac{4m_\ell^2}{q^2}\right)+|C_P|^2\right]\frac{q^2}{m_c^2}(m_D^2-m_P^2)^2 f_0^2 \\
&\quad + 4\left[|C_T|^2+|C_{T5}|^2\right]\left(1-\frac{4m_\ell^2}{q^2}\right)\frac{q^2}{(m_D+m_P)^2}\lambda_{DP}f_T^2 \\
&\quad + 8\,\mathrm{Re}\left[\left(C_9 + C_7\frac{2m_c}{m_D+m_P}\frac{f_T}{f_+}\right)C_T^*\right]\frac{m_\ell}{m_D+m_P}\lambda_{DP}f_+ f_T \\
&\quad \left. + 4\,\mathrm{Re}\left[C_{10}C_P^*\right]\frac{m_\ell}{m_c}(m_D^2-m_P^2)^2 f_0^2 + 16\,|C_T|^2\frac{m_\ell^2}{(m_D+m_P)^2}\lambda_{DP}f_T^2\right\},
\end{aligned}
\tag{5.2}
$$

where all Wilson coefficients C_i, with the exception of the tensor ones, are understood as $C_i \to C_i + C_i'$, which is a general feature of the $D \to P$ transition. We have also introduced the integrated rate as the normalization, which we define to be dependent on the q^2 bin

$$
\Gamma = \Gamma(q^2_{\min},\, q^2_{\max}) = \int_{q^2_{\min}}^{q^2_{\max}} \frac{\mathrm{d}\Gamma}{\mathrm{d}q^2}\,\mathrm{d}q^2 = 2\int_{q^2_{\min}}^{q^2_{\max}}\left(a(q^2)+\frac{c(q^2)}{3}\right)\mathrm{d}q^2\,. \tag{5.3}
$$

Fig. 5.1 shows the flat term in the full q^2 region for $D^+ \to \pi^+\mu^+\mu^-$ (left) and $D_s^+ \to K^+\mu^+\mu^-$ (right) for the resonant SM[1].

Clearly, F_H is similarly shaped as the differential branching ratio in Fig. 3.2, due to the resonance dominance. Both distributions are stable in the high q^2 region, where NP effects can be sizable.

This is illustrated in the lower row plots of Fig. 5.2, where NP benchmark scenarios are shown. We use the notation $C_{i\,(j)}$ for C_i or C_j, whenever the contributions are indistinguishable. Again, the left plot shows F_H for $D^+ \to \pi^+\mu^+\mu^-$ and the right plot is for $D_s^+ \to K^+\mu^+\mu^-$. Note that here also the normalization is restricted to the high q^2 region, *i.e.* $q^2_{\min} = (1.25\,\mathrm{GeV})^2$. The upper row of Fig. 5.2 shows several NP benchmark scenarios for the forward-backward asymmetry $\tilde{A}_{\mathrm{FB}}^{\ell}$, where again the left (right) plot is for $D^+_{(s)} \to \pi^+(K^+)\mu^+\mu^-$.

We learn

- Due to larger uncertainties in the high q^2 region for the resonance contributions in $D_s^+ \to K^+\mu^+\mu^-$ with respect to $D^+ \to \pi^+\mu^+\mu^-$, see Fig. 3.2 and also Fig. 5.1, the same NP benchmarks can yield larger contributions in the angular observables, illustrated by using the same y-scale in left and right plots in Fig. 5.2. Note, however the larger overall signal is expected for $D^+ \to \pi^+\mu^+\mu^-$, as

[1] In Ref. [1] also the non-resonant contribution is shown. However, these contributions cannot be observed in experiments, due to the resonance dominance in numerator and denominator, which is why we do not show them here.

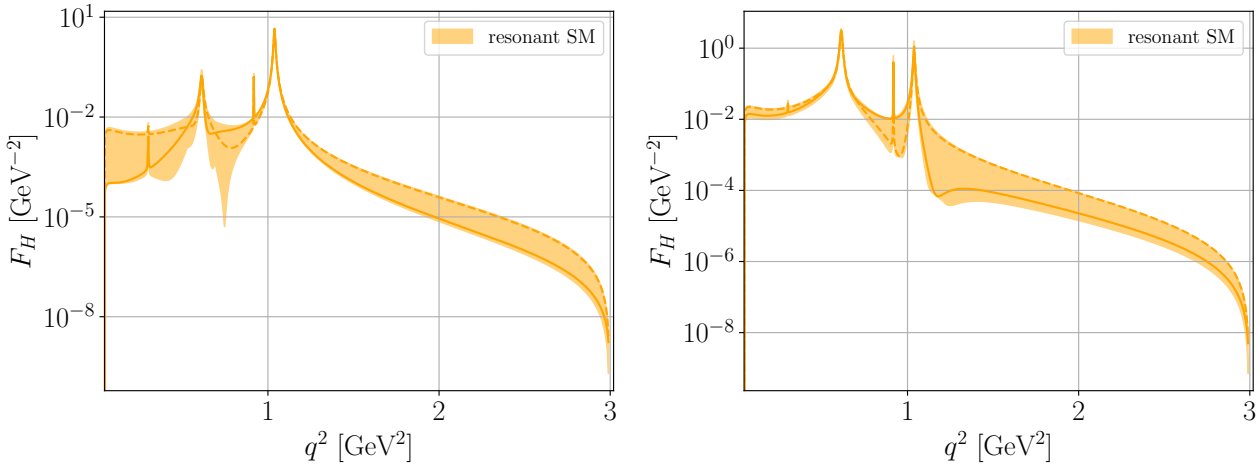

Figure 5.1: The SM contributions to $F_H(q^2)$, see Eq. (5.2), using C_9^R and C_P^R as in Eq. (3.11) for $D^+ \to \pi^+\mu^+\mu^-$ (plot to the left) and $D_s^+ \to K^+\mu^+\mu^-$ (plot to the right) decays. Uncertainties predominantly stem from unknown strong phases varied in the plot. In accordance to Fig. 3.2 the solid (dashed) line shows the evaluation at central values of input and fixed strong phases $\delta_\rho = 0$, $\delta_\phi = \pi$ ($\delta_\rho = \delta_\phi = 0$).

discussed in Tab. 3.2.

- $F_H(D \to Pe^+e^-)$ in the SM is tiny as effects from C_9^R are m_ℓ^2 suppressed.
- F_H is most sensitive to (pseudo-)tensor contributions, $\tilde{A}_{\rm FB}^\ell$ requires NP contributions to at least two Wilson coefficients to have a significant signal, the largest effects are obtained for scenarios with C_S and C_T.
- $\tilde{A}_{\rm FB}^\ell$ is a SM null test, as no $C_9^R C_P^R$ interference terms exist. The axial vector coupling C_{10} can be probed if pseudotensor contributions C_{T5} exist as well.
- Large effects in both $\tilde{A}_{\rm FB}^\ell$ and F_H indicate non-negligible tensor and scalar NP.

5.1.2 $B_0 \to B_1\ell^+\ell^-$

Similar to the discussion of the $D \to P\ell^+\ell^-$ angular distribution, the three-body decay of a charmed baryon, here commonly denoted as $B_0 \to B_1\ell^+\ell^-$ allows to define two angular observables next to the branching ratio. The reason to go beyond the simpler meson decay is two-fold. The first argument is simply to add more opportunities to test the SM and thus provide a road to a larger significance. The second point is complementarity. Due to the spin structure in the decay, several combinations of Wilson coefficients enter the angular coefficients. Instead of only $C_i + C_i'$, also $C_i - C_i'$ terms exist in the angular coefficients, such that it becomes possible to disentangle various NP contributions. For the

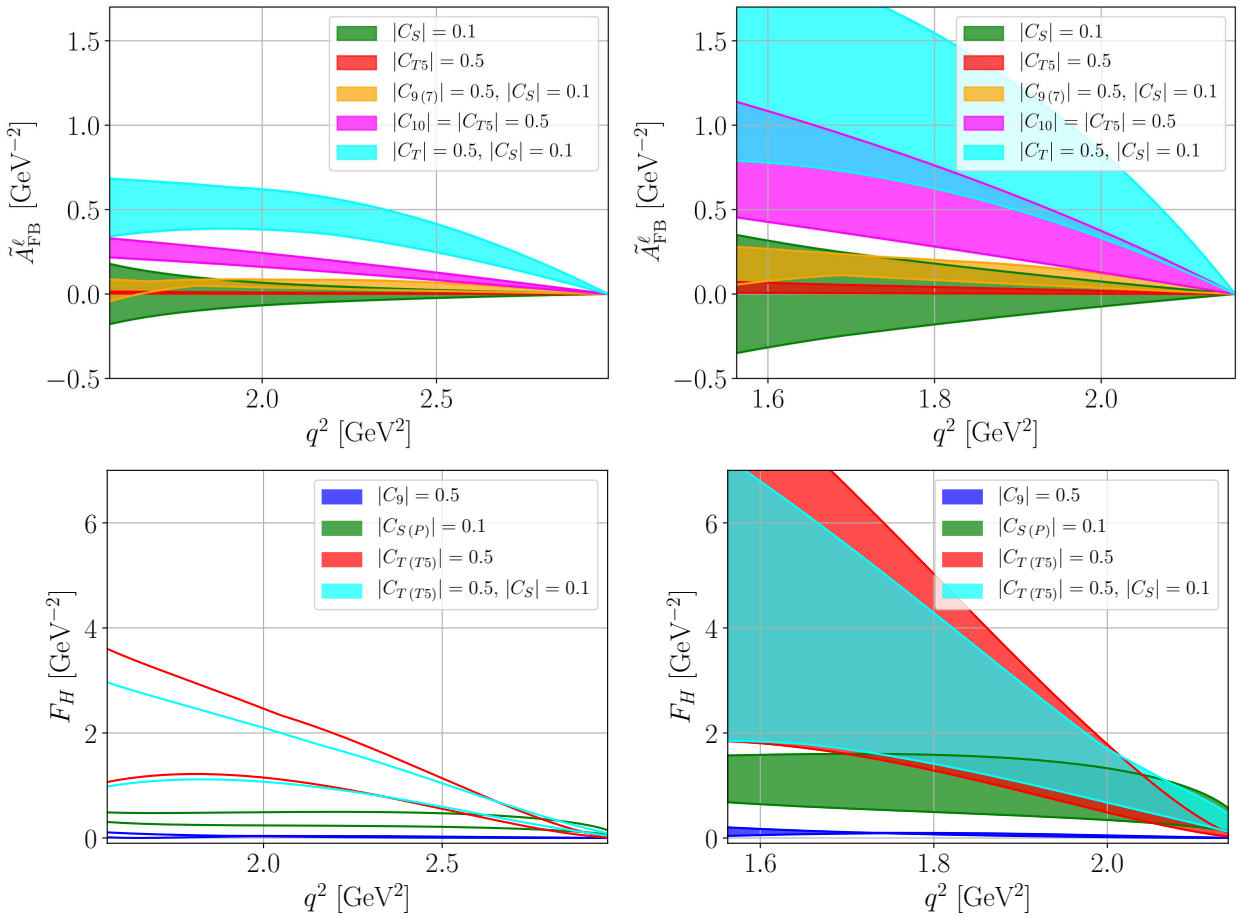

Figure 5.2: The upper (lower) plots show the forward-backward asymmetry $\tilde{A}^{\ell}_{\rm FB}$ (the flat term F_H) in the high q^2 region in different BSM scenarios for $D^+ \to \pi^+\mu^+\mu^-$ (plots to the left) and $D_s^+ \to K^+\mu^+\mu^-$ (plots to the right).

baryon decays we only consider NP contributions to vector and axial vector operators $C_9^{(\prime)}$, $C_{10}^{(\prime)}$ as well as dipole operators $C_7^{(\prime)}$. Large effects in (pseudo-)scalar and (pseudo-)tensor operators are probed in the purely leptonic decay $D^0 \to \ell^+\ell^{-(\prime)}$ and angular observables in $D \to P\ell^+\ell^{-(\prime)}$, which is a result of previous sections.

Again, we write the angular distribution as in Eq. (3.17), introducing the coefficients K_{1ss}, K_{1cc} and K_{1c}. The complete dependence on Wilson coefficients, form factors and kinematic variables for these coefficients is given in App. E.2. To obtain these contributions the helicity formalism is used, see Refs. [190–193], which we introduce and discuss separately in App. F. We define the fraction of

longitudinal polarized dimuons as

$$F_L = \frac{2\,K_{1ss} - K_{1cc}}{2\,K_{1ss} + K_{1cc}}\,, \tag{5.4}$$

where the normalization is given by the q^2 differential decay rate $\mathrm{d}\Gamma/\mathrm{d}q^2 = 2\,K_{1ss} + K_{1cc}$. F_L is not a null test, as it contains similar contributions as the differential decay rate. Due to the differential normalization in Eq. (5.4) uncertainties from resonance contributions cancel in the SM in F_L. This is because the Wilson coefficients in numerator and denominator cancel in scenarios where only one Wilson coefficient dominates, which is exactly the case in the SM with C_9^R. The distribution is then only affected by form factor uncertainties and mostly dictated by helicity, see Refs. [247, 248]. Most importantly at both kinematic endpoints $F_L = \frac{1}{3}$, which holds in the SM and beyond. The implications for the SM are the following. As depicted in Fig. 5.3 where F_L is shown for $\Lambda_c \to p\mu^+\mu^-$, F_L first increases from the low q^2 endpoint to a maximum $F_L \sim 0.7$ and then decreases to the high q^2 endpoint, where again $F_L = \frac{1}{3}$. The solid line in Fig. 5.3 is obtained when only C_9^R is included. The band illustrates interference effects of C_7^{eff}, whereas including C_9^{eff} has no effect. Note that these perturbative contributions are negligible for all other purposes and only enter here, because C_9^R cancels in F_L. The pale band illustrates a 10 % effect of splitting between a_M parameters for the longitudinal versus transverse polarization. The band is fading out towards the high q^2 region because this splitting is forbidden by symmetry at the endpoint.

The second angular observable is again the forward-backward asymmetry of the leptons, defined as

$$A_{\text{FB}}^{\ell} = \frac{1}{\mathrm{d}\Gamma/\mathrm{d}q^2}\left[\int_0^1 - \int_{-1}^0\right]\frac{\mathrm{d}^2\Gamma}{\mathrm{d}q^2\mathrm{d}\cos\theta_\ell}\,\mathrm{d}\cos\theta_\ell = \frac{3}{2}\,\frac{K_{1c}}{2\,K_{1ss} + K_{1cc}}\,. \tag{5.5}$$

Similar to the meson case, the numerator of A_{FB}^{ℓ} only contains interference terms of two different Wilson coefficients. The main important difference is that A_{FB}^{ℓ} includes the following interference terms, see App. E.2

$$A_{\text{FB}}^{\ell} \propto C_7C_{10},\, C_7C_{10}',\, C_7'C_{10},\, C_7'C_{10}',\, C_9C_{10},\, C_9'C_{10}'\,, \tag{5.6}$$

so that

- A_{FB}^{ℓ} constitutes a null test of the SM in rare charm decays.

- C_{10} can be probed even in the absence of further BSM contributions as an interference term with C_9 and thus the resonance contributions exist. On the other hand, if there is only NP in C_{10}' it cannot be seen in A_{FB}^{ℓ}, as this would require further BSM couplings to be present, *i.e.* C_7, C_7', C_9'.

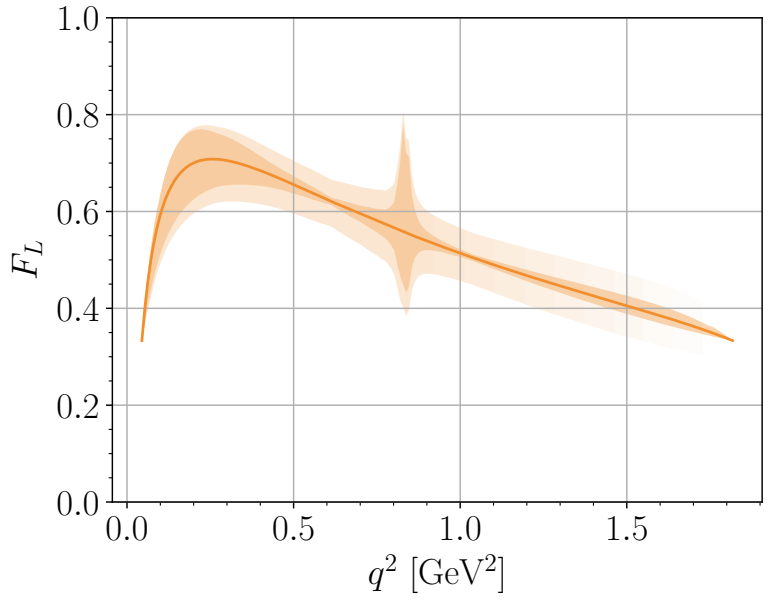

Figure 5.3: SM contribution for the fraction of longitudinally polarized dimuons F_L, see Eq. (5.4), in $\Lambda_c \to p\mu^+\mu^-$. The solid orange line is for C_9^R contributions only. The orange band illustrates effects of additionally including $C_{7,9}^{\text{eff}}(q^2)$. The pale band is obtained by adding a 10% splitting between the a_M parameters entering the longitudinal and the transverse polarization, which is forbidden at $q^2_{\text{max}} = (m_{\Lambda_c} - m_p)^2$, see text. At both endpoints $F_L = 1/3$ holds model-independently.

We also define

$$\tilde{A}^\ell_{\text{FB}} = \frac{1}{\Gamma}\left[\int_0^1 - \int_{-1}^0\right] \frac{\mathrm{d}^2\Gamma}{\mathrm{d}q^2 \mathrm{d}\cos\theta_\ell}\,\mathrm{d}\cos\theta_\ell = \frac{3}{2}\,\frac{K_{1c}}{\int_{q^2_{\text{min}}}^{q^2_{\text{max}}}(2\,K_{1ss} + K_{1cc})\,\mathrm{d}q^2}\,, \tag{5.7}$$

with the integrated decay rate as normalization in order to discuss the differences and advantages of each of these normalization schemes. Fig. 5.4 shows A^ℓ_{FB} and $\tilde{A}^\ell_{\text{FB}}$ for $\Lambda_c \to p\mu^+\mu^-$ in the upper and lower row plots, respectively. The left panel is for the full q^2 region and decreasing NP contribution in C_{10} thus illustrating the sensitivity, whereas the right plots are in the high q^2 region for several different NP benchmark scenarios. Here, the red uncertainty band of the scenario with $C_{10} = 0.3$ is bounded by black lines, as the red band is partly covered by other scenarios.

In A^ℓ_{FB} contributions are suppressed around the resonances, which is due to the peaking denominator, whereas $\tilde{A}^\ell_{\text{FB}}$ with constant denominator shows that contributions to the numerator are actually enhanced at the resonances. This is understood as C_9^R obtains maxima exactly at the resonance masses. Due to the significant uncertainties in the strong phases, the sign of A^ℓ_{FB} and therefore C_{10} cannot be predicted. The sensitivity to C_{10} is down to ~ 0.01 (few $\times\, 0.01$) level, depending on the normalization.

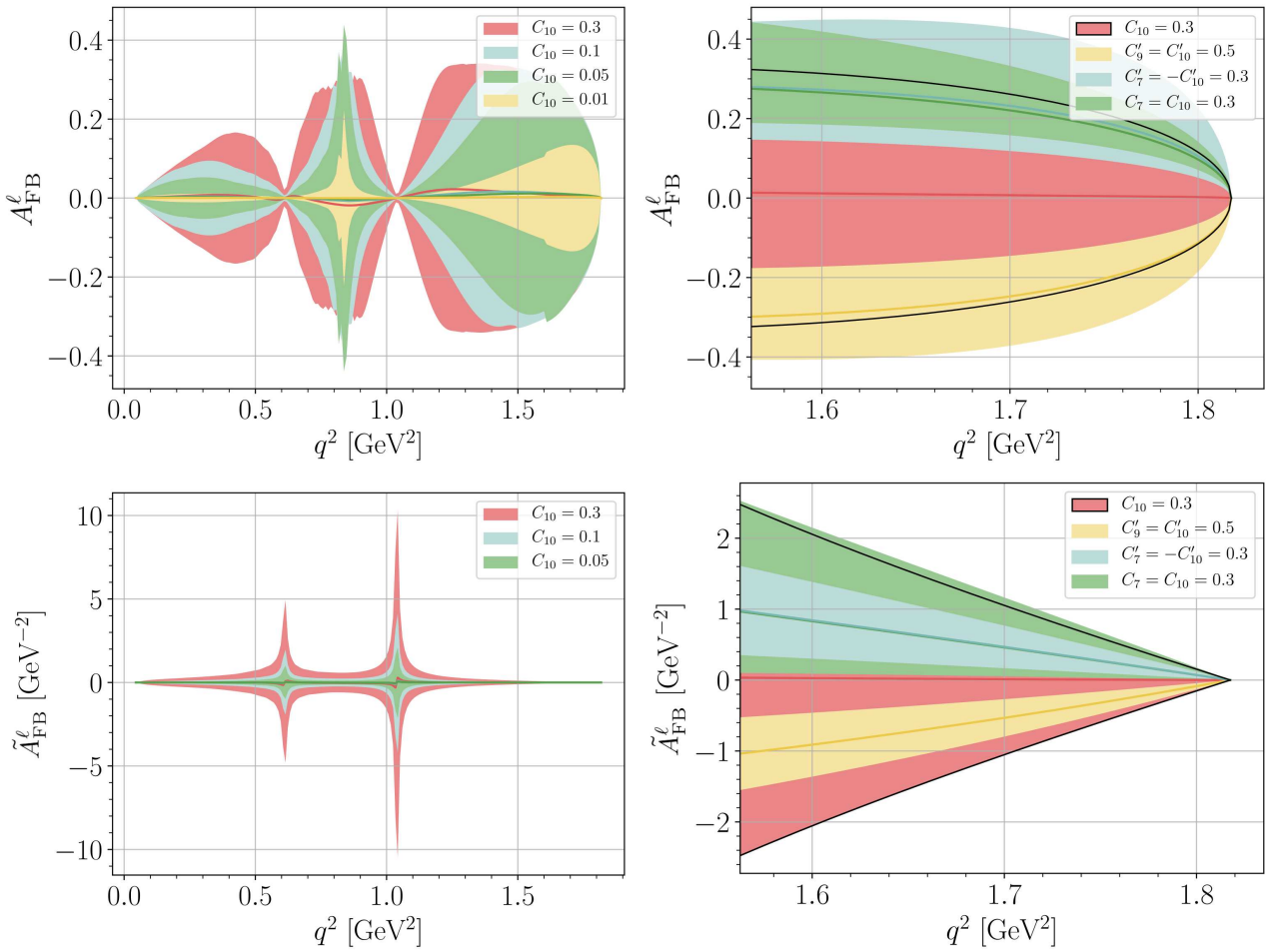

Figure 5.4: The top row shows the forward-backward asymmetry A_{FB}^{ℓ} normalized as in Eq. (5.5) and the bottom row displays $\tilde{A}_{\mathrm{FB}}^{\ell}$ as in Eq. (5.7) with normalization to the decay rate for $\Lambda_c \to p\mu^+\mu^-$ decays. The left panel shows different values of C_{10} in the full q^2 region. In the right panel various NP benchmark scenarios are shown in the high q^2 region.

The right plots for the high q^2 region show that uncertainties are more well behaved when only parts of the phase space are looked at. Also the dipole operators C_7 and C_7' can only be tested along with C_{10} or C_{10}'.

A better sensitivity independent of axial vector currents is achieved if NP contributions are tested in F_L, as illustrated in the upper plot of Fig. 5.5 for $\Lambda_c \to p\mu^+\mu^-$. Here, scenarios with only C_9, C_{10} or C_{10}' are indistinguishable from the SM curve in orange, which is also shown in Fig. 5.3. Small perturbations around the SM prediction are induced by contributions to C_9', which are then modulated by resonance uncertainties. More significantly, contributions to dipole operators $C_7^{(\prime)}$ lead to a strongly

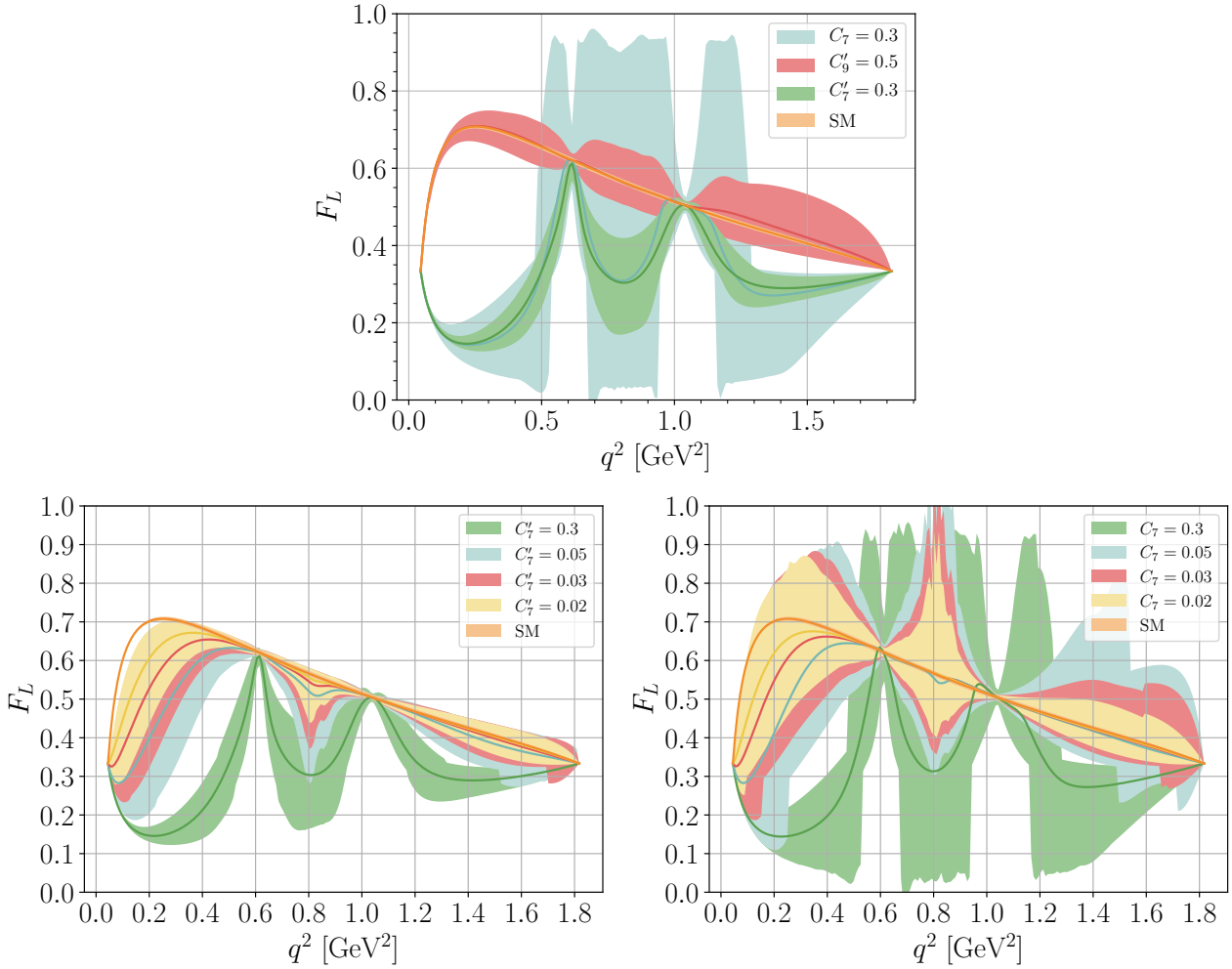

Figure 5.5: Various BSM scenarios contributing to the fraction of longitudinally polarized dimuons F_L of $\Lambda_c \to p\mu^+\mu^-$ decays. Theoretical uncertainties from form factors and resonance parameters are included. The orange band corresponds to the resonant SM contribution. The upper plot shows effects of C_9' and dipole operators $C_7^{(\prime)}$ and the bottom plots test the sensitivity of the dipole operators C_7' (left) and C_7 (right).

altered shape of F_L, thus also lifting the cancellation of resonance uncertainties present in the SM. These uncertainties remain sizable in C_7' scenarios and are huge in C_7 scenarios, however a measurement of F_L can clearly test the presence of sizable dipole operators down to $\mathcal{O}(0.01)$, which is apparent from the lower plots in Fig. 5.5, where the right plot shows the SM curve in orange and different decreasing values for $C_7' = 0.3$, 0.05, 0.03 and 0.02 in green, blue, red and yellow, respectively. The bottom right plot is similar, but for BSM physics in C_7. The extraordinary sensitivity to dipole operators in F_L can

be understood qualitatively by examining the different helicity contributions in the limit of vanishing lepton masses $q^2 \gg m_\ell^2$. In this limit, we find

$$F_L = \frac{L^{11+22}}{U^{11+22} + L^{11+22}}\,, \tag{5.8}$$

where U^{11+22} and L^{11+22} contain quadratic terms of helicity amplitudes and denote unpolarized transverse (U) and unpolarized longitudinal (L) terms. The full expressions are given in App. E.2. Here, we only take a closer look at prefactors in U and L and note that Wilson coefficients drop out in F_L in the limit of only considering one Wilson coefficient at a time. For C_9, C_{10}, C_9', C_{10}' contributions in L scale with $m_{\Lambda_c}^2/q^2$, whereas contributions to U are multiplied by a factor two. In this case, the leading q^2 dependence in F_L is given as

$$F_L \sim \frac{\frac{m_{\Lambda_c}^2}{q^2}}{2 + \frac{m_{\Lambda_c}^2}{q^2}} = \frac{1}{\frac{2q^2}{m_{\Lambda_c}^2} + 1}\,, \tag{5.9}$$

which decreases from $\mathcal{O}(1)$ for small q^2 values to the high q^2 endpoint where $F_L = \frac{1}{3}$. On the other hand dipole operators $C_7^{(\prime)}$ receive an additional factor of $2m_c/q^2$ from the photon to lepton pair coupling, resulting in a $1/q^2$ scaling in L and a $2m_{\Lambda_c^2}/q^4$ scaling in U, which leads to

$$F_L \sim \frac{\frac{1}{q^2}}{2\frac{m_{\Lambda_c}^2}{q^4} + \frac{1}{q^2}} = \frac{1}{\frac{2m_{\Lambda_c}^2}{q^2} + 1}\,, \tag{5.10}$$

which increases from $F_L \ll 1$ to endpoint $F_L = 1/3$. For the endpoint at $q^2 = 4m_\ell^2$ the m_ℓ^2 terms are mandatory to find $F_L = 1/3$ as well, which along with interference effects and the q^2 dependence of the resonance contributions lead to the shape displayed in Fig. 5.5.

5.1.3 $B_0 \to B_1(\to B_2\pi)\ell^+\ell^-$

In the case of the (quasi-)four-body rare charm baryon decays, the number of independent angular coefficients increases from three to ten, see Eq. (3.20). Among those it is easy to identify further null tests of the SM, due to proportionality to the axial vector couplings C_{10} and C_{10}' while no terms proportional to $|C_9|^2$ enter. Next to $K_{1c} \propto \tilde{A}_{FB}^\ell$, we find

$$K_{1c}^{\text{SM}} = K_{2c}^{\text{SM}} = K_{3s}^{\text{SM}} = K_{4s}^{\text{SM}} = 0\,. \tag{5.11}$$

Note again that all of these clean null tests except K_{1c} vanish in the limit $\alpha = 0$, *i.e.* when no secondary decay polarization is available. The NP sensitivity in K_{2c}, K_{3s} and K_{4s} is discussed in this section.

First, we discuss the possibility to measure the forward-backward asymmetry in the hadron system,

defined as

$$\begin{aligned} A_{\rm FB}^{\rm H} &= \frac{1}{{\rm d}\Gamma/{\rm d}q^2}\left[\int_0^1 - \int_{-1}^0\right]\int_{-1}^1\int_0^{2\pi}\frac{{\rm d}^4\Gamma}{{\rm d}q^2{\rm d}\cos\theta_\ell{\rm d}\cos\theta_\pi{\rm d}\phi}{\rm d}\phi{\rm d}\cos\theta_\ell{\rm d}\cos\theta_\pi \\ &= \frac{1}{2}\frac{2\,K_{2ss}+K_{2cc}}{2\,K_{1ss}+K_{1cc}}\,. \end{aligned} \tag{5.12}$$

$A_{\rm FB}^{\rm H}$ is not a null test, however, similar to F_L, a strong sensitivity to *some* NP Wilson coefficients is present. The top row plot of Fig. 5.6 shows $A_{\rm FB}^{\rm H}$ in the SM in orange and in NP benchmark scenarios $C_7 = 0.3$, $C'_{9,\,(10)} = 0.5$ and $C'_7 = 0.3$ in blue, red and green, respectively, for the four-body mode $\Xi_c^+ \to \Sigma^+(\to p\pi^0)\mu^+\mu^-$. Similar to discussions of the meson decays, $C_{i,\,(j)}$ refers to C_i *or* C_j, and we explicitly checked that the two cases are indistinguishable within uncertainties. Scenarios with BSM in C_9 only or C_{10} only are SM-like. The lower row plots in Fig. 5.6 exemplary illustrate sensitivities of C'_7 (left plot) and C'_{10} (right plot). Again, within uncertainties a plot with sensitivities of C'_9 is indistinguishable from the bottom right plot (C'_{10}). We see that right-handed dipole operators can be tested at the level of ~ 0.01, whereas significant deviations for C'_9 and C'_{10} require BSM effects close to $\mathcal{O}(0.1)$.

Similar to F_L, SM uncertainties are comparatively small as for a single Wilson coefficient scenario, the Wilson coefficient drops out in the ratio. Phase uncertainties entering in C_9^R are then irrelevant. For F_L endpoint relations enforce $F_L = \frac{1}{3}$, but $A_{\rm FB}^{\rm H}$ is only vanishing at the high q^2 endpoint, and non-vanishing, however model-dependent at the low q^2 endpoint. Also, it is not dipole couplings that strongly alter the shape of $A_{\rm FB}^{\rm H}$. Instead, one is sensitive to the difference of LH and RH quark currents, *i.e.* primed and unprimed operators. The behavior of C_7, C_9 and C_{10} with little or no effect on the SM curve, versus strong altered distribution in scenarios of C'_7, C'_9, C'_{10} can be attributed to the properties of the involved angular coefficients under parity. K_{1ss} and K_{1cc} are P–even, and K_{2ss} and K_{2cc} are P–odd. This leads to a cancellation of effects in numerator and denominator only for LH contributions. This is illustrated exemplarily in the limit $m_\ell = 0$ where $A_{\rm FB}^{\rm H}$ with effects from C_9, C_{10} and C'_{10} can be written as

$$A_{\rm FB}^{\rm H} = -\alpha\cdot\frac{\left(|C_9|^2+|C_{10}|^2-|C'_{10}|^2\right)A(q^2)\sqrt{s_+s_-}}{\left(\left(|C_9|^2+|C_{10}-C'_{10}|^2\right)B(q^2)s_+ + \left(|C_9|^2+|C_{10}+C'_{10}|^2\right)C(q^2)s_-\right)}\,, \tag{5.13}$$

where

$$\begin{aligned} A(q^2) &= 2\,f_\perp g_\perp + f_+ g_+\,\frac{m_{B_0}^2-m_{B_1}^2}{q^2}\,, \\ B(q^2) = 2\,g_\perp^2 + g_+^2\,\frac{\left(m_{B_0}-m_{B_1}\right)^2}{q^2}\,, &\quad C(q^2) = 2\,f_\perp^2 + f_+^2\,\frac{\left(m_{B_0}+m_{B_1}\right)^2}{q^2}\,. \end{aligned} \tag{5.14}$$

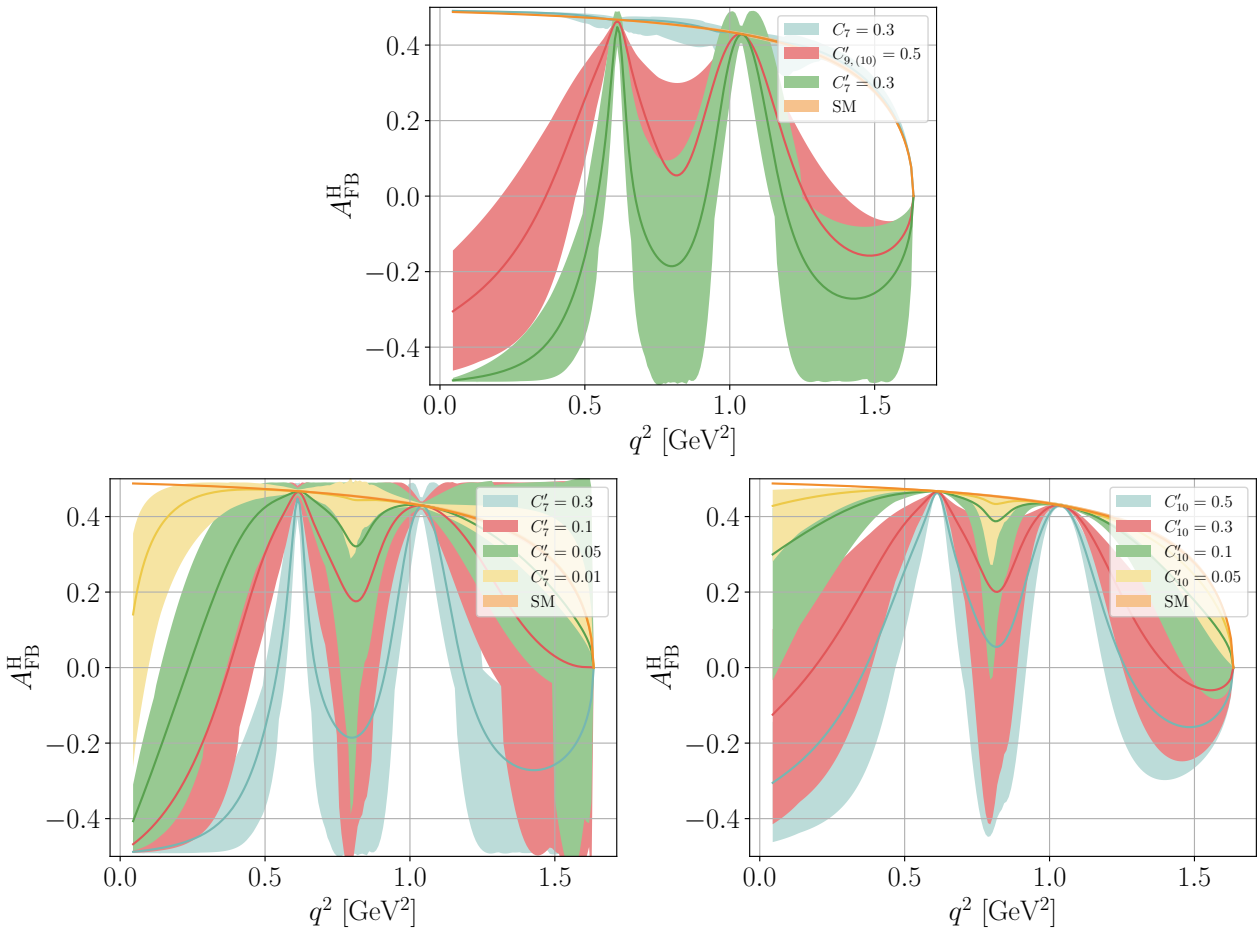

Figure 5.6: The top row plot shows the forward-backward asymmetry in the hadronic scattering angle θ_π for the decay mode $\Xi_c^+ \to \Sigma^+(\to p\pi^0)\mu^+\mu^-$ in the SM in orange and in NP scenarios with $C_7 = 0.3$, C'_9 or $C'_{10} = 0.5$ and $C'_7 = 0.3$ in blue, red and green, respectively. A NP scenario with C_9 only or C_{10} only is not shown, as it is indistinguishable from the SM curve. The bottom row plots show decreasing values of C'_7 (left) and C'_{10} (right), see the respective legend and the main text.

In the SM $C_9 = C_9^R$ and $C_{10}^{(\prime)} = 0$ and the Wilson coefficient cancels. Similarly $|C_9^R|^2 + |C_{10}|^2$ drops out as long as $C'_{10} = 0$, which is why no scenario with NP only in C_{10} is shown in Fig. 5.6. On the other hand, for $C'_{10} \neq 0$ the Wilson coefficients do not cancel, and the q^2 shape is driven by resonances in C_9^R. The additional minus sign in front of C'_{10} is because of the parity behavior of the numerator and hence a similar discussion also holds for C'_7 and C'_9. Interference terms of C_7 and C_9 softly break the exact cancellation, see the blue band in Fig. 5.6.

Next, we turn to another null test. The combined forward-backward asymmetry in both hadronic

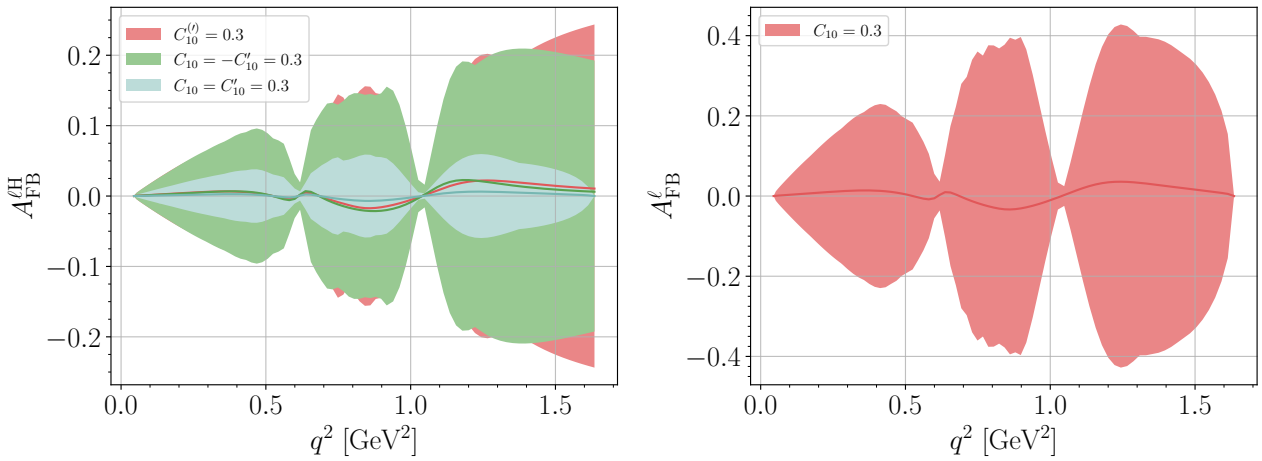

Figure 5.7: Combined forward-backward asymmetry in both hadronic and leptonic scattering angles θ_π, θ_ℓ for the decay mode $\Xi_c^+ \to \Sigma^+(\to p\pi^0)\mu^+\mu^-$ in NP scenarios with C_{10} or $C_{10}' = 0.3$, $C_{10} = -C_{10}' = 0.3$ and $C_{10} = C_{10}' = 0.3$ in red, green and blue, respectively. The right plot shows A_{FB}^{ℓ} only in the $C_{10} = 0.3$ scenario, but for the same decay channel for comparison. The SM prediction for both $A_{\mathrm{FB}}^{\ell\mathrm{H}}$ and A_{FB}^{ℓ} is exactly zero.

and leptonic scattering angles can be defined as

$$\begin{aligned} A_{\mathrm{FB}}^{\ell\mathrm{H}} &= \frac{1}{\mathrm{d}\Gamma/\mathrm{d}q^2}\left[\int_0^1 - \int_{-1}^0\right]\left[\int_0^1 - \int_{-1}^0\right]\int_0^{2\pi} \frac{\mathrm{d}^4\Gamma}{\mathrm{d}q^2\,\mathrm{d}\cos\theta_\ell\,\mathrm{d}\cos\theta_\pi}\mathrm{d}\phi\,\mathrm{d}\cos\theta_\ell\,\mathrm{d}\cos\theta_\pi \\ &= \frac{3}{4}\,\frac{K_{2c}}{2\,K_{1ss} + K_{1cc}}\,. \end{aligned} \tag{5.15}$$

Here, again C_{10} or C_{10}' are a necessity for a non-vanishing signal. In Fig. 5.7 the left plot shows $A_{\mathrm{FB}}^{\ell\mathrm{H}}$ for $\Xi_c^+ \to \Sigma^+(\to p\pi^0)\mu^+\mu^-$ in BSM benchmark scenarios $C_{10}^{(\prime)} = 0.3$ and $C_{10} = \pm C_{10}' = 0.3$ in red, green and blue, respectively. For better comparison the right plot shows A_{FB}^{ℓ} also evaluated for $\Xi_c^+ \to \Sigma^+(\to p\pi^0)\mu^+\mu^-$ and for $C_{10} = 0.3$. This plot is similar to the same benchmark in the upper left plot of Fig. 5.4 showing the three-body mode $\Lambda_c \to p\mu^+\mu^-$ up to differences in masses and the additional $\mathcal{B}(\Sigma^+ \to p\pi^0)$ suppression. The green and blue benchmarks are not shown in the right plot as they yield the same result since no sensitivity to C_{10}' is available in A_{FB}^{ℓ} as long as $C_7 = C_7' = C_9' = 0$ (interference with C_7^{eff} is neglected).

Now, $A_{\mathrm{FB}}^{\ell\mathrm{H}}$ is also induced by a term proportional to $C_9 C_{10}'$ and hence is able to test both axial vector couplings, even in absence of further BSM effects. From Fig. 5.7 we further learn that

- The scenario C_{10} or $C_{10}' = 0.3$ is indistinguishable from $C_{10} = -C_{10}' = 0.3$ within the large uncertainties induced by the strong phases in C_9^R.
- $C_{10} = C_{10}'$ leads to a partial cancellation of contributions and a decreased signal with respect to

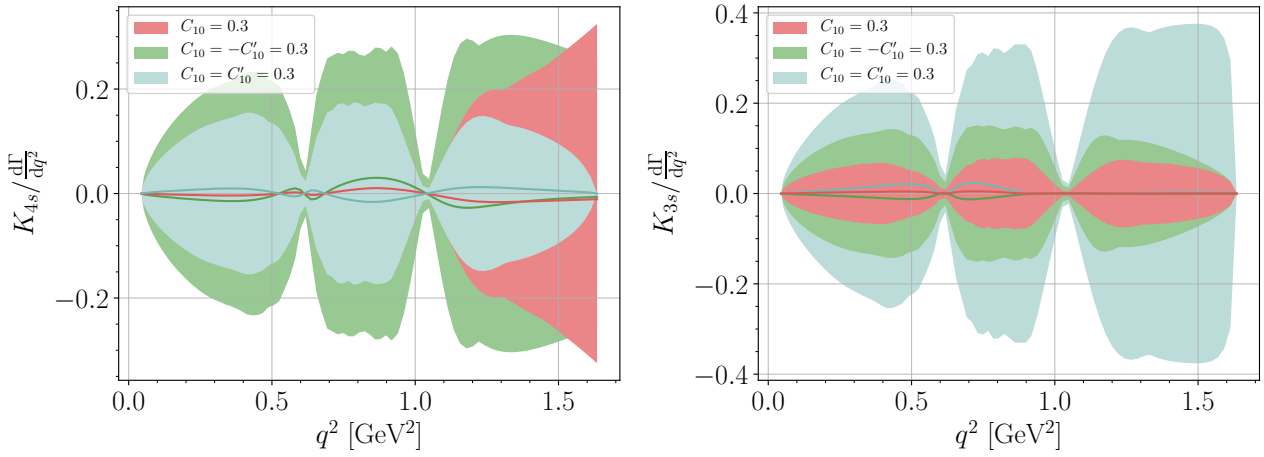

Figure 5.8: The angular null-test observables K_{4s} and K_{3s} for $\Xi_c^+ \to \Sigma^+(\to p\pi^0)\mu^+\mu^-$ and normalized to the differential decay rate in various NP scenarios for C_{10} and C'_{10}.

the other scenarios.

- The lepton forward-backward asymmetry vanishes at both kinematic endpoints, whereas $A_{\rm FB}^{\ell \rm H} = 0$ at $q^2 = 4m_\ell^2$, but does not necessarily vanish at the high q^2 endpoint.

5.1.4 Further angular null tests

Two more angular null tests exist for the (quasi-)four-body decay chain, K_{3s} and K_{4s}. Both contain terms proportional to both $C_9 C_{10}$ and $C_9 C'_{10}$, just like $K_{2c} \propto A_{\rm FB}^{\ell \rm H}$, and different from $K_{1c} \propto A_{\rm FB}^{\ell}$. Structurally, this makes K_{3s} and K_{4s} similar to $A_{\rm FB}^{\ell \rm H}$, discussed previously. Fig. 5.8 shows $K_{4s}(\mathrm{d}\Gamma/\mathrm{d}q^2)^{-1}$ (left) and $K_{3s}(\mathrm{d}\Gamma/\mathrm{d}q^2)^{-1}$ (right) in the same scenarios as $A_{\rm FB}^{\ell \rm H}$ in Fig. 5.7 for $\Xi_c^+ \to \Sigma^+(\to p\pi^0)\mu^+\mu^-$.

The endpoint behavior is understood. At zero hadronic recoil, $K_{3s} = K_{1c} = 0$, and $K_{4s}(\mathrm{d}\Gamma/\mathrm{d}q^2)^{-1} = -K_{2c}(\mathrm{d}\Gamma/\mathrm{d}q^2)^{-1}$ and finite, however dependent on the model [248]. Further differences to $A_{\rm FB}^{\ell \rm H}$ are only given by different Wilson coefficient times form factor combinations, which only results in little benefit from the view of complementarity. However, two more null tests also imply further opportunities increasing statistics and enhancing the sensitivity in a global analysis.

To go even beyond these opportunities in unpolarized rare charm baryon decays, the study of decays of initially polarized charm baryons introduces further null-test observables. This might be useful as some of those null tests already appear in polarized three-body decays, and hence can be probed with $\Lambda_c \to p\mu^+\mu^-$. From an experimental perspective the sensitivity to these more exotic baryon null tests in (quasi-)four-body decays depends on the (yet) unknown fragmentation fraction of exotic charmed baryons such as Ξ_c^+, Ξ_c^0, Ω_c^0 and the efficiency loss due to the reconstruction of the final state particles such as neutral pions. Although the $\mathcal{B}(B_1 \to B_2\pi)$ suppression is negligible, see Tab. 3.4,

the signal loss due to a reduced efficiency and fragmentation fraction can be severe. On the other hand opportunities in three-body decays of polarized Λ_c can suffer from a similar suppression, if the initial state polarization P_{Λ_c} is measured to be small. A detailed study is beyond the scope of this work, however eight additional null tests probing axial vector couplings $C_{10}^{(\prime)}$ proportional to the B_0–polarization P_{B_0} are easily identified in the four-body angular distribution

$$K_{5c}, K_{6c}, K_{7s}, K_{8s}, K_{9s}, K_{10s}, K_{11s}, K_{12s}|_{\rm SM} \simeq 0\,, \tag{5.16}$$

with angular coefficients from the differential distribution defined similar to [249], however following previously used notation

$$\begin{aligned}
\frac{\mathrm{d}^6\Gamma}{\mathrm{d}q^2\,\mathrm{d}\vec{\Omega}} = \frac{3}{32\pi^2}\cdot\Big(&\left(K_{1ss}\sin^2\theta_\ell + K_{1cc}\cos^2\theta_\ell + K_{1c}\cos\theta_\ell\right) + \\
&\left(K_{2ss}\sin^2\theta_\ell + K_{2cc}\cos^2\theta_\ell + K_{2c}\cos\theta_\ell\right)\cos\theta_\pi + \\
&\left(K_{3sc}\sin\theta_\ell\cos\theta_\ell + K_{3s}\sin\theta_\ell\right)\sin\theta_\pi\sin\left(\phi_c+\phi_\ell\right) + \\
&\left(K_{4sc}\sin\theta_\ell\cos\theta_\ell + K_{4s}\sin\theta_\ell\right)\sin\theta_\pi\cos\left(\phi_c+\phi_\ell\right) + \\
&\left(K_{5ss}\sin^2\theta_\ell + K_{5cc}\cos^2\theta_\ell + K_{5c}\cos\theta_\ell\right)\cos\theta_c + \\
&\left(K_{6ss}\sin^2\theta_\ell + K_{6cc}\cos^2\theta_\ell + K_{6c}\cos\theta_\ell\right)\cos\theta_\pi\cos\theta_c + \\
&\left(K_{7sc}\sin\theta_\ell\cos\theta_\ell + K_{7s}\sin\theta_\ell\right)\sin\theta_\pi\cos\left(\phi_c+\phi_\ell\right)\cos\theta_c + \\
&\left(K_{8sc}\sin\theta_\ell\cos\theta_\ell + K_{8s}\sin\theta_\ell\right)\sin\theta_\pi\sin\left(\phi_c+\phi_\ell\right)\cos\theta_c + \\
&\left(K_{9sc}\sin\theta_\ell\cos\theta_\ell + K_{9s}\sin\theta_\ell\right)\sin\phi_\ell\sin\theta_c + \\
&\left(K_{10sc}\sin\theta_\ell\cos\theta_\ell + K_{10s}\sin\theta_\ell\right)\cos\phi_\ell\sin\theta_c + \\
&\left(K_{11sc}\sin\theta_\ell\cos\theta_\ell + K_{11s}\sin\theta_\ell\right)\sin\phi_\ell\cos\theta_\pi\sin\theta_c + \\
&\left(K_{12sc}\sin\theta_\ell\cos\theta_\ell + K_{12s}\sin\theta_\ell\right)\cos\phi_\ell\cos\theta_\pi\sin\theta_c + \\
&\left(K_{13cc}\cos^2\theta_\ell + K_{13ss}\sin^2\theta_\ell\right)\sin\theta_\pi\sin\phi_c\sin\theta_c + \\
&\left(K_{14cc}\cos^2\theta_\ell + K_{14ss}\sin^2\theta_\ell\right)\sin\theta_\pi\cos\phi_c\sin\theta_c + \\
&\left(K_{15ss}\sin^2\theta_\ell\right)\sin\theta_\pi\cos\left(2\phi_\ell+\phi_c\right)\sin\theta_c + \\
&\left(K_{16ss}\sin^2\theta_\ell\right)\sin\theta_\pi\sin\left(2\phi_\ell+\phi_c\right)\sin\theta_c\Big)\,.
\end{aligned} \tag{5.17}$$

Eq. (3.20) is recovered by the first four lines in (5.17) with $\phi_c + \phi_\ell = \phi$. ϕ_c and θ_c are new angles associated with the initial state polarization. We refer to Ref. [249] for details.

Among the eight additional null tests in Eq. (5.16), K_{5c}, K_{9s} and K_{10s} do not vanish for $\alpha = 0$ and can be tested in $\Lambda_c \to p\mu^+\mu^-$, given a sufficient polarization of the Λ_c. Note that $K_{5c} = -P_{B_0}\,K_{2c}$, which implies that a test of K_{5c} in polarized three-body decays of Λ_c is equivalent to testing $A_{\rm FB}^{\ell\rm H}$, only available for self-analyzing four-body modes.

Angular null tests have already been tested recently in four-body meson decays $D^0 \to h^+h^-\mu^+\mu^-$ [72], and a first global fit might be in reach. The difficulty of these four-body charmed meson decays is that

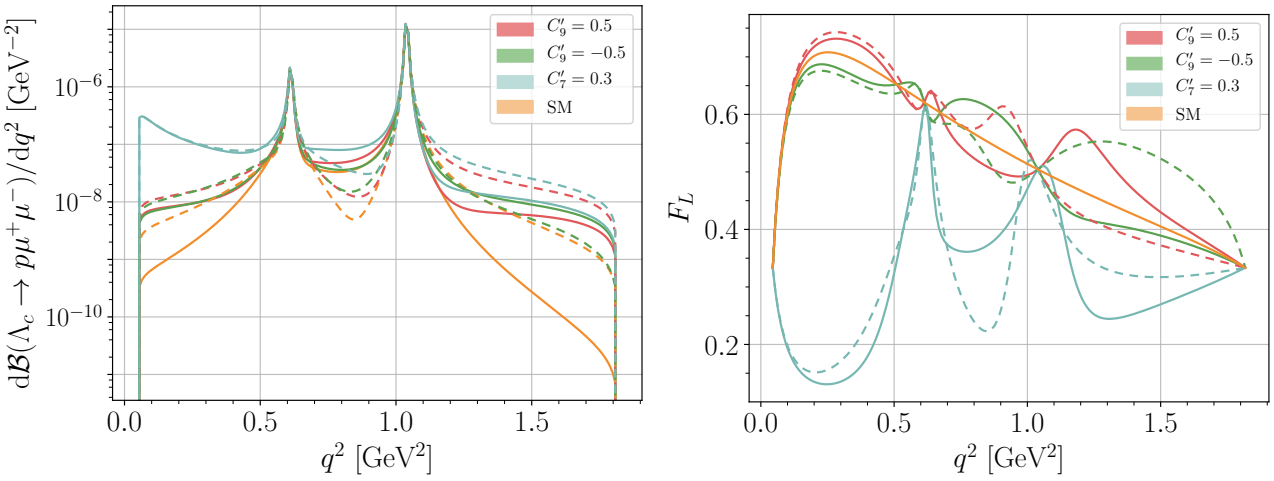

Figure 5.9: $\mathrm{d}\mathcal{B}(\Lambda_c \to p\mu^+\mu^-)/\mathrm{d}q^2\ [\mathrm{GeV}^{-2}]$ and F_L in the same mode are shown in the left and right plot, respectively, for the resonant SM in orange and for $C_9' = \pm 0.5$ and $C_7' = 0.3$ in red, green and blue, respectively. Solid lines show fixed strong phases $\delta_\omega = \delta_\phi = 0$ and dashed curves are for $\delta_\omega = 0$, $\delta_\phi = \pi$. In the right plot uncertainties due to strong phases cancel in the SM, which is why no dashed orange curve is shown.

resonances in the hadron and the lepton part of the final state need to be modeled [88]. A detailed investigation of the results in [72] is beyond the scope of this work and shall be given elsewhere.

5.1.5 Towards a global fit

We summarize the complementarity in different angular observables presented in this section and discuss the possibility to disentangle contributions from NP Wilson coefficients and QCD resonance parameters. As evident from Figs. 5.2, 5.4, 5.5, 5.6, 5.7 and 5.8 uncertainties from resonance parameters hamper the straightforward extraction of Wilson coefficients in rare charm decays. In that sense only a simultaneous extraction of Wilson coefficients and resonance parameters in a global fit to several angular observables will help to disentangle NP contributions. Fig. 5.9 illustrates the sensitivity of the differential branching ratio (left) and the fraction of longitudinally polarized dimuons (right) for the three-body baryon decay $\Lambda_c \to p\mu^+\mu^-$ by showing the SM in orange and NP scenarios with $C_9' = \pm 0.5$ and $C_7' = 0.3$ and strong phases fixed to $\delta_\omega = \delta_\phi = 0$ (solid curves) and $\delta_\omega = 0$, $\delta_\phi = \pi$ (dashed curves). In F_L, phase uncertainties cancel in the SM and only a solid curve is shown, whereas in the differential branching ratio, the phase matters. Note that without information on strong phases the sign of Wilson coefficients remains unknown, as a sign flip is equivalent to flipping all strong phases simultaneously.

Clearly, q^2 differential measurements in both observables would be able to distinguish between the different scenarios. This is already clear as for example the benchmark $C_7' = 0.3$, $\delta_\omega = 0$, $\delta_\phi = \pi$ (blue dashes curve) is already excluded by the experimental upper limit in Eq. (3.22), however at the moment neither the exact phase combination nor the value for C_7' can be excluded. It is only the

combination of all parameters that is tested.

On the other hand the complementarity of the presented observables is already sufficient to disentangle most of the different NP Wilson coefficients as follows

- Tensor and scalar contributions are tested in angular observables of charmed meson decays, see Fig. 5.2. The scalars are tightly constrained from upper limits on purely leptonic decays $D^0 \to \ell^+\ell^-$ and updates are expected to be available in the near future.
- Dipole operators C_7 and C_7' are probed in F_L and can be distinguished by $A_{\rm FB}^{\rm H}$.
- NP in C_9' can be identified if F_L is SM–like and the null tests remain zero, but $A_{\rm FB}^{\rm H}$ shows signal of RH quark currents.
- Axial vector couplings C_{10} and C_{10}' show up in various null-test observables and LH and RH can be disentangled again in $A_{\rm FB}^{\rm H}$, and further in $A_{\rm FB}^{\ell}$, where only C_{10} enters, as long as no further BSM couplings are present.
- Only in the scenario of NP only entering in C_9 no final conclusion can be achieved without better knowledge of resonance parameters.

Note, that these statements are independent of the actual resonance model used for the parametrization of long-range effects. In any case a global fit can only be performed taking into account resonance parameters and Wilson coefficients at the same time. However, interesting physics is tested in angular observables of rare charm decays despite the significant uncertainties induced by the dominant resonance contributions.

Beyond angular observables, even more null tests of the SM are available for rare charm decays and are discussed in the remainder of this section.

5.2 CP–asymmetries

We discuss CP–violating NP contributions in semileptonic rare charm decays and correlations to CP–violation in $\Delta A_{\rm CP}$. As pointed out in Sec. 3.5, we focus on *direct* CP–violation.

5.2.1 Resonance-enhanced CP–asymmetries in $D \to P\ell^+\ell^-$

The CP–asymmetry in rare semileptonic charm decays constitutes another promising null-test observable [90, 92]. Similar to the discussion of the lepton forward-backward asymmetry in Sec. 5.1.2, we distinguish two definitions, differing in their normalization

$$\tilde{A}_{\rm CP}(q^2) = \frac{{\rm d}\Gamma/{\rm d}q^2 - {\rm d}\overline{\Gamma}/{\rm d}q^2}{\Gamma + \overline{\Gamma}}\,, \qquad A_{\rm CP}(q^2) = \frac{{\rm d}\Gamma/{\rm d}q^2 - {\rm d}\overline{\Gamma}/{\rm d}q^2}{{\rm d}\Gamma/{\rm d}q^2 + {\rm d}\overline{\Gamma}/{\rm d}q^2}\,, \tag{5.18}$$

where $\overline{\Gamma}$ corresponds to the CP–conjugated decay mode and the integrated decay rate Γ and similarly $\overline{\Gamma}$ are defined as in Eq. (5.3). The explicit form of the difference of the differential rates reads

$$\begin{aligned}\frac{\mathrm{d}\Gamma}{\mathrm{d}q^2} - \frac{\mathrm{d}\overline{\Gamma}}{\mathrm{d}q^2} = \frac{G_F^2\alpha_e^2}{256\pi^5 m_D^3}\sqrt{\lambda_{DP}}\,\beta_\ell \Bigg\{ & \\ & \frac{2}{3}\,\mathrm{Im}\left[C_9 + 2C_7\frac{m_c}{m_D+m_P}\frac{f_T}{f_+}\right]\mathrm{Im}\left[C_9^R\right]\left(1+\frac{2m_\ell^2}{q^2}\right)\lambda_{DP} f_+^2 \\ & + \mathrm{Im}\left[C_P\right]\mathrm{Im}\left[C_P^R\right]\frac{q^2}{m_c^2}(m_D^2-m_P^2)^2 f_0^2 \\ & + 4\,\mathrm{Im}\left[C_T\right]\mathrm{Im}\left[C_9^R\right]\frac{m_\ell}{m_D+m_P}\lambda_{DP} f_+ f_T \\ & + 2\,\mathrm{Im}\left[C_{10}\right]\mathrm{Im}\left[C_P^R\right]\frac{m_\ell}{m_c}(m_D^2-m_P^2)^2 f_0^2\Bigg\}\,.\end{aligned} \tag{5.19}$$

In the SM, effects are proportional to $\mathrm{Im}(C_9^{\mathrm{eff}})$ and $\mathrm{Im}(C_7^{\mathrm{eff}})$, defined in Eq. (2.25), and negligible due to the involved small phases of the CKM factors. Effects from the resonant decay $A_{\mathrm{CP}}(D^+ \to \phi\pi^+)$ are consistent with CP–symmetry [250] and since $\phi \to \mu\mu$ is an CP–conserving electromagnetic decay, no SM background is expected, which makes these type of CP–asymmetries null tests of the SM.

On the other hand, the resonance contributions catalyze CP–violating NP effects around the resonance masses, where strong phases are large and the largest statistics is available [92]. This makes CP–asymmetries promising candidates in the search for new sources of CP–violation beyond the SM, as illustrated in Fig. 5.10. Here, we show the CP–asymmetries of $D^+ \to \pi^+\mu^+\mu^-$ (left panel) and $D_s^+ \to K^+\mu^+\mu^-$ (right panel) around the squared mass of the ϕ resonance and in the high q^2 region for a NP benchmark $C_9 = 0.1\,\exp(\mathrm{i}\phi_{\mathrm{NP}})$ with CP–violating phase $\phi_{\mathrm{NP}} = \pi/4$ and for several fixed strong phases $\delta_\phi = \pi,\, 0,\, \pi/2,\, -\pi/2$. in blue, yellow, red and green, respectively. In Fig. 5.10 we use the integrated decay rates as normalization.

CP–violation from other Wilson coefficients would be generated from dipole couplings $C_7^{(\prime)}$, but is suppressed for C_P, C_T, C_{10} by the light lepton mass, or negligibly small $\mathrm{Im}[C_P^R(q^2 \sim m_\pi^2)]$. $\mathrm{Im}[C_P^R]$ is larger around the η and η' mass, however their small widths make probes for CP–violation in C_P, C_T, C_{10} inaccessible.

As evident from Fig. 5.10 large effects can be observed in both kinematic regimes and irrespective of the value of the strong phase δ_ϕ, however binning might be necessary especially around the resonance mass region, as effects might be washed out by integration. The chosen benchmark is not the maximally allowed value for the absolute value of the Wilson coefficient C_9, however, depending on the model, constraints and correlations from CP–violation in $D^0 - \overline{D}^0$ mixing and hadronic decays (ΔA_{CP}) might be more stringent. This scenario is investigated in detail in the framework of flavorful $U(1)'$ extensions in Sec. 5.2.3.

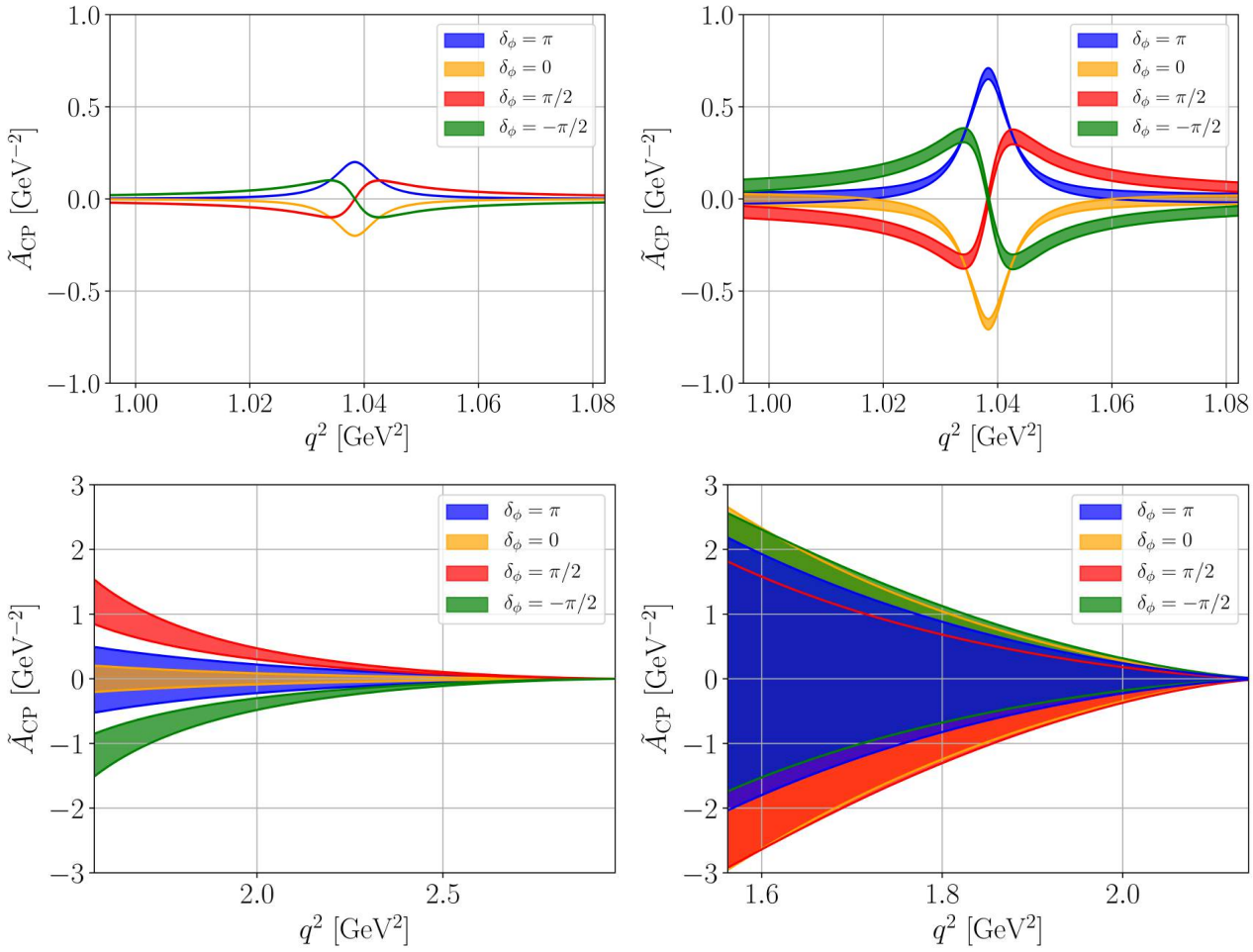

Figure 5.10: The CP–asymmetry for $C_9 = 0.1\exp(\mathrm{i}\,\pi/4)$ in $D^+ \to \pi^+\mu^+\mu^-$ ($D_s^+ \to K^+\mu^+\mu^-$) decays is shown in the left (right) plot in the region around the ϕ resonance $[(m_\phi - 5\Gamma_\phi)^2, (m_\phi + 5\Gamma_\phi)^2]$ (upper plots) and in the high q^2 region (lower plots). Strong phases are fixed to $\delta_\phi = 0, \pm\pi/2, \pi$, see legend. The uncertainties are due to the remaining strong phases (δ_ρ, δ_η) and the form factors.

5.2.2 CP–asymmetries in $\Lambda_c \to p\ell^+\ell^-$

CP–asymmetries around the resonances can also be studied in rare charm baryon decays, which we discuss for the example of $\Lambda_c \to p\mu^+\mu^-$. Here, we investigate in more detail the importance of the normalization used in Eq. (5.18). We use a similar benchmark scenario $C_9 = 0.5e^{\mathrm{i}\pi/4}$ and the same fixed strong phases $\delta_\phi = 0$, $\pm\pi/2$, π in yellow, green, red and blue, respectively, and plot A_{CP} in the full q^2 region and zoomed into the region around the ϕ resonance in the top row of Fig. 5.11. The plot

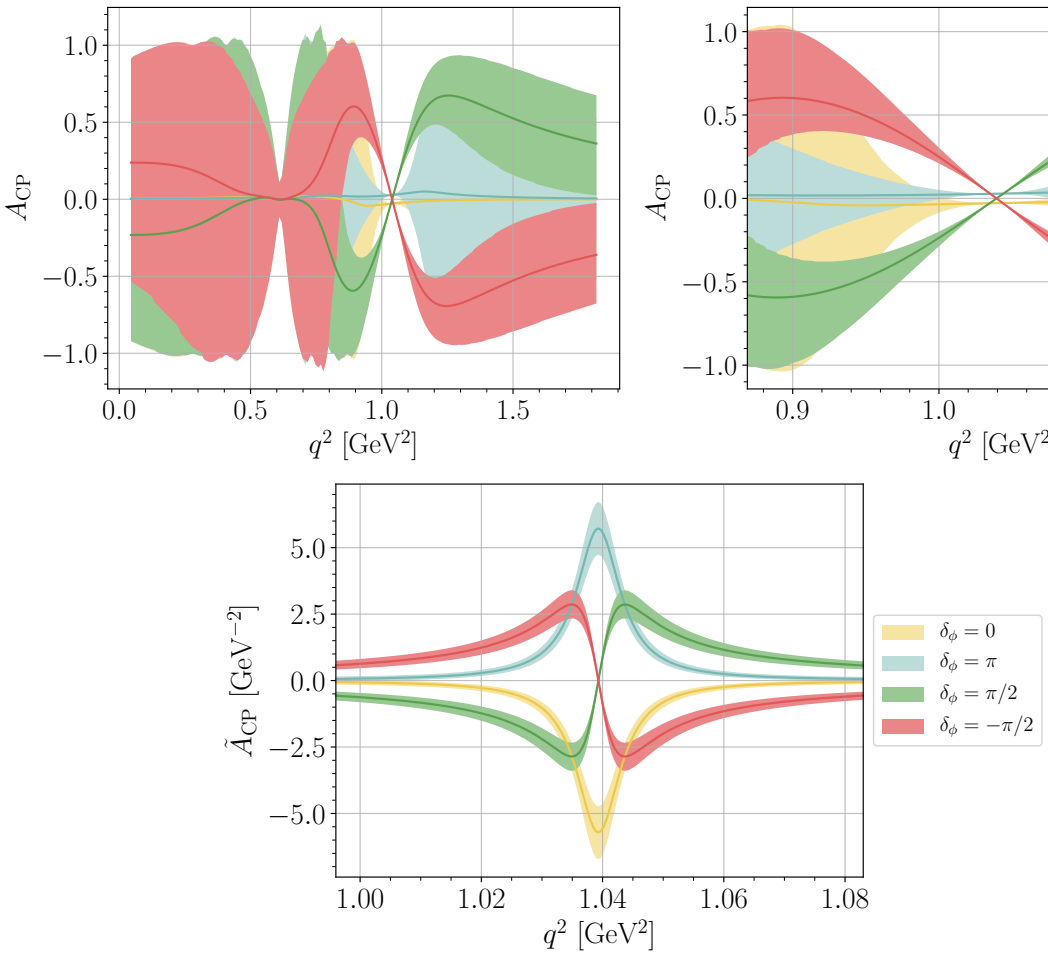

Figure 5.11: Direct CP–asymmetry of $\Lambda_c \to p\mu^+\mu^-$ decays for the CP–violating benchmark $C_9 = 0.5e^{i\pi/4}$ with q^2-differential normalization in the full q^2 range (left) and the region around the ϕ resonance (right). δ_ϕ fixed to $0, \pi, \pm\frac{\pi}{2}$ is displayed in yellow, blue, green and red, respectively, where uncertainties are due to form factors and strong phase variation in δ_ω. $\tilde{A}_{CP}$ with integrated decay rate as normalization is shown in the lower plot for $q^2 \in [(m_\phi - 5\,\Gamma_\phi)^2, (m_\phi + 5\,\Gamma_\phi)^2]$.

on the bottom shows the analogous $\tilde{A}_{CP}$ for the baryon mode around the ϕ resonance for comparison.

For A_{CP}, *i.e.* for differential decay rates in numerator and denominator, the signal decreases towards the resonance masses, which is contrary to the findings for constant normalization ($\tilde{A}_{CP}$), see also Fig. 5.10 and Ref. [92], where the signal is enhanced around the resonances. The reason is simply that the denominator in A_{CP} peaks at the resonance mass and therefore eradicates the signal in the numerator. In the upper left plot one can also see how the full phase variation of δ_ω leads to a blurred

signal around the ρ, ω masses, whereas the fixed phases δ_ϕ lead to a rather disentangled picture around the ϕ resonance, also visible in the zoom-in plot (upper right).

Also, large, localized cancellations are circumvented by the integrated denominator of $\tilde{A}_{\rm CP}$, leading to reduced uncertainty bands in the lower plot of Fig. 5.11 with respect to the upper row plots.

As a combination of presented null-test opportunities, we define the CP–asymmetry of the lepton forward-backward asymmetry as

$$A_{\rm FB}^{\rm CP} = \frac{A_{\rm FB}^{\ell} + \overline{A}_{\rm FB}^{\ell}}{A_{\rm FB}^{\ell} - \overline{A}_{\rm FB}^{\ell}} = \frac{K_{1c} - \overline{K}_{1c}}{K_{1c} + \overline{K}_{1c}}\,, \tag{5.20}$$

with $\overline{K}_{1c}$ the angular coefficient after CP–conjugation. This type of CP–asymmetry was already studied for inclusive charm decays [251] and for rare B decays [252]. Again small CP–phases and the GIM cancellation protect $A_{\rm FB}^{\rm CP}$ in the SM, thus providing yet another null test, this time with sensitivity to the imaginary part of C_{10}. Note that $A_{\rm FB}^{\ell}$ is a CP–odd observable, thus $A_{\rm FB}^{\ell} = -\overline{A}_{\rm FB}^{\ell}$ in the CP–conserving limit.

$A_{\rm FB}^{\rm CP}$ can be used for two purposes. Firstly, it tests imaginary parts in axial vector coupling C_{10}. We find $K_{1c} \propto {\rm Re}(C_9^R\, C_{10}^*)$, which leads to

$$A_{\rm FB}^{\rm CP} = \frac{{\rm Im}\, C_9^R}{{\rm Re}\, C_9^R}\, \frac{{\rm Im}\, C_{10}}{{\rm Re}\, C_{10}}\,, \tag{5.21}$$

and therefore constitutes a very clean null test of the SM, where hadronic uncertainties mostly cancel and are only induced via strongly suppressed contributions from $C_9^{\rm eff}$ and $C_7^{\rm eff}$, which break the exact cancellation of form factors in numerator and denominator.

Secondly, $A_{\rm FB}^{\rm CP}$ is very sensitive to the values of strong phases. This can be seen as follows. Consider a single resonance contribution, *e.g.* the ϕ resonance, in the definition of C_9^R, then

$$A_{\rm FB}^{\rm CP} = \frac{{\rm Im}\, C_9^R}{{\rm Re}\, C_9^R}\, \frac{{\rm Im}\, C_{10}}{{\rm Re}\, C_{10}} \;=\; \frac{(q^2 - m_\phi^2)\, \tan\delta_\phi - m_\phi \Gamma_\phi}{q^2 - m_\phi^2 + m_\phi \Gamma_\phi\, \tan\delta_\phi} \cdot \frac{{\rm Im}\, C_{10}}{{\rm Re}\, C_{10}}\,, \tag{5.22}$$

with unknown strong phase δ_ϕ, which however determines the value of q^2 at which a zero in the denominator leads to a diverging $A_{\rm FB}^{\rm CP}$. The interference of several Breit-Wigner shapes then leads to further divergences, which however coincide with the zeros in $A_{\rm FB}^{\ell}$ and provide information on the sizes of the strong phases, which again motivates a joint global fit of Wilson coefficients and strong phases.

For illustration we define the CP–violating difference and the CP–average, as

$$\Delta A_{\rm FB}^{\rm CP} = \frac{1}{2}\left(A_{\rm FB} + \bar{A}_{\rm FB}\right), \qquad \Sigma A_{\rm FB}^{\rm CP} = \frac{1}{2}\left(A_{\rm FB} - \bar{A}_{\rm FB}\right), \tag{5.23}$$

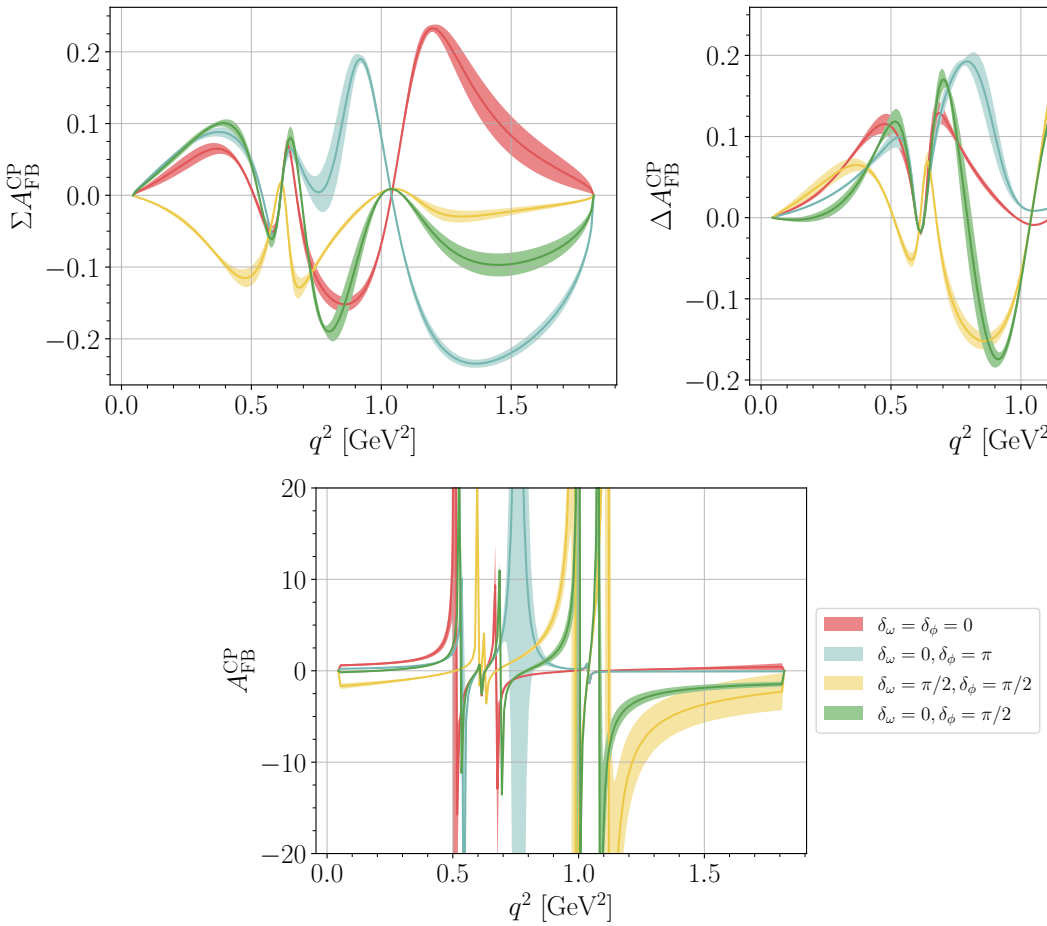

Figure 5.12: CP–asymmetry of the forward-backward asymmetry $A_{\rm FB}^{\rm CP}$ for $\Lambda_c \to p\mu^+\mu^-$ decays and the $C_{10} = 0.5\, e^{i\pi/4}$ scenario. We use several different, fixed combinations of strong phases, see legend. The upper row displays the CP–average and the CP–difference as in Eq. (5.23) in the left and right plot, respectively, and the bottom plot shows their ratio Eqs. (5.20), (5.24).

where again $A_{\rm FB}$ is CP–odd, so that Eq. (5.20) is recovered as

$$A_{\rm FB}^{\rm CP} = \frac{\Delta A_{\rm FB}^{\rm CP}}{\Sigma A_{\rm FB}^{\rm CP}}\,. \tag{5.24}$$

Fig. 5.12 displays $\Sigma A_{\rm FB}^{\rm CP}$, $\Delta A_{\rm FB}^{\rm CP}$ and their ratio in the upper left, upper right and bottom plot, respectively for various fixed combinations of strong phases, see the legend, and for $C_{10} = 0.5\, \exp(i\pi/4)$.

Since $A_{\rm FB}^{\rm CP}$ is highly sensitive to the strong phases via q^2 positions of divergences, it is impossible

to provide integrated values of the CP–violating forward-backward asymmetry. Also note again that $A_{\rm FB}^{\rm CP}$ is insensitive to imaginary parts of C_{10}' as no interference terms with C_9^R exist. As demonstrated in Sec. 5.1.3, other null-test observables, such as the combined forward-backward asymmetry in both lepton and hadron system $A_{\rm FB}^{\ell \rm H}$ exist in (quasi-)four-body baryon decays and test C_{10}' via interference terms with C_9^R. Therefore, the CP–asymmetry of $A_{\rm FB}^{\ell \rm H}$ has sensitivity to $\text{Im}(C_{10}')$. In general, CP–asymmetries of all angular observables can be defined and studied. We leave a detailed analysis to future studies, which may be needed as soon as data become available.

5.2.3 Correlations to $\Delta A_{\rm CP}$

CP–violation is observed in the charm sector in the measurement of $\Delta A_{\rm CP} = A_{\rm CP}(D^0 \to K^+K^-) - A_{\rm CP}(D^0 \to \pi^+\pi^-)$ [85], see discussion in Sec. 3.5.2. Since the NP nature of the recent LHCb measurement is subject of ongoing discussion, we study how correlations between CP–violation measurements in semileptonic and hadronic charm decays may help to interpret this experimental result. We choose to study these correlations within the framework of flavorful, anomaly-free Z'–extensions, introduced in Sec. 4.3 and further details compiled in App. D. The advantage of these type of models is that they induce these CP–asymmetries for both hadronic and semileptonic decay modes at tree level. The most stringent constraint is then the $D^0 - \overline{D}^0$ mixing amplitude, which is also generated at tree level.

We expect the branching ratio of hadronic decays $D^0 \to P_1^+ P_2^-$ to be dominated by the SM single-Cabibbo-suppressed decay amplitude, which is why we split contributions for K^+K^- and $\pi^+\pi^-$ final states as in Eq. (3.32). Here, the first term exactly defines the single-Cabibbo-suppressed contribution, the second term is responsible for CP–violating effects in the SM and the third term corresponds to BSM contributions from Z'–interactions. Again, $\mathcal{A}_{K(\pi)}^{\rm NP}$ is assumed to have a negligible effect on the branching ratio. Within these assumptions SM and BSM effects to $\Delta A_{\rm CP}$ can be separated as in Eq. (3.33), where [2]

$$\Delta r^{\rm NP} = r_K \sin\delta_K \, \sin\phi_K + r_\pi \sin\delta_\pi \, \sin\phi_\pi \ , \tag{5.25}$$

where δ_K, δ_π are unknown strong phases, which we take to be maximal, as we are interested in maximal NP effects and

$$r_K = \frac{\mathcal{A}_K^{\rm NP}}{(\mathcal{A}_K^s - \mathcal{A}_K^d)_{\rm SM}} \ , \quad r_\pi = \frac{\mathcal{A}_\pi^{\rm NP}}{(\mathcal{A}_\pi^d - \mathcal{A}_\pi^s)_{\rm SM}} \ . \tag{5.26}$$

The absolute values of the denominators in Eq. (5.26) are fixed by branching ratio measurements, see App. D.3.

As discussed at the end of Sec. 4.3, large CP–violating effects while simultaneously evading severe kaon constraints are possible if the LH quark current is zero, while the RH one exhausts the $D^0 - \bar{D}^0$ mixing bound. This can be achieved with $\Delta F_L = F_{Q_2} - F_{Q_1} = 0$, possible in models 2, 4, 5, 9 and 10

[2] $\lambda_d = -\lambda_s + O(\lambda_b)$ leads to an additional minus sign between the pion and kaon amplitudes.

Table 5.1: Parameters $c_{K,\pi}, d_{K,\pi}$ and d_{π',π^0} in $(\text{TeV})^2$, see App. D.3 for definitions and details, and for increasing Z'–masses in TeV.

$M_{Z'}$ [TeV]	2	4	6	8	10
c_K	1.133	1.217	1.266	1.302	1.330
d_K	−0.046	−0.054	−0.058	−0.061	−0.063
c_π	−1.446	−1.553	−1.616	−1.661	−1.698
d_π	0.058	0.068	0.074	0.077	0.080
$d_{\pi'}$	0.071	0.083	0.090	0.094	0.098
d_{π^0}	0.077	0.090	0.097	0.102	0.106

in Tab. D.1 in App. D. Simultaneously, we need $\Delta F_R = F_{u_2} - F_{u_1} \neq 0$, since

$$g_R^{uc} = g_4 \, \sin\theta_u \cos\theta_u e^{\mathrm{i}\phi_R} \, \Delta F_R \,, \tag{5.27}$$

where θ_u and the CP–phase ϕ_R parametrize the misalignment of flavor and mass basis for RH up-type quarks.

With details on the calculation given in App. D.3, we find that ΔA_{CP} can be written as

$$\Delta A_{\text{CP}}^{\text{NP}} = A_{\text{CP}}^{\text{NP}}\left(D^0 \to K^+K^-\right) - A_{\text{CP}}^{\text{NP}}\left(D^0 \to \pi^+\pi^-\right) \,, \tag{5.28}$$

with

$$\begin{aligned} A_{\text{CP}}^{\text{NP}}\left(D^0 \to K^+K^-\right) &\sim \frac{g_4^2}{M_{Z'}^2}\theta_u \, \Delta F_R \left[c_K \, F_{Q_2} + d_K \, F_{d_2}\right] \,, \\ A_{\text{CP}}^{\text{NP}}\left(D^0 \to \pi^+\pi^-\right) &\sim \frac{g_4^2}{M_{Z'}^2}\theta_u \, \Delta F_R \left[c_\pi \, F_{Q_1} + d_\pi \, F_{d_1}\right] \,. \end{aligned} \tag{5.29}$$

Numerical values for the parameters c_K, d_K, c_π, d_π are collected in Tab. 5.1 and details on their calculation are compiled in App. D.3.

We explicitly demonstrate how large values for ΔA_{CP} are achieved, while evading the $D^0 - \overline{D}^0$ mixing bound for model 2 of Tab. D.1 with $\Delta F_R = 12$ and $\theta_u = 1 \cdot 10^{-4}$ in Fig. 5.13, where we show increasing contributions to ΔA_{CP} see green bands and legend, as well as constraints from mixing on $x_{12}\sin\phi_{12}$, shown as a red exclusion region and on the absolute value x_{12} as red hatched region[3] in the plane of the remaining model parameters $g_4/M_{Z'}$ and CP–violating phase ϕ_R. The golden star

[3]The red exclusion regions in Fig. 5.13 are more stringent than in Ref. [2], due to improved fit values for x_{12} and ϕ_{12} in the update of Ref. [176] when including Ref. [253].

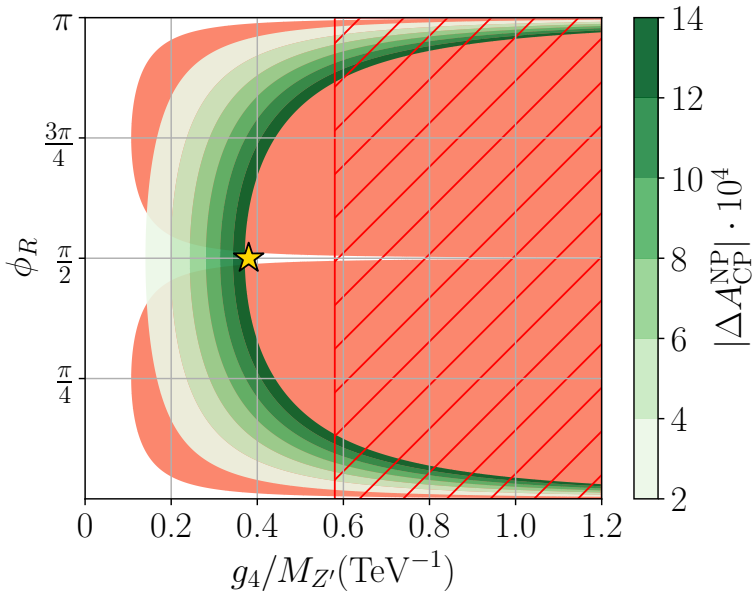

Figure 5.13: ϕ_R–$g_4/M_{Z'}$ (TeV^{-1}) plane for $\theta_u = 1 \cdot 10^{-4}$ with increasing contributions to $|\Delta A_{\mathrm{CP}}^{\mathrm{NP}}|$ (green bands) versus exclusion regions from D^0–$\overline{D}^0$ mixing, see (D.6). The imaginary part $x_{12} \sin \phi_{12}$ is shown as the red area and the absolute value x_{12} as a red-hatched region. F_ψ–charges are taken from model 2, see TABLE D.1. The golden star indicates a benchmark point (5.30) as discussed in the main text.

indicates a benchmark value resulting in $\Delta A_{\mathrm{CP}}^{\mathrm{NP}} \sim 10^{-3}$

$$\phi_R \sim \frac{\pi}{2}, \quad \frac{g_4}{M_{Z'}} \sim 0.38\,\mathrm{TeV}^{-1}, \quad \theta_u \sim 10^{-4}\,. \tag{5.30}$$

Fig. 5.13 shows that the weak phase ϕ_R needs to be slightly fine-tuned, as a value around $\phi_R \sim \pi/2$ drops out in the mixing amplitude but gives maximal CP–violating effects in hadronic and semileptonic decays.

Another benchmark point used in Ref. [2] based on charges from model 10 of Tab. D.1 is now excluded, due to updates in mixing parameters and improved bounds on $\mathcal{B}(D^+ \to \pi^+\mu^+\mu^-)$. We demonstrate this via Fig. 5.14, where we show the plane spanned by $\Delta\tilde{F}_R = \Delta F_R \cdot \theta_u$ and $g_4/M_{Z'}$ for charge assignments as in model 2 (left) and model 10 (right). In light green, dark green, blue and cyan we plot decreasing contributions to ΔA_{CP}, in red and black we show exclusion regions from $D^0 - \overline{D}^0$ mixing and perturbativity plus searches in dimuon and dielectron spectra [184] ($g_4 < 4\pi$, $M_{Z'} < 5\,\mathrm{TeV}$), respectively. We also show the upper limit from $\mathcal{B}(D^+ \to \pi^+\mu^+\mu^-)$ as dash–dotted lines. In the right plot, we distinguish two different possibilities for model 10 charge assignments. The first scenario has large muon charges $F_{L_2} = 15$, $F_{e_2} = 18$ and severe constraints from $\mathcal{B}(D^+ \to \pi^+\mu^+\mu^-)$ are shown as a

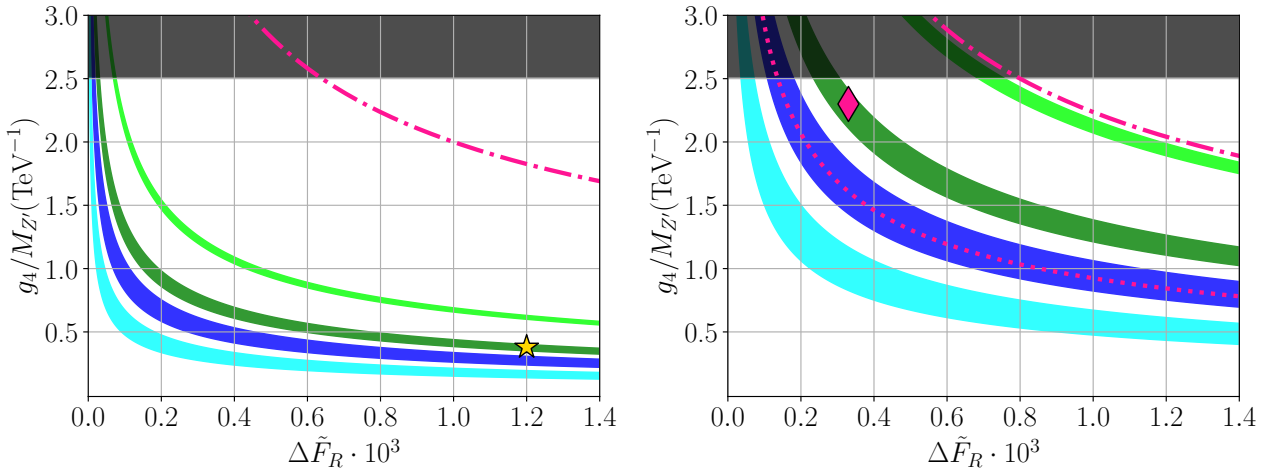

Figure 5.14: ΔA_{CP}^{NP} for Z'–models 2 (left) and 10 (right) in the plane of $g_4/M_{Z'}$ (TeV^{-1}) and $\Delta\tilde{F}_R = \Delta F_R \cdot \theta_u$ and exclusion regions from D^0–$\overline{D}^0$ mixing in red and perturbativity plus direct searches in dimuon and dielectron spectra [184] ($g_4 \leq 4\pi$ and $M_{Z'} \geq 5$ TeV) in black. Light green, dark green, blue and cyan bands correspond to $|\Delta A_{CP}^{NP}| = (4.0 \pm 0.2) \cdot 10^{-3}$, $|\Delta A_{CP}^{NP}| = (1.5 \pm 0.2) \cdot 10^{-3}$, $|\Delta A_{CP}^{NP}| = (8 \pm 2) \cdot 10^{-4}$ and $|\Delta A_{CP}^{NP}| = (3 \pm 1) \cdot 10^{-4}$, respectively. The magenta dash–dotted and dotted lines show the upper limit from $\mathcal{B}(D^+ \to \pi^+\mu^+\mu^-)$. In the right plot the dotted line corresponds to model 10 with large muon charges and the dash–dotted to model 10 with the smallest possible muon charges. In both cases the cyan band is still viable, and the green band is excluded. The golden star and pink diamond are benchmark points.

dotted line. The second scenario has the smallest possible muon charges, $F_{L_2} = 0$, $F_{e_2} = -4$, and the limit from $\mathcal{B}(D^+ \to \pi^+\mu^+\mu^-)$ (dash-dotted line) is irrelevant. Two similar plots for models 2 and 9, also presented in Ref. [2], are shown in App. D.4.

It is still possible to obtain large contributions to ΔA_{CP}, while evading constraints from mixing, direct searches and semileptonic data. However, the viable parameter region is shrinking, and some models (9 and 10) are not able to fully account for the measured value of ΔA_{CP}. In model 10, it is still possible to avoid $\mathcal{B}(D^+ \to \pi^+\mu^+\mu^-)$ with small muon charges, however, the joint bounds from $D^0 - \overline{D}^0$ mixing and the perturbativity limit object benchmark points within the green band in Fig. 5.14.

In order to further pin down models, it is crucial to investigate correlations between various CP–violating measurements. We briefly discuss possibilities with U–spin and isospin patterns in hadronic decays, *i.e.* individual measurements of $A_{CP}(D^0 \to K^+K^-)$, $A_{CP}(D^0 \to \pi^+\pi^-)$, $A_{CP}(D^0 \to \pi^0\pi^0)$ and $A_{CP}(D^+ \to \pi^+\pi^0)$, as well as correlations to semileptonic rare charm decays.

In the U–spin limit $A_{CP}(D^0 \to K^+K^-) = -A_{CP}(D^0 \to \pi^+\pi^-)$. Hence, an estimator for the breaking

of U–spin symmetry reads

$$U_{\text{break}}^{\text{tot}} = \begin{cases} \left|1 + \frac{A_{\text{CP}}(D^0\to K^+K^-)}{A_{\text{CP}}(D^0\to\pi^+\pi^-)}\right| , & \text{for } A_{\text{CP}}(D^0\to K^+K^-) \geq A_{\text{CP}}(D^+\to\pi^+\pi^0)\,, \\ \left|1 + \frac{A_{\text{CP}}(D^0\to\pi^+\pi^-)}{A_{\text{CP}}(D^0\to K^+K^-)}\right| , & \text{for } A_{\text{CP}}(D^0\to K^+K^-) < A_{\text{CP}}(D^+\to\pi^+\pi^0)\,, \end{cases} \tag{5.31}$$

and can be quantified within our framework for Z'–models via Eq. (5.29). Isospin breaking can be analyzed in $A_{\text{CP}}(D^+ \to \pi^+\pi^0)$, which is a clean SM null test [254]. Z'–models induce this CP–asymmetry with

$$A_{\text{CP}}^{\text{NP}}(D^+\to\pi^+\pi^0) \sim \frac{g_4^2}{M_{Z'}^2}\,\theta_u\,\Delta F_R\,d_{\pi'}\,(F_{d_1} - F_{u_1})\,. \tag{5.32}$$

Numerical values of $d_{\pi'}$ for different values of $M_{Z'}$ are given in Tab. 5.1. Inserting Eq. (5.28) into Eq. (5.32), we find

$$A_{\text{CP}}^{\text{NP}}(D^+\to\pi^+\pi^0) \sim \beta_{\pi'}\cdot\Delta A_{\text{CP}}^{\text{NP}}\,, \quad \beta_{\pi'} = \frac{d_{\pi'}\,(F_{d_1} - F_{u_1})}{c_K\,F_{Q_2} + d_K\,F_{d_2} - c_\pi\,F_{Q_1} - d_\pi\,F_{d_1}}\,, \tag{5.33}$$

and similarly

$$\begin{aligned} A_{\text{CP}}^{\text{NP}}(D^0\to\pi^0\pi^0) &\sim \frac{g_4^2}{M_{Z'}^2}\,\theta_u\,\Delta F_R\,d_{\pi^0}\,(F_{d_1} - F_{u_1})\,, \\ A_{\text{CP}}^{\text{NP}}(D^0\to\pi^0\pi^0) &\sim \beta_{\pi^0}\cdot\Delta A_{\text{CP}}^{\text{NP}}\,, \quad \beta_{\pi^0} = \frac{d_{\pi^0}\,(F_{d_1} - F_{u_1})}{c_K\,F_{Q_2} + d_K\,F_{d_2} - c_\pi\,F_{Q_1} - d_\pi\,F_{d_1}}\,. \end{aligned} \tag{5.34}$$

Finally, using Eq. (4.16), we find the following connection between hadronic and semileptonic CP–asymmetries

$$\text{Im}(C_{9/10}^{(\ell)}) \;\sim\; \frac{\pi}{\sqrt{2}\,G_F\,\alpha_e}\,\beta_{9/10}^{\ell}\cdot\Delta A_{\text{CP}}^{\text{NP}}\,, \quad \beta_{9/10}^{\ell} = \frac{F_{e_i} \pm F_{L_i}}{c_K\,F_{Q_2} + d_K\,F_{d_2} - c_\pi\,F_{Q_1} - d_\pi\,F_{d_1}}\,. \tag{5.35}$$

Assuming the models suffice $\Delta A_{\text{CP}}^{\text{NP}} \sim 10^{-3}$ we find

$$\text{Im}(C_{9/10}^{(\ell)}) \;\sim\; 0.03\cdot\beta_{9/10}^{\ell\ell}\,(\text{TeV})^2\,. \tag{5.36}$$

Values for β_9^ℓ, β_{10}^ℓ for both $\ell = e, \mu$, as well as $\beta_{\pi^0}, \beta_{\pi'}$ and $U_{\text{break}}^{\text{tot}}$ for models 2, 4, 5, 9, 10 and $M_{Z'} = 6\,\text{TeV}$ are displayed in Tab. 5.2. We distinguish model 10 with large muon charges and model 10μ with the smallest possible muon charges. Fig. 5.15 shows the plane of $A_{\text{CP}}(D^0\to K^+K^-)$ versus $A_{\text{CP}}(D^0\to\pi^+\pi^-)$. Predictions in models 2, 5, 9, $10(\mu)$ are shown in blue, magenta, yellow and cyan respectively. The red dashed line shows the U–spin limit and the light red cone illustrates SM-like 30 %

Table 5.2: Numerical values for dimensionless $\beta_{\pi'}$, β_{π^0} and $\beta^{\ell}_{9/10}$ ($\ell = \mu$, e) in $(\text{TeV})^{-2}$, see Eqs. (5.34), (5.33)) and (5.35), as well as $\text{U}^{\text{tot}}_{\text{break}}$ from Eq. (5.31), for fixed $M_{Z'} = 6$ TeV.

model	β^{μ}_{9}	β^{μ}_{10}	β^{e}_{9}	β^{e}_{10}	β_{π^0}	$\beta_{\pi'}$	$\text{U}^{\text{tot}}_{\text{break}}$
2	0.57	−0.57	−0.68	0.68	−0.02	−0.02	0.42
4	−1.04	−0.35	1.04	0.35	−0.03	−0.03	0.22
5	−0.67	0	0.67	0	−0.10	−0.09	0.32
9	−20.56	−14.07	15.15	−2.17	−1.89	−1.75	0.22
10	37.25	3.39	−32.73	1.13	1.31	1.22	0.91
10μ	−4.52	−4.52	−32.73	1.13	1.31	1.22	0.91

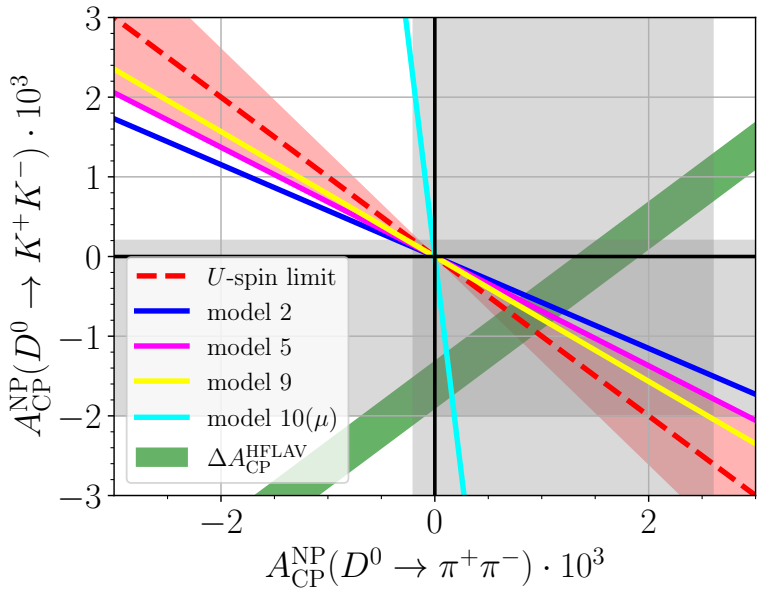

Figure 5.15: $A_{\text{CP}}(D^0 \to K^+K^-)$ versus $A_{\text{CP}}(D^0 \to \pi^+\pi^-)$ plane with predictions in the Z'–models 2, 5, 9 and 10(μ) in blue, magenta, yellow and cyan, respectively. The green band shows the experimental world average of ΔA_{CP} at 1 σ, see Eq. (3.27). The gray bands indicate the present experimental 1σ regions [176]. We illustrate the U–spin limit as a red dashed line and $\lesssim 30$ % SM-like U–spin breaking as a light red area.

U–spin breaking effects. The green band shows the current 1σ world average of ΔA_{CP} as in Eq. (3.27) and the gray bands show 1σ regions for individual CP–asymmetries $A_{\text{CP}}(D^0 \to \pi^+\pi^-) = (1.2 \pm 1.4) \times 10^{-3}$ and $A_{\text{CP}}(D^0 \to K^+K^-) = (-0.9 \pm 1.1) \times 10^{-3}$ [176]. Future sensitivities of the individual asymmetries reach few$\times 10^{-4}$ at LHCb until Run 3 and Belle II with 50 ab^{-1} [64, 255].

We find that large values for β_{π^0} and $\beta_{\pi'}$ and hence contributions in $A_{\text{CP}}^{\text{NP}}(D^0 \to \pi^0\pi^0)$ and

$A_{\rm CP}^{\rm NP}(D^+ \to \pi^+\pi^0)$ at the level of $\Delta A_{\rm CP}$ are generated in models 9 and 10. U–spin breaking effects are large in model 2 and close to maximal in model 10. Typical models (2, 4, 5) generate contributions in rare semileptonic decays at the level of $\text{Im}(C_{9/10}^{(\ell)}) \sim$ few $\times$ 0.01 for both electron and muon Wilson coefficients. Larger values are possible in models 9 and 10, where $F_{Q_1} = F_{Q_2} = 0$. On the other hand, these models are strongly constrained by updated measurements of $D^0 - \overline{D}^0$ mixing parameters and upper limits from semileptonic decays, which object large contributions to $\Delta A_{\rm CP}$ and therefore also suppress maximal contributions to CP–violation in semileptonic decays as well as $A_{\rm CP}^{\rm NP}(D^0 \to \pi^0\pi^0)$ and $A_{\rm CP}^{\rm NP}(D^+ \to \pi^+\pi^0)$. In any case, CP–violation in semileptonic decays and $A_{\rm CP}^{\rm NP}(D^+ \to \pi^+\pi^0)$ are null tests of the SM and any signal supports the NP interpretation of $\Delta A_{\rm CP}$. Cross checks in hadronic patterns, such as large U–spin and isospin breaking effects further help to pin down the NP nature of CP–violation in the charm sector. Flavorful anomaly-free Z'–models further naturally induce a violation of LFU, which can be probed in ratios of muon over electron branching ratios, see Sec. 5.3.

5.3 Lepton universality ratios

LFU is deeply rooted in the gauge sector of the SM and only softly broken by mass corrections, which become irrelevant at high energies. It is therefore straightforward to put LFU to test in semileptonic charmed meson and baryon decays with the ratios [88, 93], in analogy to R_K, R_{K^*} and similar ratios in rare B–meson and Λ_b–baryon decays [147, 148]

$$\begin{aligned} R_P^D &= \int_{q^2_{\rm min}}^{q^2_{\rm max}} \frac{\mathrm{d}\mathcal{B}(D \to P\mu^+\mu^-)}{\mathrm{d}q^2}\,\mathrm{d}q^2 \Big/ \int_{q^2_{\rm min}}^{q^2_{\rm max}} \frac{\mathrm{d}\mathcal{B}(D \to Pe^+e^-)}{\mathrm{d}q^2}\,\mathrm{d}q^2\,, \\ R_{B_1}^{B_0} &= \int_{q^2_{\rm min}}^{q^2_{\rm max}} \frac{\mathrm{d}\mathcal{B}(B_0 \to B_1\mu^+\mu^-)}{\mathrm{d}q^2}\,\mathrm{d}q^2 \Big/ \int_{q^2_{\rm min}}^{q^2_{\rm max}} \frac{\mathrm{d}\mathcal{B}(B_0 \to B_1e^+e^-)}{\mathrm{d}q^2}\,\mathrm{d}q^2\,. \end{aligned} \tag{5.37}$$

Here, $q^2_{\rm min}$ and $q^2_{\rm max}$ denote the lower and upper dilepton mass cut and necessarily need to be identical for electron and muon modes to ensure an efficient cancellation of hadronic uncertainties and hence a controlled SM prediction close to unity [148].

We therefore study the NP sensitivity of these ratios as SM null tests. We give SM predictions for R_π^D, $R_K^{D_s}$ and $R_p^{\Lambda_c}$ in the full, low and high q^2 region in Tab. 5.3. For these predictions we assume the same resonance contributions in the muon and electron mode entering via C_9^R, C_P^R, as these contain QCD$\times$QED effects, which are LFU. The kinematic regions are defined for $D \to P\ell^+\ell^-$ ($\Lambda_c \to p\ell^+\ell^-$) as

$$\begin{aligned} &\text{full } q^2: && 0.250\,\text{GeV} \leq \sqrt{q^2} \leq m_D - m_P\,, && (2m_\mu \leq \sqrt{q^2} \leq m_{\Lambda_c} - m_p)\,, \\ &\text{low } q^2: && 0.250\,\text{GeV} \leq \sqrt{q^2} \leq 0.525\,\text{GeV}\,, && (2m_\mu \leq \sqrt{q^2} \leq 0.525\,\text{GeV})\,, \\ &\text{high } q^2: && 1.25\,\text{GeV} \leq \sqrt{q^2} \leq m_D - m_P\,, && (1.25\,\text{GeV} \leq \sqrt{q^2} \leq m_{\Lambda_c} - m_p)\,. \end{aligned} \tag{5.38}$$

Deviations from unity from lepton mass effects are $\mathcal{O}(m_\ell^2/m_{h_c}^2)$ with $h_c = D$, D_s, Λ_c and only matter

Table 5.3: SM predictions for LFU ratios $R_\pi^D, R_K^{D_s}$ and $R_p^{\Lambda_c}$ in the full, low and high q^2 region, respectively, see text.

	$R_\pi^D\|_{\text{SM}}$	$R_K^{D_s}\|_{\text{SM}}$	$R_p^{\Lambda_c}\|_{\text{SM}}$
full q^2	$1.00 \pm \mathcal{O}(\%)$	$1.00 \pm \mathcal{O}(\%)$	$1.00 \pm \mathcal{O}(\%)$
low q^2	$0.95 \pm \mathcal{O}(\%)$	$0.94 \pm \mathcal{O}(\%)$	$0.94 \pm \mathcal{O}(\%)$
high q^2	$1.00 \pm \mathcal{O}(\%)$	$1.00 \pm \mathcal{O}(\%)$	$1.00 \pm \mathcal{O}(\%)$

Table 5.4: R_π^D and $R_K^{D_s}$ (5.37) in various NP scenarios with couplings to muons only for different q^2 bins. We give ranges corresponding to uncertainties from form factors and resonance parameters. In some cases only the order of magnitude of the largest values is given, see text.

	$\|C_9^{(\mu)}\| = 0.5$	$\|C_{10}^{(\mu)}\| = 0.5$	$\|C_{S(P)}^{(\mu)}\| = 0.1$	$\|C_T^{(\mu)}\| = 0.5$	$\|C_{T5}^{(\mu)}\| = 0.5$	$\|C_9^{(\mu)}\| = \pm\|C_{10}^{(\mu)}\| = 0.5$
R_π^D						
full q^2	SM-like	SM-like	SM-like	SM-like	SM-like	SM-like
low q^2	$\mathcal{O}(100)$	$\mathcal{O}(100)$	0.9 ... 1.4	$\mathcal{O}(10)$	1.0 ... 5.9	$\mathcal{O}(100)$
high q^2	0.2 ... 11	3 ... 7	1 ... 2	1 ... 5	2 ... 4	2 ... 17
$R_K^{D_s}$						
full q^2	SM-like	SM-like	SM-like	SM-like	SM-like	SM-like
low q^2	0.1 ... 3.0	1.3 ... 1.5	SM-like	0.7 ... 1.2	SM-like	0.5 ... 3.6
high q^2	0.2 ... 16	3 ... 11	1.5 ... 3.7	1 ... 6	1.6 ... 4.1	2 ... 26

for the low q^2 region. Higher-order QED effects are beyond the precision aimed for in this work, but may become important as soon as the first data are available.

For a brief BSM induced sensitivity study we assume various NP benchmark scenarios with additional contributions to muon Wilson coefficients only. We collect results in Tabs. 5.4 and 5.5 for $D^+ \to \pi^+\ell^+\ell^-$, $D_s^+ \to K^+\ell^+\ell^-$ and $\Lambda_c^+ \to p\ell^+\ell^-$. Note that dipole operators C_7, C_7' produce the final state lepton pair via a single $\gamma \to \ell^+\ell^-$ electromagnetic coupling. Hence, BSM in $C_7^{(\prime)}$ leads to LFU contributions and is SM–like, $R_\pi^D|_{C_7^{(\prime)}} = R_K^{D_s}|_{C_7^{(\prime)}} = R_p^{\Lambda_c}|_{C_7^{(\prime)}} = 1$.

For the meson decays we do not distinguish primed and unprimed Wilson coefficients, as only $|C_i + C_i'|^2$ contributions enter in the differential distribution, see Sec. 5.1.1. We put "SM-like entries", whenever our results equal unity within $\mathcal{O}(20\,\%)$, which is much smaller than the resonance induced uncertainties. For deviating entries we either put a range, or the order of magnitude of the largest values found. We learn that results strongly depend on the chosen mode, as R_π^D can reach $\mathcal{O}(100)$ in the low q^2 region, whereas $R_K^{D_s}$ ($R_p^{\Lambda_c}$) is more pronounced (equally large) at high q^2. This is mainly due to huge uncertainties from strong phases, which coincide with uncertainties in the differential

Table 5.5: $R_p^{\Lambda_c}$ as in Eq. (5.37) in NP-scenarios with couplings to muons only for different q^2 bins. See Tab. 5.4 and text.

	$\lvert C^{(\mu)}\rvert = 0.5$	$\lvert C_{10}^{(\mu)}\rvert = 0.5$	$\lvert C_9^{(\mu)}\rvert = \lvert C_{10}^{(\mu)}\rvert = 0.5$	$\lvert C_9^{\prime(\mu)}\rvert = 0.5$	$\lvert C_{10}^{\prime(\mu)}\rvert = 0.5$	$\lvert C_9^{\prime(\mu)}\rvert = \lvert C_{10}^{\prime(\mu)}\rvert = 0.5$
$R_p^{\Lambda_c}$						
full q^2	SM-like	SM-like	SM-like	SM-like	SM-like	SM-like
low q^2	7.5 ... 20	4.4 ... 13	11 ... 32	4.6 ... 14	4.4 ... 13	8.2 ... 26
high q^2	$\mathcal{O}(100)$	$\mathcal{O}(100)$	$\mathcal{O}(100)$	$\mathcal{O}(100)$	$\mathcal{O}(100)$	$\mathcal{O}(100)$

branching ratios, see Figs. 3.2 and 3.3. Also NP effects are washed out in the full q^2 region due to the LFU resonance dominance. It is therefore crucial to measure LFU ratios in several low and high q^2 bins, where BSM effects can be huge.

Although predictions strongly depend on the resonance model, and therefore experimental input, LFU ratios are clean SM null tests and might even be useful to pin down strong phases in a future global fit.

We note that the low q^2 bin may suffer from a pollution due to $\eta \to \ell^+\ell^-\gamma$ with soft photon γ not seen in experimental analysis [256]. A dedicated study of this pollution is beyond the scope of this work, however needed as soon as data at low q^2 become available.

5.4 Lepton flavor violating decay modes

As a final null test opportunity discussed in this thesis, LFV can be probed. We have already presented available upper limits on LFV Wilson coefficients in Sec. 4.1.

Distributions for several benchmark scenarios are shown in Fig. 5.16 for $D^+ \to \pi^+ e^\pm \mu^\mp$ and $D_s^+ \to K^+ e^\pm \mu^\mp$ in the left and right plot, respectively. We show the sum of both lepton charge combinations, *i.e.* $\mathcal{B}(D^+ \to \pi^+ e^\pm \mu^\mp) = \mathcal{B}(D^+ \to \pi^+ e^+ \mu^-) + \mathcal{B}(D^+ \to \pi^+ e^- \mu^+)$. Explicit expressions for the LFV decay distributions are given in App. E.1 and App. E.2 for three-body meson and baryon decays, respectively.

Here, again $K_{i\,(j)}$ implies K_i or K_j. We learn that different contributions can be disentangled via their size. Comparing the low q^2 behavior of tensor and scalar contributions with the (axial) vector contributions, we also find differences in the shape of the respective distributions. Furthermore, resonance contributions are absent, which explains the reduced uncertainty bands, now dominated by form factor uncertainties.

Similar distributions can be obtained exemplary for $D^+ \to \pi^+ e^\pm \mu^\mp$ and $\Lambda_c \to p \mu^\pm e^\mp$ in concrete BSM models, see Fig. 5.17.

The chosen LQ–scenarios S_1, S_2 avoid constraints from other flavor sectors by construction and hence can have close to maximal possible effects in RH quark currents, $K_9' = \pm K_{10}' = 0.5$. The other BSM examples are constrained from rare kaon decays in the SUSY scenarios and from LFV decays of charged leptons in the Z'–scenarios. We refer to Ref. [1] for further details.

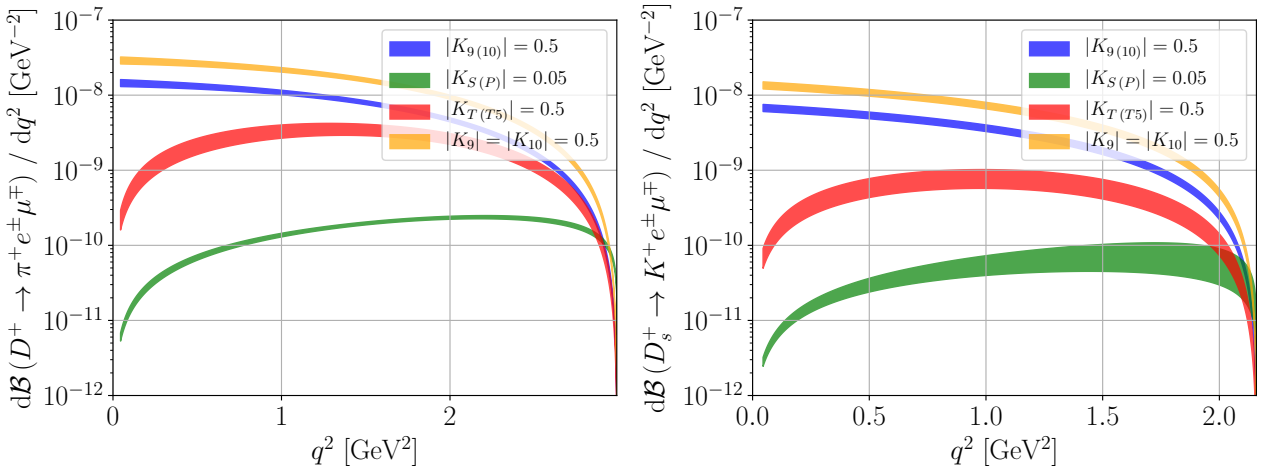

Figure 5.16: The plots show the differential branching ratios of $D^+ \to \pi^+ e^\pm \mu^\mp$ (left) and $D_s^+ \to K^+ e^\pm \mu^\mp$ (right) decays for different benchmark values of LFV-BSM Wilson coefficients.

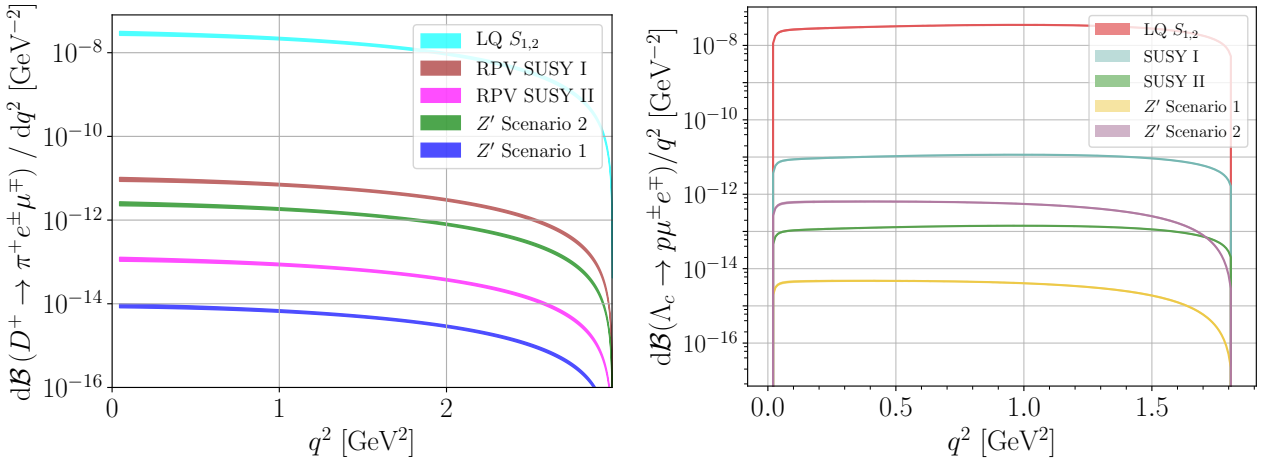

Figure 5.17: The differential branching fractions, including form factor uncertainties, for $D^+ \to \pi^+ e^\pm \mu^\mp$ and $\Lambda_c \to p\mu^\pm e^\mp$ with LFV NP contributions in a (close to maximal) LQ scenario with S_1 or S_2 ($K'_9 = \pm K'_{10} = 0.5$), two R-parity violating SUSY ($K_9 = -K_{10} = 0.009$ and $K_9 = -K_{10} = 0.001$) and two different Z'–scenarios ($K'_9 = K'_9 = -K'_{10} = -K'_{10} = 1.4 \cdot 10^{-4}$ and $K_9 = K'_9 = -K_{10} = -K'_{10} = 2.3 \cdot 10^{-4}$). The BSM benchmarks are adapted from Ref. [1], see text for details.

We see, that LQ–scenarios easily reach branching ratios of $\mathcal{O}(10^{-8})$, while the other scenarios are at the level of $\mathcal{O}(10^{-12})$ or even below. Model-independently, LFV decays of mesons were used to obtain

limits on Wilson coefficients, see Eq. (4.11), and imply

$$|K_{9\,10}^{(\mu e)(\prime)}| \lesssim 1.6. \tag{5.39}$$

Using a single maximal coupling scenario, we obtain indirect upper limits on LFV three- and four-body baryon modes, which read

$$\begin{aligned}
\mathcal{B}(\Lambda_c^+ \to p\mu^\pm e^\mp) &\lesssim 8.2\times10^{-7}\,, & & \\
\mathcal{B}(\Xi_c^+ \to \Sigma^+\mu^\pm e^\mp) &\lesssim 1.6\times10^{-6}\,, & \mathcal{B}(\Xi_c^+ \to \Sigma^+(\to p\pi^0)\mu^\pm e^\mp) &\lesssim 8.3\times10^{-7}\,, \\
\mathcal{B}(\Xi_c^0 \to \Sigma^0\mu^\pm e^\mp) &\lesssim 2.6\times10^{-7}\,, & & \\
\mathcal{B}(\Xi_c^0 \to \Lambda^0\mu^\pm e^\mp) &\lesssim 1.2\times10^{-7} & \mathcal{B}(\Xi_c^0 \to \Lambda^0(\to p\pi^-)\mu^\pm e^\mp) &\lesssim 7.7\times10^{-8}\,, \\
\mathcal{B}(\Omega_c^0 \to \Xi^0\mu^\pm e^\mp) &\lesssim 1.4\times10^{-6}\,, & \mathcal{B}(\Omega_c^0 \to \Xi^0(\to \Lambda^0\pi^0)\mu^\pm e^\mp) &\lesssim 1.4\times10^{-6}\,,
\end{aligned} \tag{5.40}$$

and are well above the scenarios presented in Fig. 5.17, however better than the only available upper limits from BaBar at 90 % C.L. [210],

$$\mathcal{B}(\Lambda_c^+ \to p\mu^- e^+) < 9.9\times10^{-6}\,, \qquad \mathcal{B}(\Lambda_c^+ \to p\mu^+ e^-) < 19\times10^{-6}\,. \tag{5.41}$$

5.5 Summary of the null-test paradigm in rare charm decays

Long-range QCD resonances enforce the need to study observables beyond simple branching ratios in semileptonic rare charm decays. Null tests constitute the single possible road towards experimental evidence for NP in the charm sector. Any observation coincides with the existence of BSM physics. Angular observables in three-body meson decays $D \to P\ell^+\ell^-$ and upper limits on branching ratios of purely leptonic decays $D^0 \to \ell^+\ell^-$ probe (pseudo-)scalar and (pseudo-)tensor Wilson coefficients and can be assisted by plenty of possibilities with semileptonic rare charm baryon decays with three and four particles in the final state. Here, the angular distribution offers several clean null tests, along with several observables with finite, however, clean SM predictions and high sensitivity to BSM effects. Barring large (pseudo-)scalar and (pseudo-)tensor contributions, already four angular observables in rare charm baryon decays, F_L, $A_{\rm FB}^{\ell}$, $A_{\rm FB}^{\rm H}$ and $A_{\rm FB}^{\ell\rm H}$ suffice to qualitatively disentangle NP contributions to $C_7^{(\prime)}$, $C_9^{\prime}$ and $C_{10}^{(\prime)}$. In angular observables and in measurements of direct CP–violation around the resonance masses, contributions from intermediate QCD resonances catalyze NP effects. Correlations of CP–asymmetries in semileptonic decays and hadronic decays may help to pin down the NP nature of the measurement of $\Delta A_{\rm CP}$. LFU and LFV can be probed directly and large effects are still viable. Interestingly, these two SM symmetries can also be probed indirectly in dineutrino modes, which are studied globally in several flavor sectors in the next section. In charm they pose yet another null-test opportunity due to the severe GIM cancellation and the lack of resonance contributions.

6 Flavor tests with dineutrino modes in charm and beyond

In this chapter we present opportunities to connect different sectors in both quark and lepton flavor space. The main focus lies on branching ratios of FCNCs with dineutrinos in the final state. Experimentally, dineutrinos cannot be detected in a flavor physics experiment so that the signature is missing energy. This complication prohibits dineutrino studies at a hadron collider and demands a clean e^+e^-–machine. On the other hand also the neutrino flavor is not tagged in a missing energy signature, which leads to a flavor inclusiveness of the observables, schematically $O(\nu\bar{\nu}) = \sum_{i,j} O(\nu_i \bar{\nu}_j)$ with i, j summing neutrino flavors. Since neutrinos in the SM only exist as parts of a weak doublet, an $SU(2)_L$–link exists between charged lepton and dineutrino couplings. For the same reason, the quark doublets lead to further connections between different flavor sectors, which needs to be taken into account when exploiting the $SU(2)_L$–link. This chapter is based on Refs. [3, 4, 7] and organized as follows. In Sec. 6.1 we present the general idea by discussing flavor summed dineutrino branching ratios and relate Wilson coefficients of different sectors via the SMEFT. Sec. 6.2 discusses applications of this new $SU(2)_L$–link to the charm sector. Here, dineutrino modes represent further null-test opportunities, as resonance contributions are absent, while the efficient GIM cancellation still holds. Additionally, upper limits on dineutrino branching ratios within different flavor assumptions are worked out so that LFU and cLFC can be tested indirectly. Next, we investigate opportunities of the $SU(2)_L$–link in rare B–decays in Sec. 6.3. Here, the correlation of two rare dineutrino modes can be used to indirectly test LFU in the charged lepton sector. Furthermore, couplings involving τ leptons can be constrained via dineutrino upper limits. Sec. 6.4 summarizes the chapter and briefly presents the interplay between the various different sectors, also investigating possible tests that can be done in the future in observables involving t-quarks. Consequently, this chapter aims at a more general view of FCNCs in the SM, which is why the notation to keep track of two quark and two flavor indices can be exhausting. For that reason, flavor indices are skipped whenever possible and we stick to the following notation.

- The superscript U refers to up-type FCNCs: $t \to c$, $t \to u$, $c \to u$.
- The superscript D refers to down-type FCNCs: $b \to s$, $b \to d$, $s \to d$.
- qq' can be any of the above-mentioned FCNCs.
- α, β refer to both up- and down-type quark flavor indices, while i, j are flavor indices for either charged leptons or neutrinos.

6.1 $SU(2)_L$–links in SMEFT

In our analysis, we consider SMEFT operators contributing to FCNC quark transitions with both dileptons and dineutrinos at lowest order, *i.e.* four-fermion operators at dimension six with Wilson coefficients $C_{\ell q}^{(1)}$, $C_{\ell q}^{(3)}$, $C_{\ell u}$, $C_{\ell d}$,

$$\mathcal{O}_{\ell q}^{(1)} = \overline{Q}\gamma_\mu Q\, \overline{L}\gamma^\mu L\,, \quad \mathcal{O}_{\ell q}^{(3)} = \overline{Q}\gamma_\mu \tau^a Q\, \overline{L}\gamma^\mu \tau^a L\,, \quad \mathcal{O}_{\ell u} = \overline{U}\gamma_\mu U\, \overline{L}\gamma^\mu L\,, \quad \mathcal{O}_{\ell d} = \overline{D}\gamma_\mu D\, \overline{L}\gamma^\mu L\,. \tag{6.1}$$

No further operators contribute at LO. Note that four-fermion operators in SMEFT carry four flavor indices, two for the quark transition and two for the leptons, all of which are dropped for the moment.

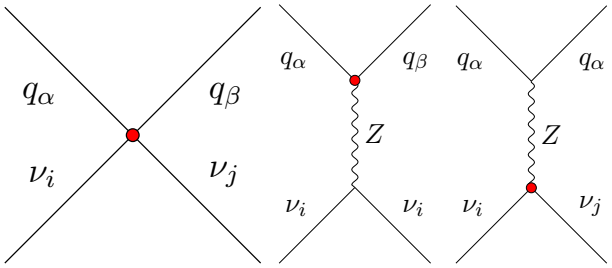

Figure 6.1: Feynman diagrams for contributions of four-fermion operators from Eq. (6.1) (left) and sub-leading ones involving Z–exchange (middle and right) to FCNC processes involving quarks q and neutrinos, with flavor indices α, β, i, j. Red blobs indicate operator insertions.

The validity of this framework that only considers the four operators in Eq. (6.1) is justified by the following reasoning

- The four-quark operators are invariant under QCD-evolution [257] and electroweak effects [258] amount to a correction of less than 5 % for a NP scale of $\Lambda_{\rm NP} \sim 10\,\text{TeV}$, explicitly calculated in [7]. With typical form factor uncertainties at the level of $\mathcal{O}(10\,\%)$ we neglect running effects.
- Operators with either quarks or leptons and two Higgs fields Φ and a covariant derivative D^μ,

$$\begin{aligned} &\bar{Q}\gamma_\mu Q\,\Phi^\dagger D^\mu \Phi\,, && \bar{Q}\gamma_\mu \tau^a Q\,\Phi^\dagger D^\mu \tau^a \Phi\,, && \bar{U}\gamma_\mu U\,\Phi^\dagger D^\mu \Phi\,, \\ &\bar{D}\gamma_\mu D\,\Phi^\dagger D^\mu \Phi\,, && \bar{L}\gamma_\mu L\,\Phi^\dagger D^\mu \Phi\,, && \bar{L}\gamma_\mu \tau^a L\,\Phi^\dagger D^\mu \tau^a \Phi, \end{aligned}$$

  are neglected. This is because these operators contribute via modified Z–couplings, see Fig. 6.1, where Feynman diagrams are sketched for the four-quark operators and the tree-level Z–exchanges with red blobs indicating an operator insertion. For the Z–exchanges, the modified quark coupling still obeys LFU for the leptons and the modified lepton coupling conserves the quark flavor, *i.e.* no FCNC is induced. Operators inducing LFU violating FCNC transitions, the ones we are interested in, are of higher order in SMEFT. In addition, operators with modified Z–couplings are constrained by electroweak and top observables, as well as mixing, see Refs. [259, 260].

The four-quark operators in Eq. (6.1) therefore provide a model-independent basis for dineutrino modes. Comparing Hamiltonians in Eqs. (2.23), (2.26) and (2.34) and expanding the operators in Eq. (6.1) into their $SU(2)_L$–components, one finds the following matching conditions from SMEFT to WET coefficients

$$\begin{aligned} C_L^U = K_L^D &= \frac{2\pi}{\alpha_e}\left(C_{\ell q}^{(1)} + C_{\ell q}^{(3)}\right), \qquad & C_R^U = K_R^U &= \frac{2\pi}{\alpha_e} C_{\ell u}\,, \\ C_L^D = K_L^U &= \frac{2\pi}{\alpha_e}\left(C_{\ell q}^{(1)} - C_{\ell q}^{(3)}\right), \qquad & C_R^D = K_R^D &= \frac{2\pi}{\alpha_e} C_{\ell d}\,, \end{aligned} \tag{6.2}$$

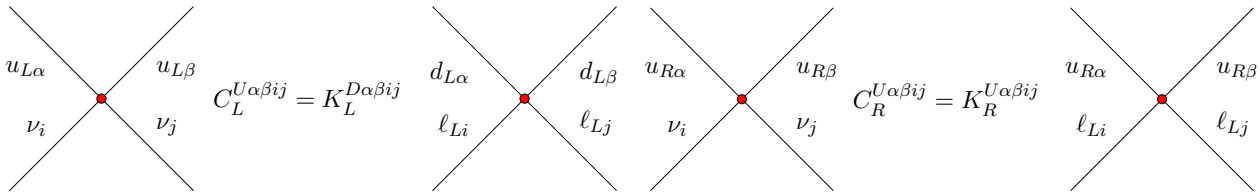

Figure 6.2: Wilson coefficients and effective four-fermion Feynman diagram for up and down quark transitions with dineutrinos $C^U_{L,R}$ and dileptons K^D_L and K^U_R, corresponding to the operators in Eq. (6.1) with flavor indices α, β, i, j. The $SU(2)_L$–based relation between neutrino and charged lepton operators holds in the fermions' flavor eigenstate basis and enters in (6.7) in the mass basis.

where U and D refer to a up-type and down-type quark transition, respectively. The coefficients $C_{L,R}$ refer to operators in WET with dineutrinos, whereas the coefficients $K_{L,R}$ are associated with charged leptons. Clearly, a direct link between RH dineutrino and dilepton coefficients exists for both up- and down-type sectors. However, for the LH operators, due to different signs of $C^{(1)}_{\ell q}$ and $C^{(3)}_{\ell q}$, up-type dineutrino couplings are linked to down-type coefficients involving charged leptons and similarly down-type dineutrino coefficients are identical to the up-type charged lepton couplings. This link is illustrated in Fig. 6.2 including the four flavor indices.

A few comments are in order. The $SU(2)_L$–link in Eq. (6.2) holds for BSM couplings only, because in the language of SMEFT all Wilson coefficients are understood as BSM couplings as higher-dimensional operators are added to the SM Lagrangian in Eq. (2.34). In WET this separation is treated differently in the literature, some include the SM into the Wilson coefficients, *e.g.* Ref. [261] for $b \to s\ell^+\ell^-$ or for instance Refs. [90, 93, 98] for $c \to u\ell^+\ell^-$, some explicitly separate SM and NP contributions, Refs. [262, 263]. Here, we stick to the clear separation of SM and NP Wilson coefficients, *i.e.* we explicitly add the SM contributions. Further, Eq. (6.2) in principle also holds for couplings involving two quarks with identical flavor $U = tt$, cc, uu and $D = bb$, ss, dd, however our main interest is in semileptonic FCNC decays.

Since Eq. (6.2) utilizes SMEFT, it is required to switch from gauge to mass eigenstates for the quarks and leptons

$$Q_\alpha = \begin{pmatrix} u_{L\alpha} \\ V_{\alpha\beta} d_{L\beta} \end{pmatrix}, \quad L_i = \begin{pmatrix} \nu_{Li} \\ W^*_{ji} \ell_{Lj} \end{pmatrix}, \tag{6.3}$$

with the CKM matrix V and the PMNS matrix W. By doing so we switch from standard to calligraphic notation for the Wilson coefficients. After applying the rotation, the $SU(2)_L$–link in the mass basis reads

$$\mathcal{C}^M_L = W^\dagger \mathcal{K}^N_L W + \mathcal{O}(\lambda), \qquad \mathcal{C}^M_R = W^\dagger \mathcal{K}^M_R W, \tag{6.4}$$

where either $M = U$, $N = D$ or vice versa and first corrections appear at first order in Wolfenstein λ. This link can be exploited in dineutrino observables. As stated already in Sec. 2.2.2, only two dineutrino Wilson coefficients exist in WET, therefore for each FCNC quark transition $q \to q'$ all dineutrino differential branching ratios can be written in terms of two combinations of these couplings plus the (LH) SM contribution

$$x^{\pm}_{qq'} = \sum_{ij} |\mathcal{C}^{qq'ij}_{\text{SM}} + \mathcal{C}^{qq'ij}_{L} \pm \mathcal{C}^{qq'ij}_{R}|^2 \,. \tag{6.5}$$

A third combination $x_{qq'}$ is a linear combination of these two and implies the following relation

$$x_{qq'} = \frac{x^{+}_{qq'} + x^{-}_{qq'}}{2} = \sum_{ij} \left(|\mathcal{C}^{qq'ij}_{\text{SM}} + \mathcal{C}^{qq'ij}_{L}|^2 + |\mathcal{C}^{qq'ij}_{R}|^2 \right) , \qquad x^{\pm}_{qq'} \leq 2\, x_{qq'} \,. \tag{6.6}$$

For these combinations the $SU(2)_L$–link can be employed resulting in

$$\begin{aligned}
\sum_{\nu=i,j} \left(|\mathcal{C}^{Mij}_{\text{SM}} + \mathcal{C}^{Mij}_{L}|^2 + |\mathcal{C}^{Mij}_{R}|^2 \right) &= \text{Tr}\left[(\mathcal{C}^{M}_{\text{SM}} + \mathcal{C}^{M}_{L})\, (\mathcal{C}^{M\dagger}_{\text{SM}} + \mathcal{C}^{M\dagger}_{L}) \,+\, \mathcal{C}^{M}_{R}\, \mathcal{C}^{M\dagger}_{R} \right] \\
&= \text{Tr}\Big[(\mathcal{C}^{M}_{\text{SM}} + W^\dagger \mathcal{K}^{N}_{L} W)(\mathcal{C}^{M\dagger}_{\text{SM}} + W^\dagger \mathcal{K}^{N\dagger}_{L} W) \\
&\qquad + W^\dagger \mathcal{K}^{M}_{R} W W^\dagger \mathcal{K}^{M\dagger}_{R} W \Big] + \mathcal{O}(\lambda) \\
&= \text{Tr}\left[(\mathcal{C}^{M}_{\text{SM}} + \mathcal{K}^{N}_{L})(\mathcal{C}^{M\dagger}_{\text{SM}} + \mathcal{K}^{N\dagger}_{L}) + \mathcal{K}^{M}_{R} \mathcal{K}^{M\dagger}_{R} \right] + \mathcal{O}(\lambda) \\
&= \sum_{\ell=i,j} \left(|\mathcal{C}^{Mij}_{\text{SM}} + \mathcal{K}^{Nij}_{L}|^2 + |\mathcal{K}^{Mij}_{R}|^2 \right) + \mathcal{O}(\lambda) \,,
\end{aligned} \tag{6.7}$$

where again $M = U$ and $N = D$ or vice versa, implying as a first possibility an up-type dineutrino FCNC being connected to a LH down-type and the RH up-type FCNC with charged leptons. The second case is a connection of down-type dineutrino FCNCs to LH up- and RH down-type charged lepton FCNCs. This relation is independent of the PMNS rotation and holds up to $\mathcal{O}(\lambda)$ corrections induced by the CKM rotation, *i.e.* Eq. (6.7) is exact, in the limit $V_{\text{CKM}} = 1$. The reason why the PMNS matrix drops out in Eq. (6.7) is threefold:

- W is unitary, $WW^\dagger = 1$.
- The trace is cyclic, $\text{Tr}(W^\dagger \mathcal{K} \mathcal{K}^\dagger W) = \text{Tr}(W W^\dagger \mathcal{K} \mathcal{K}^\dagger)$.
- The SM obeys LFU, $\mathcal{C}^{ij}_{\text{SM}} = c_{SM} \cdot \delta_{ij}$ and therefore commutes with any other matrix.

More details on the $\mathcal{O}(\lambda)$ corrections are compiled in App. G. The main feature of Eq. (6.7) is that it is bidirectional. On the one hand information on charged dilepton couplings gives indirect bounds on dineutrino branching ratios, on the other hand upper limits and measurements of dineutrino branching ratios constrain charged lepton couplings. Hence, the direction in which the $SU(2)_L$–link can be

exploited is a matter of the current experimental situation in the dineutrino and charged lepton sectors, respectively.

Now, any differential branching ratio of a decay of the form $h_q \to F_{q'}\nu\bar{\nu}$ can be written as

$$\frac{\mathrm{d}\mathcal{B}(h_q \to F_{q'}\nu\bar{\nu})}{\mathrm{d}q^2} = a_+^{h_q F_{q'}}(q^2)\, x_{qq'}^+ + a_-^{h_q F_{q'}}(q^2)\, x_{qq'}^-\,, \tag{6.8}$$

where $h_q \to F_q$ is the transition of a hadron h_q into a hadronic final state with flavor q' induced by the FCNC $q \to q'$, *e.g.* $D^0 \to \pi^+\pi^-\nu\bar{\nu}$ with $h_c = D^0$ and $F_u = \pi^+\pi^-$ induced by a $c \to u$ quark transition. The factors $a_\pm^{h_q F_{q'}}$ only depend on form factors, masses, lifetimes and the dineutrino invariant mass squared q^2. We collect explicit expressions for numerous of these factors in App. E.4. The respective branching ratios can be obtained after q^2 integration

$$\mathcal{B}(h_q \to F_{q'}\nu\bar{\nu}) = A_+^{h_q F_{q'}}\, x_{qq'}^+ + A_-^{h_q F_{q'}}\, x_{qq'}^-\,, \tag{6.9}$$

with

$$A_\pm^{h_q F_{q'}} = \int_{q^2_{\mathrm{min}}}^{q^2_{\mathrm{max}}} \mathrm{d}q^2 a_\pm^{h_q F_{q'}}(q^2)\,. \tag{6.10}$$

We collect the factors $A_\pm^{h_q F_{q'}}$ along with the applied q^2 limits for integration in Tab. 6.1 and Tab. 6.2 for multiple $c \to u$, $b \to s$ and $b \to d$ induced modes as well as for the $s \to d$ induced mode $K^+ \to \pi^+\nu\bar{\nu}$. We also indicate whether or not a τ–background needs to be considered, which will be discussed separately in the following sections. App. C contains details on form factors utilized for the integration in Eq. (6.9).

As mentioned earlier, the direction in which the $SU(2)_L$–link Eq. (6.7) and results from Tab. 6.1 can be exploited depends on the available experimental input, which is why the following subsections discuss applications for different flavor sectors separately.

Table 6.1: Coefficients $A_{\pm}^{h_q F_{q'}}$ as in Eq. (6.9) with integration limits for various $c \to u$ induced modes. The necessity to take a τ–background into account is indicated with a check mark. We do not include any cuts in inclusive modes. We only provide central values.

$h_q \to F_{q'}$	$A_+^{h_q F_{q'}}$ $[10^{-8}]$	$A_-^{h_q F_{q'}}$ $[10^{-8}]$	τ–background	q^2_{min} $[\text{GeV}^2]$	q^2_{max} $[\text{GeV}^2]$
$c \to u$					
$D^0 \to \pi^0$	0.9	0		0	$(m_{D^0} - m_{\pi^0})^2$
$D^+ \to \pi^+$	3.6	0	✓	0.34	$(m_{D^+} - m_{\pi^+})^2$
$D_s^+ \to K^+$	0.7	0	✓	0.66	$(m_{D_s^+} - m_{K^+})^2$
$D^0 \to \pi^0\pi^0$	$0.7 \cdot 10^{-3}$	0.21		0	$(m_{D^0} - 2\,m_{\pi^0})^2$
$D^0 \to \pi^+\pi^-$	$1.4 \cdot 10^{-3}$	0.41		0	$(m_{D^0} - 2\,m_{\pi^+})^2$
$D^0 \to K^+K^-$	$4.7 \cdot 10^{-6}$	0.004		0	$(m_{D^0} - 2m_{K^+})^2$
$\Lambda_c^+ \to p^+$	1.0	1.7		0	$(m_{\Lambda_c^+} - m_p)^2$
$\Xi_c^+ \to \Sigma^+$	1.8	3.5		0	$(m_{\Xi_c^+} - m_{\Sigma^+})^2$
$\Xi_c^0 \to \Sigma^0$	0.3	0.6		0	$(m_{\Xi_c^0} - m_{\Sigma^0})^2$
$\Xi_c^0 \to \Lambda^0$	0.1	0.3		0	$(m_{\Xi_c^0} - m_{\Lambda^0})^2$
$\Omega_c^0 \to \Xi^0$	1.7	3.3		0	$(m_{\Omega_c^0} - m_{\Xi^0})^2$
$D^0 \to X$	2.2	2.2		0	m_c^2
$D^+ \to X$	5.6	5.6		0	m_c^2
$D_s^+ \to X$	2.7	2.7		0	$(m_{D^+} - m_{K^+})^2$

Table 6.2: Coefficients $A_{\pm}^{h_q F_{q'}}$ as in Eq. (6.9) with integration limits for various $b \to s$, $b \to d$, $s \to d$ induced modes. Similar to Tab. 6.1, however taking into account uncertainties and correlations induced by form factors.

$h_q \to F_{q'}$	$A_+^{h_q F_{q'}}$ $[10^{-8}]$	$A_-^{h_q F_{q'}}$ $[10^{-8}]$	τ–background	q^2_{min} $[\text{GeV}^2]$	q^2_{max} $[\text{GeV}^2]$
$b \to s$					
$B^0 \to K^0$	516 ± 68	0		0	$(m_{B^0} - m_{K^0})^2$
$B^+ \to K^+$	558 ± 74	0	✓	0	$(m_{B^+} - m_{K^+})^2$
$B^0 \to K^{*0}$	200 ± 29	888 ± 108		0	$(m_{B^0} - m_{K^{*0}})^2$
$B^+ \to K^{*+}$	217 ± 32	961 ± 116		0	$(m_{B^+} - m_{K^{*+}})^2$
$B_s^0 \to \phi$	184 ± 9	1110 ± 85		0	$(m_{B_s^0} - m_{\phi})^2$
$B^0 \to X_s$	1834 ± 193	1834 ± 193		0	$(m_b - m_s)^2$
$B^+ \to X_s$	1978 ± 208	1978 ± 208		0	$(m_b - m_s)^2$
$b \to d$					
$B^0 \to \pi^0$	154 ± 16	0		0	$(m_{B^0} - m_{\pi^0})^2$
$B^+ \to \pi^+$	332 ± 34	0	✓	0	$(m_{B^+} - m_{\pi^+})^2$
$B^0 \to \rho^0$	59 ± 12	573 ± 233		0	$(m_{B^0} - m_{\rho^0})^2$
$B^+ \to \rho^+$	126 ± 26	1236 ± 502		0	$(m_{B^+} - m_{\rho^+})^2$
$B_s^0 \to K^0$	383 ± 74	0		0	$(m_{B_s^0} - m_{K^0})^2$
$B_s^0 \to K^{*0}$	153 ± 9	891 ± 86		0	$(m_{B^0} - m_{K^{*0}})^2$
$B^0 \to X_d$	1840 ± 194	1840 ± 194		0	$(m_b - m_d)^2$
$B^+ \to X_d$	1985 ± 209	1985 ± 209		0	$(m_b - m_d)^2$
$s \to d$					
$K^+ \to \pi^+$	68.0 ± 1.9	0		0	$(m_{K^+} - m_{\pi^+})^2$

6.2 Dineutrino possibilities in rare charm decays

In $|\Delta c| = |\Delta u| = 1$ transitions the effective GIM cancellation also affects SM contributions to dineutrino modes. More significantly, long-distance contributions via intermediate vector mesons as in Sec. 3.3.2 are strongly suppressed, as they can only proceed via Z–boson exchange. Both long-distance contributions of this type as well as short-distance effects are estimated to give branching ratios $\mathcal{B}(c \to u\nu\bar{\nu}) \lesssim 10^{-15}$ [98], well beyond current experimental reach. Therefore, it is perfectly valid to drop SM contributions

$$\mathcal{C}_{\rm SM}^{cuij} = 0 \quad \forall\, ij\,, \tag{6.11}$$

in Eqs. (6.5), (6.6) and (6.7). For the charged modes $D^+ \to \pi^+\nu\bar{\nu}$ and $D_s^+ \to K^+\nu\bar{\nu}$ however contributions from intermediate τ leptons need to be taken into account, since decays $D^+ \to \tau^+\nu$ with $\tau^+ \to P^+\bar{\nu}$ lead to the same final state as the dineutrino modes. These effects can be controlled with appropriate cuts [264]

$$q^2 > (m_\tau^2 - m_P^2)(m_D^2 - m_\tau^2)/m_\tau^2\,, \tag{6.12}$$

with either $m_D = m_{D^+}$, $m_P = m_{\pi^+}$ or $m_D = m_{D_s^+}$, $m_P = m_{K^+}$, see $q^2_{\rm min}$ for these modes in Tab. 6.1. After applying these cuts and in the light of Chapter 5, rare charm dineutrino branching ratios constitute further null tests, as any signal within current experimental reach clearly indicates BSM physics. In this section, we provide even more motivation to study dineutrino modes, by investigating opportunities to indirectly probe charged lepton flavor.

Searches for rare charm dineutrino modes are in an early stage and only a few experimental limits exist. Recently, the BESIII collaboration reported an upper limit for $\mathcal{B}(D^0 \to \pi^0\nu\bar{\nu}) < 2.1 \times 10^{-4}$ at 90 % C.L. [78]. This is the only available direct experimental input constraining $c \to u\nu\bar{\nu}$ couplings and implies with $A_+^{D^0\pi^0}$ from Tab. 6.1

$$x_{cu}^+ \lesssim 2.3 \times 10^4\,, \tag{6.13}$$

which is at least two orders of magnitude weaker than indirect limits placed later in this section. Due to helicity suppression by two powers of neutrino mass, the upper limit $\mathcal{B}(D^0 \to \text{inv.}) < 9.4 \times 10^{-5}$ at 90 % C.L. [265] interpreted as $D^0 \to \nu\bar{\nu}$ is of even less significance.

Since the direct bounds on $c \to u\nu\bar{\nu}$ are so poor we make use of the $SU(2)_L$–link Eq. (6.7) by placing upper limits on x_{cu} utilizing constraints on charged lepton couplings. We distinguish three flavor benchmark scenarios. In the most general case LFV couplings are allowed and the sum in Eq. (6.7) runs over all charged lepton flavor combinations. The second benchmark is cLFC where only the diagonal couplings $ij = ee$, $\mu\mu$, $\tau\tau$ exist and enter in the sum. The third benchmark is LFU, where the diagonal couplings have to be identical and are constrained by the tightest, *i.e.* the muon bound.

Explicitly, the three coupling matrices in lepton flavor space can be written as

$$\mathcal{K}^{U,D}_{L,R}|_{\text{general}} = \begin{pmatrix} k_e & k_{e\mu} & k_{e\tau} \\ k_{e\mu} & k_\mu & k_{\mu\tau} \\ k_{e\tau} & k_{\mu\tau} & k_\tau \end{pmatrix}, \; \mathcal{K}^{U,D}_{L,R}|_{\text{cLFC}} = \begin{pmatrix} k_e & 0 & 0 \\ 0 & k_\mu & 0 \\ 0 & 0 & k_\tau \end{pmatrix}, \; \mathcal{K}^{U,D}_{L,R}|_{\text{LFU}} = \begin{pmatrix} k & 0 & 0 \\ 0 & k & 0 \\ 0 & 0 & k \end{pmatrix}. \quad (6.14)$$

Upper limits on these charged lepton couplings exist from measurements in semileptonic charm and kaon data and from high–p_T Drell-Yan searches, see Sec. 4.1 and App. G.

Within the different flavor assumptions in Eq. (6.14) we are able to give upper limits on x_{cu} and along with $x^{\pm}_{cu} \leq 2\,x_{cu}$ from Eq. (6.6) we calculate flavor specific upper limits for all rare charm dineutrino branching ratios listed in Tab. 6.1. These limits are obtained in two different scenarios. First, we use a unified framework and only include limits on four-fermion couplings from high–p_T Drell-Yan searches. In the second scenario we assume no large cancellations between LH and RH couplings and include bounds from low-energy measurements, see App. G for details. Limits within the first (the second) approach read

$$\begin{aligned} x_{cu} &= 3\,x^{\mu\mu}_{cu} && \lesssim 34 \quad (\lesssim 2.6)\,, && \text{[LFU]} \\ x_{cu} &= x^{ee}_{cu} + x^{\mu\mu}_{cu} + x^{\tau\tau}_{cu} && \lesssim 196 \quad (\lesssim 156)\,, && \text{[cLFC]} \\ x_{cu} &= x^{ee} + x^{\mu\mu}_{cu} + x^{\tau\tau}_{cu} + 2(x^{e\mu}_{cu} + x^{e\tau}_{cu} + x^{\mu\tau}_{cu}) && \lesssim 716 \quad (\lesssim 655)\,. && \text{[general]} \end{aligned} \quad (6.15)$$

The resulting branching ratio limits for both scenarios are compiled in Tab. 6.3.
The main features of these results are the following

- A measurement above the respective bound implies the breakdown of the corresponding flavor symmetry, *e.g.* a measurement $1.5\times10^{-7} < \mathcal{B}(D^0 \to \pi^+\pi^-\nu\bar{\nu}) < 1.6\times10^{-6}$ implies LFU violation, whereas a measurement $3.5\times10^{-6} < \mathcal{B}(D^0 \to \pi^0\nu\bar{\nu}) < 13\times10^{-6}$ indicates a violation of cLFC. The absolute maxima listed in Tab. 6.3 correspond to limits within our framework, *i.e.* a violation of these limits are only possible through BSM physics beyond our EFT, for instance in models including light NP particles.

- The limits are data-driven and will evolve in the future. Clearly, already the two different scenarios presented involving only Drell-Yan data or also including low-energy data (barring cancellations) have a significant impact on the resulting limits.

- The only available limit to date from BESIII Ref. [78] is still two orders above limits presented in Tab. 6.3.

- These upper limits in Tab. 6.3 hold, as long as no light RH neutrinos, nor lepton number violating (LNV) contributions spoil our framework due to (pseudo-)scalar contributions, which is briefly discussed in the following.

In the case of RH neutrinos, the operators in Eq. (2.33) also contribute to rare charm dineutrino modes. While the contributions from further vector and axial vector contributions can remain

Table 6.3: Upper limits on branching ratios in the LFU scenario $\mathcal{B}^{\max}_{\text{LFU}}$, the cLFC scenario $\mathcal{B}^{\max}_{\text{cLFC}}$ and the general case $\mathcal{B}^{\max}$ corresponding to Eq. (6.15), using Eq. (6.9) and Tab. 6.1 for various different rare charm dineutrino modes. The first three entries correspond to the conservative ansatz only utilizing constraints from high–p_T Drell-Yan searches. The last three entries include low energy data assuming no large cancellations between LH and RH Wilson coefficients, see main text and App. G for details.

$h_c \to F_u$	$\mathcal{B}^{\max}_{\text{LFU}}$ $[10^{-7}]$	$\mathcal{B}^{\max}_{\text{cLFC}}$ $[10^{-6}]$	$\mathcal{B}^{\max}$ $[10^{-6}]$	$\mathcal{B}^{\max}_{\text{LFU}}$ $[10^{-7}]$	$\mathcal{B}^{\max}_{\text{cLFC}}$ $[10^{-6}]$	$\mathcal{B}^{\max}$ $[10^{-6}]$
$D^0 \to \pi^0$	6.1	3.5	13	0.5	2.8	12
$D^+ \to \pi^+$	25	14	52	1.9	11	47
$D_s^+ \to K^+$	4.6	2.6	9.6	0.3	2.1	8.8
$D^0 \to \pi^0\pi^0$	1.5	0.8	3.1	0.1	0.7	2.8
$D^0 \to \pi^+\pi^-$	2.8	1.6	5.9	0.2	1.3	5.4
$D^0 \to K^+K^-$	0.03	0.02	0.06	0.002	0.01	0.06
$\Lambda_c^+ \to p^+$	18	11	39	1.4	8.4	35
$\Xi_c^+ \to \Sigma^+$	36	21	76	2.7	17	70
$\Xi_c^0 \to \Sigma^0$	6.2	3.6	1.3	0.5	2.9	12
$\Xi_c^0 \to \Lambda^0$	2.7	1.5	5.6	0.2	1.2	5.1
$\Omega_c^0 \to \Xi^0$	34	19	71	2.6	15	65
$\Xi_c^+ \to \Sigma^+(\to p\pi^0)$	19	11	39	1.4	8.8	36
$\Xi_c^0 \to \Lambda^0(\to p\pi^-)$	1.7	1.0	3.6	0.1	0.8	3.3
$\Omega_c^0 \to \Xi^0(\to \Lambda^0\pi^0)$	34	19	71	2.6	15	65
$D^0 \to X$	15	8.7	32	1.1	6.9	29
$D^+ \to X$	38	22	80	2.9	17	74
$D_s^+ \to X$	18	10	38	1.4	8.3	35

sizable, it is possible to estimate effects from (pseudo-)scalar operators. The combination $y_{cu} = \sum_{i,j} \left(|C_S^{ij} - C_S^{ij\prime}|^2 + |C_P^{ij} - C_P^{ij\prime}|^2 \right)$ is constrained by the Belle upper limit $\mathcal{B}(D^0 \to \text{inv.}) < 9.4 \times 10^{-5}$ at 90 % C.L. [265] interpreted as a purely leptonic dineutrino final state,

$$y_{cu} \lesssim \frac{64\,\pi^3\, m_c^2\, \mathcal{B}(D^0 \to \text{inv.})}{G_{\text{F}}^2\, \alpha_e^2\, m_D^5\, f_D^2\, \tau_D} \sim 67\,. \tag{6.16}$$

Barring cancellation, this bound implies scalar and pseudoscalar contributions to semileptonic branching ratios at the level of few $\times\, 10^{-6}$ [4], which would spoil our indirect flavor probes presented in Tab. 6.3.

Table 6.4: Charm fragmentation fractions $f(c \to h_c)$ from Ref. [266] for different charmed hadrons h_c and their expected number, $N(h_c)$, at benchmarks with $N(c\bar{c}) = 550 \cdot 10^9$ (FCC-ee) and $N(c\bar{c}) = 65 \cdot 10^9$ (Belle II with $50\,\text{ab}^{-1}$) [68].

h_c	$f(c \to h_c)$	$N(h_c)$ (FCC-ee)	$N(h_c)$ (Belle II)
D^0	0.59	$6 \cdot 10^{11}$	$8 \cdot 10^{10}$
D^+	0.24	$3 \cdot 10^{11}$	$3 \cdot 10^{10}$
D_s^+	0.10	$1 \cdot 10^{11}$	$1 \cdot 10^{10}$
Λ_c^+	0.06	$7 \cdot 10^{10}$	$8 \cdot 10^9$

On the other hand, these contributions become irrelevant within uncertainties, *i.e.* roughly 10 % on LFU upper limits using the high–p_T limits (second column in Tab. 6.3), as soon as the bound on $\mathcal{B}(D^0 \to \text{inv.})$ can be improved by roughly two orders of magnitude [4]. Similarly, the improved limit would exclude large effects from LNV NP, which otherwise is possible as missing energy signatures do not distinguish $\nu\bar{\nu}$, $\nu\nu$ and $\bar{\nu}\bar{\nu}$ final states, see discussion in [4].

In App. G we provide differential distributions for rare charm dineutrino decay modes using the flavor dependent limits in Eq. (6.15). Here, we know from our analyses with charged dileptons that distributions can help to disentangle NP contributions, *e.g.* the difference between large scalar versus vector contributions. In summary, the situation in rare charm dineutrino modes is very special. Any observation of dineutrino modes implies NP to be present, and due to missing resonance contributions, dineutrino branching ratios are clean null tests. Beyond that, charged lepton flavor can be tested indirectly and binned measurements as well as the search for $D^0 \to$ inv. test for the existence of light RH neutrinos.

To estimate the future potential of these (very) rare charm dineutrino modes, we investigate the sensitivity for Belle II with $50\,\text{ab}^{-1}$ [64] and for the possible future collider FCC-ee running at the Z [68]. Tab. 6.4 contains fragmentation fractions $f(c \to h_c)$ from Ref. [266] along with the estimated number of various charm hadrons $N(h_c) = 2f(c \to h_c)N(c\bar{c})$ produced at FCC-ee and Belle II, respectively.

We illustrate (future) experimental reach in Fig. 6.3. Here, we use that the relative statistical uncertainty of a branching ratio measurement is given by

$$\delta\mathcal{B}(h_c \to F_u\nu\bar{\nu}) = \frac{\Delta\mathcal{B}(h_c \to F_u\nu\bar{\nu})}{\mathcal{B}(h_c \to F_u\nu\bar{\nu})} = \frac{1}{\sqrt{N_{F_u}^{\text{exp}}}}\,, \tag{6.17}$$

where $N_{F_u}^{\text{exp}}$ is the number of signal events and reads

$$N_{F_u}^{\text{exp}} = \eta_{\text{eff}}\, N(h_c)\, \mathcal{B}(h_c \to F_u\nu\bar{\nu})\,, \tag{6.18}$$

given the overall reconstruction efficiency η_{eff}. In Fig. 6.3 we plot $\delta\mathcal{B} = 1/\sqrt{\eta_{\text{eff}}\, N(h_c)\, \mathcal{B}}$ for $N(h_c)$ from Tab. 6.4 and assuming two benchmarks for the efficiency $\eta_{\text{eff}} = 1,\ 10^{-3}$. By doing so, the experimental

sensitivity only depends on the number of available charmed hadrons h_c and not on the final state. Fig. 6.3 also presents results from the first three columns of Tab. 6.3, *i.e.* the conservative bounds using data from Drell-Yan searches only. The limits are given in different colors and the solid, dotted and dashed lines correspond to the LFU, cLFC and general limit, respectively. The black dotted and dashed lines illustrate the $3\sigma\,(5\sigma)$ limits, which correspond to $\delta\mathcal{B} = 1/3\,(1/5)$.

Fig. 6.3 demonstrates the possibilities to test charged lepton flavor in rare charm dineutrino modes. A dedicated analysis of the expected efficiency η_{eff} for Belle II or the FCC-ee is desirable to estimate the experimental reach, however the naïve estimate of $\eta_{\text{eff}} \sim 10^{-3}$ yields 5σ discovery potential for branching ratios as small as at least few$\times 10^{-6}$ at Belle II for D^0 and D^+ decays. For Λ_c baryon decays discovery potential is still possible at Belle II if branching ratios are not far below 10^{-5}. These sensitivities probe most of the upper limits extracted via the $SU(2)_L$–link and presented in Tab. 6.3.

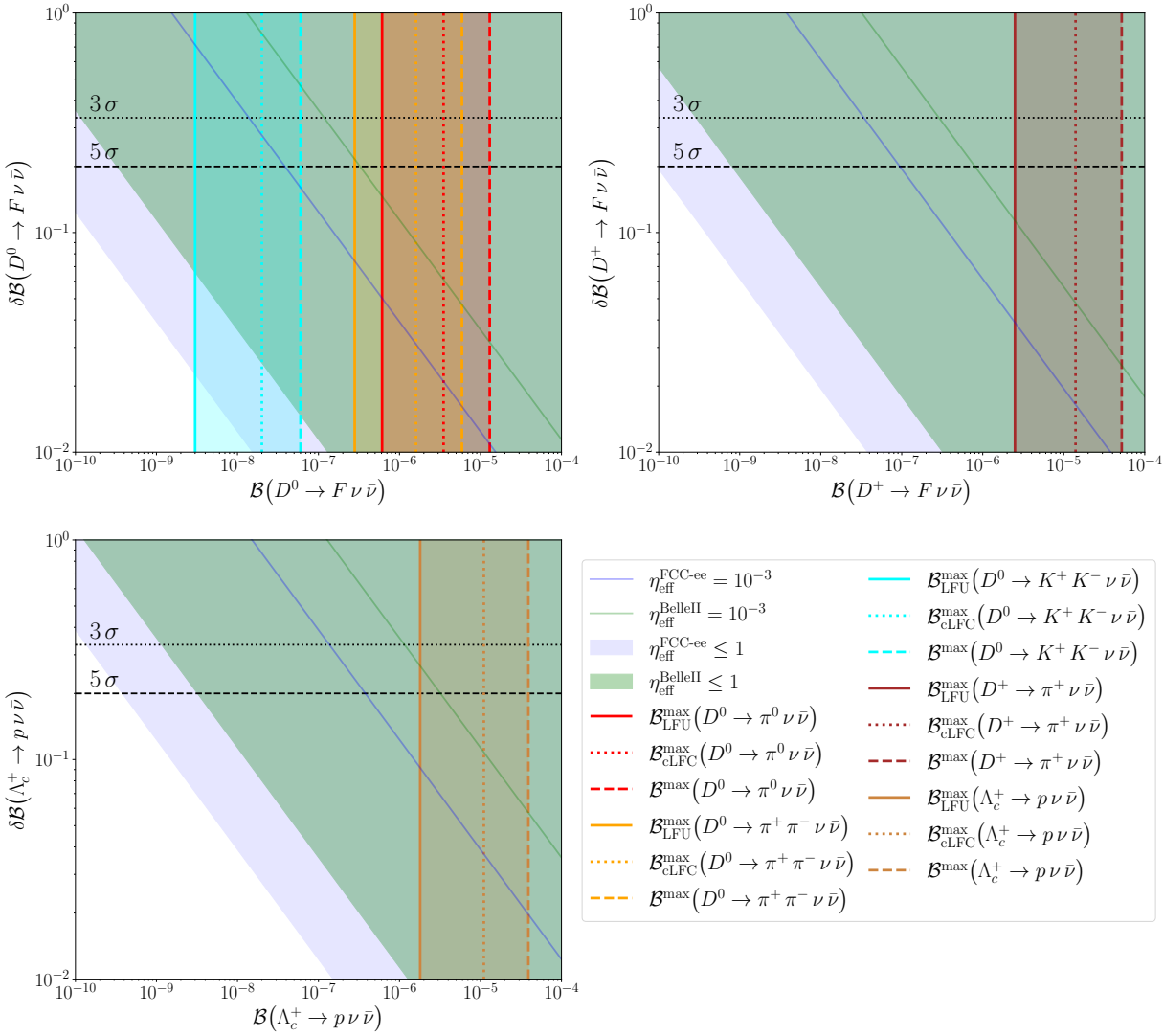

Figure 6.3: The figure shows the plane of the relative statistical uncertainty of the branching ratio $\delta\mathcal{B}$ versus the branching ratio itself $\mathcal{B}$ for dineutrino decays of the D^0, the D^+ and the Λ_c^+ in the upper left, upper right and lower left, respectively. The lilac and green shaded areas illustrate the maximal reach ($\eta_{\text{eff}} = 1$) for FCC-ee and Belle II, respectively, whereas the solid tilted lines depict $\eta_{\text{eff}} = 10^{-3}$. The dotted and dashed black horizontal lines correspond to $3\,\sigma$ ($\delta\mathcal{B} = 1/3$) and $5\,\sigma$ ($\delta\mathcal{B} = 1/5$), respectively. The vertical lines show upper limits assuming LFU (solid), cLFC (dotted) and generic lepton flavor (dashed) for different modes, given in Tab 6.3, where for each of the three lines corresponding to the same decay channel, the lines are grouped together by a shaded band to improve the visibility in the plot.

6.3 Opportunities with rare B–decays into dineutrinos

In this section, we exploit the implications of the general $SU(2)_L$–link for rare b–decays, including $b \to s$ and $b \to d$ induced modes. The main difference to the charm sector is the existence of a significant SM contribution, induced by the heavy top quark running in one-loop diagrams. We find for $q = s,\, d$

$$\mathcal{C}_{L,\mathrm{SM}}^{bqij} = V_{tb}V_{tq}^* X_{\mathrm{SM}}\, \delta_{ij} \ , \tag{6.19}$$

with $X_{\mathrm{SM}} = -\frac{2\,X(x_t)}{\sin^2\theta_W} = -12.64 \pm 0.15$ [267, 268], where $X(x_t)$ is a loop function depending on $x_t = \frac{m_t^2}{M_W^2}$ [269, 270]. Along with $A_\pm^{h_q F_{q'}}$ factors from Tab. 6.2 and the most stringent available upper limits from $B^+ \to K^+\,\nu\bar{\nu}$ and $B^0 \to K^{*0}\,\nu\bar{\nu}$ for $b \to s$ and $B^+ \to \pi^+\,\nu\bar{\nu}$ and $B^+ \to \rho^+\,\nu\bar{\nu}$ for $b \to d$, we are able to derive upper limits on the combinations $x_{bq}^\pm$ defined in Eq. (6.5),

$$\begin{aligned} x_{bs}^+ &\lesssim 2.9 \ , \quad x_{bs}^- + 0.2\, x_{bs}^+ \lesssim 2.0 \, , \\ x_{bd}^+ &\lesssim 4.2 \ , \quad x_{bd}^- + 0.1\, x_{bd}^+ \lesssim 2.4 \, , \end{aligned} \tag{6.20}$$

which include the SM contribution. We collect the SM prediction, based on the numerical evaluation in Ref. [7] (and this work) and based on other available literature along with available experimental upper limits, the upper limits derived within our EFT via Eq. (6.20), and the future expected sensitivity with Belle II data for several $b \to s$ and $b \to d$ induced rare beauty dineutrino decays in Tab. 6.5. Differences between SM predictions as in Ref. [7] and values from other available literature can be explained by updated CKM values and form factor improvements.

Similar to the discussion in the previous section, one needs to take into account resonant backgrounds in charged meson decays through τ–leptons, see check marks in Tab. 6.2. The long-distance decay chain is given by $B^+ \to \tau^+(\to P^+\bar{\nu}_\tau)\nu_\tau$ with $P^+ = \pi^+,\, K^+$. Different from similar effects in the charm sector, it is not helpful to apply cuts, as applying Eq. (6.12) would exclude 83 % and 88 % of the available phase space in $B^+ \to K^+\nu\bar{\nu}$ and $B^+ \to \pi^+\nu\bar{\nu}$, respectively. Instead, we treat these backgrounds as irreducible uncertainties and estimate their size via [278]

$$\mathcal{B}(B^+ \to P^+\,\bar{\nu}_\tau\nu_\tau)_{\mathrm{LD}} = \frac{G_F^4 |V_{ub}V_{uq}^*|^2 f_{B^+}^2 f_{P^+}^2}{128\,\pi^2\, m_{B^+}^3 \Gamma_\tau \Gamma_{B^+}} \cdot m_\tau (m_{B^+}^2 - m_\tau^2)^2 (m_{P^+}^2 - m_\tau^2)^2 \ , \tag{6.21}$$

where $\Gamma_{\tau,\,B^+}$ are the decay widths of the τ and the B^+–meson, while f_{B^+} and f_{P^+} refer to the decay constants of the B^+ and P^+ mesons, respectively. In agreement with Ref. [278] we find

$$\mathcal{B}(B^+ \to K^+\,\bar{\nu}_\tau\nu_\tau)_{\mathrm{LD}} \sim 5 \times 10^{-7} \ , \qquad \mathcal{B}(B^+ \to \pi^+\,\bar{\nu}_\tau\nu_\tau)_{\mathrm{LD}} \sim 8 \times 10^{-6} \ . \tag{6.22}$$

Since interferences between long- and short-distance contributions are negligible [264], resonant τ–backgrounds correspond to an additional uncertainty of 10 % on the SM value in $B^+ \to K^+\nu\bar{\nu}$, but yield branching ratios two orders of magnitude above the respective SM expectation in $B^+ \to \pi^+\nu\bar{\nu}$. We

Table 6.5: SM predictions for branching ratios of rare beauty dineutrino modes evaluated as in Ref. [7], as well as predictions available in the literature, current experimental limits at 90 % C.L., derived EFT limits using Eqs. (6.20), and Belle II sensitivities for $5\,\text{ab}^{-1}$ ($50\,\text{ab}^{-1}$) from Ref. [64] are displayed in the second to last column, respectively. [a] Marked limits serve as input. See text for details.

$B \to F_q$	SM, Ref. [7] $[10^{-8}]$	SM, literature $[10^{-8}]$	Exp. limit (90 % CL) $[10^{-6}]$	Derived EFT limits $[10^{-6}]$	Belle II $5\,\text{ab}^{-1}$ ($50\,\text{ab}^{-1}$) %
$B^0 \to K^0$	391 ± 52	460 ± 50 [64]	26 [271]	15	–
$B^+ \to K^+$	423 ± 56	460 ± 50 [64]	16 [272]	16[a]	30 (11) [64]
$B^0 \to K^{*0}$	824 ± 99	960 ± 90 [64]	18 [271]	18[a]	26 (9.6) [64]
$B^+ \to K^{*+}$	893 ± 107	960 ± 90 [64]	40 [273]	19	25 (9.3) [64]
$B_s^0 \to \phi$	981 ± 69	1400 ± 500 [274]	5400 [275]	23	–
$B^0 \to X_s$	$(28 \pm 3) \times 10^2$	$(29 \pm 3) \times 10^2$ [276]	640 [277]	78	–
$B^+ \to X_s$	$(30 \pm 3) \times 10^2$	$(29 \pm 3) \times 10^2$ [276]	640 [277]	84	–
$B^0 \to \pi^0$	5.4 ± 0.6	7.3 ± 0.7 [278]	9 [271]	6	–
$B^+ \to \pi^+$	12 ± 1	14 ± 1 [278]	14 [271]	14[a]	–
$B^0 \to \rho^0$	22 ± 8	20 ± 10 [274]	40 [271]	14	–
$B^+ \to \rho^+$	48 ± 18	42 ± 20 [274]	30 [271]	30[a]	–
$B_s^0 \to K^0$	13 ± 3	27 ± 16 [274]	–	26	–
$B_s^0 \to K^{*0}$	36 ± 3	–	–	24	–
$B^0 \to X_d$	$(1.3 \pm 0.1) \times 10^2$	$(1.7 \pm 0.5) \times 10^2$ [274]	–	114	–
$B^+ \to X_d$	$(1.4 \pm 0.1) \times 10^2$	$(1.7 \pm 0.5) \times 10^2$ [274]	–	123	–

use the full available phase space for integration in both modes, but note that resonant τ–backgrounds need to be taken into account as soon as future measurements in these modes become available.

Now, in order to connect rare beauty dineutrino modes to charged lepton couplings, we apply the $SU(2)_L$–link, discussed in Sec. 6.1 and rewrite the combinations of dineutrino couplings as

$$x_{bs}^{\pm} = \sum_{i,j} \left| \mathcal{C}_{L,\text{SM}}^{bsij} + \mathcal{K}_L^{tcij} \pm \mathcal{K}_R^{bsij} \right|^2 , \qquad x_{bd}^{\pm} = \sum_{i,j} \left| \mathcal{C}_{L,\text{SM}}^{bdij} + \mathcal{K}_L^{tuij} \pm \mathcal{K}_R^{bdij} \right|^2 , \tag{6.23}$$

where the sum runs over charged lepton flavors $i, j = e, \mu, \tau$. We further factorize CKM matrix elements as follows

$$\kappa_R^{bqij} = \mathcal{K}_R^{bqij} \cdot \left(V_{tb} V_{tq}^*\right)^{-1} , \quad \kappa_L^{tcij} = \mathcal{K}_L^{tcij} \cdot \left(V_{tb} V_{ts}^*\right)^{-1} , \quad \kappa_L^{tuij} = \mathcal{K}_L^{tuij} \cdot \left(V_{tb} V_{td}^*\right)^{-1} . \tag{6.24}$$

We use Eq. (6.20), conservatively neglect x_{bq}^{+} in the second inequalities, since $x_{bq}^{\pm} \geq 0$ and find

$$\begin{aligned}
\sum_{i,j} \left| X_{\rm SM}\, \delta_{ij} + \kappa_L^{tcij} + \kappa_R^{bsij} \right|^2 &\lesssim 1.8 \times 10^3 \;, & \sum_{i,j} \left| X_{\rm SM}\, \delta_{ij} + \kappa_L^{tuij} + \kappa_R^{bdij} \right|^2 &\lesssim 5.8 \times 10^4 \;, \\
\sum_{i,j} \left| X_{\rm SM}\, \delta_{ij} + \kappa_L^{tcij} - \kappa_R^{bsij} \right|^2 &\lesssim 1.3 \times 10^3 \;, & \sum_{i,j} \left| X_{\rm SM}\, \delta_{ij} + \kappa_L^{tuij} - \kappa_R^{bdij} \right|^2 &\lesssim 3.3 \times 10^4 \;,
\end{aligned} \tag{6.25}$$

for $b \to s\,\nu\bar{\nu}$ and $b \to d\,\nu\bar{\nu}$ transitions, respectively. Eq. (6.25) constrains charged lepton couplings and results in the best available limits on RH couplings with flavor indices $bd\tau\tau$, $bde\tau$, as well as $bs\tau\tau$, $bse\tau$, $bs\mu\tau$. Limits for all flavor combinations entering in Eq. (6.25) from dineutrinos, semileptonic rare B–decays to charged leptons and Drell-Yan high–p_T searches are collected in App. G along with further details. The interplay of bounds from dineutrino modes on $\kappa_R^{bq\tau\tau}$ and Drell-Yan data, bounding also $\kappa_L^{bq\tau\tau}$, allows to improve current experimental upper limits on branching ratios of $b \to q\,\tau^+\tau^-$ induced modes, or even obtain novel ones. The current available upper limits at 90 % C.L. read [184]

$$\begin{aligned}
\mathcal{B}(B^0 \to \tau^+\tau^-)_{\rm exp} &< 1.6 \times 10^{-3} \;, \\
\mathcal{B}(B_s^0 \to \tau^+\tau^-)_{\rm exp} &< 5.2 \times 10^{-3} \;, \\
\mathcal{B}(B^+ \to K^+\tau^+\tau^-)_{\rm exp} &< 2.25 \times 10^{-3} \;,
\end{aligned} \tag{6.26}$$

whereas we obtain using *flavio* [279], neglecting effects from scalar and tensor operators, and considering two couplings at a time with $\kappa_L \sim 2\,\mathcal{C}_9 \sim 2\,\mathcal{C}_{10}$ and $\kappa_R \sim 2\,\mathcal{C}_9' \sim 2\,\mathcal{C}_{10}'$ and varying signs of Wilson coefficients to avoid large cancellations

$$\begin{aligned}
\mathcal{B}(B_s \to \tau^+\tau^-) &\lesssim 5.0 \times 10^{-3} \,, \\
\mathcal{B}(B^0 \to K^0\,\tau^+\tau^-)^{[15,\,22]} &\lesssim 7.8 \times 10^{-4} \,, \\
\mathcal{B}(B^+ \to K^+\,\tau^+\tau^-)^{[15,\,22]} &\lesssim 8.4 \times 10^{-4} \,, \\
\mathcal{B}(B^0 \to K^{*0}\,\tau^+\tau^-)^{[15,\,19]} &\lesssim 7.4 \times 10^{-4} \,, \\
\mathcal{B}(B^+ \to K^{*+}\,\tau^+\tau^-)^{[15,\,19]} &\lesssim 8.1 \times 10^{-4} \,, \\
\mathcal{B}(B_s \to \phi\,\tau^+\tau^-)^{[15,\,18.8]} &\lesssim 6.8 \times 10^{-4} \,,
\end{aligned} \tag{6.27}$$

well above their SM predictions

$$\begin{aligned}
\mathcal{B}(B_s \to \tau^+\tau^-)_{\rm SM} &= (7.78 \pm 0.31) \times 10^{-7} \,, \\
\mathcal{B}(B^0 \to K^0\tau^+\tau^-)_{\rm SM}^{[15,\,22]} &= (1.17 \pm 0.12) \times 10^{-7} \,, \\
\mathcal{B}(B^+ \to K^+\tau^+\tau^-)_{\rm SM}^{[15,\,22]} &= (1.26 \pm 0.14) \times 10^{-7} \,, \\
\mathcal{B}(B^0 \to K^{*0}\tau^+\tau^-)_{\rm SM}^{[15,\,19]} &= (0.97 \pm 0.10) \times 10^{-7} \,, \\
\mathcal{B}(B^+ \to K^{*+}\tau^+\tau^-)_{\rm SM}^{[15,\,19]} &= (1.05 \pm 0.11) \times 10^{-7} \,, \\
\mathcal{B}(B_s \to \phi\,\tau^+\tau^-)_{\rm SM}^{[15,\,18.8]} &= (0.90 \pm 0.07) \times 10^{-7} \,.
\end{aligned} \tag{6.28}$$

The superscripts in Eqs. (6.27) and (6.28) correspond to the q^2–range in GeV^2 for the dilepton invariant mass squared. These bins are chosen to remove the $\psi(2S)$ resonance, while simultaneously supporting the use of the OPE in $1/Q, Q = (m_b, \sqrt{q^2})$ [280].

Similarly, we obtain the following upper limits for $b \to d\,\tau^+\tau^-$ transitions

$$\begin{aligned} \mathcal{B}(B^0 \to \tau^+\tau^-) &\lesssim 6.0 \times 10^{-4} \,, \\ \mathcal{B}(B^0 \to \pi^0\tau^+\tau^-)^{[15,22]} &\lesssim 2.5 \times 10^{-5} \,, \\ \mathcal{B}(B^+ \to \pi^+\tau^+\tau^-)^{[15,22]} &\lesssim 5.3 \times 10^{-5} \,, \end{aligned} \tag{6.29}$$

again, several orders above their respective SM predictions

$$\begin{aligned} \mathcal{B}(B^0 \to \tau^+\tau^-)_{\rm SM} &= (2.39 \pm 0.24) \times 10^{-8} \,, \\ \mathcal{B}(B^0 \to \pi^0\tau^+\tau^-)^{[15,22]}_{\rm SM} &= (0.20 \pm 0.02) \times 10^{-8} \,, \\ \mathcal{B}(B^+ \to \pi^+\tau^+\tau^-)^{[15,22]}_{\rm SM} &= (0.44 \pm 0.05) \times 10^{-8} \,. \end{aligned} \tag{6.30}$$

Belle II is expected to place (projected) upper limits with $5\,\text{ab}^{-1}$ ($50\,\text{ab}^{-1}$) on the branching ratios [64], which read

$$\begin{aligned} \mathcal{B}(B_s^0 \to \tau^+\tau^-)_{\rm proj} &< 8.1\,(-) \times 10^{-5} \,, \\ \mathcal{B}(B^+ \to K^+\,\tau^+\tau^-)_{\rm proj} &< 6.5\,(2.0) \times 10^{-5} \,, \\ \mathcal{B}(B^0 \to \tau^+\tau^-)_{\rm proj} &< 30\,(9.6) \times 10^{-5} \,, \end{aligned} \tag{6.31}$$

and cover the regions (6.27), (6.29).

Another possibility to make use of the *bidirectional* $SU(2)_L$–link is to use stringent constraints on $b \to s\mu\mu$ and $b \to d\mu\mu$ couplings to constrain dineutrino branching ratios assuming LFU. This is achieved in the following manner.

In the LFU limit, the branching ratios for $B \to V\nu\bar{\nu}$ and $B \to P\nu\bar{\nu}$ decays can be written as

$$\begin{aligned} \mathcal{B}(B \to V\nu\bar{\nu})_{\rm LFU} &= A_+^{BV} x_{bq,\rm LFU}^+ + A_-^{BV} x_{bq,\rm LFU}^- \,, \\ \mathcal{B}(B \to P\nu\bar{\nu})_{\rm LFU} &= A_+^{BP} x_{bq,\rm LFU}^+ \,, \end{aligned} \tag{6.32}$$

where

$$x_{bq,\rm LFU}^{\pm} = 3\,\left|V_{tb}V_{tq}^*\right|^2 \cdot \left(X_{\rm SM} + \kappa_L^{tq'\mu\mu} \pm \kappa_R^{bq\mu\mu}\right)^2 \,, \tag{6.33}$$

with $q' = u$, (c) for $q = d$, (s), respectively. In Eq. (6.33), the sum over lepton flavors i, j gave way to the factor 3 and we particularize to the $\mu\mu$ couplings, as these are constrained best.

Now, we can solve $\mathcal{B}(B \to P\nu\bar{\nu})_{\rm LFU}$ for $\kappa_L^{tq'\mu\mu}$ and obtain two solutions

$$\kappa_L^{tq'\mu\mu} = -X_{\rm SM} - \kappa_R^{bq\mu\mu} \pm \sqrt{\frac{\mathcal{B}(B \to P\nu\bar{\nu})_{\rm LFU}}{3\left|V_{tb}V_{tq}^*\right|^2 A_+^{BP}}} \,. \tag{6.34}$$

These can be used to eliminate $\kappa_L^{tq'\mu\mu}$ from $\mathcal{B}(B \to V\nu\bar{\nu})_{\rm LFU}$, leading to

$$\mathcal{B}(B \to V\nu\bar{\nu})_{\rm LFU} = \frac{A_+^{BV}}{A_+^{BP}}\mathcal{B}(B \to P\nu\bar{\nu})_{\rm LFU} + 3\,A_-^{BV}\left|V_{tb}V_{tq}^*\right|^2\left(\sqrt{\frac{\mathcal{B}(B \to P\nu\bar{\nu})_{\rm LFU}}{3\left|V_{tb}V_{tq}^*\right|^2 A_+^{BP}}} \mp 2\,\kappa_R^{bq\mu\mu}\right)^2 . \tag{6.35}$$

Eq. (6.35) allows to probe charged LFU with measurements of dineutrino modes, since $\kappa_R^{bq\mu\mu}$ is constrained from global fits and small, see App. G, the correlation between $B \to P$ and $B \to V$ is dominated by form factor uncertainties entering in $A_\pm^{BP(BV)}$. We illustrate this indirect LFU test in Fig. 6.4, split into $b \to s\nu\bar{\nu}$ induced modes in the left panel and $b \to d\nu\bar{\nu}$ in the right panel. In the upper left, we display the correlation between $\mathcal{B}(B^0 \to K^{*0}\nu\bar{\nu})$ and $\mathcal{B}(B^+ \to K^+\nu\bar{\nu})$, whereas the lower plot shows $\mathcal{B}(B^0 \to K^{*0}\nu\bar{\nu})$ versus $\mathcal{B}(B^0 \to K^0\nu\bar{\nu})$. We use $\kappa_R^{bs\mu\mu} \sim 0.5 \pm 0.25$ and display the 1σ (2σ) LFU region as a red cone (dashed red lines). A measurement of the displayed modes, which lies outside of this cone implies the violation of LFU, while a measurement insight the red region does not necessarily imply LFU conservation. We display the SM prediction as a blue diamond with uncertainties as bars, where we add 10 % uncertainty for $B^+ \to K^+\nu\bar{\nu}$ from resonant τ–backgrounds. The irreducible background from $B^+ \to \tau^+\bar{\nu}_\tau$ decays is indicated as a blue vertical line in the upper left plot. The green region illustrates the validity of our EFT framework, *i.e.* a measurement outside the green region implies missing degrees of freedom in our framework, for instance light RH neutrinos. The gray hatched region are direct upper limits, while the light gray region displays the upper limit derived within our framework and collected in Tab. 6.5. Again a measurement inside this light gray region indicates NP outside of our EFT framework. The yellow boxes illustrate the projected experimental sensitivity (10 % at the chosen point) of Belle II with $50\,{\rm ab}^{-1}$.

In the right panel, we project the $\mathcal{B}(B^0 \to \rho^0\nu\bar{\nu})$ –$\mathcal{B}(B^+ \to \pi^+\nu\bar{\nu})$ plane (upper right plot) and the $\mathcal{B}(B^0 \to \rho^0\nu\bar{\nu})$ –$\mathcal{B}(B^0 \to \pi^0\nu\bar{\nu})$ plane (lower right plot) using $\kappa_{R,\,\rm NP}^{bd\mu\mu} \sim 0 \pm 4$. We use inserts to visualize the SM prediction. Note that for $B^+ \to \pi^+\nu\bar{\nu}$ the resonant τ–background dominates effects from the weak effective theory. Both lower plots, which show correlations between neutral B-decays, are not affected by long-distance τ contributions.

Similar to the analysis presented in the previous section, possible effects of (pseudo-)scalar operators, which may arise in the presence of light RH neutrinos, can be estimated by available limits on $\mathcal{B}(B_q \to \nu\bar{\nu})$ for $q = d,\, s$. For $B^0 \to \nu\bar{\nu}$ an upper limit is available in [184] and reads

$$\mathcal{B}\left(B^0 \to \nu\bar{\nu}\right)_{\rm exp} < 2.4 \times 10^{-5}\,, \tag{6.36}$$

at 90 % C.L., while $B_s^0 \to \nu\bar{\nu}$ currently remains unconstrained. However, projections for Belle with

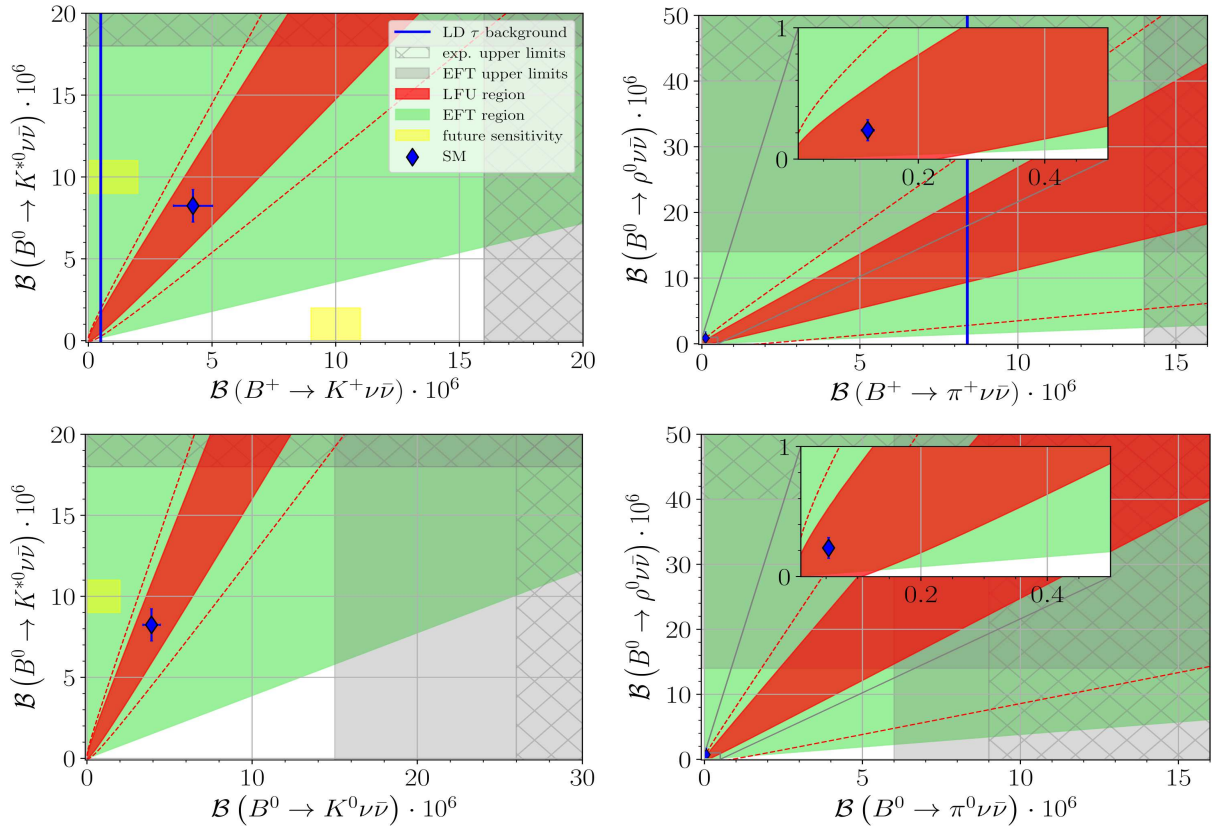

Figure 6.4: The left panel of the figure is for $b \to s$ and the right panel for $b \to d$ transitions. **Upper left:** $\mathcal{B}(B^0 \to K^{*0}\,\nu\bar{\nu})$ versus $\mathcal{B}(B^+ \to K^+\,\nu\bar{\nu})$. We show SM predictions with their uncertainties from Tab. 6.5 as a blue diamond with blue bars, respectively, where the resonant τ–background is included as an additional 10 % uncertainty. The region on the left of the solid blue line is dominated by pure resonant contributions. The dark red region (dashed red lines) display the LFU region given by Eq. (6.35) where $\kappa_R^{bs\mu\mu}$ and $A_\pm$ have been scanned within their $1\,\sigma$ ($2\,\sigma$) uncertainties. The validity of our EFT framework, Eq. (6.20) is depicted as the light green region. Hatched gray bands correspond to the current experimental 90% C.L. upper limits in Tab. 6.5. The widths of the yellow boxes illustrate the projected experimental sensitivity of Belle II with $50\,\text{ab}^{-1}$ in Tab. 6.5. **Lower left:** Similar to the upper left plot, but for $\mathcal{B}(B^0 \to K^{*0}\,\nu\bar{\nu})$ versus $\mathcal{B}(B^0 \to K^0\,\nu\bar{\nu})$. There is no resonant τ–background, but in light gray we show the upper limit derived within our EFT, see Tab. 6.5. **Upper right:** $\mathcal{B}(B^0 \to \rho^0\nu\bar{\nu})$ versus $\mathcal{B}(B^+ \to \pi^+\nu\bar{\nu})$ with equivalent labeling as in the upper left plot. The plot includes a zoom into the region around the SM expectation. The τ–background (solid blue line) is not included as an uncertainty in $\mathcal{B}^+ \to \pi^+\,\nu\bar{\nu}$ as it dominates the SM prediction by two orders of magnitude. **Lower right:** Similar to upper right plot but for $\mathcal{B}(B^0 \to \rho^0\,\nu\bar{\nu})$ versus $\mathcal{B}(B^0 \to \pi^0\,\nu\bar{\nu})$.

$0.12\,\text{ab}^{-1}$ (Belle II with $0.5\,\text{ab}^{-1}$) exist [64],

$$\mathcal{B}\left(B_s^0 \to \nu\bar{\nu}\right)_{\text{proj}} < 9.7\,(1.1) \times 10^{-5}\ . \tag{6.37}$$

We use the limit in Eq. (6.36) and the projections in Eq. (6.37) to constrain

$$y_{bq} = \sum_{i,j} \left(|\mathcal{C}_S^{bqij} - \mathcal{C}_S^{\prime bqij}|^2 + |\mathcal{C}_P^{bqij} - \mathcal{C}_P^{\prime bqij}|^2 \right)\ , \tag{6.38}$$

via

$$\mathcal{B}(B^0 \to \nu\bar{\nu}) = \frac{G_{\text{F}}^2\,\alpha_e^2\,m_B^5\,f_B^2\,\tau_B}{64\,\pi^3\,m_b^2} \cdot y_{bq}\ . \tag{6.39}$$

Contributions from (axial) vector operators are helicity suppressed and negligible, (pseudo-)tensor operators do not contribute. We find

$$y_{bd} \lesssim 0.3\ , \qquad y_{bs} \lesssim 0.79\,(0.09)\ . \tag{6.40}$$

Barring cancellations, these contributions imply

$$\begin{aligned} \mathcal{B}\left(B^{0,+} \to \pi^{0,+}\,\nu\bar{\nu}\right)_{S,P} &\lesssim 1.2 \times 10^{-7}\ , \\ \mathcal{B}\left(B^0 \to K^0\,\nu\bar{\nu}\right)_{S,P}^{\text{proj}} &\lesssim 11.4\,(1.3) \times 10^{-7}\ , \\ \mathcal{B}\left(B^+ \to K^+\,\nu\bar{\nu}\right)_{S,P}^{\text{proj}} &\lesssim 12.3\,(1.4) \times 10^{-7}\ . \end{aligned} \tag{6.41}$$

The (projected) upper limits in Eq. (6.41) imply an $\mathcal{O}(100\%)$ correction to the SM prediction for $b \to d\nu\bar{\nu}$ induced modes in Tab. 6.5 from (pseudo-)scalar contributions. Improving the existing upper limit on $\mathcal{B}(B^0 \to \nu\bar{\nu})$ to the level of $\sim 5 \cdot 10^{-7}$ or smaller would imply negligible percent-level corrections to the SM predictions and reinforce the framework and results of this section. Similarly, the projected reach in the decay $B_s \to \nu\bar{\nu}$ from Eq. (6.37) constrains S, P-contributions to $b \to s$ transitions to be less than a $\mathcal{O}(30\%)$ (Belle with $0.12\,\text{ab}^{-1}$), and a $\mathcal{O}(3\%)$ (Belle II with $0.5\,\text{ab}^{-1}$) correction to the SM branching ratios. Again, no signal in $\mathcal{B}(B_s \to \nu\bar{\nu})$ at the level of the latter case would imply (pseudo-)scalar contributions to small to be observable in $b \to s$ dineutrino modes such as $B \to K\,\nu\bar{\nu}$ within uncertainties.

6.4 Dineutrino probes in other sectors and summary

Due to the flavor inclusiveness of missing energy observables, the $SU(2)_L$–link in Eq. (6.2) is shown to have useful implications for flavor probes of $cu\ell\ell$, $bs\ell\ell$ and $bd\ell\ell$ couplings. In rare charm decays, dineutrino modes per se are interesting, due to the strong GIM suppression, which turn any observation in the foreseeable future into a NP discovery. On top, the observed branching ratios can indicate

the breakdown of charged lepton flavor assumptions, *i.e.* LFU and cLFC. In the down-type sector, correlations between rare b–decays into dineutrinos can be exploited by obtaining indirect bounds on branching ratios for all possible modes, coming from experimental input, available for a few of those modes. Furthermore, indirect bounds on rare b–decay modes involving ditaus in the final state are also obtained, which are better than currently available experimental limits. The direct correlation between a $B \to P\nu\bar{\nu}$ and a $B \to V\nu\bar{\nu}$ mode can even test LFU, see Fig. 6.4. All of these studies rely on experimental input and therefore improve in time. Here, the direction for the $SU(2)_L$–link, *i.e.* whether experimental information on dineutrino modes constrains charged lepton couplings or vice versa, is dictated by experimental constraints. Either upper limits of dineutrino branching ratios constrain charged lepton couplings, or charged lepton couplings serve as input to upper limits on dineutrino branching ratios.

Beyond the presented analyses, there are only a few FCNCs in the quark sector of the SM not covered in this work in previous sections so far. In the down sector $s \to d$ transitions are already tightly constrained. In fact, translating the current measurement $\mathcal{B}(K^+ \to \pi^+\nu\bar{\nu})_{\text{exp}} = \left(8^{+6}_{-4}\right) \times 10^{-11}$ [184] into the 90% C.L. upper limit $\mathcal{B}(K^+ \to \pi^+\nu\bar{\nu})_{\text{exp}} \lesssim 1.7 \times 10^{-10}$ yields

$$x^+_{sd} = \sum_{i,\,j} \left|\mathcal{C}^{sd}_{\text{SM}}\delta_{ij} + \mathcal{K}^{cuij}_L + \mathcal{K}^{sdij}_R\right|^2 \lesssim 2.5 \times 10^{-4}\,. \tag{6.42}$$

With $\mathcal{C}^{sd}_{\text{SM}} = 0.0059 - 0.0017\,\text{i}$ [268] and assuming no large cancellations to be present, rare kaon to dineutrino measurements imply in the LFU limit, *i.e.* assuming $\mathcal{K}^{cuee}_L = \mathcal{K}^{cu\mu\mu}_L = \mathcal{K}^{cu\tau\tau}_L$ and $\mathcal{K}^{sdee}_R = \mathcal{K}^{sd\mu\mu}_R = \mathcal{K}^{sd\tau\tau}_R$

$$-0.015 \lesssim \mathcal{K}^{cu\ell\ell}_L, \mathcal{K}^{sd\ell\ell}_R \lesssim 0.003\,, \quad \ell = e, \mu, \tau\,. \tag{6.43}$$

Relaxing the LFU assumption, a single flavor diagonal coupling is constrained to be within

$$-0.019 \lesssim \mathcal{K}^{cu\tau\tau}_L, \mathcal{K}^{sd\tau\tau}_R \lesssim 0.007\,, \tag{6.44}$$

where we assumed $\ell\ell = \tau\tau$ for concreteness. Finally, a single LFV coupling is constrained to be bounded as, *e.g.* $\mathcal{K}^{\tau e}_{L,R} = \mathcal{K}^{e\tau}_{L,R}$,

$$|\mathcal{K}^{cu\ell\ell'}_L|, |\mathcal{K}^{sd\ell\ell'}_R| \lesssim 0.008\,, \quad \text{for} \quad \ell \neq \ell'\,. \tag{6.45}$$

These limits are used in the second scenario in Eq. (6.15) and also provide indirect guidance for future global fits in semileptonic rare charm decays. The limits on $\mathcal{K}^{cu\ell\ell'}_L$ are stronger than limits presented in Sec. 4.1 and exclude scenarios with large NP contributions in $C_9 \sim -C_{10}$, a scenario currently preferred in global fits as a solution to the B–decay anomalies for $b \to s\mu\mu$ couplings, see Table 9 and 10 in Ref. [7].

For the top sector the situation is somewhat different from the other sectors, as the top quark decays before hadronization. However, qualitatively the same relations between charged lepton and dineutrino couplings exist. CMS [281] already obtains upper limits on $e\mu$ final states, corresponding to rare FCNC

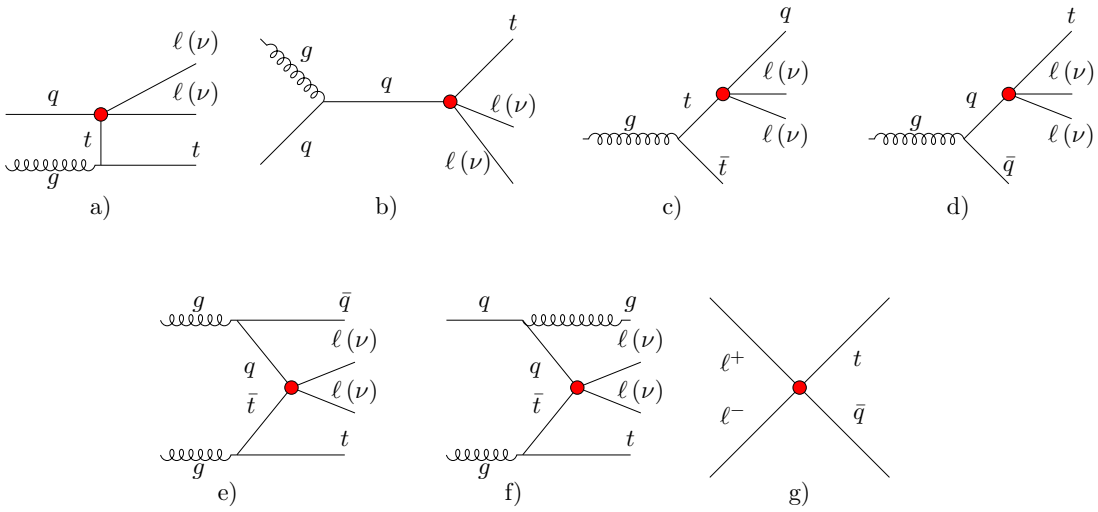

Figure 6.5: Feynman diagrams with semileptonic four-fermion operators at every red blob involving $qt\ell\ell'$ or $qt\nu\bar{\nu}$, and $q = u, c$. The diagrams contribute to a)+b): single top plus dileptons, or single top plus missing energy, c)-f): single top plus jet plus opposite sign dileptons, or single top plus jet plus missing energy. For a lepton collider c)+d) are possible with the gluon replaced by γ, Z. Contribution g) only matters for lepton colliders, with $\ell^+\ell^-$ directly annihilating into $t\bar{q}$.

top branching ratios

$$\mathcal{B}(t \to u\, e^+\mu^- + u\, e^-\mu^+)_{\text{exp}} < 0.135 \times 10^{-6}\,, \quad \mathcal{B}(t \to c\, e^+\mu^- + c\, e^-\mu^+)_{\text{exp}} \quad < 1.31 \times 10^{-6}\,. \tag{6.46}$$

ATLAS [282] also provides bounds on LFV modes involving taus at 95 % C.L.

$$\mathcal{B}(t \to q\,\tau(e,\mu))_{\text{exp}} < 1.86 \times 10^{-5}\,, \quad q = u, c\,. \tag{6.47}$$

Four-fermion operators for $qt\ell\ell$ or $qt\nu\bar{\nu}$ with $q = c$, u also contribute to single top plus dileptons, single top plus missing energy or single top plus jet plus opposite sign dileptons (missing energy) signatures. At a possible future electron [68] or muon [67, 283, 284] collider, the $qt\ell\ell$ coupling can be probed directly. Feynman diagrams for these contributions are illustrated in Fig. 6.5. Single top production of these types are searched for at the LHC at least for the charged lepton couplings [281, 282, 285].

A detailed analysis of implications for the top sector is beyond the scope of this work. However, a global SMEFT analysis will become crucial in the future to globally test flavor in the SM and beyond and an overview of available limits on charged lepton couplings for all quark sectors is presented in App. G.2, see Tab. G.3 for sd, cu, bs and bd and Tab. G.4 for tc and tu. The applications of the simple $SU(2)_L$–link already helped to exploit connections between different flavor sectors and since these type of analyses are data-driven, they will evolve in the future.

7 Conclusion and outlook

In this thesis we have studied rare charm FCNC transitions. In Chapters 2 and 3 we discussed SM Wilson coefficients relevant for semileptonic rare charm decays in the framework of the WET and the SMEFT, summarized in Sec. 2.3, as well as the SM phenomenology of exclusive rare charmed meson decays, $D^0 \to \ell^+\ell^-$, $D \to P\ell^+\ell^-$, and rare charmed baryon decays, $B_0 \to B_1\ell^+\ell^-$ and $B_0 \to B_1(\to B_2\pi)\ell^+\ell^-$. The main observations are the following.

Perturbative NNLLO SM contributions to rare charm Wilson coefficients are completely negligible for phenomenological applications. Instead, $c \to u\ell^+\ell^-$ induced modes are dominated by non-perturbative effects, for which at present no reliable first-principle calculation is at hand. Therefore, we have modeled effects from intermediate resonances in a simple phenomenological ansatz fit to data, which induces sizable hadronic uncertainties, see Eq. (3.11), resulting differential branching ratios in orange in Figs. 3.2 and 3.3, as well as branching ratio estimates in Tab. 3.2 and Eq. (3.23).

Furthermore, we have shown in Chapter 4 that a sizable model-independent BSM parameter space is still unconstrained and we have discussed contributions induced in LQ– and flavorful, anomaly-free Z'–models. Despite the resonance dominance in branching ratios, we have demonstrated in Chapter 5 how the available BSM parameter space is tested in clean null-test observables. These are based on angular distributions and (approximate) symmetries of the SM, such as CP–conservation, LFU and cLFC. The main findings are summarized as follows, see also Sec. 5.5:

- Angular analysis exploits complementarity between contributions induced by different combinations of Wilson coefficients and between meson and baryon decays. Upper limits on $D^0 \to \ell^+\ell^-$ and angular observables in $D \to P\ell^+\ell^-$ test (pseudo-)scalar and (pseudo-)tensor Wilson coefficients and four angular observables from three- and four-body rare charm baryon decays, F_L, $A_{\rm FB}^{\ell}$, $A_{\rm FB}^{\rm H}$ and $A_{\rm FB}^{\ell{\rm H}}$, suffice to qualitatively disentangle NP contributions to the Wilson coefficients $C_7^{(\prime)}$, C_9' and $C_{10}^{(\prime)}$. This summarizes results presented in Figs. 5.2, 5.4, 5.5, 5.6, 5.7 and 5.8 and is discussed in Sec. 5.1.5.

- CP–asymmetries are resonance-enhanced and thus probe new sources of CP–violation in the resonance regions. Measurements of these CP–asymmetries in semileptonic rare charm decays might also help to interpret the NP nature of $\Delta A_{\rm CP}$, which quantifies the difference of direct CP–asymmetries of the decays $D^0 \to K^+K^-$ and $D^0 \to \pi^+\pi^-$, see Sec. 5.2.

- Direct probes of accidental SM lepton flavor symmetries, such as LFU and cLFC, are possible via ratios of branching fractions of rare charm decays into muons over electrons, Eq. (5.37), and searches for LFV decay modes, respectively. These clean null tests yield probes of the flavor structure realized in nature and complement similar searches in rare $b \to s\ell\ell^{(\prime)}$ transitions.

Chapter 6 globally investigates the interplay of dineutrino modes with charged lepton FCNC couplings via an $SU(2)_L$–link implied by LO contributions from SMEFT operators. Rare charm dineutrino modes are null tests of the SM due to the efficient GIM mechanism. In addition, Sec. 6.2 discloses the predictive power of the $SU(2)_L$–link. Upper limits on dineutrino branching ratios presented in Tab. 6.3 have been shown to indirectly probe LFU and cLFC and are suitable for current and future colliders, as illustrated in Fig. 6.3. These types of probes have even been proved to be useful beyond charm in other quark flavor sectors in Secs. 6.3 and 6.4. For rare B–decays, Fig. 6.4 shows the correlation of $B \to P\nu\bar{\nu}$ and $B \to V\nu\bar{\nu}$, which constitutes an indirect test of LFU, complementary to direct probes

in ratios of branching fractions, which currently point towards the breakdown of LFU. Furthermore, indirect upper limits on semileptonic branching ratios involving τ's have been obtained from upper limits on rare semileptonic dineutrino branching ratios of B–mesons. As for the other sectors, we have shown that rare kaon decays to dineutrinos strongly constrain LH charm couplings and future flavor probes of FCNC four-fermion operators involving top quarks are possible at current and future colliders, see Fig. 6.5 and discussion in Sec. 6.4.

By and large, rare charm decays offer the unique possibility to perform flavor tests of the SM with up-type FCNCs with present data. Alas, they are subject to a severe resonance dominance, which hinders reliable access to weak SM contributions and BSM physics in simple observables such as branching ratios. As we have demonstrated, null-test observables are able to overcome precisely this resonance dominance, with plenty of possibilities in angular distributions alone, and enriched with observables based on (approximate) symmetries of the SM, such as CP–conservation, LFU and cLFC. Systematically performing these types of tests in all quark and lepton flavor sectors of the SM allows to reveal the origin of flavor.

With upcoming experimental updates of $D^0 \to \ell^+\ell^-$, $D^+ \to \pi^+\ell^+\ell^-$, $\Lambda_c \to p\ell^+\ell^-$ ahead, where at least the latter two call for imminent detection, and with the recently published angular analyses of $D^0 \to \pi^+\pi^-\mu^+\mu^-$ and $D^0 \to K^+K^-\mu^+\mu^-$ at hand, the future experimental physics program for rare charm decays is excitingly gaining speed. The inclusion of polarization studies of Λ_c and triggers for more exotic rare charm baryon modes, including decays of Ξ_c^+, Ξ_c^0 and Ω_c^0, into future experimental programs is desirable. On the other hand, the results presented in this thesis and new data on $D^0 \to \pi^+\pi^-\mu^+\mu^-$ and $D^0 \to K^+K^-\mu^+\mu^-$ call for further theoretical studies and a first global fit of $c \to u\ell^+\ell^-$ Wilson coefficients.

To conclude this thesis, we note that the status of rare charm decays strongly benefits from the joint effort of experiment and theory now and in future, and rare charm decays have the potential to yield deeper and unique insights both into non-perturbative QCD dynamics and the NP nature of flavor in the up-quark sector.

A Parameters and experimental input

This appendix collects numerical values used as input throughout the thesis. Input for form factors and decay constants is discussed separately in App. C. Unless stated otherwise we provide upper limits at 90 % C.L. and add uncertainties σ_i in quadrature, $\sigma = \sqrt{\sum \sigma_i^2}$. Parameters are given within their 68 % C.L. region or only their central value whenever the numerical effect of the respective uncertainty is negligible. We further assume uncertainties to be uniformly distributed. We take experimental information on particle masses and total widths from [184], with $\Gamma = \frac{\hbar}{\tau}$ and τ the associated average lifetime, and the reduced Planck constant $\hbar = 6.582119569 \cdot 10^{-25}\,\text{GeV}\cdot\text{s}$.

$$
\begin{aligned}
m_{\pi^0} &= 0.1349768\,\text{GeV}\,, & \tau_{\pi^+} &= (8.43 \pm 0.13) \times 10^{-17}\,\text{s}\,,\\
m_{\pi^+} &= 0.13957039\,\text{GeV}\,, & \tau_{\pi^0} &= (2.6033 \pm 0.0005) \times 10^{-8}\,\text{s}\,,\\
\\
m_{\eta} &= 0.54782\,\text{GeV}\,, & \Gamma_{\eta} &= (1.31 \pm 0.05)\,\text{keV}\,,\\
m_{\rho^+} &= 0.77526\,\text{GeV}\,, & \Gamma_{\rho^+} &= (149.1 \pm 0.8)\,\text{MeV}\,,\\
m_{\rho^0} &= 0.77526\,\text{GeV}\,, & \Gamma_{\rho^0} &= (147.4 \pm 0.8)\,\text{MeV}\,,\\
m_{\omega} &= 0.78266\,\text{GeV}\,, & \Gamma_{\omega} &= (8.68 \pm 0.13)\,\text{MeV}\,,\\
m_{\eta'} &= 0.95778\,\text{GeV}\,, & \Gamma_{\eta'} &= (0.188 \pm 0.006)\,\text{MeV}\,,\\
m_{\phi} &= 1.019461\,\text{GeV}\,, & \Gamma_{\phi} &= (4.249 \pm 0.013)\,\text{MeV}\,,\\
\\
m_{K^0} &= 0.497611\,\text{GeV}\,, & \tau_{K_S} &= (8.954 \pm 0.004) \times 10^{-11}\,\text{s}\,,\\
& & \tau_{K_L} &= (5.116 \pm 0.021) \times 10^{-8}\,\text{s}\,,\\
\\
m_{K^\pm} &= 0.493677\,\text{GeV}\,, & \tau_{K^\pm} &= (1.238 \pm 0.002) \times 10^{-8}\,\text{s}\,,\\
m_{K^{0\star}} &= 0.89555\,\text{GeV}\,, & \Gamma_{K^{0\star}} &= (47.3 \pm 0.5)\,\text{MeV}\,,\\
m_{K^{\pm\star}} &= 0.89167\,\text{GeV}\,, & \Gamma_{K^{\pm\star}} &= (51.4 \pm 0.8)\,\text{MeV}\,,\\
\\
m_{D^0} &= 1.86484\,\text{GeV}\,, & \tau_{D^0} &= (4.101 \pm 0.015) \times 10^{-13}\,\text{s}\,,\\
m_{D^\pm} &= 1.86966\,\text{GeV}\,, & \tau_{D^\pm} &= (1.040 \pm 0.007) \times 10^{-12}\,\text{s}\,,\\
m_{D_s^\pm} &= 1.96835\,\text{GeV}\,, & \tau_{D_s^\pm} &= (5.04 \pm 0.04) \times 10^{-13}\,\text{s}\,,\\
\\
m_{B^0} &= 5.27965\,\text{GeV}\,, & \tau_{B^0} &= (1.519 \pm 0.004) \times 10^{-12}\,\text{s}\,,\\
m_{B^\pm} &= 5.27934\,\text{GeV}\,, & \tau_{B^\pm} &= (1.638 \pm 0.004) \times 10^{-12}\,\text{s}\,,\\
m_{B_s^0} &= 5.36688\,\text{GeV}\,, & \tau_{B_s^0} &= (1.52 \pm 0.06) \times 10^{-12}\,\text{s}\,,\\
\\
m_{e} &= 0.000511\,\text{GeV}\,,\\
m_{\mu} &= 0.106\,\text{GeV}\,,\\
m_{\tau} &= 1.777\,\text{GeV}\,.
\end{aligned}
\tag{A.1}
$$

For baryon masses and lifetimes, we use

$$\begin{aligned}
m_{\Lambda_c^+} &= (2.28646 \pm 0.00014)\,\text{GeV}\,, & \tau_{\Lambda_c^+} &= (2.024 \pm 0.031) \times 10^{-13}\,\text{s}\,,\\
m_{\Xi_c^+} &= (2.46771 \pm 0.00023)\,\text{GeV}\,, & \tau_{\Xi_c^+} &= (4.56 \pm 0.05) \times 10^{-13}\,\text{s}\,,\\
m_{\Xi_c^0} &= (2.47044 \pm 0.00028)\,\text{GeV}\,, & \tau_{\Xi_c^0} &= (1.53 \pm 0.06) \times 10^{-13}\,\text{s}\,,\\
m_{\Omega_c^0} &= (2.6952 \pm 0.0017)\,\text{GeV}\,, & \tau_{\Omega_c^0} &= (2.68 \pm 0.26) \times 10^{-13}\,\text{s}\,,
\end{aligned} \tag{A.2}$$

$$\begin{aligned}
m_p &= 0.938272\,\text{GeV}\,,\\
m_{\Sigma^+} &= (1.18937 \pm 0.00007)\,\text{GeV}\,,\\
m_{\Sigma^0} &= (1.192642 \pm 0.000024)\,\text{GeV}\,,\\
m_{\Lambda^0} &= (1.115683 \pm 0.000006)\,\text{GeV}\,,\\
m_{\Xi^0} &= (1.3149 \pm 0.0002)\,\text{GeV}\,.
\end{aligned}$$

For the calculation of the Wilson coefficients in Sec. 2.2.1 and App. B the following input has been used

$$\begin{aligned}
m_t(m_t) &= \left(162.5^{+2.1}_{-1.5}\right)\,\text{GeV}\,, & m_b(m_b) &= \left(4.18^{+0.03}_{-0.02}\right)\,\text{GeV}\,,\\
m_Z &= 91.19\,\text{GeV}\,, & m_c(m_c) &= (1.27 \pm 0.02)\,\text{GeV}\,,\\
m_W &= 80.4\,\text{GeV}\,, & m_s(2\,\text{GeV}) &= \left(0.093^{+0.011}_{-0.005}\right)\,\text{GeV}\,,
\end{aligned} \tag{A.3}$$

$$\begin{aligned}
\alpha_s(m_Z) &= 0.1182 \pm 0.0012\,, & G_F &= 1.1663787 \times 10^{-5}\,\text{GeV}^{-2}\,,\\
\alpha_e &= 7.29735257 \times 10^{-3}\,, & \sin^2\theta_W(m_Z) &= 0.23121\,.
\end{aligned}$$

Note that input in App. B taken from Ref. [86] uses the following pole masses for the quarks

$$m_b = 4.85\,\text{GeV}\,, \quad m_c = 1.47\,\text{GeV}\,, \quad m_s = 0.13\,\text{GeV}\,, \quad m_{u,\,d} \approx 0\,. \tag{A.4}$$

The running of α_s is handled with RunDec [286] and $m(\mu)$ denotes an $\overline{\text{MS}}$ mass.

The elements of the CKM matrix are obtained via the Wolfenstein parametrization as in Eq. (2.10). We follow Ref. [184] and use the most recent fit result of the CKMfitter group, see Ref. [287] and updates at http://ckmfitter.in2p3.fr

$$\begin{aligned}
\lambda &= 0.224837^{+0.000251}_{-0.0000060}\,, & A &= 0.8235^{+0.0056}_{-0.0145}\,,\\
\overline{\rho} &= 0.1569^{+0.0102}_{-0.0061}\,, & \overline{\eta} &= 0.3499^{+0.0079}_{-0.0065}\,.
\end{aligned} \tag{A.5}$$

Another fit result is available from the UTfit collaboration, see Ref. [288] and updates at http://www.utfit.org.

For the calculation of a_M parameters in Secs. 3.3.2 and 3.4, we use the following branching ratios

from Ref. [184]

$$\begin{aligned}
\mathcal{B}(D^+ \to \pi^+\eta) &= (3.77 \pm 0.09) \times 10^{-3}\,, & \mathcal{B}(D^0 \to \pi^0\eta) &= (6.3 \pm 0.6) \times 10^{-4}\,,\\
\mathcal{B}(D^+ \to \pi^+\eta') &= (4.97 \pm 0.19) \times 10^{-3}\,, & \mathcal{B}(D^0 \to \pi^0\eta') &= (9.2 \pm 1.0) \times 10^{-4}\,,\\
\mathcal{B}(D^+ \to \pi^+\rho) &= (8.3 \pm 1.5) \times 10^{-4}\,, & \mathcal{B}(D^0 \to \pi^0\rho) &= (3.86 \pm 0.23) \times 10^{-3}\,,\\
\mathcal{B}(D^+ \to \pi^+\omega) &= (2.8 \pm 0.6) \times 10^{-4}\,, & \mathcal{B}(D^0 \to \pi^0\omega) &= (1.17 \pm 0.35) \times 10^{-4}\,,\\
\mathcal{B}(D^+ \to \pi^+\phi) &= (5.6 \pm 0.2) \times 10^{-3}\,,
\end{aligned} \tag{A.6}$$

$$\begin{aligned}
\mathcal{B}(D_s^+ \to K^+\eta) &= (1.60 \pm 0.11) \times 10^{-3}\,, & \mathcal{B}(\eta \to \mu^+\mu^-) &= (5.8 \pm 0.8) \times 10^{-6}\,,\\
\mathcal{B}(D_s^+ \to K^+\eta') &= (2.65 \pm 0.25) \times 10^{-3}\,, & \mathcal{B}(\rho \to \mu^+\mu^-) &= (4.55 \pm 0.28) \times 10^{-5}\,,\\
\mathcal{B}(D_s^+ \to K^+\rho) &= (2.5 \pm 0.4) \times 10^{-3}\,, & \mathcal{B}(\omega \to \mu^+\mu^-) &= (7.4 \pm 1.8) \times 10^{-5}\,,\\
\mathcal{B}(D_s^+ \to K^+\omega) &= (8.7 \pm 2.5) \times 10^{-4}\,, & \mathcal{B}(\phi \to \mu^+\mu^-) &= (2.86 \pm 0.19) \times 10^{-4}\,.
\end{aligned}$$

For $\mathcal{B}(\eta' \to \mu^+\mu^-)$ the branching ratio is not measured yet. In Ref. [289] the authors even propose to measure it via investigations of rare charm decays. We follow Ref. [290] and estimate from unitarity

$$\mathcal{B}(\eta' \to \mu\mu) \sim \mathcal{B}(\eta' \to \gamma\gamma)\frac{\alpha_e}{2}\frac{\beta}{\sqrt{1-4\beta}} \times \ln^2\left[\frac{1+\sqrt{1-4\beta}}{1-\sqrt{1-4\beta}}\right] \sim 10^{-7}\,, \tag{A.7}$$

with $\beta = m_\mu^2/m_{\eta'}^2$ and $\mathcal{B}(\eta' \to \gamma\gamma) = (2.307 \pm 0.033)\,\%$ [184]. Eq. (A.7) evaluated for η yields $\mathcal{B}(\eta \to \mu^+\mu^-) \sim 4.4 \times 10^{-6}$ in good agreement with the direct measurement, see Eq. (A.6). The estimate in Eq. (A.7) also agrees with Refs. [289, 291].

In addition, we can use [184]

$$\begin{aligned}
\mathcal{B}(D^0 \to \pi^0\phi(\to K^+K^-)) &= (6.6 \pm 0.4) \times 10^{-4}\,,\\
\mathcal{B}(D_s^+ \to K^+\phi(\to K^+K^-)) &= (8.8 \pm 2.0) \times 10^{-5}\,,
\end{aligned} \tag{A.8}$$

and

$$\mathcal{B}(D \to P\phi) = \frac{\mathcal{B}(D \to P\phi(\to K^+K^-))}{\mathcal{B}(\phi \to K^+K^-)}\,, \qquad \mathcal{B}(\phi \to K^+K^-) = (0.492 \pm 0.005)\,. \tag{A.9}$$

And similarly for the baryons [184]

$$\begin{aligned}
\mathcal{B}(\Lambda_c^+ \to p\eta) &= (1.24 \pm 0.3) \times 10^{-3}\,, & \mathcal{B}(\Lambda_c^+ \to p\omega) &= (8 \pm 1) \times 10^{-4}\ \ [292]\,,\\
\mathcal{B}(\Lambda_c^+ \to p\eta') &= (4.73 \pm 0.98) \times 10^{-4}\ \ [187]\,, & \mathcal{B}(\Lambda_c^+ \to p\phi) &= (1.06 \pm 0.14) \times 10^{-3}\,,\\
\mathcal{B}(\Xi_c^0 \to \Lambda^0\phi) &= (4.9 \pm 1.5) \times 10^{-4}\,,
\end{aligned} \tag{A.10}$$

where the η' and ω have recently been updated by the Belle collaboration [187, 292] and are not yet included in Ref. [184].

B Details on Standard Model Wilson coefficients at the charm scale

In this appendix, we provide further input explicit expressions for the calculation of C_7^{eff} and C_9^{eff} in Eq. (2.25). First, we display in Tabs. B.1, B.2 and B.3 the individual numerical values for Wilson coefficients $\tilde{C}_j^{(i)}(\mu)$ including the charm scale variation with $(i) = (0)$, (1), (2) and $j \in [1, 10]$, where the separation and notation into LO, NLO and NNLO contribution follows Eq. (2.22).

Table B.1: LO SM Wilson coefficients $\tilde{C}_j^{(0)}(\mu)$ for $j \in [1, 10]$. In the first three columns we display the values obtained for the three different choices of the charm mass scale $\mu = \sqrt{2}\, m_c$, $\mu = m_c$ and $\mu = m_c/\sqrt{2}$. The last column gives the central value and symmetrized uncertainty and is used as an input to further calculations, see main text.

	$\mu = \sqrt{2}\, m_c$	$\mu = m_c$	$\mu = m_c/\sqrt{2}$	$\tilde{C}_j^{(0)}$	$\pm$	$\Delta\tilde{C}_j^{(0)}$
$\tilde{C}_1(\mu)$	−0.84817	−1.04210	−1.31824	−1.04	$\pm$	0.24
$\tilde{C}_2(\mu)$	1.06571	1.09488	1.14274	1.09	$\pm$	0.04
$\tilde{C}_3(\mu)$	−0.00150	−0.00384	−0.00893	−0.0038	$\pm$	0.0037
$\tilde{C}_4(\mu)$	−0.03607	−0.06246	−0.10564	0.06	$\pm$	0.04
$\tilde{C}_5(\mu)$	0.00004	0.00037	0.00085	0.00037	$\pm$	0.00041
$\tilde{C}_6(\mu)$	0.00029	0.00077	0.00185	0.00077	$\pm$	0.00078
$\tilde{C}_7(\mu)$	0.00000	0.00000	0.00000	0	$\pm$	0
$\tilde{C}_8(\mu)$	0.00000	0.00000	0.00000	0	$\pm$	0
$\tilde{C}_9(\mu)$	−0.00233	−0.00303	−0.00296	−0.0030	$\pm$	0.0003
$\tilde{C}_{10}(\mu)$	0.00000	0.00000	0.00000	0	$\pm$	0

Table B.2: Same as Tab. B.1, but for NLO: $\frac{\alpha_s(\mu)}{4\pi}\tilde{C}_j^{(1)}(\mu)$ for $j \in [1, 10]$.

	$\mu = \sqrt{2}\, m_c$	$\mu = m_c$	$\mu = m_c/\sqrt{2}$	$(\tilde{C}_j$	$\pm$	$\Delta\tilde{C}_j) \cdot \frac{\alpha_s(\mu)}{4\pi}$
$\tilde{C}_1(\mu)$	0.27648	0.32393	0.40323	0.324	$\pm$	0.063
$\tilde{C}_2(\mu)$	−0.03895	−0.05609	−0.08814	−0.056	$\pm$	0.025
$\tilde{C}_3(\mu)$	−0.00111	−0.00258	−0.00600	−0.0026	$\pm$	0.0024
$\tilde{C}_4(\mu)$	−0.02228	−0.03201	−0.05426	0.032	$\pm$	0.016
$\tilde{C}_5(\mu)$	0.00000	0.00004	0.00016	0.00004	$\pm$	0.00008
$\tilde{C}_6(\mu)$	−0.00023	−0.00020	0.00026	−0.0002	$\pm$	0.0003
$\tilde{C}_7(\mu)$	0.00194	0.00364	0.00677	0.0036	$\pm$	0.0024
$\tilde{C}_8(\mu)$	−0.00112	−0.00206	−0.00383	−0.002	$\pm$	0.0014
$\tilde{C}_9(\mu)$	−0.00416	−0.00651	−0.01059	−0.0065	$\pm$	0.0032
$\tilde{C}_{10}(\mu)$	0.00000	0.00000	0.00000	0	$\pm$	0

Table B.3: Same as Tab. B.1, but for NNLO: $\frac{\alpha_s^2(\mu)}{(4\pi)^2}\tilde{C}_j^{(2)}(\mu)$ for $j \in [1, 10]$.

	$\mu = \sqrt{2}\, m_c$	$\mu = m_c$	$\mu = m_c/\sqrt{2}$	$(\tilde{C}_j^{(2)}$	$\pm$	$\Delta\tilde{C}_j^{(2)}) \cdot \frac{\alpha_s^2(\mu)}{(4\pi)^2}$
$\tilde{C}_1(\mu)$	0.05582	0.07794	0.12482	0.078	$\pm$	0.035
$\tilde{C}_2(\mu)$	−0.00108	−0.00390	−0.01150	−0.0039	$\pm$	0.0052
$\tilde{C}_3(\mu)$	−0.00112	−0.00199	−0.00351	−0.0020	$\pm$	0.0012
$\tilde{C}_4(\mu)$	0.00003	−0.00087	−0.00504	−0.00087	$\pm$	0.0025
$\tilde{C}_5(\mu)$	0.00007	0.00010	0.00011	0.00010	$\pm$	0.00002
$\tilde{C}_6(\mu)$	0.00013	0.00034	0.00100	0.00034	$\pm$	0.00043
$\tilde{C}_7(\mu)$	0.00010	0.00018	0.00034	0.00018	$\pm$	0.00012
$\tilde{C}_8(\mu)$	−0.00015	−0.00033	−0.00080	−0.00033	$\pm$	0.0003
$\tilde{C}_9(\mu)$	−0.00185	−0.00376	−0.00787	−0.0038	$\pm$	0.0030
$\tilde{C}_{10}(\mu)$	0.00000	0.00000	0.00000	0	$\pm$	0

In Sec. 2.2.1 we discussed the SM contributions to the phenomenological basis, which can compactly be encoded in

$$C_{7,9}^{\text{eff}} = \frac{4\pi}{\alpha_s}\left[V_{cd}^* V_{ud}\, C_{7,9}^{\text{eff}(d)}(q^2) \,+\, V_{cs}^* V_{us}\, C_{7,9}^{\text{eff}(s)}(q^2)\right] . \tag{B.1}$$

We now follow Ref. [166] and give explicit expressions for the effective coefficients $C_{7,9}^{\text{eff}(q)}$, where the results of Tabs. B.1, B.2 and B.3 can be used as an input. We use the notation $\tilde{C}_i^{(0)+(1)} = \tilde{C}_i^{(0)} + \frac{\alpha_s(\mu)}{4\pi}\tilde{C}_i^{(1)}$ and analogous for other orders in agreement with Eq. (2.22). Note that entries in Tabs. B.1, B.2 and B.3 already include the factors $\frac{\alpha_s(\mu)}{4\pi}$, such that $\tilde{C}_i^{(0)+(1)}$ is obtained as the sum of the entries for $\tilde{C}_i$ in Tab. B.1 and B.2. Utilizing this notation one obtains

$$\begin{aligned} C_7^{\text{eff}(q)}(q^2) = \tilde{C}_7^{(0+1+2)} &+ \frac{\alpha_s}{4\pi}\left[\frac{2}{3}\tilde{C}_3 + \frac{8}{9}\tilde{C}_4 + \frac{40}{3}\tilde{C}_5 + \frac{160}{9}\tilde{C}_6\right]^{(0+1)} \\ &+ \left(\frac{\alpha_s}{4\pi}\right)^2\left[\left(-\frac{1}{6}\tilde{C}_1^{(0)} + \tilde{C}_2^{(0)}\right) F_{2,q}^{(7)}(m_c^2, q^2) + F_8^{(7)}(m_c^2, q^2)\, C_8^{\text{eff}}\right], \end{aligned} \tag{B.2}$$

$$C_8^{\text{eff}} = \tilde{C}_8^{(0)+(1)} \quad + \tilde{C}_3^{(0)} - \frac{1}{6}\tilde{C}_4^{(0)} + 20\,\tilde{C}_5^{(0)} - \frac{10}{3}\tilde{C}_6^{(0)} , \tag{B.3}$$

$$
\begin{aligned}
C_9^{\mathrm{eff}(q)}(q^2) = \tilde{C}_9^{(0+1+2)} &+ \frac{\alpha_s}{4\pi}\Bigg[\frac{8}{27}\tilde{C}_1 + \frac{2}{9}\tilde{C}_2 - \frac{8}{9}\tilde{C}_3 - \frac{32}{27}\tilde{C}_4 - \frac{128}{9}\tilde{C}_5 - \frac{512}{27}\tilde{C}_6 \\
&+ L(m_c^2,q^2)\left(\frac{28}{9}\tilde{C}_3 + \frac{16}{27}\tilde{C}_4 + \frac{304}{9}\tilde{C}_5 + \frac{256}{27}\tilde{C}_6\right) \\
&+ L(m_s^2,q^2)\left(-\frac{4}{3}\tilde{C}_3 - \frac{40}{3}\tilde{C}_5\right) \\
&+ L(0,q^2)\left(\frac{16}{9}\tilde{C}_3 + \frac{16}{27}\tilde{C}_4 + \frac{184}{9}\tilde{C}_5 + \frac{256}{27}\tilde{C}_6\right) \\
&+ \left(\delta_{qs}L(m_s^2,q^2) + \delta_{qd}L(0,q^2)\right)\left(-\frac{8}{27}\tilde{C}_1 - \frac{2}{9}\tilde{C}_2\right)\Bigg]^{(0+1)} \\
&+ \left(\frac{\alpha_s}{4\pi}\right)^2\left[F_{1,q}^{(9)}(m_c^2,q^2)\,\tilde{C}_1^{(0)} + F_{2,q}^{(9)}(m_c^2,q^2)\,\tilde{C}_2^{(0)} + F_8^{(9)}(m_c^2,q^2)\,C_8^{\mathrm{eff}}\right].
\end{aligned}
\tag{B.4}
$$

The various q^2 depending functions appearing in Eqs. (B.2), (B.3) and (B.4) are defined as [166]

$$
\begin{aligned}
L(m^2,q^2) &= \frac{5}{3} + \ln\frac{\mu_c^2}{m^2} + x - \frac{1}{2}(2+x)|1-x|^{1/2}\begin{cases}\ln\frac{1+\sqrt{1-x}}{1-\sqrt{1-x}} - \mathrm{i}\pi & x \equiv \frac{(2m)^2}{q^2} < 1 \\ 2\tan^{-1}\left[\frac{1}{\sqrt{x-1}}\right] & x \equiv \frac{(2m)^2}{q^2} > 1\end{cases}, \\
L(0,q^2) &= \frac{5}{3} + \ln\frac{\mu_c^2}{q^2} + \mathrm{i}\pi\,,
\end{aligned}
\tag{B.5}
$$

and $F_8^{(7)}(m_c^2,q^2) = F_8^{(7)}(\rho = q^2/m_c^2)$, $F_8^{(9)}(m_c^2,q^2) = F_8^{(9)}(\rho = q^2/m_c^2)$ from [166, 293] with

$$
\begin{aligned}
F_8^{(7)}(\rho) &= \frac{8\pi^2}{27}\frac{(2+\rho)}{(1-\rho)^4} - \frac{8}{9}\frac{(11-16\rho+8\rho^2)}{(1-\rho)^2} - \frac{16}{9}\frac{\sqrt{\rho}\sqrt{4-\rho}}{(1-\rho)^3}\,(9-5\rho+2\rho^2)\arcsin\frac{\sqrt{\rho}}{2} \\
&\quad - \frac{32}{3}\frac{(2+\rho)}{(1-\rho)^4}\arcsin^2\frac{\sqrt{\rho}}{2} - \frac{16}{9}\frac{\rho}{(1-\rho)}\ln\rho - \frac{32}{9}\ln\frac{\mu_c^2}{m_c^2} - \frac{16}{9}\,\mathrm{i}\,\pi\,, \\
F_8^{(9)}(\rho) &= -\frac{16\pi^2}{27}\frac{(4-\rho)}{(1-\rho)^4} + \frac{16}{9}\frac{(5-2\rho)}{(1-\rho)^2} + \frac{32}{9}\frac{\sqrt{4-\rho}}{\sqrt{\rho}(1-\rho)^3}\,(4+3\rho-\rho^2)\arcsin\frac{\sqrt{\rho}}{2} \\
&\quad + \frac{64}{3}\frac{(4-\rho)}{(1-\rho)^4}\arcsin^2\frac{\sqrt{\rho}}{2} + \frac{32}{9}\frac{1}{(1-\rho)}\ln\rho\,.
\end{aligned}
\tag{B.6}
$$

For the functions $F_{1,q}^{(9)}$, $F_{2,q}^{(9)}$ and $F_{2,q}^{(7)}$ we use supplementary files of Ref. [86], where fits are provided, which we implement in a *python* script.

C Form factors and decay constants

In this appendix, we collect numerical values and additional information on form factors and decay constants utilized throughout this thesis.

Decay constants are calculated in LQCD with averaged values presented in recent dedicated reviews [294, 295]. These results are in agreement with averages provided in [184] and read

$$\begin{aligned} f_\pi &= (130.2 \pm 1.2)\,\text{MeV}\,, & f_D &= (212.0 \pm 0.7)\,\text{MeV}\,, & f_B &= (190.0 \pm 1.3)\,\text{MeV}\,, \\ f_{K^+} &= (155.7 \pm 0.3)\,\text{MeV}\,, & f_{D_s^+} &= (249.9 \pm 0.5)\,\text{MeV}\,, & f_{B_s^0} &= (230.0 \pm 1.3)\,\text{MeV}\,. \end{aligned} \tag{C.1}$$

In Eq. (C.1) f_π, f_D and f_B are valid in the isospin symmetric limit and are thus used for the charged and the neutral pion, D–meson and B–meson, respectively, see discussion in Ref. [184] and references therein. We discussed form factor input for $D^{+\,(0)} \to \pi^{+\,(0)}$ and $D_s^+ \to K$ transitions in Sec. 3.3.1 based on results in Refs. [179, 180]. We also use input from the same references for f_0 in the $D \to K$ transition for fitting the SM decay amplitude $D^0 \to K^+K^-$, see App. D.3. It is parametrized as

$$f_0^{D\to K}(q^2) = f_0^{D\to K}(0) + c_0^{D\to K}\,(z - z_0)\left(1 + \frac{z + z_0}{2}\right). \tag{C.2}$$

For completeness we collect numerical values for the form factor parameters taken from Refs. [179, 180],

$$\begin{aligned} f_+^{D\to\pi}(0) &= 0.6117 \pm 0.0354\,, & c_+^{D\to\pi} &= -1.985 \pm 0.347\,, & P_+^{D\to\pi} &= (0.1314 \pm 0.127)\,\text{GeV}^{-2}\,, \\ f_0^{D\to\pi}(0) &= 0.6117 \pm 0.0354\,, & c_0^{D\to\pi} &= -1.188 \pm 0.256\,, & P_0^{D\to\pi} &= (0.0342 \pm 0.122)\,\text{GeV}^{-2}\,, \\ f_T^{D\to\pi}(0) &= 0.5063 \pm 0.0786\,, & c_T^{D\to\pi} &= -1.10 \pm 1.03\,, & P_T^{D\to\pi} &= (0.1461 \pm 0.681)\,\text{GeV}^{-2}\,. \\ f_0^{D\to K}(0) &= 0.7647 \pm 0.0308\,, & c_0^{D\to K} &= -2.084 \pm 0.283\,, \end{aligned} \tag{C.3}$$

Note that covariance matrices are given in Refs. [179, 180] and included in our analyses.

Similarly, the baryon form factors for the $\Lambda_c \to p$ transition can be inferred from Ref. [103]. Here, the helicity-based definition is used and reads

$$\begin{aligned} \langle p(k,\, s_p)|\overline{u}\gamma^\mu c|\Lambda_c(p,\, s_{\Lambda_c})\rangle = \\ \overline{u}_p(k,\, s_p)\left[f_0(q^2)\,(m_{\Lambda_c} - m_p)\,\frac{q^\mu}{q^2} + f_+(q^2)\,\frac{m_{\Lambda_c} + m_p}{s_+}\left(p^\mu + k^\mu - (m_{\Lambda_c} - m_p)\frac{q^\mu}{q^2}\right)\right. \\ \left. + f_\perp(q^2)\left(\gamma^\mu - \frac{2m_p}{s_+}\,p^\mu - \frac{2m_{\Lambda_c}}{s_+}\,k^\mu\right)\right] u_{\Lambda_c}(p,\, s_{\Lambda_c})\,, \end{aligned} \tag{C.4}$$

$$\begin{aligned}\langle p(k,\,s_p)|\overline{u}\gamma^\mu\gamma_5 c|\Lambda_c(p,\,s_{\Lambda_c})\rangle =\\ -\overline{u}_p(k,\,s_p)\gamma_5\left[g_0(q^2)\,(m_{\Lambda_c}+m_p)\,\frac{q^\mu}{q^2}\right. &+g_+(q^2)\,\frac{m_{\Lambda_c}-m_p}{s_-}\,\left(p^\mu+k^\mu-(m_{\Lambda_c}-m_p)\frac{q^\mu}{q^2}\right)\\ &\left.+g_\perp(q^2)\,\left(\gamma^\mu+\frac{2m_p}{s_-}\,p^\mu-\frac{2m_{\Lambda_c}}{s_-}\,k^\mu\right)\right]u_{\Lambda_c}(p,\,s_{\Lambda_c})\,,\end{aligned} \tag{C.5}$$

$$\begin{aligned}\langle p(k,\,s_p)|\overline{u}\mathrm{i}\sigma^{\mu\nu}q_\nu c|\Lambda_c(p,\,s_{\Lambda_c})\rangle =\\ -\overline{u}_p(k,\,s_p)\left[h_+(q^2)\frac{q^2}{s_+}\left(p^\mu+k^\mu-(m_{\Lambda_c}^2-m_p^2)\frac{q^\mu}{q^2}\right)\right.\\ \left.+h_\perp(q^2)(m_{\Lambda_c}+m_p)\left(\gamma^\mu-\frac{2m_p}{s_+}\,p^\mu-\frac{2m_{\Lambda_c}}{s_+}\,k^\mu\right)\right]u_{\Lambda_c}(p,\,s_{\Lambda_c})\,,\end{aligned} \tag{C.6}$$

$$\begin{aligned}\langle p(k,\,s_p)|\overline{u}\mathrm{i}\sigma^{\mu\nu}q_\nu\gamma_5 c|\Lambda_c(p,\,s_{\Lambda_c})\rangle =\\ -\overline{u}_p(k,\,s_p)\gamma_5\left[\tilde{h}_+(q^2)\frac{q^2}{s_-}\left(p^\mu+k^\mu-(m_{\Lambda_c}^2-m_p^2)\frac{q^\mu}{q^2}\right)\right.\\ \left.+\tilde{h}_\perp(q^2)(m_{\Lambda_c}-m_p)\left(\gamma^\mu+\frac{2m_p}{s_-}\,p^\mu-\frac{2m_{\Lambda_c}}{s_-}\,k^\mu\right)\right]u_{\Lambda_c}(p,\,s_{\Lambda_c})\,.\end{aligned} \tag{C.7}$$

The following endpoint relations hold for these form factors

$$\begin{aligned} f_0(0) &= f_+(0)\,, & g_\perp(q^2_{\rm max}) &= g_+(q^2_{\rm max})\,,\\ g_0(0) &= g_+(0)\,, & \tilde{h}_\perp(q^2_{\rm max}) &= \tilde{h}_+(q^2_{\rm max})\,.\\ h_\perp(0) &= \tilde{h}_\perp(0)\,, \end{aligned} \tag{C.8}$$

The third relation at $q^2=0$ between the dipole form factors $h_\perp, \tilde{h}_\perp$ follows from $\sigma^{\mu\nu}\gamma_5 = -i/2\epsilon^{\mu\nu\alpha\beta}\sigma_{\alpha\beta}$, and is in agreement with [248, 296], where, however, different form factor parametrizations are employed. Although this relation is missing in the fit in [103], the relation is numerically satisfied within uncertainties $h_\perp(0) = 0.511 \pm 0.027$, $\tilde{h}_\perp(0) = 0.51 \pm 0.05$.

Again, numerical values and correlation matrices for form factor parameters are given in [103] and

Table C.1: m^f_{pole} masses and quantum numbers of the D–mesons producing poles for different form factors. Table taken from [103].

f	J^P	m^f_{pole} [GeV]
f_+, $f_\perp$, h_+, $h_\perp$	1^-	2.010
f_0	0^+	2.351
g_+, $g_\perp$, $\tilde{h}_+$, $\tilde{h}_\perp$	1^+	2.423
g_0	0^-	1.870

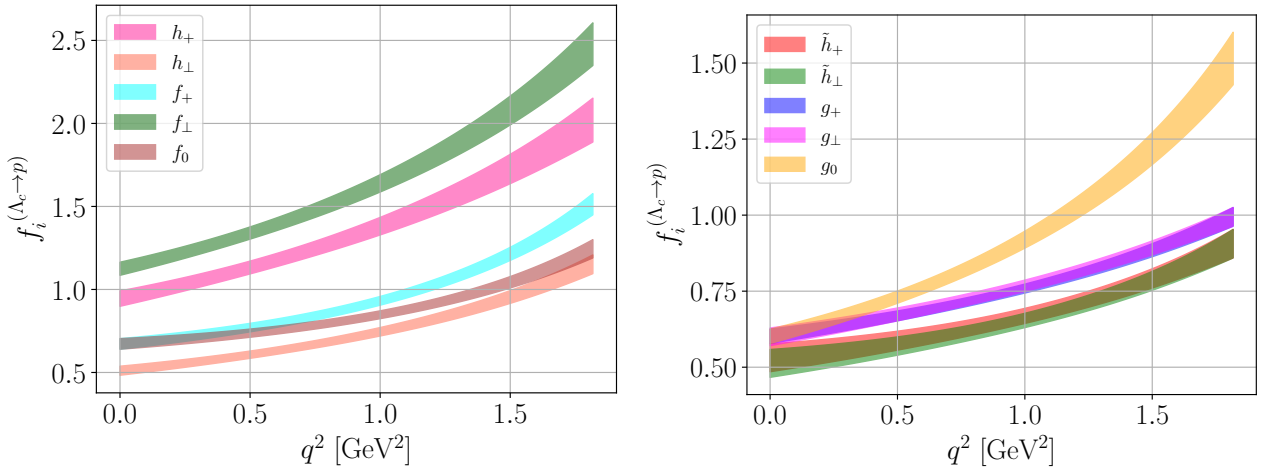

Figure C.1: The $\Lambda_c \to p$ form factors from LQCD [103] with 1σ uncertainties split into h_+, $h_\perp$, f_+, $f_\perp$, f_0 in the left plot and $\tilde{h}_+$, $\tilde{h}_\perp$, g_+, $g_\perp$, g_0 in the right plot, see text for details.

supplemented files, using the following z-expansion

$$f_i(q^2) = \frac{1}{1 - q^2/(m^f_{\text{pole}})^2} \sum_{n=0}^{2} a^f_n \left[z(q^2)\right]^n , \qquad z(q^2) = \frac{\sqrt{t_+ - q^2} - \sqrt{t_+ - t_0}}{\sqrt{t_+ - q^2} + \sqrt{t_+ - t_0}} , \tag{C.9}$$

with $t_+ = (m_D + m_\pi)^2$ and $t_0 = (m_{\Lambda_c} - m_p)^2$. The value of m^f_{pole} needs to be picked differently for each form factor according to Tab. C.1.

Resulting form factors are shown in Fig. C.1. In addition, we use the same input for rare charm baryon decays other than the Λ_c with the following modifications

- Replacements of masses in the definitions of the form factors Eqs. (C.4)-(C.7) and t_0 in the z-expansion in Eq. (C.9) are understood.
- We use flavor symmetries to employ the $\Lambda_c \to p$ form factors to all other modes. Here, we use that

any $\bar{u}c$-type current conserves U–spin and violates isospin by $|\Delta I| = \frac{1}{2}$. Then $\Xi_c^+ \to \Sigma^+$ is related by U–spin to $\Lambda_c \to p$, $\Xi_c^0 \to \Sigma^0$ receives an additional $\frac{1}{\sqrt{2}}$ factor with respect to $\Xi_c^+ \to \Sigma^+$, due to isospin and again from U–spin $\Xi_c^0 \to \Sigma^0$ and $\Xi_c^0 \to \Lambda^0$ are related with a relative factor of $\frac{1}{\sqrt{3}}$ [297, 298]. Only the $\Omega_c^0 \to \Xi^0$ is not connected to the other modes, as it sits in another multiplet. As pointed out already in Sec. 3.4, the decays $\Xi_c'^+ \to \Sigma^+\ell^+\ell^+$ and $\Xi_c'^0 \to \Lambda^0\ell^+\ell^-$ are also possible rare charm baryon decays and are connected to the Ω_c^0 decay via flavor symmetries. They are, however, not studied here, as their lifetimes remain unknown. Due to the lack of further input we assume the same form factors for $\Omega_c^0 \to \Xi^0$ as for $\Lambda_c \to p$. In summary, we use for any of the ten form factors $f_i(q^2), g_i(q^2), i = +, \perp, 0$ and $h_j(q^2), \tilde{h}_j(q^2), j = +, \perp$, commonly denoted as $f_{B_0 \to B_1}$

$$f_{\Lambda_c \to p} = f_{\Xi_c^+ \to \Sigma^+} = \sqrt{2} f_{\Xi_c^0 \to \Sigma^0} = \sqrt{6} f_{\Xi_c^0 \to \Lambda^0} \simeq f_{\Omega_c^0 \to \Xi^0} \,. \tag{C.10}$$

For further details on these flavor relations we refer to Ref. [112].

- We explicitly checked that available predictions for $f_{\Xi_c^0 \to \Sigma^0}$ from Table 9 of [189] are consistent with our framework within 30 % flavor breaking.

- We use the same flavor factors as in Eq. (C.10) in the calculation of the resonance parameters a_M in Tab. 3.3, *i.e.* we estimate branching ratios of the form $\mathcal{B}(B_0 \to B_1 M)$ with $M = \rho, \omega, \phi, \eta, \eta'$ assuming two-body phase space and a single dominant decay amplitude, which we take to be the same as for $\mathcal{B}(\Lambda_c \to pM)$ except for the correction factor from flavor symmetries.

In Sec. 6.2 the aforementioned form factors and decay constants are also used. In addition, for $D^0 \to P_1 P_2$ transitions, transversity form factors are needed. These can be expressed in terms of three heavy hadron chiral perturbation theory (HHχPT) form factors $\omega_\pm$ and h, as [88, 299]

$$\begin{aligned} \mathcal{F}_0 &= \frac{\mathcal{N}_{\rm nr}}{2} \left[\sqrt{\lambda}\, \omega_+ + \frac{\omega_-}{p^2} \left[(m_{P_1}^2 - m_{P_2}^2)\sqrt{\lambda} - (m_D^2 - q^2 - p^2)\sqrt{\lambda_p}\, \cos\theta_{P_1} \right] \right], \\ \mathcal{F}_\parallel &= \mathcal{N}_{\rm nr} \sqrt{\lambda_p \frac{q^2}{p^2}}\, \omega_- \,, \qquad \mathcal{F}_\perp = \frac{\mathcal{N}_{\rm nr}}{2} \sqrt{\lambda \lambda_p \frac{q^2}{p^2}}\, h \,, \qquad \mathcal{N}_{\rm nr} = \frac{G_{\rm F}\, \alpha_e}{2^7\, \pi^4\, m_D} \sqrt{\pi \frac{\sqrt{\lambda\, \lambda_p}}{m_D\, p^2}} \,, \end{aligned} \tag{C.11}$$

where $\lambda = \lambda(m_D^2, q^2, p^2)$, $\lambda_p = \lambda(p^2, m_{P_1}^2, m_{P_2}^2)$ and

$$\omega_\pm = \pm \frac{\hat{g}}{2} \frac{f_D}{f_{P_1}^2} \frac{m_D}{v \cdot p_{P_1} + \Delta} \,, \qquad h = \frac{\hat{g}^2}{2} \frac{f_D}{f_{P_1}^2} \frac{1}{(v \cdot p_{P_1} + \Delta)\,(v \cdot p + \Delta)} \,. \tag{C.12}$$

We further use $\Delta = (m_{D^{*0}} - m_{D^0})$, $\hat{g} = 0.570 \pm 0.006$ [300] and the dot products

$$\begin{aligned} v \cdot p_{P_1} &= \frac{1}{4\, m_D} \left((m_D^2 - q^2 + p^2) - \sqrt{\lambda(m_D^2,\, q^2,\, p^2) \left(1 - \frac{4\, m_{P_1}^2}{p^2}\right)} \cos\theta_{P_1} \right), \\ v \cdot p &= \frac{m_D^2 - q^2 + p^2}{2\, m_D}\,. \end{aligned} \tag{C.13}$$

Again an isospin factors of $1/\sqrt{2}$ is understood to be multiplied to the form factors for each π^0 in the final state, *i.e.* with the statistical factor for identical particles, the $D^0 \to \pi^0\pi^0\nu\bar{\nu}$ mode receives an overall suppression by 1/2 with respect to $D^0 \to \pi^+\pi^-\nu\bar{\nu}$ in the isospin limit.

In Sec. 6.3 several form factors are needed for $b \to q$ transitions with $q = d,\, s$. Here, we write any form factor, denoted by $\mathcal{F}$ as [142]

$$\mathcal{F}(q^2) = \frac{1}{1 - \frac{q^2}{m_{R_\mathcal{F}}^2}} \sum_{k=0}^{2} \alpha_k^{(\mathcal{F})} \left[z(q^2) - z(0) \right]^2 \,, \quad z(q^2) = \frac{\sqrt{t_+ - q^2} - \sqrt{t_+ - t_0}}{\sqrt{t_+ - q^2} + \sqrt{t_+ - t_0}}\,, \tag{C.14}$$

with $t_\pm = (m_B \pm m_{P,V})^2$ and $t_0 = t_+(1 - \sqrt{1 - t_-/t_+})$. Again, $m_{R_\mathcal{F}}$ represents the mass of the first sub-threshold resonance compatible with the quantum numbers of the form factor $\mathcal{F}$ and we use the values of $m_{R_\mathcal{F}}$ given in Refs. [142, 144]. Refs. [142, 144] both perform simultaneous fits of LCSR and LQCD data and central values for $\alpha_k^{(\mathcal{F})}$ as well as uncertainties and correlation matrices for each form factor $\mathcal{F}$ are given in supplemented files.

For the $B \to \pi$ tensor form factor no lattice results were included in Ref. [144]. A update for all three $B \to \pi$ form factors including LQCD and LCSR is given in Ref. [301], however not used here as the tensor form factor does not contribute to dineutrino observables. For $B \to \rho$ a simultaneous fit of LQCD and LCSR is also missing in Refs. [142, 144]. We perform a fit using LCSR input from Ref. [144] and available LQCD data from the SPQcdR [302] and UKQCD [303] collaborations. We refer to Ref. [7] and ancillary files for further details and fit results.

D Details on anomaly-free flavorful $Z^{'}$–models

This appendix extends the framework discussed in Sec. 4.3. We discuss anomaly cancellation conditions in App. D.1. The calculation of constraints from $D^0 - \overline{D}^0$ mixing is outlined in App. D.2. We further provide supplementing details on the calculation of Z'–contributions to $\Delta A_{\rm CP}$ and other CP–asymmetries in hadronic decays in App. D.3. Finally, App. D.4 also presents a figure similar to Fig. 5.14, but for different charge assignments, *i.e.* different solutions to anomaly cancellation conditions from Tab. D.1.

D.1 Anomaly cancellation conditions

Anomaly-free Z'–extensions of the SM with generation-dependent $U(1)'$–charges F_{ψ_i} for quarks and leptons $\psi = Q, u, d, L, e, \nu$ are built in the following way. SM fields have representations under $SU(3)_C \times SU(2)_L \times U(1)_Y \times U(1)'$

$$\begin{aligned} Q_i &\sim (3, 2, 1/6, F_{Q_i})\,, \quad u_i \sim (3, 1, 2/3, F_{u_i})\,, \quad d_i \sim (3, 1, -1/3, F_{d_i})\,, \\ L_i &\sim (1, 2, -1/2, F_{L_i})\,, \quad e_i \sim (1, 1, -1, F_{e_i})\,, \quad \nu_i \sim (1, 1, 0, F_{\nu_i})\,, \end{aligned} \tag{D.1}$$

where we allow three RH neutrinos ν as SM singlets, however charged under $U(1)'$. The charges F_{ψ_i} are subject to constraints from gauge anomaly cancellation conditions, see Ref. [244] for an introduction and Refs. [238, 243, 304–306] for recent phenomenological applications. Following [304], the anomaly cancellation conditions read:

$$\begin{aligned} SU(3)_C^2 \times U(1)_F' &: \quad \sum_{i=1}^{3} \left(2F_{Q_i} - F_{u_i} - F_{d_i}\right) = 0\,, \\ SU(2)_L^2 \times U(1)_F' &: \quad \sum_{i=1}^{3} \left(3F_{Q_i} + F_{L_i}\right) = 0\,, \\ U(1)_Y^2 \times U(1)_F' &: \quad \sum_{i=1}^{3} \left(F_{Q_i} + 3F_{L_i} - 8F_{u_i} - 2F_{d_i} - 6F_{e_i}\right) = 0\,, \\ \text{gauge-gravity:} &: \quad \sum_{i=1}^{3} \left(6F_{Q_i} + 2F_{L_i} - 3F_{u_i} - 3F_{d_i} - F_{e_i} - F_{\nu_i}\right) = 0\,, \\ U(1)_Y \times U(1)_F'^2 &: \quad \sum_{i=1}^{3} \left(F_{Q_i}^2 - F_{L_i}^2 - 2F_{u_i}^2 + F_{d_i}^2 + F_{e_i}^2\right) = 0\,, \\ U(1)_F'^3 &: \quad \sum_{i=1}^{3} \left(6F_{Q_i}^3 + 2F_{L_i}^3 - 3F_{u_i}^3 - 3F_{d_i}^3 - F_{e_i}^3 - F_{\nu_i}^3\right) = 0\,. \end{aligned} \tag{D.2}$$

Note that RH neutrinos only enter in the gauge gravity and the $U(1)_F'^3$ conditions as they are SM singlets. This results in six conditions for either 15 BSM charges with the SM particle content or 18 BSM charges when RH neutrinos are added. We note the following features of the conditions in Eq. (D.2), see [304] and references therein for details.

- We assume that all $U(1)'$–charges are rational numbers $F_\psi \in \mathbb{Q}$.

Table D.1: Sample solutions of the anomaly cancellation conditions from Eq. (D.2) in $U(1)'$ extensions of the SM+$3\nu_R$. Solutions 4 and 7 have non-zero RH neutrinos, such that for all other models the SM particle content is sufficient. The ordering of generation dependent charges for each fermion species is arbitrary. Models 2, 4, 5 allow for $F_{Q_1} = F_{Q_2}$, models 9 and 10 even have $F_{Q_1} = F_{Q_2} = 0$.

sol. #	F_{Q_i}			F_{u_i}			F_{d_i}			F_{L_i}			F_{e_i}			F_{ν_i}		
1	-4	-2	6	-2	1	1	0	0	0	-8	3	5	-3	-3	6	0	0	0
2	-6	3	3	-8	4	4	-10	0	10	-6	1	5	0	0	0	0	0	0
3	-20	7	8	-29	3	6	-19	4	25	0	6	9	3	13	14	0	0	0
4	-1	-1	2	-1	-1	2	0	0	0	-1	0	1	-2	0	2	-2	-1	3
5	-1	-1	2	-1	-1	2	-1	-1	2	-1	0	1	-1	0	1	0	0	0
6	-10	2	6	-13	2	3	-11	2	13	-6	3	9	2	4	6	0	0	0
7	1	1	1	1	1	1	1	1	1	-3	-3	-3	-3	-3	-3	-3	-3	-3
8	-15	6	7	-14	2	4	-25	9	20	-24	11	19	1	3	8	0	0	0
9	0	0	0	-11	-2	13	7	7	-14	-8	3	5	-6	16	-10	0	0	0
10	0	0	0	-13	6	7	-1	-14	15	-15	15	0	-14	18	-4	0	0	0

- Any solution of Eq. (D.2) can be rescaled by any rational number $k \in \mathbb{Q}$, $F_\psi \to kF_\psi$, $\forall \psi \in \{Q_i, u_i, d_i, L_i, e_i, \nu_i\}$, while simultaneously rescaling the $U(1)'$ gauge coupling. Solutions connected via this *rescaling invariance* are in the same equivalence class.
- Due to the first two arguments, we assume integer solutions $F_\psi \in \mathbb{Z}$ without loss of generality.
- Within each species ψ any solution has a *permutation invariance* of the generation indices.

Concrete solutions of the non-linear conditions in Eq. (D.2) are obtained using computational algebraic geometry and performing a Gröbner basis computation [305] with *Mathematica* and analytical expressions for the charges F_ψ[1]. The aim of the search for solutions is to obtain large $c \to u$ FCNCs, *i.e.* solutions with $F_{Q_1} \neq F_{Q_2}$ and/or $F_{u_1} \neq F_{u_2}$ and consistent with $D^0 - \overline{D}^0$ mixing constraints, see the next section.

In Tab. D.1 we present solutions to the anomaly cancellation conditions. Due to the permutation invariance, the ordering of generations within each fermion species is arbitrary. Solutions 4 and 7 are also discussed in Ref. [304] and are the only solutions with non-vanishing charges for RH neutrinos considered in this work. Solutions 1 and 4 share the feature $F_{d_i} = 0$ for all three generations, therefore avoiding RH down-type FCNCs. Solutions 2, 4, 5, 9 and 10 are investigated in Sec. 5.2.3, because at least two of the three F_{Q_i}'s are equal, such that $\Delta F_L = F_{Q_2} - F_{Q_1} = 0$ can be fulfilled. Among these only solution 4 then avoids down-type FCNCs without further assumptions, as $F_{d_i} = 0$. In solution 7 only generation-independent couplings exist, which implies the absence of Z'–induced FCNCs at tree level. Sizable RG coefficients are induced in models with large $U(1)'$–charges. However, the study of the UV–properties of these models is beyond the scope of this work.

[1] This procedure is part of the research work of Rigo Bause, published in Refs. [1, 2] and will be discussed in detail in his PhD thesis.

In general Z'–models induce FCNCs via gauge to mass basis rotations. Four of these rotations are possible, for both LH and RH up-type and down-type quarks. The LH rotations necessarily need to reproduce the CKM matrix, which yields to either CKM-like contributions in the up- or the down-sector for LH quark currents, depending on assuming the CKM matrix to predominantly stem from up- or down-type rotations. In principle effects could also be split and scenarios where the mixing between second and third generation is due to down-type rotations and the mixing between first and second generation due to up-type rotations. A detailed investigation of these possibilities, however, is beyond the scope of this work.

D.2 Constraints from $D^0 - \overline{D}^0$ mixing

Constraints from charm meson mixing are severe for Z'–models, as they are generated on tree level. We discuss these constraints in detail. The D^0–$\overline{D}^0$ transition amplitude can be written as

$$\langle D^0 | \mathcal{H}_{\text{eff}}^{\Delta c=2} | \overline{D}^0 \rangle \;=\; M_{12} \;-\; \frac{\mathrm{i}}{2}\, \Gamma_{12} \;, \tag{D.3}$$

which is then parametrized in terms of the three physical quantities, see also Eq. (3.26)

$$x_{12} = 2\,\frac{|M_{12}|}{\Gamma}\,, \qquad y_{12} = \frac{|\Gamma_{12}|}{\Gamma}\,, \qquad \phi_{12} = \arg\!\left(\frac{M_{12}}{\Gamma_{12}}\right) . \tag{D.4}$$

x_{12} and y_{12} are CP–conserving, while ϕ_{12} quantifies CP–violation in mixing. The most general global fit from the HFLAV collaboration [176] results in the 95 % C.L. ranges

$$x_{12} \in [0.314\,,\, 0.503]\,\% \;, \qquad y_{12} \in [0.495\,,\, 0.715]\,\% \;, \qquad \phi_{12} \in [-1.2^\circ,\, 2.4^\circ] \;. \tag{D.5}$$

Since the SM predictions for the mixing parameters are not sufficiently controlled, we require the NP contributions to saturate the current world averages (D.5),

$$x_{12}^{\text{NP}} \leq x_{12} \;, \qquad x_{12}^{\text{NP}} \sin\phi_{12}^{\text{NP}} \leq x_{12} \sin\phi_{12} \;. \tag{D.6}$$

We compute constraints from the current world average of the $D^0 - \overline{D}^0$ mixing parameter x_D [176], which is obtained assuming no sub-leading amplitudes in indirect CP–violation, see [176] for details

$$x_D^{\text{exp}} = (4.09 \pm 0.048) \times 10^{-3}\,. \tag{D.7}$$

x_D is obtained as

$$x_D = \frac{\Delta m_{D^0}}{\Gamma_{D^0}} = \frac{2\,|M_{12}|}{\Gamma_{D^0}} = \frac{2}{\Gamma_{D^0}}\,\frac{1}{2m_{D^0}}\,\langle D^0 | \mathcal{H}_{\text{eff}}^{\Delta c=2} | \overline{D}^0 \rangle\,. \tag{D.8}$$

Here, $\mathcal{H}_{\text{eff}}^{\Delta c=2} = \sum_i c_i Q_i$ and [100]

$$\begin{aligned} Q_1 &= (\overline{u}_L\gamma_\mu c_L)(\overline{u}_L\gamma^\mu c_L)\,, & Q_5 &= (\overline{u}_R\sigma_{\mu\nu} c_L)(\overline{u}_R\sigma^{\mu\nu} c_L)\,, \\ Q_2 &= (\overline{u}_L\gamma_\mu c_L)(\overline{u}_R\gamma^\mu c_R)\,, & Q_6 &= (\overline{u}_R\gamma_\mu c_R)(\overline{u}_R\gamma^\mu c_R)\,, \\ Q_3 &= (\overline{u}_L c_R)(\overline{u}_R c_L)\,, & Q_7 &= (\overline{u}_L c_R)(\overline{u}_L c_R)\,, \\ Q_4 &= (\overline{u}_R c_L)(\overline{u}_R c_L)\,, & Q_8 &= (\overline{u}_L\sigma_{\mu\nu} c_R)(\overline{u}_L\sigma^{\mu\nu} c_R)\,. \end{aligned} \tag{D.9}$$

Tree-level matching of the Z'–model at the scale $\mu = M_{Z'}$ induces the following $\Delta C = 2$ Wilson coefficients ($g_L = g_L^{uc}$ and $g_R = g_R^{uc}$)

$$c_1(M_{Z'}) = \frac{g_L^2}{2M_{Z'}^2}\,, \qquad c_2(M_{Z'}) = \frac{g_L\, g_R}{M_{Z'}^2}\,, \qquad c_6(M_{Z'}) = \frac{g_R^2}{2M_{Z'}^2}\,. \tag{D.10}$$

The operator Q_3 is induced radiatively and therefore taken into account. At the scale $\mu = 3$ GeV the Z'–contribution is given as [100, 101]

$$\begin{aligned} x_D^{Z'} = \frac{1}{\Gamma_{D^0} m_{D^0}} \Big[& \; r_1\, c_1(M_{Z'})\,\langle Q_1\rangle + \sqrt{r_1}\, c_2(M_{Z'})\,\langle Q_2\rangle \\ & + \frac{2}{3}\, c_2(M_{Z'})\,(\sqrt{r_1} - r_1^{-4})\,\langle Q_3\rangle + r_1\, c_6(M_{Z'})\,\langle Q_6\rangle \;\Big]\,, \end{aligned} \tag{D.11}$$

with the renormalization factor

$$r_1 = \left(\frac{\alpha_s(M_{Z'})}{\alpha_s(m_t)}\right)^{2/7} \left(\frac{\alpha_s(m_t)}{\alpha_s(m_b)}\right)^{6/23} \left(\frac{\alpha_s(m_b)}{\alpha_s(\mu)}\right)^{6/25}\,, \tag{D.12}$$

and the hadronic matrix elements computed at $\mu = 3\,\text{GeV}$ [307]

$$\langle Q_1\rangle = 0.0805(55) = \langle Q_6\rangle\,, \qquad \langle Q_2\rangle = -0.2070(142)\,, \qquad \langle Q_3\rangle = \;\; 0.2747(129)\,. \tag{D.13}$$

Writing Eq. (D.11) with Z'–model parameters one arrives at

$$x_D^{Z'} = \frac{r_1\langle Q_1\rangle}{2\,\Gamma_{D^0}\, m_{D^0}}\, \frac{g_L^2 + g_R^2 - X g_L g_R}{M_{Z'}^2}\,, \tag{D.14}$$

where we define

$$X = -2\left(\sqrt{r_1}\,\langle Q_2\rangle + \frac{2}{3}\,(\sqrt{r_1} - r_1^{-4})\,\langle Q_3\rangle\right)(r_1\langle Q_1\rangle)^{-1}\,. \tag{D.15}$$

This exactly coincides with Eq. (4.18) and we find $X = 19.2, 24.0, 26.2$ for $M_{Z'} = 1, 5, 10$ TeV, respectively. In order to investigation the possibility of cancellations in Eq. (4.18), we further simplify

$$|g_L| = |g_R| \frac{X}{2} \left(1 \pm \sqrt{1 - \frac{4}{X^2}}\right) . \tag{D.16}$$

In this scenario the mixed contribution $X g_L g_R$ exactly cancels the term $g_L^2 + g_R^2$ and the bound from $D^0 - \overline{D}^0$ mixing becomes irrelevant. We investigate this possibility by employing $4/X^2 \ll 1$, which along with the symmetry in $L \leftrightarrow R$ yields the following two scenarios

$$g_L \approx X g_R \quad \text{or} \quad g_L \approx \frac{1}{X} g_R \,, \tag{D.17}$$

which we refer to as LH dominated and RH dominated, respectively. Note that we put "≈" to highlight the following. In Eq. (D.17) no perfect cancellation is achieved, rather one obtains

$$\begin{aligned} & g_L^2 + g_R^2 - X g_L g_R < \tilde{x} \,, \\ g_L = X\, g_R \quad &\Rightarrow \quad g_R^2 < \tilde{x} \,, \quad g_R^2 < X^2 \tilde{x} \quad \text{(LH dominated)} \,, \\ g_R = X\, g_L \quad &\Rightarrow \quad g_L^2 < \tilde{x} \,, \quad g_R^2 < X^2 \tilde{x} \quad \text{(RH dominated)} \,, \end{aligned} \tag{D.18}$$

where, $\tilde{x} = \frac{2\, x_D^{\text{exp}}\, \Gamma_{D^0}\, m_{D^0}\, M_{Z'}^2}{r_1 \langle Q_1 \rangle}$. This implies that the larger coupling can be enhanced by one factor of X with respect to a scenario of a single coupling, which is bounded by $|g_{L/R}| < \sqrt{\tilde{x}}$. However, Eq. (D.16) yields an exact cancellation, such that the allowed size of the coupling depends on the level of fine tuning. This can be seen using the Taylor expansion of Eq. (D.16) $|g_L| \approx |g_R| \left(X - \frac{1}{X} - \frac{1}{X^3} + \mathcal{O}(X^{-5})\right)$. Using more terms of this expansion instead of Eq. (D.17) yields the following bounds for g_L

$$\begin{aligned} |g_L| &\lesssim X^2 \sqrt{\tilde{x}} \quad \text{for} \quad g_L = \left(X - \frac{1}{X}\right) g_R \,, \\ |g_L| &\lesssim X^3 \sqrt{\tilde{x}} \quad \text{for} \quad g_L = \left(X - \frac{1}{X} - \frac{1}{X^3}\right) g_R \,. \end{aligned} \tag{D.19}$$

As corrections of higher powers in X are negligible with respect to running effects in the numerical evaluation of X itself, due to the unknown Z'–mass, we will use the approximation in Eq. (D.17) and assume perfect cancellation of the $D^0 - \overline{D}^0$ mixing bound.

Experimental constraints on CP–violation in $D^0 - \overline{D}^0$ mixing, $x_{12} \sin\phi_{12} \lesssim 2 \times 10^{-4}$, are stronger than (D.7) by about ~ 0.04 [176, 308]. Further, a cancellation of the mixing bound is only possible when the phases in g_L and g_R are aligned $\text{Arg}(g_L) = \text{Arg}(g_R)$, see Sec. 5.2.3 and App. D.3 for an analysis of CP–violating effects in Z'–models.

Table D.2: Branching ratio measurements [184] and a_P–parameters from Eq. (D.20) for different two-body hadronic D–meson decay modes.

mode	BR (mode)	a_P
$D^0 \to K^+K^-$	$(4.08 \pm 0.06) \times 10^{-3}$	1.19 ± 0.04
$D^0 \to \pi^+\pi^-$	$(1.453 \pm 0.024) \times 10^{-3}$	0.94 ± 0.07
$D^0 \to \pi^0\pi^0$	$(8.26 \pm 0.25) \times 10^{-4}$	0.71 ± 0.05
$D^+ \to \pi^0\pi^+$	$(1.247 \pm 0.033) \times 10^{-3}$	0.77 ± 0.05

D.3 Details on $Z^{'}$–contributions to CP–asymmetries in hadronic charm decays

We derive Eqs. (5.29), (5.32) and (5.34). First, we fit the modulus of the SM decay amplitudes to data on branching ratios [184] given in Tab. D.2. We use [309]

$$\mathrm{BR}(D \to P_1 P_2) = \frac{|\mathcal{A}_P|^2}{16\,\pi\, m_D} \sqrt{1 - \frac{4\,m_P^2}{m_D^2}}\,\tau_D \ , \quad \mathcal{A}_P = \eta_P \lambda_P a_P \frac{G_F}{\sqrt{2}}\,(m_D^2 - m_P^2)\; f_0^{D\to P}(m_P^2)\, f_P \ , \tag{D.20}$$

with $P = \pi, \pi^0, \pi'$, K, $\lambda_\pi = \lambda_d$ and $\lambda_K = \lambda_s$ and $\eta_\pi = \eta_{\pi^0} = \eta_K = 1$, whereas $\eta_{\pi'} = 1/\sqrt{2}$ and π' corresponds to the $D^+ \to \pi^+\pi^0$ channel, and π^0 to $D^0 \to \pi^0\pi^0$.

Tab D.2 collects resulting values of $a_P > 0$, which include U–spin breaking effects within the SM.

The second step is the extension of the effective Hamiltonian with further operators. Due to the generation-dependent quark-couplings proportional to F_ψ charges, additional operators in the effective weak Hamiltonian beyond the ones considered usually, *i.e.* Ref. [310], are needed. At the scale $m_b < \mu < \mu_t$,

$$\mathcal{H}_{\text{eff}}^{|\Delta \text{c}|=1} \supset \frac{G_F}{\sqrt{2}} \sum_i \widetilde{C}_i^{(\prime)}\, \widetilde{Q}_i^{(\prime)} + \text{h.c.} \ , \tag{D.21}$$

with the new operators

$$\begin{aligned}
\widetilde{Q}_7 &= (\bar{u}c)_{V-A} \sum_q F_{u_i,d_i} (\bar{q}q)_{V+A} \,, & \widetilde{Q}'_7 &= (\bar{u}c)_{V+A} \sum_q F_{Q_i} (\bar{q}q)_{V-A} \,, \\
\widetilde{Q}_8 &= (\bar{u}_\alpha c_\beta)_{V-A} \sum_q F_{u_i,d_i} (\bar{q}_\beta q_\alpha)_{V+A} \,, & \widetilde{Q}'_8 &= (\bar{u}_\alpha c_\beta)_{V+A} \sum_q F_{Q_i} (\bar{q}_\beta q_\alpha)_{V-A} \,, \\
\widetilde{Q}_9 &= (\bar{u}c)_{V-A} \sum_q F_{Q_i} (\bar{q}q)_{V-A} \,, & \widetilde{Q}'_9 &= (\bar{u}c)_{V+A} \sum_q F_{u_i,d_i} (\bar{q}q)_{V+A} \,, \\
\widetilde{Q}_{10} &= (\bar{u}_\alpha c_\beta)_{V-A} \sum_q F_{Q_i} (\bar{q}_\beta q_\alpha)_{V-A} \,, & \widetilde{Q}'_{10} &= (\bar{u}_\alpha c_\beta)_{V+A} \sum_q F_{u_i,d_i} (\bar{q}_\beta q_\alpha)_{V+A} \,.
\end{aligned} \tag{D.22}$$

where $(V \pm A)$ refers to the Dirac structures $\gamma_\mu(1 \pm \gamma_5)$, $q = u, c, d, s, b$ and α, β are the color indices.

Within the Z'–model, the matching conditions at the NP scale read

$$\begin{aligned}
\widetilde{C}_7 (M_{Z'}) = \widetilde{C}_9 (M_{Z'}) &= \frac{\sqrt{2}}{G_F} g_L^{uc} \frac{g_4}{4\, M_{Z'}^2} \,, \\
\widetilde{C}'_7 (M_{Z'}) = \widetilde{C}'_9 (M_{Z'}) &= \frac{\sqrt{2}}{G_F} g_R^{uc} \frac{g_4}{4\, M_{Z'}^2} \,, \\
\widetilde{C}_8^{(\prime)} (M_{Z'}) = \widetilde{C}_{10}^{(\prime)} (M_{Z'}) &= 0 \,.
\end{aligned} \tag{D.23}$$

These contributions are evolved from $M_{Z'}$ to m_c and finite values of $\widetilde{C}_8^{(\prime)}$ and $\widetilde{C}_{10}^{(\prime)}$ arise from the RG mixing at the charm mass scale.

The anomalous dimension matrix at LO in α_s for the operators $\widetilde{Q}_{7,8,9,10}$ can be inferred from Ref. [161] and reads

$$\gamma_F^0 = \begin{pmatrix} 2 & -6 & 0 & 0 \\ 0 & -16 & 0 & 0 \\ 0 & 0 & -2 & 6 \\ 0 & 0 & 6 & -2 \end{pmatrix} . \tag{D.24}$$

Since QCD conserves parity, γ_F^0 is identical for $\widetilde{Q}_i$ and $\widetilde{Q}'_i$. Using Eq. (D.24), the Wilson coefficients are evolved to the charm scale, integrating out degrees of freedom at the (Z', t, b)–scales,

$$\vec{C}(\mu) \;=\; U_4(\mu, m_b)\, \widehat{U}_5(m_b, m_t)\, \widehat{U}_6(m_t, M_{Z'})\, \vec{C}(M_{Z'}) \;,$$

where $\widehat{U}_f(m_1, m_2) \equiv M_f(m_1)\, U_f(m_1, m_2)$ and $U_f(m_1, m_2)$ is the evolution matrix from scale m_2 to scale m_1 in an EFT with f active flavors; M_f is the threshold matrix that matches the two effective theories with $f-1$ and f active flavors. At LO in α_s, the M_f matrices are equal to the identity matrix.

For $\mu = m_c$ and $M_{Z'} = 6\,\text{TeV}$, one finds

$$\begin{aligned}
\widetilde{C}_7^{(\prime)}(m_c) &= \quad 0.829\,\widetilde{C}_7^{(\prime)}(M_{Z'})\ , \\
\widetilde{C}_8^{(\prime)}(m_c) &= \quad 1.224\,\widetilde{C}_7^{(\prime)}(M_{Z'}) + 4.502\,\widetilde{C}_8^{(\prime)}(M_{Z'})\ , \\
\widetilde{C}_9^{(\prime)}(m_c) &= \quad 1.404\,\widetilde{C}_9^{(\prime)}(M_{Z'}) - 0.718\,\widetilde{C}_{10}^{(\prime)}(M_{Z'})\ , \\
\widetilde{C}_{10}^{(\prime)}(m_c) &= -0.718\,\widetilde{C}_9^{(\prime)}(M_{Z'}) + 1.404\,\widetilde{C}_{10}^{(\prime)}(M_{Z'})\ .
\end{aligned} \tag{D.25}$$

The last missing ingredient is the evaluation of hadronic matrix elements. Here, we employ factorization of currents, $P = \pi, K$,

$$\langle P^+\,P^-|\,Q_i\,|D^0\rangle = \langle P^+|\,(\bar{q}_1\,\Gamma_1\,q_2)\,|0\rangle\ \langle P^-|\,(\bar{q}_3\,\Gamma_2\,q_4)\,|D^0\rangle\ , \tag{D.26}$$

where $Q_i = (\bar{q}_1\,\Gamma_1\,q_2)\,(\bar{q}_3\,\Gamma_2\,q_4)$ is any 4–quark operator from Eq. (D.22) and $\Gamma_{1,2}$ represent possible Dirac and color structures while q_j denote quarks. After employing Fierz identities in the flavor and color space, we find for $D^0 \to K^+K^-$ and $\pi^+\pi^-$ decays

$$\begin{aligned}
\langle\widetilde{Q}_7\rangle_{K,\pi} &= \frac{1}{N_C}\,\langle\widetilde{Q}_8\rangle_{K,\pi}\ , & \langle\widetilde{Q}_9\rangle_{K,\pi} &= \frac{1}{N_C}\,\langle\widetilde{Q}_{10}\rangle_{K,\pi}\ , \\
\langle\widetilde{Q}_8\rangle_{K,\pi} &= F_{d_2,\,d_1}\,\chi_{K,\pi}(\mu)\,\langle Q_1^{s,\,d}\rangle_{K,\pi}\ , & \langle\widetilde{Q}_{10}\rangle_{K,\pi} &= F_{Q_2,\,Q_1}\,\langle Q_1^{s,\,d}\rangle_{K,\pi}\ ,
\end{aligned} \tag{D.27}$$

where $\langle ...\rangle_P = \langle P^+P^-|...|D^0\rangle$, $Q_1^p = (\bar{u}p)_{V-A}(\bar{p}c)_{V-A}$ and $\chi_{K,\pi}(\mu)$ are chiral enhancement factors generated by $(V-A)\times(V+A)$ operators,

$$\chi_K(\mu) = \frac{2\,M_K^2}{m_c(\mu)\,m_s(\mu)}\ , \qquad \chi_\pi(\mu) = \frac{2\,M_\pi^2}{m_c(\mu)\,(m_d+m_u)(\mu)}\ . \tag{D.28}$$

We find $\chi_K(m_c) \approx 3.626$ and $\chi_\pi(m_c) \approx 3.655$ at the charm mass scale. For the $\widetilde{Q}_i'$ operators the same relations hold but with the proper exchange of charges $F_{Q_i} \leftrightarrow F_{d_i}$.

For $D^+ \to \pi^0\pi^+$ decays we find

$$\begin{aligned}
\langle\widetilde{Q}_7\rangle_{\pi'} &= \frac{1}{N_C}\,\langle\widetilde{Q}_8\rangle_{\pi'}\ , & \langle\widetilde{Q}_7'\rangle_{\pi'} &= \frac{1}{N_C}\,\langle\widetilde{Q}_8'\rangle_{\pi'} = 0\ , \\
\langle\widetilde{Q}_8\rangle_{\pi'} &= \frac{\chi_\pi(\mu)}{\sqrt{2}}\,(F_{u_1} - F_{d_1})\,\langle Q_1^u\rangle_u\ , & \langle\widetilde{Q}_9'\rangle_{\pi'} &= \frac{1}{N_C}\,\langle\widetilde{Q}_{10}'\rangle_{\pi'}\ , \\
\langle\widetilde{Q}_9\rangle_{\pi'} &= \frac{1}{N_C}\,\langle\widetilde{Q}_{10}\rangle_{\pi'} = 0\ , & \langle\widetilde{Q}_{10}'\rangle_{\pi'} &= \frac{1}{\sqrt{2}}\,(F_{u_1} - F_{d_1})\,\langle Q_1^u\rangle_u\ .
\end{aligned} \tag{D.29}$$

Finally, for $D^0 \to \pi^0\pi^0$ decays we obtain

$$\begin{aligned}
\langle \widetilde{Q}_7 \rangle_{\pi^0} &= \frac{1}{N_C} \langle \widetilde{Q}_8 \rangle_{\pi^0} \ , & \langle \widetilde{Q}'_7 \rangle_{\pi^0} &= \frac{1}{N_C} \langle \widetilde{Q}'_8 \rangle_{\pi^0} = 0 \ , \\
\langle \widetilde{Q}_8 \rangle_{\pi^0} &= \frac{\chi_\pi(\mu)}{2} \left(F_{u_1} - F_{d_1}\right) \langle Q_1^u \rangle_u \ , & \langle \widetilde{Q}'_9 \rangle_{\pi^0} &= \frac{1}{N_C} \langle \widetilde{Q}'_{10} \rangle_{\pi^0} \ , \\
\langle \widetilde{Q}_9 \rangle_{\pi^0} &= \frac{1}{N_C} \langle \widetilde{Q}_{10} \rangle_{\pi^0} = 0 \ , & \langle \widetilde{Q}'_{10} \rangle_{\pi^0} &= \frac{1}{2} \left(F_{u_1} - F_{d_1}\right) \langle Q_1^u \rangle_u \ .
\end{aligned} \tag{D.30}$$

Again, our notation is $\langle ... \rangle_{\pi'} = \langle \pi^+\pi^0 | ... | D^+ \rangle$, $\langle ... \rangle_{\pi^0} = \langle \pi^0\pi^0 | ... | D^0 \rangle$ and $\langle ... \rangle_q = \langle \bar{q}q | ... | D^+ \rangle$. We have employed the isospin limit, $m_u = m_d$ and $e = 0$, since these induce isospin breaking in the SM, however negligible with respect to NP isospin breaking, induced by $F_{u_i,d_i,Q_i} \neq 0$.

All hadronic matrix elements are now related to the dominant SM contributions $\langle Q_1^{s,\,d} \rangle_{K,\pi}$, which we have fixed to experiment, see Eq. (D.20). This yields for the NP contribution to $\Delta A_{\rm CP}$

$$|\Delta A_{\rm CP}^{\rm NP}| \simeq \frac{2}{\lambda_s} \cdot \left(\frac{\mathcal{A}_{\rm NP}^K}{a^K} \underbrace{\sin\phi_{\rm NP}^K \sin\delta_{\rm NP}^K}_{=1} + \frac{\mathcal{A}_{\rm NP}^\pi}{a^\pi} \underbrace{\sin\phi_{\rm NP}^\pi \sin\delta_{\rm NP}^\pi}_{=1} \right) \ , \tag{D.31}$$

where the relative sign of λ_s and λ_d is used, we assume maximally strong phase differences and the NP weak phase is also fixed to $\phi_{\rm NP} = \frac{\pi}{2}$ to avoid $D^0 - \bar{D}^0$ mixing bounds, see discussion in Sec. 5.2.3. The a^P with $P = K, \pi$ are given in Tab. D.2 and

$$\begin{aligned}
\mathcal{A}_{\rm NP}^K &= \tilde{C}_7 \frac{\chi_K F_{d_2}}{N_C} + \tilde{C}'_7 \frac{\chi_K F_{Q_2}}{N_C} + \tilde{C}_8 \chi_K F_{d_2} + \tilde{C}'_8 \chi_K F_{Q_2} + \tilde{C}_9 \frac{F_{Q_2}}{N_C} + \tilde{C}'_9 \frac{F_{d_2}}{N_C} + \tilde{C}_{10} F_{Q_2} + \tilde{C}'_{10} F_{d_2} \ , \\
\mathcal{A}_{\rm NP}^\pi &= \tilde{C}_7 \frac{\chi_\pi F_{d_1}}{N_C} + \tilde{C}'_7 \frac{\chi_\pi F_{Q_1}}{N_C} + \tilde{C}_8 \chi_\pi F_{d_1} + \tilde{C}'_8 \chi_\pi F_{Q_1} + \tilde{C}_9 \frac{F_{Q_1}}{N_C} + \tilde{C}'_9 \frac{F_{d_1}}{N_C} + \tilde{C}_{10} F_{Q_1} + \tilde{C}'_{10} F_{d_1} \ .
\end{aligned} \tag{D.32}$$

Since the Wilson coefficients in Eq. (D.32) need to be evaluated at the charm mass scale, contributions from Eq. (D.23) are evolved down to this scale as previously discussed. Finally, we find contributions of the Z'–models to hadronic CP–asymmetries via the compactly written Eqs. (5.29), (5.32) and (5.34), with the following parameters

$$\begin{aligned}
c_K &= \frac{\chi_K}{a_K} r_1(m_c, M_{Z'}) \ , & d_K &= \frac{1}{a_K} r_2(m_c, M_{Z'}) \ , \\
c_\pi &= -\frac{\chi_\pi}{a_\pi} r_1(m_c, M_{Z'}) \ , & d_\pi &= -\frac{1}{a_\pi} r_2(m_c, M_{Z'}) \ , \\
d_{\pi'} &= -\frac{1}{a_{\pi'}} r_2(m_c, M_{Z'}) \ , & d_{\pi^0} &= -\frac{1}{a_{\pi^0}} r_2(m_c, M_{Z'}) \ ,
\end{aligned} \tag{D.33}$$

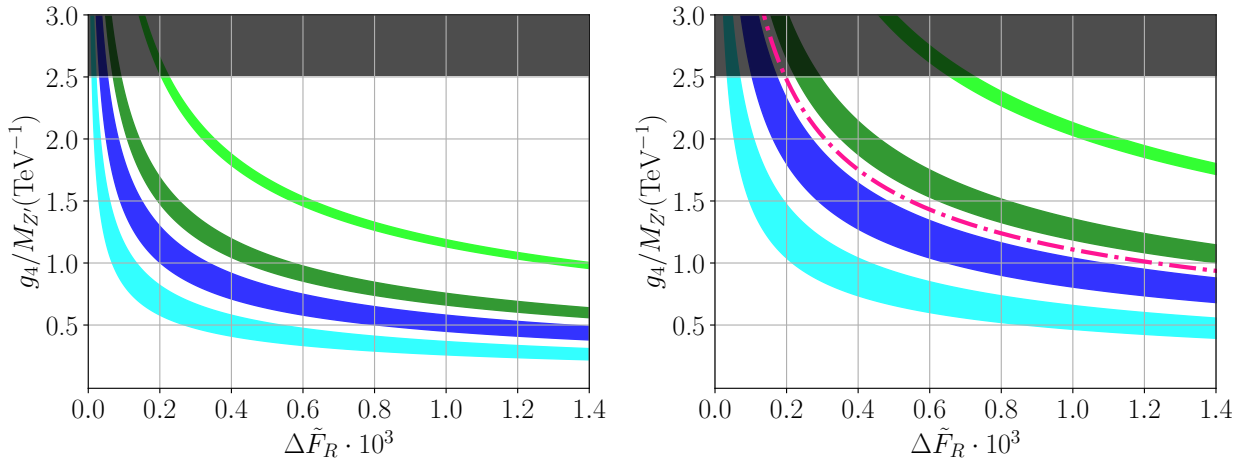

Figure D.1: Similar to Fig. 5.14 in Sec. 5.2.3, but for Z'–models 5 (left) and 9 (right).

where, again, the a_P factors are taken from Tab. D.2 and the following RG factors enter

$$r_1(m_c, M_{Z'}) = \frac{R^{-2}}{3\sqrt{2}\, G_F \lambda_s}\,, \qquad r_2(m_c, M_{Z'}) = \frac{2\, R^{1/2} - R^{-1}}{3\sqrt{2}\, G_F \lambda_s}\,, \tag{D.34}$$

with

$$R = \left(\frac{\alpha_s^{(4)}(m_b)}{\alpha_s^{(4)}(m_c)}\right)^{\frac{12}{25}} \left(\frac{\alpha_s^{(5)}(m_t)}{\alpha_s^{(5)}(m_b)}\right)^{\frac{12}{23}} \left(\frac{\alpha_s^{(6)}(M_{Z'})}{\alpha_s^{(6)}(m_t)}\right)^{\frac{4}{7}}\,. \tag{D.35}$$

D.4 Parameter space for further Z'–model solutions

In Sec. 5.2.3 Fig. 5.14 displays the available parameter space for models 2 and 10 along with bands illustrating increasing contributions to ΔA_{CP}. We show similar plots for models 5 (left) and model 9 (right) in Fig. D.1. Here, model 5 still is a viable candidate to evade constraints from mixing (red region), the perturbativity and direct search limit (black band) and constraints from semileptonic rare D–decays (pink, dash-dotted line, too weak to be displayed in the left plot). Model 9 is constructed to have no charges to any LH quark doublet, similar to model 10. In these models isospin, U–spin breaking effects can be pronounced and larger contributions to rare semileptonic decays are induced. Similar to model 10, model 9 is not a viable candidate to simultaneously have $\Delta A_{\mathrm{CP}}^{\mathrm{NP}} \sim 10^{-3}$, while evading the displayed bounds. Both models were presented as viable candidates in Ref. [2], however both mixing bound and limits from rare semileptonic charm decays have improved and exclude these models.

E Distributions and Observables

In this appendix, we collect the full dependence on Wilson coefficients, form factors and kinematic factors of several differential distributions and further observables used throughout the thesis. First, we give results for $D \to P\ell^+\ell^-$ in App. E.1, followed by results for the three- and four-body baryon modes in Apps. E.2 and E.3. Here, we just display the results compactly, whereas we discuss the helicity formalism utilized to obtain these results separately in App. F. Finally, App. E.4 provides explicit expressions for $a_\pm^{h_q F_{q'}}$ factors utilized in Chapter 6.

E.1 $D \to P\ell^+\ell^-$

In Agreement with Refs. [90, 166, 177], the double differential decay distribution of $D \to P\ell^+\ell^-$ neglecting the up-quark mass can be written as

$$\begin{aligned}
\left(\frac{G_F^2\alpha_e^2}{2048\pi^5 m_D^3}\right)^{-1} \frac{\mathrm{d}^2\Gamma}{\mathrm{d}q^2\mathrm{d}u} =& \left|C_9 + C_7\frac{2m_c}{m_D+m_P}\frac{f_T}{f_+}\right|^2 f_+^2\,(\lambda_{DP}-u^2) \\
&+|C_{10}|^2\left[(v^2\,\lambda_{DP}-u^2)\,f_+^2 + \frac{4m_\ell^2}{q^2}(m_D^2-m_P^2)^2 f_0^2\right] \\
&+\left[|C_S|^2 v^2 + |C_P|^2\right]\frac{q^2}{m_c^2}(m_D^2-m_P^2)^2 f_0^2 \\
&+4\left[|C_T|^2+|C_{T5}|^2\right]\frac{q^2}{(m_D+m_P)^2} f_T^2 u^2 \\
&+4\,\mathrm{Re}\left[\left(C_9 + C_7\frac{2m_c}{m_D+m_P}\frac{f_T}{f_+}\right)C_S^*\right]\frac{m_\ell}{m_c}\,(m_D^2-m_P^2)\,f_0\,f_+\,u \\
&+8\,\mathrm{Re}\left[C_{10}C_{T5}^*\right] m_\ell\,(m_D-m_P)\,f_0\,f_T\,u \\
&+4\,\mathrm{Re}\left[C_S C_T^* + C_P C_{T5}^*\right]\frac{q^2\,(m_D-m_P)}{m_c}\,f_0\,f_T\,u \\
&+8\,\mathrm{Re}\left[\left(C_9 + C_7\frac{2m_c}{m_D+m_P}\frac{f_T}{f_+}\right)C_T^*\right]\frac{m_\ell}{m_D+m_P}\lambda_{DP} f_+ f_T \\
&+4\,\mathrm{Re}\left[C_{10}C_P^*\right]\frac{m_\ell}{m_c}(m_D^2-m_P^2)^2 f_0^2 + 16\,|C_T|^2\frac{m_\ell^2}{(m_D+m_P)^2}\lambda_{DP} f_T^2\,,
\end{aligned} \tag{E.1}$$

where

$$u = -\cos\theta_\ell\sqrt{\lambda_{DP}}\,\beta_\ell\,, \tag{E.2}$$

and, again, $\lambda_{DP} = m_D^4 + m_P^4 + q^4 - 2m_D^2\,m_P^2 - 2m_D^2\,q^2 - 2m_P^2 q^2$ and $\beta_\ell = \sqrt{1-\frac{4m_\ell^2}{q^2}}$. For $D \to P\ell^+\ell^-$ all Wilson coefficients C_i, with the exception of the tensor ones, are understood as

$$C_i \to C_i + C_i'\,. \tag{E.3}$$

The q^2 differential distribution is obtained by integrating u, where θ_ℓ is constrained by $-1 < \cos\theta_\ell < 1$. We find, again in agreement with Refs. [90, 166, 177]

$$\begin{aligned}
\frac{\mathrm{d}\Gamma}{\mathrm{d}q^2} = \frac{G_F^2\alpha_e^2}{1024\pi^5 m_D^3}\sqrt{\lambda_{DP}}\beta_\ell \Bigg\{ & \\
& \frac{2}{3}\left|C_9 + C_7\frac{2m_c}{m_D+m_P}\frac{f_T}{f_+}\right|^2\left(1+\frac{2m_\ell^2}{q^2}\right)\lambda_{DP}f_+^2 \\
& + |C_{10}|^2\left[\frac{2}{3}\beta_\ell^2\,\lambda_{DP}f_+^2 + \frac{4m_\ell^2}{q^2}(m_D^2-m_P^2)^2 f_0^2\right] \\
& + \left[|C_S|^2\beta_\ell^2 + |C_P|^2\right]\frac{q^2}{m_c^2}(m_D^2-m_P^2)^2 f_0^2 \\
& + \frac{4}{3}\left[|C_T|^2 + |C_{T5}|^2\right]\beta_\ell^2\frac{q^2}{(m_D+m_P)^2}\lambda_{DP}f_T^2 \\
& + 8\,\mathrm{Re}\left[\left(C_9 + C_7\frac{2m_c}{m_D+m_P}\frac{f_T}{f_+}\right)C_T^*\right]\frac{m_\ell}{m_D+m_P}\lambda_{DP}f_+ f_T \\
& + 4\,\mathrm{Re}\left[C_{10}C_P^*\right]\frac{m_\ell}{m_c}(m_D^2-m_P^2)^2 f_0^2 + 16\,|C_T|^2\frac{m_\ell^2}{(m_D+m_P)^2}\lambda_{DP}f_T^2\Bigg\}.
\end{aligned} \tag{E.4}$$

In the LFV case we neglect the electron mass and find for $D \to Pe^\pm\mu^\mp$

$$\begin{aligned}
\frac{\mathrm{d}\Gamma(D\to Pe^\pm\mu^\mp)}{\mathrm{d}q^2} = \frac{G_F^2\alpha_e^2}{1024\pi^5 m_D^3}\sqrt{\lambda_{DP}}\Bigg\{ & \frac{2}{3}\left(|K_9|^2+|K_{10}|^2\right)\lambda(m_D^2,m_P^2,q^2)f_+^2 \\
& + \left(|K_S|^2+|K_P|^2\right)\frac{q^2}{m_c^2}(m_D^2-m_P^2)^2 f_0^2 \\
& + \frac{4}{3}\left(|K_T|^2+|K_{T5}|^2\right)\frac{q^2}{(m_D+m_P)^2}\lambda_{DP}f_T^2 \\
& + 2\mathrm{Re}\left[\pm K_9 K_S^* + K_{10}K_P^*\right]\frac{m_\mu}{m_c}(m_D^2-m_P^2)^2 f_0^2 \\
& + 4\mathrm{Re}\left[K_9 K_T^* \pm K_{10}K_{T5}^*\right]\frac{m_\mu}{m_D+m_P}\lambda_{DP}f_+ f_T\Bigg\} + \mathcal{O}\left(m_\mu^2\right),
\end{aligned} \tag{E.5}$$

where $K_i = K_i^{(\mu e)} + K_i'^{(\mu e)}$ for $D \to Pe^+\mu^-$ and $K_i = K_i^{(e\mu)} + K_i'^{(e\mu)}$ for $D \to Pe^-\mu^+$.

E.2 $B_0 \to B_1\ell^+\ell^-$

For the three-body baryon decays we find the following double differential decay width

$$\frac{\mathrm{d}^2\Gamma}{\mathrm{d}q^2\mathrm{d}\cos\theta_\ell} = \frac{3}{2}\cdot\left(K_{1ss}\sin^2\theta_\ell + K_{1cc}\cos^2\theta_\ell + K_{1c}\cos\theta_\ell\right), \tag{E.6}$$

with the following q^2-dependent angular coefficients

$$\begin{aligned} K_{1ss} &= q^2\beta_\ell^2\left(\frac{1}{2}U^{11+22}+L^{11+22}\right)+4m_\ell^2\left(U^{11}+L^{11}+S^{22}\right), \\ K_{1cc} &= q^2\beta_\ell^2 U^{11+22}+4m_\ell^2\left(U^{11}+L^{11}+S^{22}\right), \\ K_{1c} &= -2q^2\beta_\ell P^{12}, \end{aligned} \tag{E.7}$$

where we follow the notation of Ref. [296] and discuss the coefficients U, L, S in detail in App. F. They are quadratic expressions of helicity amplitudes. Here, we only give the result, which is in agreement with [296, 311] and [249]. We keep finite lepton masses and consider the operators O_7, O_9, O_{10} as well as their primed counterparts from Eq. (2.24)

$$\begin{aligned} U^{11} &= 4N^2\cdot\Bigg[\left|(C_7+C_7')\,\frac{2m_c}{q^2}(m_{B_0}+m_{B_1})\,h_\perp+(C_9+C_9')\;f_\perp\right|^2\cdot s_- \\ &\quad+\left|(C_7-C_7')\,\frac{2m_c}{q^2}(m_{B_0}-m_{B_1})\,\tilde{h}_\perp+(C_9-C_9')\;g_\perp\right|^2\cdot s_+\Bigg], \\ L^{11} &= \frac{2N^2}{q^2}\cdot\Bigg[\left|(C_7+C_7')\,2m_c\,h_+ +(C_9+C_9')\,(m_{B_0}+m_{B_1})\,f_+\right|^2\cdot s_- \\ &\quad+\left|(C_7-C_7')\,2m_c\,\tilde{h}_+ +(C_9-C_9')\,(m_{B_0}-m_{B_1})\,g_+\right|^2\cdot s_+\Bigg], \\ U^{22} &= 4N^2\cdot\Bigg[\left|(C_{10}+C_{10}')\,f_\perp\right|^2\cdot s_- +\left|(C_{10}-C_{10}')\,g_\perp\right|^2\cdot s_+\Bigg], \\ L^{22} &= \frac{2N^2}{q^2}\cdot\Bigg[\left|(C_{10}+C_{10}')\,(m_{B_0}+m_{B_1})\,f_+\right|^2\cdot s_- +\left|(C_{10}-C_{10}')\,(m_{B_0}-m_{B_1})\,g_+\right|^2\cdot s_+\Bigg], \\ S^{22} &= \frac{2N^2}{q^2}\cdot\Bigg[\left|(C_{10}+C_{10}')\,(m_{B_0}-m_{B_1})\,f_0\right|^2\cdot s_+ +\left|(C_{10}-C_{10}')\,(m_{B_0}+m_{B_1})\,g_0\right|^2\cdot s_-\Bigg], \\ P^{12} &= -8N^2\cdot\Bigg[\mathrm{Re}\big((C_7-C_7')\,(C_{10}^*+C_{10}'^*)\big)\,\frac{m_c}{q^2}(m_{B_0}-m_{B_1})\,f_\perp\,\tilde{h}_\perp \\ &\quad+\mathrm{Re}\big((C_7+C_7')\,(C_{10}^*-C_{10}'^*)\big)\,\frac{m_c}{q^2}(m_{B_0}+m_{B_1})\,g_\perp\,h_\perp \\ &\quad+\mathrm{Re}(C_9C_{10}^*-C_9'C_{10}'^*)\,g_\perp\,f_\perp\Bigg]\cdot\sqrt{s_+s_-}\,. \end{aligned} \tag{E.8}$$

Note that in Eq. (E.7) the notation $U^{11+22}=U^{11}+U^{22}$ and likewise for L^{11+22} is used. The factor

N^2 is a global normalization and reads

$$N^2 = \frac{G_F^2 \alpha_e^2 \beta_\ell \sqrt{\lambda(m_{\Lambda_c}^2,\, m_p^2,\, q^2)}}{3 \cdot 2^{11} \pi^5 m_{\Lambda_c}^3} \,. \tag{E.9}$$

As apparent from Eq. (E.8), the index 1 refers to dipole and vector operators, whereas the index 2 indicates the axial vector contributions.

For LFV decays the angular observables are given by

$$\begin{aligned}
K_{1ss} &= 2(m_\ell - m_{\ell'})^2 v_+^2 S^{11} + 2(m_\ell + m_{\ell'})^2 v_-^2 S^{22} \\
&\quad + 2q^2 v_-^2 L^{11} + 2q^2 v_+^2 L^{22} \\
&\quad + (q^2 v_-^2 + (m_\ell + m_{\ell'})^2 v_-^2)\, U^{11} + (q^2 v_+^2 + (m_\ell - m_{\ell'})^2 v_+^2)\, U^{22} \,, \\
K_{1cc} &= 2(m_\ell - m_{\ell'})^2 v_+^2 S^{11} + 2(m_\ell + m_{\ell'})^2 v_-^2 S^{22} \\
&\quad + 2(m_\ell + m_{\ell'})^2 v_-^2 L^{11} + 2(m_\ell - m_\ell)^2 v_+^2 L^{22} \\
&\quad + 2q^2 v_-^2 U^{11} + 2q^2 v_+^2 U^{22} \,, \\
K_{1c} &= -4q^2 v_+ v_- P^{12} \,,
\end{aligned} \tag{E.10}$$

where the same hadronic helicity amplitudes as for the lepton flavor conserving decays can be used with the appropriate replacement of Wilson coefficients $C_{9,10}^{(\prime)}$ with LFV Wilson coefficients $K_{9,10}^{(\prime)}$. Contributions with $C_7^{(\prime)}$ need to be skipped, since the photon only couples to opposite sign same flavor lepton pairs. Also, we use $v_\pm = \sqrt{1 - \frac{(m_\ell \pm m_{\ell'})^2}{q^2}}$.

E.3 $B_0 \to B_1(\to B_2\pi)\ell^+\ell^-$

For the (quasi-)four-body baryon decays we have to extend the angular distribution and find

$$\begin{aligned}
\frac{\mathrm{d}^4\Gamma}{\mathrm{d}q^2 \mathrm{d}\cos\theta_\ell \mathrm{d}\cos\theta_\pi \mathrm{d}\phi} = \frac{3}{8\pi} \cdot \Big[& \left(K_{1ss} \sin^2\theta_\ell + K_{1cc} \cos^2\theta_\ell + K_{1c} \cos\theta_\ell\right) \\
& + \left(K_{2ss} \sin^2\theta_\ell + K_{2cc} \cos^2\theta_\ell + K_{2c} \cos\theta_\ell\right) \cos\theta_\pi \\
& + \left(K_{3sc} \sin\theta_\ell \cos\theta_\ell + K_{3s} \sin\theta_\ell\right) \sin\theta_\pi \sin\phi \\
& + \left(K_{4sc} \sin\theta_\ell \cos\theta_\ell + K_{4s} \sin\theta_\ell\right) \sin\theta_\pi \cos\phi \Big] \,,
\end{aligned} \tag{E.11}$$

with the q^2-dependent coefficients K_i again in the notation of [296]. Note, although we adapt the notation of helicity expressions $I_{iP}^{mm'}, i = 1, 2, 3, 4$ from [296], we use them to formulate angular observables in a notation similar to [311]. Note that we dropped the subscript P from $I_2^{mm'}$, $I_3^{mm'}$ since these two interference terms are parity-even. The first three terms K_{1ss}, K_{1cc} and K_{1c} are equivalent

to the three-body case, see Eq. (E.7), except for the additional factor $\mathcal{B}(B_1 \to B_2\pi)$,

$$\begin{aligned}
\frac{K_{1ss}}{\mathcal{B}(B_1 \to B_2\pi)} &= q^2\beta_\ell^2\left(\frac{1}{2}U^{11+22} + L^{11+22}\right) + 4m_\ell^2\left(U^{11} + L^{11} + S^{22}\right), \\
\frac{K_{1cc}}{\mathcal{B}(B_1 \to B_2\pi)} &= q^2\beta_\ell^2 U^{11+22} + 4m_\ell^2\left(U^{11} + L^{11} + S^{22}\right), \\
\frac{K_{1c}}{\mathcal{B}(B_1 \to B_2\pi)} &= -2q^2\beta_\ell P^{12}.
\end{aligned} \tag{E.12}$$

The remaining additional angular coefficients read

$$\begin{aligned}
\frac{K_{2ss}}{\mathcal{B}(B_1 \to B_2\pi)\cdot\alpha} &= q^2\beta_\ell^2\left(\frac{1}{2}P^{11+22} + L_P^{11+22}\right) + 4m_\ell^2\left(P^{11} + L_P^{11} + S_P^{22}\right), \\
\frac{K_{2cc}}{\mathcal{B}(B_1 \to B_2\pi)\cdot\alpha} &= q^2\beta_\ell^2 P^{11+22} + 4m_\ell^2\left(P^{11} + L_P^{11} + S_P^{22}\right), \\
\frac{K_{2c}}{\mathcal{B}(\mathcal{B}(B_1 \to B_2\pi)\cdot\alpha} &= -2q^2\beta_\ell U^{12}, \\
\frac{K_{3sc}}{\mathcal{B}(\mathcal{B}(B_1 \to B_2\pi)\cdot\alpha} &= -2\sqrt{2}q^2\beta_\ell^2 I_2^{11+22}, \\
\frac{K_{3s}}{\mathcal{B}(B_1 \to B_2\pi)\cdot\alpha} &= 4\sqrt{2}q^2\beta_\ell I_{4P}^{12}, \\
\frac{K_{4sc}}{\mathcal{B}(B_1 \to B_2\pi)\cdot\alpha} &= 2\sqrt{2}q^2\beta_\ell^2 I_{1P}^{11+22}, \\
\frac{K_{4s}}{\mathcal{B}(B_1 \to B_2\pi)\cdot\alpha} &= -4\sqrt{2}q^2\beta_\ell I_3^{12}.
\end{aligned} \tag{E.13}$$

The q^2-dependent terms U, L, S, P, L_P, S_P denote quadratic expressions of helicity amplitudes and correspond to unpolarized transverse, longitudinal, scalar, transverse parity-odd, longitudinal parity-odd and scalar parity-odd contributions, respectively. The coefficients I_{1P}, I_{4P} and I_2, I_3 correspond to longitudinal-transverse interference terms, where the subscript P refers to the parity-odd ones. We refer to App. F for further details. As already mentioned, there is an additional branching ratio factor in the coefficients K_{1ss}, K_{1cc} and K_{1c} compared to Eq. (E.7). For all other coefficients there is the polarization parameter α on top, such that in the limit $\mathcal{B}(B_1 \to B_2\pi) = 1$ and $\alpha = 0$ one returns to the distribution of the three-body case. Also, the coefficients in Eq. (E.8) are still valid in the four-body

case and the additional coefficients are given as

$$
\begin{aligned}
L_P^{11} &= -\frac{4N^2}{q^2}\cdot\mathrm{Re}\Bigg[\Bigg(\left(C_7+C_7'\right)2m_c h_+ + \left(C_9+C_9'\right)\left(m_{B_0}+m_{B_1}\right)f_+\Bigg) \\
&\qquad\cdot\Bigg(\left(C_7^*-C_7^{*\prime}\right)2m_c\tilde{h}_+ + \left(C_9^*-C_9^{*\prime}\right)\left(m_{B_0}-m_{B_1}\right)g_+\Bigg)\Bigg]\cdot\sqrt{s_+s_-}\,, \\
P^{11} &= -8N^2\cdot\mathrm{Re}\Bigg[\Bigg(\left(C_7+C_7'\right)\frac{2m_c}{q^2}h_\perp\left(m_{B_0}+m_{B_1}\right) + \left(C_9+C_9'\right)f_\perp\Bigg) \\
&\qquad\cdot\Bigg(\left(C_7^*-C_7^{*\prime}\right)\frac{2m_c}{q^2}\tilde{h}_\perp\left(m_{B_0}-m_{B_1}\right) + \left(C_9^*-C_9^{*\prime}\right)g_\perp\Bigg)\Bigg]\cdot\sqrt{s_+s_-}\,, \\
L_P^{22} &= -\frac{4N^2}{q^2}\cdot\Bigg[\left(|C_{10}|^2-|C_{10}'|^2\right)f_+g_+\left(m_{B_0}^2-m_{B_1}^2\right)\Bigg]\cdot\sqrt{s_+s_-}, \\
P^{22} &= -8N^2\cdot\Bigg[\left(|C_{10}|^2-|C_{10}'|^2\right)f_\perp g_\perp\Bigg]\cdot\sqrt{s_+s_-}\,, \\
U^{12} &= \quad 4N^2\cdot\Bigg[\Bigg(\mathrm{Re}\left(\left(C_7+C_7'\right)\left(C_{10}^*+C_{10}^{*\prime}\right)\right)f_\perp h_\perp\frac{2m_c}{q^2}\left(m_{B_0}+m_{B_1}\right) \\
&\qquad\quad+\mathrm{Re}\left(\left(C_9+C_9'\right)\left(C_{10}^*+C_{10}^{*\prime}\right)\right)f_\perp^2\Bigg)\cdot s_- \\
&\qquad+\Bigg(\mathrm{Re}\left(\left(C_7-C_7'\right)\left(C_{10}^*-C_{10}^{*\prime}\right)\right)g_\perp\tilde{h}_\perp\frac{2m_c}{q^2}\left(m_{B_0}-m_{B_1}\right) \\
&\qquad\quad+\mathrm{Re}\left(\left(C_9-C_9'\right)\left(C_{10}^*-C_{10}^{*\prime}\right)\right)g_\perp^2\Bigg)\cdot s_+\Bigg]\,, \\
S_P^{22} &= -\frac{4N^2}{q^2}\cdot\Bigg[\left(|C_{10}|^2-|C_{10}'|^2\right)f_0g_0\left(m_{B_0}^2-m_{B_1}^2\right)\Bigg]\cdot\sqrt{s_+s_-}\,.
\end{aligned}
\tag{E.14}
$$

Finally, the interference terms are given by

$$
\begin{aligned}
I_{1P}^{11} = \quad & N^2\sqrt{\frac{2}{q^2}}\cdot\Big[\mathrm{Re}((C_7-C_7')(C_7^*+C_7^{*\prime}))\,\frac{4m_c^2}{q^2}\cdot\Big(\tilde{h}_+h_\perp(m_{B_0}+m_{B_1})-h_+\tilde{h}_\perp(m_{B_0}-m_{B_1})\Big)\\
& +\mathrm{Re}((C_9-C_9')(C_9^*+C_9^{*\prime}))\cdot\Big(g_+f_\perp(m_{B_0}-m_{B_1})-f_+g_\perp(m_{B_0}+m_{B_1})\Big)\\
& +\mathrm{Re}((C_9-C_9')(C_7^*+C_7^{*\prime}))\,2m_c\cdot\left(g_+h_\perp\frac{m_{B_0}^2-m_{B_1}^2}{q^2}-h_+g_\perp\right)\\
& +\mathrm{Re}((C_7-C_7')(C_9^*+C_9^{*\prime}))\,2m_c\cdot\left(\tilde{h}_+f_\perp-f_+\tilde{h}_\perp\frac{m_{B_0}^2-m_{B_1}^2}{q^2}\right)\Big]\cdot\sqrt{s_+s_-}\,,\\
I_{1P}^{22} = \quad & N^2\sqrt{\frac{2}{q^2}}\cdot\Big[(|C_{10}|^2-|C_{10}'|^2)\cdot\Big(f_\perp g_+(m_{B_0}-m_{B_1})-f_+g_\perp(m_{B_0}+m_{B_1})\Big)\Big]\cdot\sqrt{s_+s_-},\\
I_2^{11} = 2m_c\,N^2 & \sqrt{\frac{2}{q^2}}\cdot\Big[\mathrm{Im}((C_9+C_9')(C_7^*+C_7^{*\prime}))\cdot\left(f_\perp h_+-f_+h_\perp\,\frac{(m_{B_0}+m_{B_1})^2}{q^2}\right)\cdot s_-\\
& -\mathrm{Im}((C_9-C_9')(C_7^*-C_7^{*\prime}))\cdot\left(g_\perp\tilde{h}_+-g_+\tilde{h}_\perp\,\frac{(m_{B_0}-m_{B_1})^2}{q^2}\right)\cdot s_+\Big]\,,\\
I_2^{22} = \quad & 0\,,\\
I_3^{12} = \quad & N^2\sqrt{\frac{2}{q^2}}\cdot\Big[\mathrm{Re}((C_7+C_7')(C_{10}^*+C_{10}^{*\prime}))\,m_c\cdot\left(h_+f_\perp+f_+h_\perp\frac{(m_{B_0}+m_{B_1})^2}{q^2}\right)\cdot s_-\\
& -\mathrm{Re}((C_7-C_7')(C_{10}^*-C_{10}^{*\prime}))\,m_c\cdot\left(\tilde{h}_+g_\perp+g_+\tilde{h}_\perp\frac{(m_{B_0}-m_{B_1})^2}{q^2}\right)\cdot s_+\\
& +\mathrm{Re}((C_9+C_9')(C_{10}^*+C_{10}^{*\prime}))\cdot\Big(f_+f_\perp(m_{B_0}+m_{B_1})\Big)\cdot s_-\\
& -\mathrm{Re}((C_9-C_9')(C_{10}^*-C_{10}^{*\prime}))\cdot\Big(g_+g_\perp(m_{B_0}-m_{B_1})\Big)\cdot s_+\Big]\,,
\end{aligned}
$$

$$
\begin{aligned}
I_{4P}^{12} = \quad & N^2\sqrt{\frac{2}{q^2}}\cdot\Big[\mathrm{Im}((C_7+C_7')(C_{10}^*-C_{10}^{*\prime}))\,m_c\cdot\left(h_\perp g_+\frac{m_{B_0}^2-m_{B_1}^2}{q^2}+h_+g_\perp\right)\\
& +\mathrm{Im}((C_7-C_7')(C_{10}^*+C_{10}^{*\prime}))\,m_c\cdot\left(\tilde{h}_\perp f_+\frac{m_{B_0}^2-m_{B_1}^2}{q^2}+\tilde{h}_+f_\perp\right)\\
& +\mathrm{Im}((C_9+C_9')(C_{10}^*-C_{10}^{*\prime}))\frac{1}{2}\cdot\Big(f_\perp g_+(m_{B_0}-m_{B_1})+f_+g_\perp(m_{B_0}+m_{B_1})\Big)\\
& +\mathrm{Im}((C_9-C_9')(C_{10}^*+C_{10}^{*\prime}))\frac{1}{2}\cdot\Big(g_\perp f_+(m_{B_0}+m_{B_1})+g_+f_\perp(m_{B_0}-m_{B_1})\Big)\Big]\\
& \cdot\sqrt{s_+s_-}\,.
\end{aligned}
\tag{E.15}
$$

All additional contributions in Eqs. (E.14)-(E.15) except U^{12}, I_2^{11} and I_3^{12} are P-odd, that is, change sign for $C_i \leftrightarrow C_i'$, and vanish for $C_i = C_i'$.

E.4 $a_\pm$ factors for dineutrino distributions

In this appendix, we collect explicit expressions for $a_\pm^{h_q F_{q'}}$ as defined in Sec. 6.1 in Eq. (6.8). We start with $c \to u\nu\bar{\nu}$ induced modes, followed by $b \to s\nu\bar{\nu}$ and $b \to q\nu\bar{\nu}$ transitions. For numerical values for lifetimes, masses and form factors we refer to Apps. A and C.

$a_\pm$ factors in $c \to u\nu\bar{\nu}$ induced modes

- For the $D \to P\nu\bar{\nu}$ mode, where $D = D^0, D^+, D_s^+$ and $P = \pi^0, \pi^+, K^+$, respectively, the $a_\pm^{DP}$–functions of the differential decay width can be written as

$$a_+^{DP}(q^2) = \frac{G_F^2\,\alpha_e^2\,\tau_D \lambda(m_D^2, m_P^2, q^2)^{\frac{3}{2}}\,(f_+^{DP}(q^2))^2}{3072\,\pi^5\,m_D^3}\,, \text{ and } \quad a_-^{DP}(q^2) = 0\,. \tag{E.16}$$

- The angular distributions of $D \to P_1\,P_2\,\nu\bar{\nu}$ decays is obtained from Ref. [88]. We obtain for the $a_\pm^{DP_1P_2}$–functions,

$$a_\pm^{DP_1P_2}(q^2) = \int_{(m_{P_1}+m_{P_2})^2}^{(m_D-\sqrt{q^2})^2} \mathrm{d}p^2 \int_{-1}^{1} \mathrm{d}\cos\theta_{P_1}\, b_\pm(q^2, p^2, \theta_{P_1})\,, \tag{E.17}$$

with

$$b_-(q^2, p^2, \theta_{P_1}) = \frac{\tau_D}{6}\left[|\mathcal{F}_0|^2 + \sin^2\theta_{P_1}|\mathcal{F}_\parallel|^2\right], \qquad b_+(q^2, p^2, \theta_{P_1}) = \frac{\tau_D}{6}\,\sin^2\theta_{P_1}|\mathcal{F}_\perp|^2\,, \tag{E.18}$$

where p^2 denotes the invariant mass-squared of the (P_1P_2)-subsystem. θ_{P_1} is the angle between the P_1-momentum and the negative direction of flight of the D–meson in the (P_1P_2)-cms.

- For $\Lambda_c^+ \to p\,\nu\,\bar{\nu}$, $\Xi_c^+ \to \Sigma^+\,\nu\bar{\nu}$ and further baryon modes we find with N from Eq. (E.9)

$$\begin{aligned} a_+^{h_c^+ F}(q^2) &= \tau_{h_c}\,N \cdot \left(2f_\perp^2 s_- + f_+^2 (m_{h_c^+} + m_F)^2 \frac{s_-}{q^2}\right), \\ a_-^{h_c^+ F}(q^2) &= \tau_{h_c}\,N \cdot \left(2g_\perp^2 s_+ + g_+^2 (m_{h_c^+} - m_F)^2 \frac{s_+}{q^2}\right). \end{aligned} \tag{E.19}$$

- For $D \to X\,\nu\,\bar{\nu}$ decays, the inclusive hadronic final state either has flavor quantum number of an up-quark, $X = \pi, \pi\pi, \ldots$, for $D^{0,+}$ decays or of an anti-strange quark for D_s^+ decays, $X = K, K\pi, \ldots$. Then the corresponding dineutrino mass distribution can be written in terms of

$a_\pm^{DX}$ as [312]

$$a_\pm^{DX}(q^2) = \frac{G_{\rm F}^2\,\alpha_e^2\,\tau_D\,m_c^3}{2^{10}\,3\,\pi^5}\,\kappa(0)\,f_{\rm incl.}(q^2)\,, \tag{E.20}$$

where

$$f_{\rm incl.}(q^2) \;=\; \left(1-\frac{q^2}{m_c^2}\right)^2\left[1+2\,\frac{q^2}{m_c^2}\right]\,,\;\text{and}\quad \kappa(0)=1\,+\,\frac{\alpha_s(m_c)}{\pi}\left[\frac{25}{6}-\frac{2}{3}\,\pi^2\right]\approx 0.71\,. \tag{E.21}$$

The latter is the QCD correction to the $c\to u\,\nu\bar\nu$ matrix element inferred from Ref. [313].

$a_\pm$ factors in $b\to q\nu\bar\nu$ induced modes

- In the case of the $B\to P\nu_i\bar\nu_j$ mode, where $B=B^0$, B^+ and $P=\pi^0$, π^+, K^0, K^+, respectively, the a_+^{BP}–function of the differential branching ratio is identical to Eq. (E.16) when replacing masses, lifetimes and form factors, in agreement with Refs. [274, 314, 315].

- We obtain for $B\to V\nu_i\bar\nu_j$ [312, 314, 315]

$$\begin{aligned} a_+^{BV}(q^2) &= \frac{G_F^2\,\alpha_e^2\,\tau_B\,(\lambda_{BV}(q^2))^{3/2}}{3072\,\pi^5\,m_B^5\,c_V^2}\,\frac{2\,q^2\,(V(q^2))^2}{\left(1+\frac{m_V}{m_B}\right)^2}\,,\\ a_-^{BV}(q^2) &= \frac{G_F^2\,\alpha_e^2\,\tau_B\,(\lambda_{BV}(q^2))^{1/2}}{1536\,\pi^5\,m_B\,c_V^2}\cdot\left[32\,m_V^2(A_{12}(q^2))^2+\left(1+\frac{m_V}{m_B}\right)^2 q^2(A_1(q^2))^2\right]\,, \end{aligned} \tag{E.22}$$

where $\lambda_{BV}(q^2)=\lambda(m_B^2,m_V^2,q^2)$ and the parameter c_P accounts for the flavor content of the vector particles, in particular $c_{\rho^0}=\sqrt{2}$ and $c_{\rho^+,K^{*0},K^{*+},\phi}=1$.

- The functions $a_\pm^{BX_q}$ associated with $B\to X_q\,\nu_i\bar\nu_j$ with $q=d,s$ transitions are given by [312]

$$a_\pm^{BX_q}(q^2) = \frac{G_F^2\,\alpha_e^2\,\tau_B\,\kappa(0)}{3072\,\pi^5\,m_b^3}\sqrt{\lambda(m_b^2,m_q^2,q^2)}\cdot\left[\lambda(m_b^2,m_q^2,q^2)+3\,q^2\left(m_b^2+m_q^2-q^2\right)\right]\,, \tag{E.23}$$

where $\kappa(0)=1\,+\,\frac{\alpha_s(m_b)}{\pi}\left[\frac{25}{6}-\frac{2}{3}\,\pi^2\right]\approx 0.83$ includes QCD corrections to the $b\to q\,\nu\bar\nu$ matrix element due to virtual and bremsstrahlung contributions [313].

F Helicity formalism and helicity amplitudes for baryon decays

In this appendix, we give an introduction to the helicity formalism, and calculate helicity amplitudes for three- and four-body baryon decays as well as amplitudes for the hadronic baryon decay $B_1 \to B_2\pi$, leading to contributions to angular coefficients as displayed in the App. E.2 and E.3.

F.1 Introduction to the helicity formalism

This brief introduction to the helicity formalism is based on Refs. [190–193]. We consider the two-body decay of a particle α in its rest frame with spin J and spin projection M along an arbitrarily chosen z-axis. In the rest frame of particle α the momenta of the decay products are of equal size and opposite in direction, $\vec{p}_1 = \vec{p}_f$ and $\vec{p}_1 = -\vec{p}_f$. The helicities of the final state particles are labeled as λ_1, λ_2, such that the final state is characterized by the helicities and the direction of the decay axis with respect to the z-axis. Given the time-evolution operator propagating the initial state through the interaction U, the transition amplitude is given by

$$A = \langle \theta,\, \phi,\, \lambda_1,\, \lambda_2 | U | J\, M \rangle \,, \tag{F.1}$$

and $|A|^2$ defines the angular distribution for the helicity configuration λ_1, λ_2. If these helicities are not measured, one has to sum over all possible configurations. The main idea of the helicity formalism is to utilize rotation invariance of the helicities and define a complete set of two-particle basis states $|j,\, m,\, \lambda_1,\, \lambda_2\rangle$ with total angular momentum j and angular momentum projection m. We can insert a complete set in Eq. (F.1) and find

$$\begin{aligned} A &= \sum_{j,\,m} \langle \theta,\, \phi,\, \lambda_1,\, \lambda_2 | j,\, m,\, \lambda_1,\, \lambda_2 \rangle \langle j,\, m,\, \lambda_1,\, \lambda_2 | U | J\, M \rangle \\ &= \sum_{j,\,m} \langle \theta,\, \phi,\, \lambda_1,\, \lambda_2 | j,\, m,\, \lambda_1,\, \lambda_2 \rangle \delta_{mM} \delta_{jJ} A^J_{M,\,\lambda_1,\,\lambda_2} \\ &= \langle \theta,\, \phi,\, \lambda_1,\, \lambda_2 | J,\, M,\, \lambda_1,\, \lambda_2 \rangle A^J_{M,\,\lambda_1,\,\lambda_2} \,. \end{aligned} \tag{F.2}$$

It can be shown that this transition amplitude factorizes into [190, 191]

$$A = \sqrt{\frac{2J+1}{4\pi}} D^{*J}_{M,\,\lambda_1-\lambda_2}(\phi,\, \theta,\, -\phi) \cdot A^J_{M,\,\lambda_1,\,\lambda_2} \,, \tag{F.3}$$

where $A^J_{M,\,\lambda_1,\,\lambda_2}$ is a helicity amplitude and $D^J_{M,\,\lambda_1-\lambda_2}(\phi,\, \theta,\, -\phi)$ is a Wigner D–function, which is a $(2J+1)$-dimensional $SO(3)$ representation in the helicity basis and

$$D^j_{m',\,m}(\alpha,\, \beta,\, \gamma) = \exp(-\mathrm{i}\alpha m')\, d^j_{m,\,m'}(\beta)\, \exp(-\mathrm{i}\gamma m) \,, \tag{F.4}$$

with the Wigner d–functions [316]

$$d^j_{m,\,m'}(\beta) = \sum_{k=k_{\min}}^{k_{\max}} (-1)^{k-m+m'} \frac{\sqrt{(j+m)!(j-m)!(j+m')!(j-m')!}}{(j+m-k)!(j-k-m')!(k-m+m')!k!} \times \left(\cos\frac{\beta}{2}\right)^{2j-2k+m-m'} \left(\sin\frac{\beta}{2}\right)^{2k-m+m'}, \tag{F.5}$$

with k an integer such that $k_{\min} = \min\{0,\, m-m'\} \geq -2j$ and $k_{\max} = \max\{0,\, j+m,\, j-m'\} \leq 2j$, which enforces positive factorials in the denominator. The Wigner d–functions obey

$$d^j_{m',\,m} = (-1)^{m-m'} d^j_{m,\,m'} = d^j_{-m,\,-m'}\,. \tag{F.6}$$

The main advantage of this procedure is that it is straightforward to apply it to sequential decays, *e.g.* the amplitude for $\alpha \to aB(\to bc)$ can be written as

$$A(\alpha \to aB(\to bc)) \propto \sum_{\lambda_B} D^{*s_B}_{\lambda_B,\,\lambda_b-\lambda_c}(\phi_b,\,\theta_b,\,-\phi_b)\, D^{*J}_{\lambda_B=M,\,\lambda_B-\lambda_a}(\phi_B,\,\theta_B,\,-\phi_B)\, A^J_{\lambda_a,\,\lambda_B}\, B^{s_B}_{\lambda_b,\,\lambda_c}\,, \tag{F.7}$$

where one can further simplify be choosing $\vec{e}_z \parallel \vec{p}_B$, because then $\theta_B = 0$ and $d^J_{m,\,m'}(0) = \delta_{m,\,m'}$ yielding

$$A(\alpha \to aB(\to bc)) \propto \sum_{\lambda_B} D^{*s_B}_{\lambda_B,\,\lambda_b-\lambda_c}(\phi_b,\,\theta_b,\,-\phi_b)\, \delta_{M,\,\lambda_B-\lambda_a}\, A^J_{\lambda_a,\,\lambda_B}\, B^{s_B}_{\lambda_b,\,\lambda_c}\,. \tag{F.8}$$

The intermediate helicity λ_B needs to be summed over and two helicity amplitudes describing $\alpha \to aB$ and $B \to bc$, respectively, appear.

In the framework of semileptonic rare charm baryon decays, governed by an EFT description with factorizing lepton and hadron part this intermediate particle can be seen as a virtual photon, where one has to sum over all four helicity configurations. To see this consider the three-body $\Lambda_c \to p\ell^+\ell^-$ decay- we write

$$\langle p\ell^+\ell^-|\mathcal{H}_{\text{eff}}|\Lambda_c\rangle = \sum_a \langle H_a\rangle\langle L^a\rangle + \sum_b \langle H^\mu_b\rangle\langle L^b_\mu\rangle\,, \tag{F.9}$$

where a, b sum over contributions from different operators, for instance $\langle H_P\rangle = \langle p|C_P\bar{u}_L c_R|\Lambda_C\rangle$ and $\langle L^P\rangle = \langle \ell^+\ell^-|\bar{\ell}\gamma_5\ell|0\rangle$. For the operators involving one Lorentz index μ we rewrite the contraction between hadron and lepton part as

$$g^{\mu\nu} = \sum_{\lambda,\,\lambda'=t,\,0,\,\pm} \epsilon^\mu(\lambda)\epsilon^{*\nu}(\lambda')G_{\lambda\lambda'}, \quad G_{\lambda\lambda'} = \text{diag}(1,\,-1,\,-1,\,-1)\,. \tag{F.10}$$

By doing so we distinguish the two contributions with $\lambda = 0$ as follows: For $J = 0$ we use $\lambda = t$ instead of 0 and for $J = 1$ we use $\lambda = 0$. Also $\lambda = \pm$ refers to $\lambda = \pm 1$ in the $J = 1$ case. We use the

polarization vectors

$$\epsilon^\mu(t) = (1,\,0,\,0,\,0)^{\mathrm{T}}\,, \quad \epsilon^\mu(0) = (0,\,0,\,0,\,1)^{\mathrm{T}}\,, \quad \epsilon^\mu(\pm) = \frac{1}{\sqrt{2}}\,(0,\,\pm 1,\,-\mathrm{i},\,0)^{\mathrm{T}}\,. \tag{F.11}$$

Due to this procedure the lepton amplitude and the hadron amplitude individually are Lorentz invariant and thus can be calculated in different frames. In the following section we explicitly construct the hadron and lepton helicity amplitudes for the three- and four-body baryon decays. The angular dependence is then given via

$$\begin{aligned} A(\Lambda_c \to p\ell^+\ell^-) &\propto \sum_{\lambda_\gamma,\,J_\gamma} D^{*J_\gamma}_{\lambda_\gamma,\,\lambda_+-\lambda_-}(\phi_l,\,\theta_l,\,-\phi_\ell)\delta_{\lambda_{\Lambda_c},\lambda_\gamma-\lambda_p} A^{J_\gamma}_{\lambda_\gamma\,\lambda_+,\lambda_-}\,, \\ A(\Xi_c^+ \to \Sigma^+(\to p\pi^0)\ell^+\ell^-) &\propto \sum_{\lambda_\gamma,\,J_\gamma,\lambda_\Sigma} D^{*J_\gamma}_{\lambda_\gamma,\,\lambda_+-\lambda_-}(\phi_l,\,\theta_l,\,-\phi_\ell)\delta_{\lambda_{\Xi_c},\lambda_\gamma-\lambda_\Sigma} A^{J_\gamma}_{\lambda_\gamma\,\lambda_+,\lambda_-} \\ &\qquad \times D^{*\frac{1}{2}}_{\lambda_\Sigma,\,\lambda_p}(\phi_p,\,\theta_\pi,\,-\phi_p) h^{\frac{1}{2}}_{\lambda_\Sigma,\lambda_p}\,, \end{aligned} \tag{F.12}$$

for the three- and four-body decays, respectively. Note that the angular distribution is obtained by squaring Eq. (F.12) and one has to introduce two sets of intermediate angular momenta and helicities J_γ, λ_γ plus J'_γ, λ'_γ in the three-body case and J_γ, λ_γ, λ_Σ plus J'_γ, λ'_γ, λ'_Σ in the four-body case. All possible combinations need to be summed. In addition, one needs to average over initial state helicities and sum over final state helicities. As a last step in the three-body case, one can integrate over the angle ϕ_l and is left with the dilepton invariant mass squared q^2 and one angle, θ_ℓ, whereas in the four-body case one can get rid of only one of the two ϕ angles, thus resulting in the dependence on $q^2, \theta_\ell,\, \theta_\pi,\, \phi$.

F.2 Helicity amplitudes for three- and four-body baryon decays

The helicity amplitudes needed in Eq. (F.12) are $A^{J_\gamma}_{\lambda_\gamma\,\lambda_+,\lambda_-}$ and $h^{\frac{1}{2}}_{\lambda_\Sigma,\lambda_p}$. While the calculation of the latter is performed in App. F.3, we outline the calculation of $A^{J_\gamma}_{\lambda_\gamma\,\lambda_+,\lambda_-}$ here. It is decomposed as

$$A^{J_\gamma}_{\lambda_\gamma\,\lambda_+,\lambda_-} = \begin{cases} \sum_a \langle H_a\rangle\langle L^a\rangle + \sum_b \mathcal{H}^b_{\lambda_p,\,t}\mathcal{L}^b_{t,\,\lambda_+,\,\lambda_-} & \text{for} \quad J_\gamma = 0\,, \\ \sum_b \mathcal{H}^b_{\lambda_p,\,\lambda_\gamma}\mathcal{L}^b_{\lambda_\gamma,\,\lambda_+,\,\lambda_-} & \text{for} \quad J_\gamma = 1\,, \end{cases} \tag{F.13}$$

where

$$\mathcal{H}^b_{\lambda_p,\,\lambda_\gamma} = \langle H^\mu_b\rangle \epsilon^*_\mu(\lambda_\gamma)\,, \qquad \mathcal{L}^b_{\lambda_\gamma,\,\lambda_+\,\lambda_-} = \langle L^\mu_b\rangle \epsilon_\mu(\lambda_\gamma)\,. \tag{F.14}$$

For the remainder of this calculation we particularize to the $\Lambda_c \to p\ell^+\ell^-$ case, with momenta p for the Λ_c, k for the proton and q_+, q_- for the leptons and obvious notation for the respective helicities. Note that due to the Kronecker delta the Λ_c helicity is fixed by $\lambda_c = \lambda_\gamma - \lambda_p$. For the pseudoscalar

contributions two hadronic matrix elements contribute, whereas only one lepton amplitude is taken into account

$$\langle H_1^P\rangle = C_P\langle p(k)|\bar{u}c|\Lambda_c(p)\rangle\,, \qquad \langle H_2^P\rangle = C_P\langle p(k)|\bar{u}\gamma_5 c|\Lambda_c(p)\rangle\,, \qquad \langle L^P\rangle = \bar{u}_\ell(q_-)\gamma_5 v_\ell(q^+)\,. \quad \text{(F.15)}$$

For the contributions with open Lorentz index, more combinations are possible and we sort by hadronic matrix elements four different hadron amplitudes, and further indicate with an upper index 1, 2 whether the hadron amplitude is multiplied with a vector lepton current (upper index 1) or an axial vector lepton current (upper index 2),

$$\begin{aligned}
\langle H_1^{1\mu}\rangle =& -\frac{2m_c}{q^2}\,(C_7 + C_7')\,\langle p(k)|\bar{u}\mathrm{i}\sigma^{\mu\nu}q_\nu|\Lambda_c(p)\rangle\,,\\
\langle H_2^{1\mu}\rangle =& -\frac{2m_c}{q^2}\,(C_7 - C_7')\,\langle p(k)|\bar{u}\mathrm{i}\sigma^{\mu\nu}q_\nu\gamma_5|\Lambda_c(p)\rangle\,,\\
\langle H_3^{1\mu}\rangle =& (C_9 + C_9')\,\langle p(k)|\bar{u}\gamma_\mu|\Lambda_c(p)\rangle\,,\\
\langle H_4^{1\mu}\rangle =& (C_9 - C_9')\,\langle p(k)|\bar{u}\gamma_\mu\gamma_5|\Lambda_c(p)\rangle\,,\\
\langle H_3^{2\mu}\rangle =& (C_{10} + C_{10}')\,\langle p(k)|\bar{u}\gamma_\mu|\Lambda_c(p)\rangle\,,\\
\langle H_4^{2\mu}\rangle =& (C_{10} - C_{10}')\,\langle p(k)|\bar{u}\gamma_\mu\gamma_5|\Lambda_c(p)\rangle\,,
\end{aligned} \quad \text{(F.16)}$$

and the two lepton amplitudes read

$$\langle L_\mu^1\rangle = \bar{u}_\ell(q_-)\gamma_\mu v_\ell(q^+)\,, \qquad \langle L_\mu^2\rangle = \bar{u}_\ell(q_-)\gamma_\mu\gamma_5 v_\ell(q^+)\,. \quad \text{(F.17)}$$

Now, one hadron helicity amplitude $\mathcal{H}^m_{\lambda_p,\lambda_\gamma}$ for $m = 1, 2$ is given by the sum of the four (two) contributions with upper index m=1 (m=2) in Eq. (F.16). As anticipated the calculation of the individual hadron and lepton helicity amplitudes can be done in different frames. For the hadrons we choose the rest frame of the Λ_c, where

$$p^\mu = \begin{pmatrix} m_{\Lambda_c} \\ 0 \\ 0 \\ 0 \end{pmatrix}\,, \quad k^\mu = \begin{pmatrix} E_p \\ 0 \\ 0 \\ -|\vec{k}| \end{pmatrix}\,, \quad q^\mu = \begin{pmatrix} q_0 \\ 0 \\ 0 \\ |\vec{k}| \end{pmatrix}\,, \quad \text{(F.18)}$$

with $q^\mu = q_+^\mu + q_-^\mu$ and

$$E_p = m_{\Lambda_c} - q_0\,, \qquad q_0 = \frac{m_{\Lambda_c}^2 - m_p^2 + q^2}{2m_{\Lambda_c}}\,. \quad \text{(F.19)}$$

In this reference frame, the hadron spinors read with $\chi_+ = (1,\,0)^T$ and $\chi_- = (0,\,1)^T$ [192]

$$u_{\Lambda_c}\left(p,\,\lambda_{\Lambda_c}=\pm\frac{1}{2}\right)=\sqrt{2m_{\Lambda_c}}\begin{pmatrix}\chi_\pm\\0\end{pmatrix},\quad \bar{u}_p\left(k,\,\lambda_p=\pm\frac{1}{2}\right)=\sqrt{E_p+m_p}\left(\chi_\mp^\dagger,\,\frac{\mp|\vec{k}|}{E_p+m_p}\chi_\mp^\dagger\right). \tag{F.20}$$

These amplitudes then enter the angular observables. Following Ref. [296] we introduce ($m^{(\prime)}=1,\,2$)

$$\begin{aligned}
S^{mm'} &= N^2\cdot\mathrm{Re}\left[\mathcal{H}^m_{\frac{1}{2},t}\mathcal{H}^{\dagger m'}_{\frac{1}{2},t}+\mathcal{H}^m_{-\frac{1}{2},t}\mathcal{H}^{\dagger m'}_{-\frac{1}{2},t}\right],\\
S_P^{mm'} &= N^2\cdot\mathrm{Re}\left[\mathcal{H}^m_{\frac{1}{2},t}\mathcal{H}^{\dagger m'}_{\frac{1}{2},t}-\mathcal{H}^m_{-\frac{1}{2},t}\mathcal{H}^{\dagger m'}_{-\frac{1}{2},t}\right],\\
U^{mm'} &= N^2\cdot\mathrm{Re}\left[\mathcal{H}^m_{\frac{1}{2},1}\mathcal{H}^{\dagger m'}_{\frac{1}{2},1}+\mathcal{H}^m_{-\frac{1}{2},-1}\mathcal{H}^{\dagger m'}_{-\frac{1}{2},-1}\right],\\
P^{mm'} &= N^2\cdot\mathrm{Re}\left[\mathcal{H}^m_{\frac{1}{2},1}\mathcal{H}^{\dagger m'}_{\frac{1}{2},1}-\mathcal{H}^m_{-\frac{1}{2},-1}\mathcal{H}^{\dagger m'}_{-\frac{1}{2},-1}\right],\\
L^{mm'} &= N^2\cdot\mathrm{Re}\left[\mathcal{H}^m_{\frac{1}{2},0}\mathcal{H}^{\dagger m'}_{\frac{1}{2},0}+\mathcal{H}^m_{-\frac{1}{2},0}\mathcal{H}^{\dagger m'}_{-\frac{1}{2},0}\right],\\
L_P^{mm'} &= N^2\cdot\mathrm{Re}\left[\mathcal{H}^m_{\frac{1}{2},0}\mathcal{H}^{\dagger m'}_{\frac{1}{2},0}-\mathcal{H}^m_{-\frac{1}{2},0}\mathcal{H}^{\dagger m'}_{-\frac{1}{2},0}\right],\\
I_{1P}^{mm'} &= \frac{N^2}{4}\cdot\mathrm{Re}\left[\mathcal{H}^m_{\frac{1}{2},1}\mathcal{H}^{\dagger m'}_{-\frac{1}{2},0}+\mathcal{H}^m_{-\frac{1}{2},0}\mathcal{H}^{\dagger m'}_{\frac{1}{2},1}-\mathcal{H}^m_{\frac{1}{2},0}\mathcal{H}^{\dagger m'}_{-\frac{1}{2},-1}-\mathcal{H}^m_{-\frac{1}{2},-1}\mathcal{H}^{\dagger m'}_{\frac{1}{2},0}\right],\\
I_2^{mm'} &= \frac{N^2}{4}\cdot\mathrm{Im}\left[\mathcal{H}^m_{\frac{1}{2},1}\mathcal{H}^{\dagger m'}_{-\frac{1}{2},0}-\mathcal{H}^m_{-\frac{1}{2},0}\mathcal{H}^{\dagger m'}_{\frac{1}{2},1}-\mathcal{H}^m_{\frac{1}{2},0}\mathcal{H}^{\dagger m'}_{-\frac{1}{2},-1}+\mathcal{H}^m_{-\frac{1}{2},-1}\mathcal{H}^{\dagger m'}_{\frac{1}{2},0}\right],\\
I_3^{mm'} &= \frac{N^2}{4}\cdot\mathrm{Re}\left[\mathcal{H}^m_{\frac{1}{2},1}\mathcal{H}^{\dagger m'}_{-\frac{1}{2},0}+\mathcal{H}^m_{-\frac{1}{2},0}\mathcal{H}^{\dagger m'}_{\frac{1}{2},1}+\mathcal{H}^m_{\frac{1}{2},0}\mathcal{H}^{\dagger m'}_{-\frac{1}{2},-1}+\mathcal{H}^m_{-\frac{1}{2},-1}\mathcal{H}^{\dagger m'}_{\frac{1}{2},0}\right],\\
I_{4P}^{mm'} &= \frac{N^2}{4}\cdot\mathrm{Im}\left[\mathcal{H}^m_{\frac{1}{2},1}\mathcal{H}^{\dagger m'}_{-\frac{1}{2},0}-\mathcal{H}^m_{-\frac{1}{2},0}\mathcal{H}^{\dagger m'}_{\frac{1}{2},1}+\mathcal{H}^m_{\frac{1}{2},0}\mathcal{H}^{\dagger m'}_{-\frac{1}{2},-1}-\mathcal{H}^m_{-\frac{1}{2},-1}\mathcal{H}^{\dagger m'}_{\frac{1}{2},0}\right],
\end{aligned} \tag{F.21}$$

where the flipping of helicities results in a minus sign for the amplitudes $a=2$ and $a=4$, due to parity

$$\begin{aligned}
\mathcal{H}^1_{\lambda_p,\lambda_\gamma} &= \mathcal{H}^{1,1}_{\lambda_p,\lambda_\gamma}+\mathcal{H}^{2,1}_{\lambda_p,\lambda_\gamma}+\mathcal{H}^{3,1}_{\lambda_p,\lambda_\gamma}+\mathcal{H}^{4,1}_{\lambda_p,\lambda_\gamma},\\
\mathcal{H}^1_{-\lambda_p,-\lambda_\gamma} &= \mathcal{H}^{1,1}_{\lambda_p,\lambda_\gamma}-\mathcal{H}^{2,1}_{\lambda_p,\lambda_\gamma}+\mathcal{H}^{3,1}_{\lambda_p,\lambda_\gamma}-\mathcal{H}^{4,1}_{\lambda_p,\lambda_\gamma},\\
\mathcal{H}^2_{\lambda_p,\lambda_\gamma} &= \mathcal{H}^{3,2}_{\lambda_p,\lambda_\gamma}+\mathcal{H}^{4,2}_{\lambda_p,\lambda_\gamma},\\
\mathcal{H}^2_{-\lambda_p,-\lambda_\gamma} &= \mathcal{H}^{3,2}_{\lambda_p,\lambda_\gamma}-\mathcal{H}^{4,2}_{\lambda_p,\lambda_\gamma}.
\end{aligned} \tag{F.22}$$

For convenience we give the list of single contributions below with $s_\pm = (m_{\Lambda_c} \pm m_p)^2 - q^2$

$\lambda_{\Lambda_c} = \frac{1}{2}$, $\lambda_\gamma = t$:

$$\begin{aligned}
\mathcal{H}^{1,1}_{-\frac{1}{2},t} &= 0\,, \\
\mathcal{H}^{2,1}_{-\frac{1}{2},t} &= 0\,, \\
\mathcal{H}^{3,1(2)}_{-\frac{1}{2},t} &= (C_{9(10)} + C'_{9(10)})\frac{\sqrt{s_+}}{\sqrt{q^2}} f_0(q^2)(m_{\Xi_c} - m_\Sigma)\,, \\
\mathcal{H}^{4,1(2)}_{-\frac{1}{2},t} &= (C_{9(10)} - C'_{9(10)})\frac{\sqrt{s_-}}{\sqrt{q^2}} g_0(q^2)(m_{\Xi_c} + m_\Sigma)\,,
\end{aligned} \tag{F.23}$$

$\lambda_{\Lambda_c} = -\frac{1}{2}$, $\lambda_\gamma = 0$:

$$\begin{aligned}
\mathcal{H}^{1,1}_{\frac{1}{2},0} &= (C_7 + C'_7)\frac{2m_c}{\sqrt{q^2}}\sqrt{s_-} h_+(q^2)\,, \\
\mathcal{H}^{2,1}_{\frac{1}{2},0} &= -(C_7 - C'_7)\frac{2m_c}{\sqrt{q^2}}\sqrt{s_+}\tilde{h}_+(q^2)\,, \\
\mathcal{H}^{3,1(2)}_{\frac{1}{2},0} &= (C_{9(10)} + C'_{9(10)})\frac{1}{\sqrt{q^2}}\sqrt{s_-} f_+(q^2)(m_{\Xi_c} + m_\Sigma)\,, \\
\mathcal{H}^{4,1(2)}_{\frac{1}{2},0} &= -(C_{9(10)} - C'_{9(10)})\frac{1}{\sqrt{q^2}}\sqrt{s_+} g_+(q^2)(m_{\Xi_c} - m_\Sigma)\,,
\end{aligned} \tag{F.24}$$

$\lambda_{\Lambda_c} = \frac{1}{2}$, $\lambda_\gamma = 1$:

$$\begin{aligned}
\mathcal{H}^{1,1}_{\frac{1}{2},1} &= \sqrt{2}(C_7 + C'_7)\frac{2m_c}{q^2}\sqrt{s_-} h_\perp(q^2)(m_{\Xi_c} + m_\Sigma)\,, \\
\mathcal{H}^{2,1}_{\frac{1}{2},1} &= -\sqrt{2}(C_7 - C'_7)\frac{2m_c}{q^2}\sqrt{s_+}\tilde{h}_\perp(q^2)(m_{\Xi_c} - m_\Sigma)\,, \\
\mathcal{H}^{3,1(2)}_{\frac{1}{2},1} &= \sqrt{2}(C_{9(10)} + C'_{9(10)})\sqrt{s_-} f_\perp(q^2)\,, \\
\mathcal{H}^{4,1(2)}_{\frac{1}{2},1} &= -\sqrt{2}(C_{9(10)} - C'_{9(10)})\sqrt{s_+} g_\perp(q^2)\,.
\end{aligned} \tag{F.25}$$

Similarly, for the easier case of the pseudoscalar contribution, we find from parity

$$\begin{aligned}
\mathcal{H}^{P}_{\lambda_p} &= \mathcal{H}^{P,1}_{\lambda_p} + \mathcal{H}^{P,2}_{\lambda_p}\,, \\
\mathcal{H}^{P}_{-\lambda_p} &= \mathcal{H}^{P,1}_{\lambda_p} - \mathcal{H}^{P,2}_{\lambda_p}\,,
\end{aligned} \tag{F.26}$$

with $\lambda_{\Lambda_c} = \frac{1}{2}$, $\lambda_\gamma = t$:

$$\mathcal{H}^{P,1}_{-\frac{1}{2}} = C_P \frac{m_{\Lambda_c} - m_p}{m_c} \sqrt{s_+} f_0(q^2)\,, \qquad \mathcal{H}^{P,2}_{-\frac{1}{2}} = C_P \frac{m_{\Lambda_c} + m_p}{m_c} \sqrt{s_-} g_0(q^2)\,. \tag{F.27}$$

For the lepton helicity amplitudes we use the dilepton center of mass frame, where

$$q^\mu_+ = \begin{pmatrix} \frac{\sqrt{q^2}}{2} \\ 0 \\ 0 \\ |\vec{q}| \end{pmatrix}, \quad q^\mu_- = \begin{pmatrix} \frac{\sqrt{q^2}}{2} \\ 0 \\ 0 \\ -|\vec{q}| \end{pmatrix}, \quad q^\mu = \begin{pmatrix} \sqrt{q^2} \\ 0 \\ 0 \\ 0 \end{pmatrix}, \tag{F.28}$$

and we choose the z-axis in the direction of the ℓ^+ momentum, such that [192]

$$u(\lambda) = \begin{pmatrix} \sqrt{\frac{\sqrt{q^2}}{2} + m_\ell}\, \chi_\lambda(-\vec{e}_z) \\ 2\lambda \sqrt{\frac{\sqrt{q^2}}{2} - m_\ell}\, \chi_\lambda(-\vec{e}_z) \end{pmatrix}, \qquad v(\lambda) = \begin{pmatrix} \sqrt{\frac{\sqrt{q^2}}{2} - m_\ell}\, \chi_{-\lambda}(\vec{e}_z) \\ -2\lambda \sqrt{\frac{\sqrt{q^2}}{2} + m_\ell}\, \chi_{-\lambda}(\vec{e}_z) \end{pmatrix}, \tag{F.29}$$

where $\chi_+(\vec{e}_z) = (1,\, 0)^T$ and $\chi_-(\vec{e}_z) = (0,\, 1)^T$. We obtain the following lepton helicity amplitudes for $m = 1$

$$\mathcal{L}^1_{t,\,\frac{1}{2},\,\frac{1}{2}} = 0\,, \qquad \mathcal{L}^1_{0,\,\frac{1}{2},\,\frac{1}{2}} = -2\, m_\ell\,, \qquad \mathcal{L}^1_{+1,\,\frac{1}{2},\,-\frac{1}{2}} = -\sqrt{2q^2}\,, \tag{F.30}$$

and for $m = 2$

$$\mathcal{L}^2_{t,\,\frac{1}{2},\,\frac{1}{2}} = -2\, m_\ell\,, \qquad \mathcal{L}^2_{0,\,\frac{1}{2},\,\frac{1}{2}} = 0\,, \qquad \mathcal{L}^2_{+1,\,\frac{1}{2},\,-\frac{1}{2}} = \sqrt{2q^2}\sqrt{1 - \frac{4m_\ell^2}{q^2}}\,. \tag{F.31}$$

Again we relate to other helicity configurations via parity behavior, which implies

$$\begin{aligned} \mathcal{L}^1_{-\lambda_\gamma,\,-\lambda_+,\,-\lambda_-} &= \mathcal{L}^1_{\lambda_\gamma,\,\lambda_+,\,\lambda_-}\,, \\ \mathcal{L}^2_{-\lambda_\gamma,\,-\lambda_+,\,-\lambda_-} &= -\mathcal{L}^2_{\lambda_\gamma,\,\lambda_+,\,\lambda_-}\,. \end{aligned} \tag{F.32}$$

The last ingredient is the lepton amplitude for the pseudoscalar contribution, which we find to be

$$\mathcal{L}^P_{\frac{1}{2},\,\frac{1}{2}} = -\mathcal{L}^P_{-\frac{1}{2},\,-\frac{1}{2}} = -\sqrt{q^2}\,. \tag{F.33}$$

Our results are in agreement with Refs. [194, 296] and Ref. [311] in the limit of vanishing lepton masses. We stress that results for the helicity amplitudes are given for $\Lambda_c \to p\ell^+\ell^-$, but also apply to all other modes with appropriate replacements of masses and form factors.

F.3 Helicity amplitude description of $B_1 \to B_2\pi$

We now turn to the calculation of the hadronic helicity amplitude $h^{\frac{1}{2}}_{\lambda_\Sigma,\lambda_p}$ for the secondary baryonic decay $B_1 \to B_2\pi$, here discussed for $\Sigma^+ \to p\pi^0$. The two-body decay is parameterized by the sum, α_+, and the difference, α_-, of the helicity amplitudes squared

$$\alpha_\pm = \left|h^{\frac{1}{2}}_{\frac{1}{2},\frac{1}{2}}\right|^2 \pm \left|h^{\frac{1}{2}}_{-\frac{1}{2},-\frac{1}{2}}\right|^2 . \tag{F.34}$$

Following [317] the helicity amplitudes of a non-leptonic baryon decay involving a pion can be parametrized as

$$h^{\frac{1}{2}}_{\lambda_\Sigma,\lambda_p} = G_F m_\pi^2 \bar{u}_p(\lambda_p)(A - B\gamma_5)u_\Sigma(\lambda_\Sigma)\,, \tag{F.35}$$

where A and B are complex constants and m_π is the pion mass. We compute the amplitude in the rest frame of the Σ^+ with the z-axis pointing in the direction of the proton momentum. The spinors are then again given by

$$\begin{aligned} u_\Sigma\left(p, \lambda_\Sigma = \pm\frac{1}{2}\right) &= \sqrt{2m_\Sigma}\begin{pmatrix}\chi_\pm \\ 0\end{pmatrix}\,, \\ \bar{u}_p\left(k, \lambda_p = \pm\frac{1}{2}\right) &= \sqrt{E_p + m_p}\left(\chi^\dagger_\pm, \frac{\mp|\vec{k}|}{E_p + m_p}\chi^\dagger_\pm\right)\,, \end{aligned} \tag{F.36}$$

with p and k the four-momenta of the Σ^+ and the proton, respectively. Further, $p^0 = m_\Sigma$, $|\vec{p}| = 0$ and $E_p = \sqrt{|\vec{k}|^2 + m_p^2}$ is the energy of the proton, hence $k = (E_p, 0, 0, |\vec{k}|)^{\mathrm{T}}$, and $\chi_+ = (1,0)^{\mathrm{T}}$, $\chi_- = (0,1)^{\mathrm{T}}$. using these spinors in Eq. (F.35) and simplifying, we arrive at

$$\begin{aligned} h^{\frac{1}{2}}_{\frac{1}{2},\frac{1}{2}} &= \sqrt{2m_\Sigma}G_F m_\pi^2(\sqrt{r_+}A + \sqrt{r_-}B)\,, \\ h^{\frac{1}{2}}_{-\frac{1}{2},-\frac{1}{2}} &= \sqrt{2m_\Sigma}G_F m_\pi^2(\sqrt{r_+}A - \sqrt{r_-}B)\,, \end{aligned} \tag{F.37}$$

with $r_\pm = \sqrt{E_p \pm m_p}$. Via these helicity amplitudes $\alpha_\pm$ are expressed as

$$\begin{aligned} \alpha_+ &= 4G_F^2 m_\pi^4 m_\Sigma(r_+|A|^2 + r_-|B|^2)\,, \\ \alpha_- &= 8G_F^2 m_\pi^4 m_\Sigma\sqrt{r_+ r_-}\,\mathrm{Re}(AB^*)\,, \end{aligned} \tag{F.38}$$

and their ratio reads

$$\frac{\alpha_-}{\alpha_+} = \frac{2\sqrt{\frac{r_-}{r_+}}\mathrm{Re}(AB^*)}{|A|^2 + \frac{r_-}{r_+}|B|^2} = \alpha\,, \tag{F.39}$$

which corresponds to the decay parameter α in [184]. We can therefore factorize α_+ from the angular distribution and use $\alpha_+ = \mathcal{B}(\Sigma^+ \to p\pi)$ and $\frac{\alpha_-}{\alpha_+} = \alpha$ to arrive at the expressions given in App. E.3.

G Details on flavor probes with dineutrino modes

This appendix provides further details on the $SU(2)_L$–link in SMEFT in App. G.1, calculating the $\mathcal{O}(\lambda)$ correction, where λ is the Wolfenstein parameter. Also, App. G.2 collects all available bounds on charged lepton couplings in different flavor sectors, including global fits to low-energy data for semileptonic $b \to s$ and $b \to d$ transitions. App. G.3 presents differential distributions for rare charm and rare beauty dineutrino modes for several benchmark scenarios.

G.1 Details on the $SU(2)_L$–links in SMEFT

We investigate the $\mathcal{O}(\lambda)$ correction in the $SU(2)_L$–link in Eq. (6.4). We explicitly do this for the up-type sector, since the $\mathcal{O}(\lambda)$ correction is taken into account in Sec. 6.2 for $c \to u\nu\bar{\nu}$ induced modes. We choose the CKM (V) and PMNS (W) matrix to stem from down-type rotations and charged lepton rotations, respectively, $Q_\alpha = (u_{L\alpha}, V_{\alpha\beta}\, d_{L\beta})$ and $L_i = (\nu_{Li}, W^*_{ki}\, \ell_{Lk})$. The $SU(2)_L$–link between dineutrino Wilson coefficients $\mathcal{C}$ and charged lepton Wilson coefficients $\mathcal{K}$ reads in the mass basis of quarks and leptons

$$\begin{aligned} \mathcal{C}_L^U &= W^\dagger [V \mathcal{K}_L^D\, V^\dagger]\, W\,, \\ \mathcal{C}_R^U &= W^\dagger [\mathcal{K}_R^U]\, W\,. \end{aligned} \tag{G.1}$$

As we have seen in Sec. 6.1, the dependence the PMNS matrix drops out in flavor-summed branching ratios, Eq.(6.7), due to unitarity. For the CKM matrix we expand the cu entry in $\mathcal{C}_L^U$ in terms of the Wolfenstein parameter λ

$$\mathcal{C}_L^{cu} = W^\dagger \mathcal{K}_L^{sd} W + \lambda\, W^\dagger (\mathcal{K}_L^{ss} - \mathcal{K}_L^{dd}) W + \mathcal{O}(\lambda^2)\,. \tag{G.2}$$

Including the $\mathcal{O}(\lambda)$ correction yields for x_{cu}

$$\begin{aligned} x_{cu} &= \sum_{\nu=i,j} \left(\left|\mathcal{C}_L^{cuij}\right|^2 + \left|\mathcal{C}_R^{cuij}\right|^2 \right) = \mathrm{Tr}\left[\mathcal{C}_L^{cu}\, \mathcal{C}_L^{cu\dagger} + \mathcal{C}_R^{cu}\, \mathcal{C}_R^{cu\dagger} \right] \\ &= \mathrm{Tr}\left[\mathcal{K}_L^{sd} \mathcal{K}_L^{sd\dagger} + \mathcal{K}_R^{sd} \mathcal{K}_R^{sd\dagger} \right] + \delta x_{cu} + \mathcal{O}(\lambda^2) \\ &= \sum_{\ell=i,j} \left(\left|\mathcal{K}_L^{sdij}\right|^2 + \left|\mathcal{K}_R^{sdij}\right|^2 \right) + \delta x_{cu} + \mathcal{O}(\lambda^2)\,, \end{aligned} \tag{G.3}$$

with

$$\begin{aligned} \delta x_{cu} &= 2\,\lambda\, \mathrm{Tr}\left[\mathrm{Re}\left(\mathcal{K}_L^{sd} \left(\mathcal{K}_L^{ss\dagger} - \mathcal{K}_L^{dd\dagger} \right) \right) \right] \\ &= 2\,\lambda \sum_{\ell=i,j} \mathrm{Re}\left(\left(\mathcal{K}_L^{sdij}\, \mathcal{K}_L^{ssij^*} - \mathcal{K}_L^{sdij} \mathcal{K}_L^{ddij^*} \right) \right)\,. \end{aligned} \tag{G.4}$$

Table G.1: Upper limits on leptonic couplings $\mathcal{K}_{L,R}$ for quark flavors dd, ss, sd and cu from high–p_T [213, 214]. LFV-bounds are quoted as flavor summed, $\sqrt{|\mathcal{K}^{\ell^+\ell'^-}|^2 + |\mathcal{K}^{\ell^-\ell'^+}|^2}$.

$\lvert\mathcal{K}_A^{qq'\ell\ell'}\rvert$	ee	$\mu\mu$	$\tau\tau$	$e\mu$	$e\tau$	$\mu\tau$
$\lvert\mathcal{K}_{L,R}^{dd\ell\ell'}\rvert$	2.8	1.5	5.5	1.1	3.3	3.6
$\lvert\mathcal{K}_{L,R}^{ss\ell\ell'}\rvert$	9.0	4.9	17	5.2	17	18
$\lvert\mathcal{K}_{L,R}^{sd\ell\ell'}\rvert$	3.5	1.9	6.7	2.0	6.1	6.6
$\lvert\mathcal{K}_{L,R}^{cu\ell\ell'}\rvert$	2.9	1.6	5.6	1.6	4.7	5.1

Table G.2: Upper limits on $R^{\ell\ell'}$ and $\delta R^{\ell\ell'}$ as defined in Eqs. (G.5), as well as on their sum, $r^{\ell\ell'} = R^{\ell\ell'} + \delta R^{\ell\ell'}$.

	ee	$\mu\mu$	$\tau\tau$	$e\mu$	$e\tau$	$\mu\tau$
$R^{\ell\ell'}$	21	6.0	77	6.6	59	70
$\delta R^{\ell\ell'}$	19	5.4	69	5.7	55	63
$r^{\ell\ell'}$	39	11	145	12	115	133

Bounds on the charged lepton couplings within the different flavor assumptions can be plugged into dineutrino branching ratios as follows. We define

$$\begin{aligned} R^{\ell\ell'} &= \left|\mathcal{K}_L^{sd\ell\ell'}\right|^2 + \left|\mathcal{K}_R^{cu\ell\ell'}\right|^2, \\ R_\pm^{\ell\ell'} &= \left|\mathcal{K}_L^{sd\ell\ell'} \pm \mathcal{K}_R^{cu\ell\ell'}\right|^2, \\ \delta R^{\ell\ell'} &= 2\,\lambda\,\mathrm{Re}\left(\mathcal{K}_L^{sd\ell\ell'}\,\mathcal{K}_L^{ss\ell\ell'*} - \mathcal{K}_L^{sd\ell\ell'}\,\mathcal{K}_L^{dd\ell\ell'*}\right). \end{aligned} \tag{G.5}$$

Again, we use $R_+^{\ell\ell'} + R_-^{\ell\ell'} = 2\,R^{\ell\ell'}$, $R_\pm^{\ell\ell'} \leq 2\,R^{\ell\ell'}$ and $\delta R^{\ell\ell'} < 2\,\lambda\left|\mathcal{K}_L^{sd\ell\ell'}\right|\left(\left|\mathcal{K}_L^{ss\ell\ell'}\right| + \left|\mathcal{K}_L^{dd\ell\ell'}\right|\right)$.

In the most conservative scenario, we employ high–p_T data [213, 214] for up- and down-type charged lepton FCNCs and the flavor diagonal down-type couplings. We give bounds on lepton specific Wilson coefficients for $\ell, \ell' = e, \mu, \tau$ in Tab G.1 [1]. Corresponding bounds on $R^{\ell\ell'}$ and $\delta R^{\ell\ell'}$ are summarized in Tab. G.2.

The λ corrections in for rare charm dineutrino modes are sizable, because bounds on the diagonal quark flavor couplings, especially the ss, are worse than the FCNC constraints. This effect is less pronounced for the $\mathcal{O}(\lambda^2)$ corrections, where the diagonal quark couplings enter squared with a single λ^2 prefactor.

[1] The $d \to d$, $s \to s$, $s \to d$ entries are obtained from the $c \to u$ bounds via luminosity ratios, see Eqs. (6.9) and (6.10) in [214] and Fig. 1 in [213].

G.2 Collecting bounds on Wilson coefficients in different sectors

We collect available limits on charged lepton BSM flavor couplings for all possible SM quark FCNCs. Limits are obtained from Drell-Yan searches in high–p_T dilepton tails from Refs. [213, 214] and hold for both chiralities $|\mathcal{K}^{qq'\ell\ell'}_{L,R}|_{\rm DY}$ and quark flavors sd, cu, bs, bd. They are given in Tab. G.3 in lines one, four, seven and eleven, respectively. Drell-Yan bounds are not competitive for tc and tu couplings, since the top quark PDF is strongly suppressed, *i.e.* it is unlikely to find a top quark inside of a proton. Tab. G.3 also contains limits on couplings from low energy data. Lines 2, 5, 8, 9, 12 and 13 are obtained from semileptonic decays of flavored mesons, *i.e.* kaon decays for sd, D–meson decays for cu (see Sec. 4.1), B–meson decays for bs and bd. We quote all lepton flavor combinations that are kinematically accessible and assume no large cancellations between LH and RH contributions. Further, the limits provided are on the absolute values, whereas for $bs\mu\mu$ and $bd\mu\mu$ a separate range is given for each chirality based on global fits presented later in this appendix. The remaining lines 3, 6, 10 and 14 are obtained utilizing information on low-energy meson decays into dineutrinos and the $SU(2)_L$–link. Due to this link only one chirality is constrained. From rare kaon decays, see Sec. 6.4, the RH $sd\ell\ell'$ couplings and the LH $cu\ell\ell'$ couplings are constrained assuming no large cancellation between these two contributions is possible, hence lines three and six quote the same limits. The opposite combination would be constrained from rare charm decays into dineutrinos, however the only available limit on $D^0 \to \pi^0\nu\bar{\nu}$ is to weak to be competitive, see Sec. 6.2. Rare B–meson decays into dineutrinos constrain RH charged lepton couplings in lines 10 and 14 of Tab. G.3 and LH $tc\ell\ell'$ and $tu\ell\ell'$ couplings, quoted in lines 2 and 4 of Tab. G.4. Again, these bounds are obtained assuming no large cancellation between LH and RH contributions is present.

Tab. G.4 also presents upper limits on four-fermion operators including tops from collider studies of top plus charged dilepton processes in lines 1 and 3.

As expected, rare kaon data for charged dilepton and dineutrino final states result in tight constraints on NP $sd\ell\ell'$ couplings for all available lepton flavor combinations and are at least two orders better than bounds from Drell-Yan searches. They also impose strong bounds on the LH $cu\ell\ell$ coupling, where otherwise bounds from Drell-Yan and low-energy physics are in the same ballpark. For bs and bd couplings Drell-Yan limits are weaker than low-energy input due to the heavy bottom quark. Direct limits from rare B–meson decays are roughly two orders better than indirect limits from dineutrino final states whenever light charged leptons are involved, *i.e.* ee, $\mu\mu$ and $e\mu$. The indirect limits are, however, in the same ballpark or even better than direct ones whenever a τ is involved.

In the top sector direct experimental info is weak and indirect limits on the LH coupling from rare B–meson data is roughly two orders of magnitude better for every single charged lepton flavor combination.

Most precise experimental information is available for rare B–meson decays constraining both $bs\mu\mu$ and $bd\mu\mu$ four-fermion vector couplings. We perform a global fit for these.

The global fit to $b \to s\,\mu^+\mu^-$ data is performed using the python package *flavio* [279] and distinguishing two cases: a fit including only $b \to s\,\mu^+\mu^-$ data, and another, which includes LFU ratios R_{K^*} and dielectron observables, such as $B^0 \to K^{*0}\,e^+e^-$. We follow Refs. [55, 228, 318], which also us the *flavio* package refer to these references and Ref. [7] for further details. Observables from $b \to s\,\ell\ell$ transitions

Table G.3: Collection of upper limits on charged dilepton couplings $\mathcal{K}_A^{qq'\ell\ell'}$ for $qq' = sd$, cu, bs and bd from high–p_T [213, 214] (top rows), charged dilepton kaon and B–decays (mid rows) and derived ones from kaon and B–decays to dineutrinos (bottom rows). Numbers are quoted on the modulus, except for $bs\mu\mu$ and $bd\mu\mu$ couplings were global fit results are quoted, see text for details. LFV–bounds are quoted as flavor-summed, $\sqrt{|\mathcal{K}^{\ell^+\ell'^-}|^2 + |\mathcal{K}^{\ell^-\ell'^+}|^2}$.

	ee	$\mu\mu$	$\tau\tau$	$e\mu$	$e\tau$	$\mu\tau$
sd						
$\lvert\mathcal{K}_{L,R}^{sd\ell\ell'}\rvert_{\rm DY}$	3.5	1.9	6.7	2.0	6.1	6.6
$\lvert\mathcal{K}_{L,R}^{sd\ell\ell'}\rvert$	5×10^{-2}	1.6×10^{-2}	–	6.6×10^{-4}	–	–
$\lvert\mathcal{K}_{R}^{sd\ell\ell'}\rvert_{\nu\bar{\nu}}$	1.9×10^{-2}	1.9×10^{-2}	1.9×10^{-2}	1.1×10^{-2}	1.1×10^{-2}	1.1×10^{-2}
cu						
$\lvert\mathcal{K}_{L,R}^{cu\ell\ell'}\rvert_{\rm DY}$	2.9	1.6	5.6	1.6	4.7	5.1
$\lvert\mathcal{K}_{L,R}^{cu\ell\ell'}\rvert$	4.0	0.9	–	2.2	n.a.†	–
$\lvert\mathcal{K}_{L}^{cu\ell\ell'}\rvert_{\nu\bar{\nu}}$	1.9×10^{-2}	1.9×10^{-2}	1.9×10^{-2}	1.1×10^{-2}	1.1×10^{-2}	1.1×10^{-2}
bs						
$\lvert\mathcal{K}_{L,R}^{bs\ell\ell'}\rvert_{\rm DY}$	13	7.1	25	8.0	27	30
$\mathcal{K}_{R}^{bs\ell\ell'}$	0.04	$[-0.03; -0.01]$	32	0.1	2.8	3.4
$\mathcal{K}_{L}^{bs\ell\ell'}$	0.04	$[-0.06; -0.04]$	32	0.1	2.8	3.4
$\mathcal{K}_{R}^{bs\ell\ell'}\rvert_{\nu\bar{\nu}}$	1.4	1.4	1.4	1.8	1.8	1.8
bd						
$\lvert\mathcal{K}_{L,R}^{bd\ell\ell'}\rvert_{\rm DY}$	5.0	2.7	9.6	3.1	9.6	11
$\mathcal{K}_{R}^{bd\ell\ell'}$	0.09	$[-0.03, 0.03]$	21	0.2	3.4	2.4
$\mathcal{K}_{L}^{bd\ell\ell'}$	0.09	$[-0.07, 0.02]$	21	0.2	3.4	2.4
$\mathcal{K}_{R}^{bd\ell\ell'}\rvert_{\nu\bar{\nu}}$	1.8	1.8	1.8	2.5	2.5	2.5

listed in Tabs. B.1-B.3 in Ref. [228] are included, while adding the updated 2021 measurement of R_K from LHCb [319], as well as radiative modes, $B^0_{(s)} \to \mu\mu$ and Λ_b–decays. However, observables listed in Tabs. B.4-B.9 of Ref. [228], which incorporate observables from charged current B–decays as well as strange, charm and τ-decays, are not included. A complete list of the utilized experimental input is given in Ref. [228] and Table 7 and Table 8 of Ref. [7].

The six-dimensional fit to real Wilson coefficients C_7, C_9, C_{10} and primed counterparts in the first case, *i.e.* the scenario without LFU and dielectron data, yields the following $1\,\sigma$ fit values, when

Table G.4: Upper limits on charged dilepton couplings $\mathcal{K}_A^{tc\ell\ell'}$ and $\mathcal{K}_A^{tu\ell\ell'}$ from collider studies [281, 282, 285] of top plus charged dilepton processes (top rows) and on LH couplings derived from rare B–decays to dineutrinos (bottom rows). Numbers correspond to a limit on the modulus and LFV–bounds are quoted as flavor-summed, $\sqrt{|\mathcal{K}^{\ell^+\ell'^-}|^2 + |\mathcal{K}^{\ell^-\ell'^+}|^2}$.

	ee	$\mu\mu$	$\tau\tau$	$e\mu$	$e\tau$	$\mu\tau$
tc						
$\lvert\mathcal{K}_{L,R}^{tc\ell\ell'}\rvert$	~ 200	~ 200	n.a.	36	136	136
$\lvert\mathcal{K}_{L}^{tc\ell\ell'}\rvert_{\nu\bar{\nu}}$	1.9	1.9	1.9	1.8	1.8	1.8
tu						
$\lvert\mathcal{K}_{L,R}^{tu\ell\ell'}\rvert$	~ 200	~ 200	n.a.	12	136	136
$\lvert\mathcal{K}_{L}^{tu\ell\ell'}\rvert_{\nu\bar{\nu}}$	1.8	1.8	1.8	2.4	2.4	2.4

projected to NP couplings $\kappa_{L,R}^{bs\mu\mu}$, see also Eq. (6.24),

$$\begin{aligned} \kappa_L^{bs\mu\mu} &= C_9 - C_{10} = -1.45 \pm 0.29\,, \\ \kappa_R^{bs\mu\mu} &= C_9' - C_{10}' = 0.46 \pm 0.26\,. \end{aligned} \tag{G.6}$$

In Eq. (G.6) the clear tension between $b \to s\,\mu^+\mu^-$ data and the SM becomes apparent and is quantified by the *pull* from the SM, pull_{SM}, in units of standard deviations σ. This fit gives $\text{pull}_{\text{SM}} = 4.6\,\sigma$, with a goodness of fit $\chi^2/\text{dof} = 0.91$. LFU and dielectron data is excluded, because we are interested in the best available limit on dimuon couplings assuming LFU. As soon as dielectron modes and LFU ratios are included, one explicitly breaks LFU when performing a fit to muon Wilson coefficients only.

The 1, 2, and $3\,\sigma$ fit contours are displayed as red shaded areas in the left plot of Fig. G.1 in the $\kappa_L^{bs\mu\mu}$–$\kappa_R^{bs\mu\mu}$ plane, where the best fit point is indicated as a red point. The plot also displays the $1\,\sigma$ regions for different sets of observables in blue for $\langle F_L \rangle$, green for $\langle \mathrm{d}\,\mathcal{B}/\mathrm{d}q^2 \rangle$, orange for $\langle P_i \rangle$, and yellow for $\langle A_{\text{FB}} \rangle$. Finally, the red dashed lines show the impact of $R_{K^{(*)}}$ data on the global fit.

For the $b \to d\,\mu^+\mu^-$ transition, there is currently only first information from global fits in Refs. [278, 321, 322], which are mainly based on the current experimental information on $B^+ \to \pi^+\,\mu^+\mu^-$. However, further input can be included from the recent update on $\mathcal{B}(B^0 \to \mu^+\mu^-) = (0.56 \pm 0.7) \times 10^{-10}$ [263] at 95% CL, where the quoted value includes the recent result from LHCb [323, 324], in addition to the first evidence for $\mathcal{B}(B_s^0 \to \bar{K}^{*0}\mu^+\mu^-) = (2.9 \pm 1.1) \times 10^{-8}$ [325].

We use results from Ref. [320], where a four-dimensional fit to the aforementioned modes and data from $B^+ \to \pi^+\mu^+\mu^-$ is performed, to obtain global fit ranges for $\kappa_L^{bd\mu\mu}$ and $\kappa_R^{bd\mu\mu}$. The fit is only four-dimensional because we do not consider dipole operators C_7, C_7' in our fit. The main difference to the results in $b \to s$ is that experimental information for $b \to d$ is much less constraining and we obtain two solutions for the four-dimensional fit. We quote the solution with the smallest $\chi^2/\text{dof} = 0.28$ that

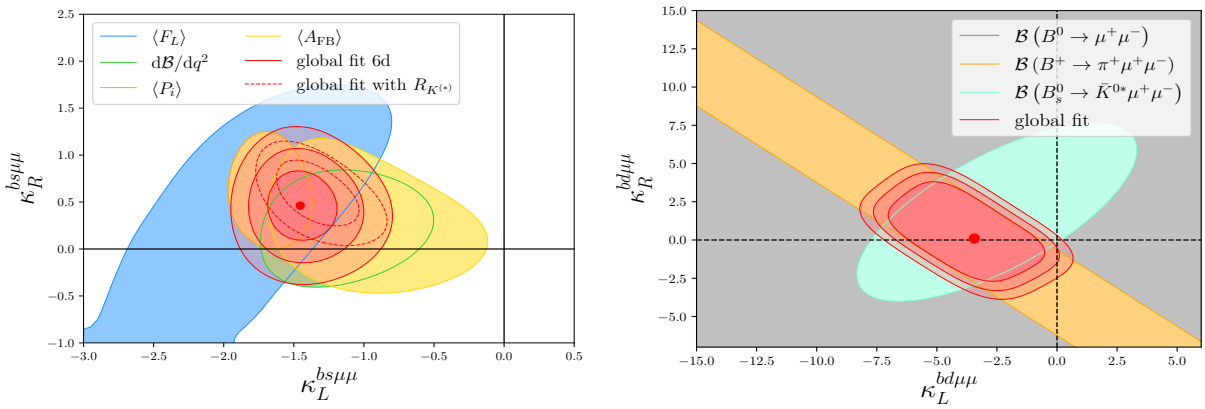

Figure G.1: Plots visualize results of global fits to rare B–decay data on $|\Delta b| = |\Delta s| = 1$ and on $|\Delta b| = |\Delta d| = 1$ transitions in the left and right plot, respectively. **Left plot:** 1, 2, and $3\,\sigma$ contours and best fit point are shown in the $\kappa_L^{bs\mu\mu}$–$\kappa_R^{bs\mu\mu}$ plane as red shaded areas and red point. blue, green, orange and yellow regions correspond to the $1\,\sigma$ contours for $\langle F_L \rangle$, $\langle \mathrm{d}\,\mathcal{B}/\mathrm{d}q^2 \rangle$, $\langle P_i \rangle$ and $\langle A_{\mathrm{FB}} \rangle$, respectively. The red dashed contours illustrate the impact of $R_{K^{(*)}}$ data on the global fit. **Right plot:** In the $\kappa_L^{bd\mu\mu}$–$\kappa_R^{bd\mu\mu}$ plane the red shaded areas correspond to 1, 2, and $3\,\sigma$ fit contours and the best fit values are shown as a red point. The impact of $\mathcal{B}(B^+ \to \pi^+\,\mu^+\mu^-)$ and $\mathcal{B}(B_s^0 \to \bar{K}^{*0}\,\mu^+\mu^-)$ is illustrated individually as 1σ contours in orange and celeste, respectively. The $B^0 \to \mu^+\mu^-$ limit is included in the global fit, but has small impact as apparent from the gray area, which fills the whole plot region. The $|\Delta b| = |\Delta d| = 1$ fit results are adapted from [320].

gives

$$\begin{aligned} \kappa_L^{bd\mu\mu} &= -3 \pm 5\,, \\ \kappa_R^{bd\mu\mu} &= 0 \pm 4\,, \end{aligned} \tag{G.7}$$

with $\mathrm{pull}_{\mathrm{SM}} = 1.92\,\sigma$. Similar to the $b \to s$ case, the right plot of Fig. G.1 displays the 1, 2, and $3\,\sigma$ fit contours as red shaded areas and the best fit values as a red point in the $\kappa_L^{bs\mu\mu}$–$\kappa_R^{bs\mu\mu}$ plane. The individual impact of $\mathcal{B}(B^+ \to \pi^+\,\mu^+\mu^-)$ and $\mathcal{B}(B_s^0 \to \bar{K}^{*0}\,\mu^+\mu^-)$ to the global fit are displayed as 1σ contours in orange and celeste, respectively. The $B^0 \to \mu^+\mu^-$ limit has basically no impact on the fit. It is illustrated as gray area, however covers the whole plot region. In order to improve the global fit and reject the possibility of various solutions, future measurements of $b \to d\ \mu^+\mu^-$ modes are necessary. For further details of the $b \to d\,\mu^+\mu^-$ global fit we refer to Ref. [320].

The fit results for κ_R for both $b \to s$ and $b \to d$ transition from Eqs. (G.6) and (G.7) serve as input in the analysis of indirect LFU tests via dineutrino modes in Sec. 6.3, see Fig. 6.4.

G.3 Differential distributions for dineutrino modes

In this appendix, we collect differential branching ratios for rare charm and rare beauty dineutrino modes in several benchmarks. For rare charm transitions Fig. G.2 no SM curve is shown, as it is suppressed by several orders of magnitude, due to the efficient GIM cancellation. We show for each mode a dotted and a solid line together with their 1σ uncertainty bands from form factors, where the solid line corresponds to the LFU upper limit, whereas the dotted line is for the cLFC upper limit from Tab. 6.3 in the first scenario, *i.e.* the scenario using upper limits from Drell-Yan high–p_T searches only and including the $\mathcal{O}(\lambda)$ corrections discussed in App. G. The upper plot in Fig. G.2 is for $D \to P\nu\bar{\nu}u$ modes, in red, brown and dark green we show the q^2 differential branching ratios for $D^0 \to \pi^0\nu\bar{\nu}$, $D^+ \to \pi^+\nu\bar{\nu}$ and $D_s^+ \to K^+\nu\bar{\nu}$, respectively. For the charged modes the τ cut, see Eq. (6.12) in Sec. 6.2, is illustrated as a vertical brown and green dashed line. The middle row plots show the q^2 and p^2 differential distributions for $D^0 \to P_1P_2\nu\bar{\nu}$ modes in the left and right plot, respectively, where p^2 is the invariant mass squared of the dihadron final state. Benchmark curves are shown for $D^0 \to \pi^0\pi^0\nu\bar{\nu}$, $D^0 \to \pi^+\pi^-\nu\bar{\nu}$ and $D^0 \to K^+K^-\nu\bar{\nu}$ in orange, pink and cyan, respectively. The $D^0 \to K^+K^-\nu\bar{\nu}$ is artificially enhanced by a factor 100 to be visible in the plots and in all modes 10 % uncertainties from form factors are illustrated. The lower left plot shows q^2 distributions for $\Lambda_c \to p\nu\bar{\nu}$ and $\Xi_c^+ \to \Sigma^+\nu\bar{\nu}$ in brown and blue, respectively, and the bottom right plot shows the benchmark distributions for inclusive dineutrino decays of the D^0–, D^+– and D_s^+–mesons in magenta, lime and green, respectively. For the inclusive modes 10 % uncertainties are illustrated as band width in the plot and the distributions are cut at $q^2_{\text{max}} = m_c^2$ for D^0 and D^+ and at the physical limit $q^2_{\text{max}} = (m_{D_s} - m_K)^2$ for the D_s [326].

In Fig. G.3 we show the prediction for the differential branching ratios of $B^0 \to K^0\nu\bar{\nu}$, $B^0 \to K^{*0}\nu\bar{\nu}$, $B_s^0 \to \phi\nu\bar{\nu}$, inclusive $B^0 \to X_s\nu\bar{\nu}$, $B^0 \to \pi^0\nu\bar{\nu}$ and $B^0 \to \rho^0\nu\bar{\nu}$ in the upper left, upper right, middle left, middle right, lower left and lower right plot, respectively , and each in the SM (black dotted line and gray uncertainty band) and two BSM benchmarks in blue and red. The blue region depicts the region spanned by varying dineutrino couplings within the ranges given in Eq. (6.20). This region corresponds to the indirectly derived EFT limits provided in the fourth column of Tab. 6.5. The red region is a combination of Eq. (6.20) and the LFU region defined in Eq. (6.35) and depicted as a red cone in Fig. 6.4. For some this additional constrain gives a bound more stringent than the general derived EFT limit, for others there is essentially no difference.

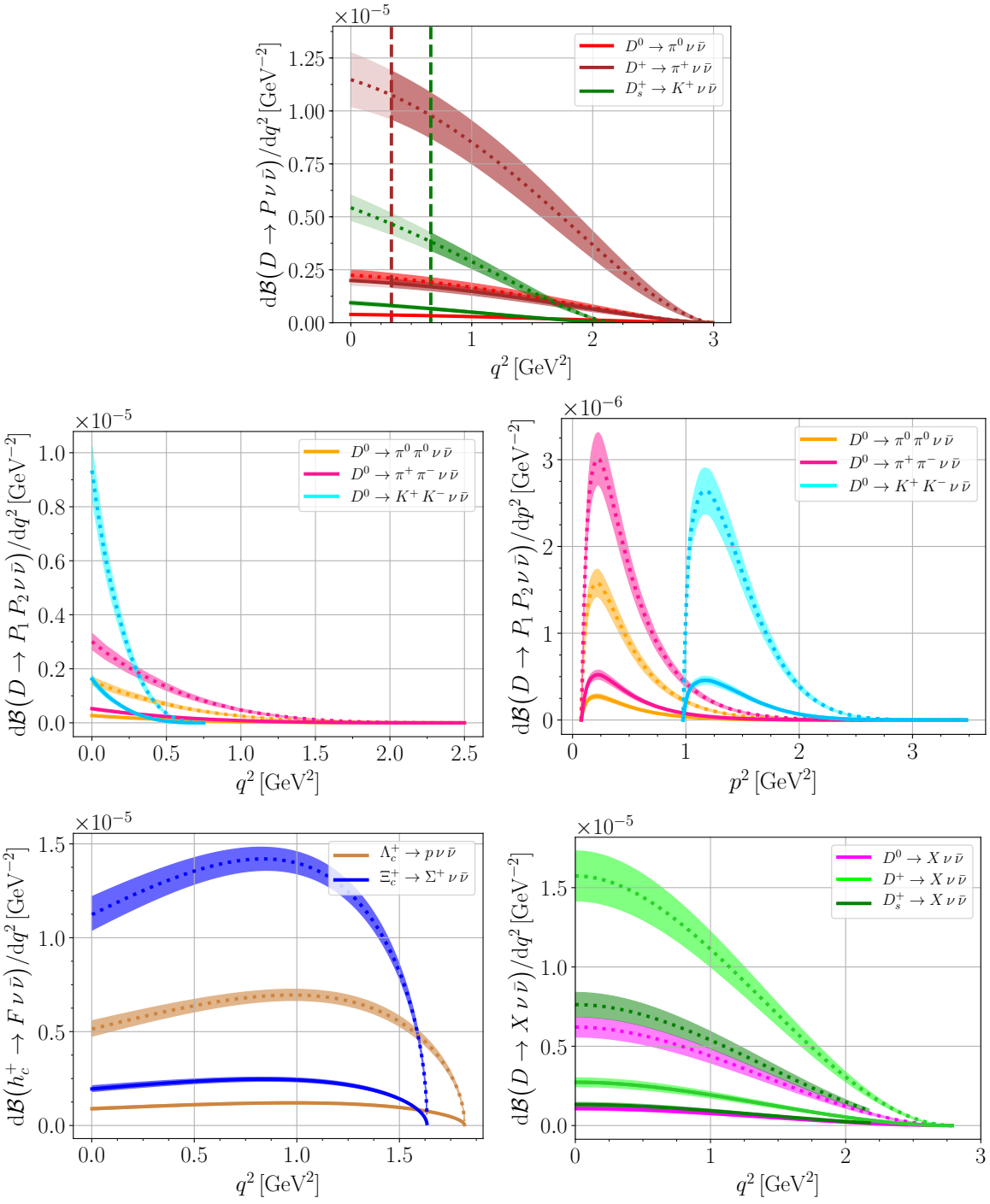

Figure G.2: Differential branching ratios for the LFU and cLFC limit as solid and dotted line, respectively, for several rare charm dineutrino modes, see y–labels, legends and text for further details.

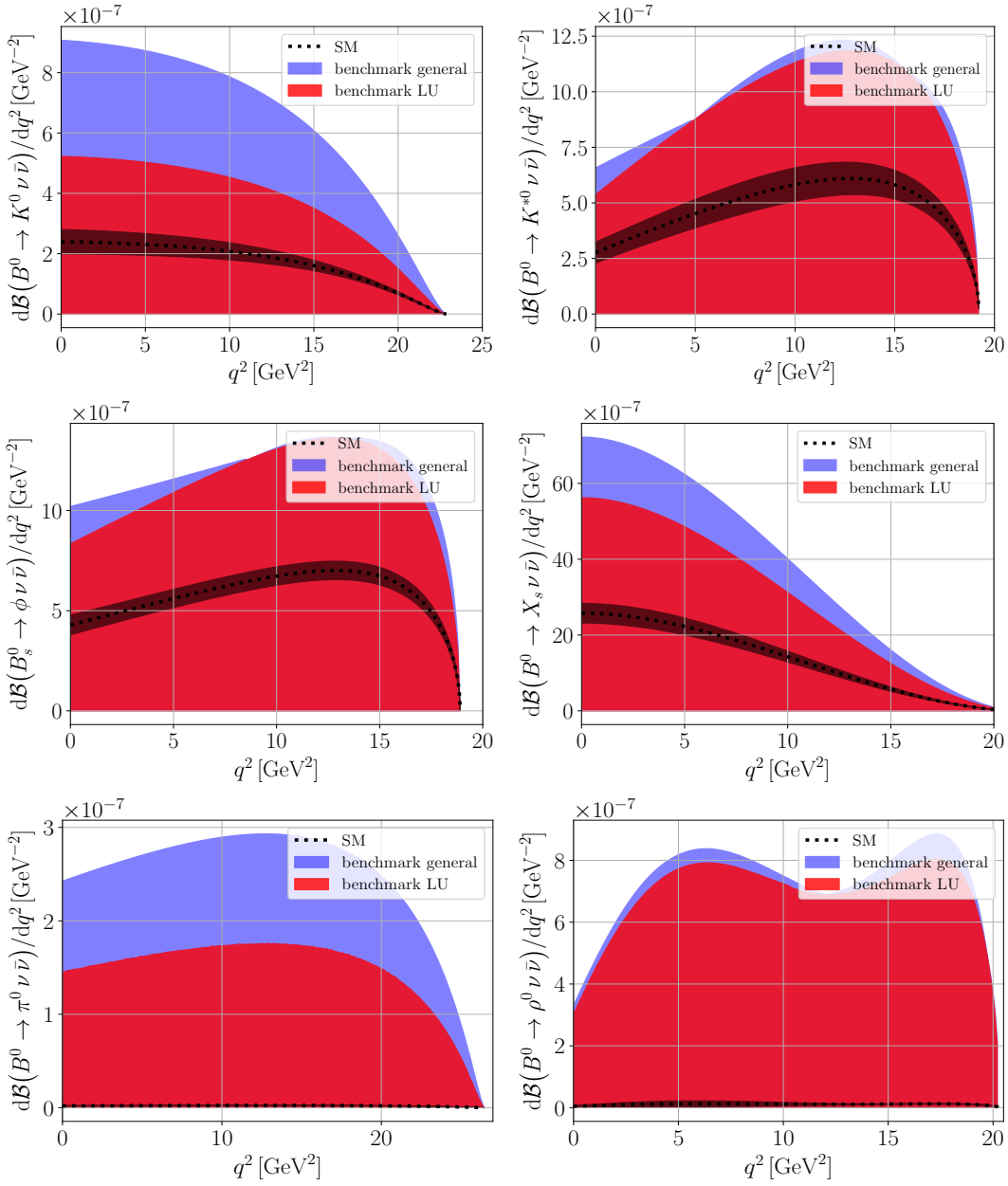

Figure G.3: Several differential branching ratios for rare B–decays to dineutrinos, see y–labels, are shown in the SM (black dotted line and gray uncertainty band) and two BSM scenarios, the derived EFT limit using Eq. (6.20) (blue region, labeled as *benchmark general*) for $b \to s\,\nu\bar{\nu}$ and $b \to d\,\nu\bar{\nu}$, respectively, and the LFU benchmark (red region, labeled as *benchmark LU*), see text for details.

Bibliography

[1] R. Bause et al. "The new physics reach of null tests with $D \to \pi\ell\ell$ and $D_s \to K\ell\ell$ decays." In: *Eur. Phys. J. C* 80.1 (2020). [Erratum: Eur.Phys.J.C 81, 219 (2021)], p. 65. arXiv: 1909.11108 [hep-ph].

[2] R. Bause et al. "Exploiting CP-asymmetries in rare charm decays." In: *Phys. Rev. D* 101.11 (2020), p. 115006. arXiv: 2004.01206 [hep-ph].

[3] R. Bause et al. "Lepton universality and lepton flavor conservation tests with dineutrino modes." In: *Eur. Phys. J. C* 82.2 (2022), p. 164. arXiv: 2007.05001 [hep-ph].

[4] R. Bause et al. "Rare charm $c \to u\,\nu\bar{\nu}$ dineutrino null tests for e^+e^- machines." In: *Phys. Rev. D* 103.1 (2021), p. 015033. arXiv: 2010.02225 [hep-ph].

[5] H. Gisbert, M. Golz, and D. S. Mitzel. "Theoretical and experimental status of rare charm decays." In: *Mod. Phys. Lett. A* 36.04 (2021), p. 2130002. arXiv: 2011.09478 [hep-ph].

[6] M. Golz, G. Hiller, and T. Magorsch. "Probing for New Physics with Rare Charm Baryon (Λ_c, Ξ_c, Ω_c) Decays." In: *JHEP* 09 (2021), p. 208. arXiv: 2107.13010 [hep-ph].

[7] R. Bause et al. "Interplay of dineutrino modes with semileptonic rare B-decays." In: *JHEP* 12 (2021), p. 061. arXiv: 2109.01675 [hep-ph].

[8] M. Golz, G. Hiller, and T. Magorsch. "Pinning down $|\Delta c| = |\Delta u| = 1$ couplings with rare charm baryon decays." In: *Eur. Phys. J. C* 82.4 (2022), p. 357. arXiv: 2202.02331 [hep-ph].

[9] M. Golz. "Physics reach of $D_{(s)} \to \pi(K)\ell\ell$ and other charming null test opportunities." In: *55th Rencontres de Moriond on Electroweak Interactions and Unified Theories*. May 2021. arXiv: 2105.03453 [hep-ph].

[10] M. Golz. "Null test searches for BSM physics with rare charm decays." In: *PoS* CHARM2020 (2021), p. 051. arXiv: 2109.07155 [hep-ph].

[11] R. Bause et al. "Dineutrino modes probing lepton flavor violation." In: *European Physical Society Conference on High Energy Physics 2021*. Oct. 2021. arXiv: 2110.08795 [hep-ph].

[12] M. Golz, G. Hiller, and T. Magorsch. "Null test BSM searches with rare charm baryon decays." In: Mar. 2022. arXiv: 2203.01965 [hep-ph].

[13] M. Gell-Mann. "A Schematic Model of Baryons and Mesons." In: *Phys. Lett.* 8 (1964), pp. 214–215.

[14] J. D. Bjorken and S. L. Glashow. "Elementary Particles and SU(4)." In: *Phys. Lett.* 11 (1964), pp. 255–257.

[15] S. L. Glashow, J. Iliopoulos, and L. Maiani. "Weak Interactions with Lepton-Hadron Symmetry." In: *Phys. Rev. D* 2 (1970), pp. 1285–1292.

[16] J. J. Aubert et al. "Experimental Observation of a Heavy Particle J." In: *Phys. Rev. Lett.* 33 (1974), pp. 1404–1406.

[17] J. E. Augustin et al. "Discovery of a Narrow Resonance in e^+e^- Annihilation." In: *Phys. Rev. Lett.* 33 (1974), pp. 1406–1408.

[18] L. Di Lella and C. Rubbia. "The Discovery of the W and Z Particles." In: *Adv. Ser. Direct. High Energy Phys.* 23 (2015), pp. 137–163.

[19] P. W. Anderson. "Plasmons, Gauge Invariance, and Mass." In: *Phys. Rev.* 130 (1963). Ed. by J. C. Taylor, pp. 439–442.

[20] P. W. Higgs. "Broken Symmetries and the Masses of Gauge Bosons." In: *Phys. Rev. Lett.* 13 (1964). Ed. by J. C. Taylor, pp. 508–509.

[21] F. Englert and R. Brout. "Broken Symmetry and the Mass of Gauge Vector Mesons." In: *Phys. Rev. Lett.* 13 (1964). Ed. by J. C. Taylor, pp. 321–323.

[22] G. S. Guralnik, C. R. Hagen, and T. W. B. Kibble. "Global Conservation Laws and Massless Particles." In: *Phys. Rev. Lett.* 13 (1964). Ed. by J. C. Taylor, pp. 585–587.

[23] G. Aad et al. "Observation of a new particle in the search for the Standard Model Higgs boson with the ATLAS detector at the LHC." In: *Phys. Lett. B* 716 (2012), pp. 1–29. arXiv: 1207.7214 [hep-ex].

[24] S. Chatrchyan et al. "Observation of a New Boson at a Mass of 125 GeV with the CMS Experiment at the LHC." In: *Phys. Lett. B* 716 (2012), pp. 30–61. arXiv: 1207.7235 [hep-ex].

[25] A. M. Sirunyan et al. "Combined measurements of Higgs boson couplings in proton–proton collisions at $\sqrt{s} = 13\,\text{TeV}$." In: *Eur. Phys. J. C* 79.5 (2019), p. 421. arXiv: 1809.10733 [hep-ex].

[26] G. Aad et al. "Combined measurements of Higgs boson production and decay using up to 80 fb^{-1} of proton-proton collision data at $\sqrt{s} = 13$ TeV collected with the ATLAS experiment." In: *Phys. Rev. D* 101.1 (2020), p. 012002. arXiv: 1909.02845 [hep-ex].

[27] B. Pontecorvo. "Mesonium and anti-mesonium." In: *Sov. Phys. JETP* 6 (1957), p. 429.

[28] B. Pontecorvo. "Inverse beta processes and nonconservation of lepton charge." In: *Zh. Eksp. Teor. Fiz.* 34 (1957), p. 247.

[29] Z. Maki, M. Nakagawa, and S. Sakata. "Remarks on the unified model of elementary particles." In: *Prog. Theor. Phys.* 28 (1962), pp. 870–880.

[30] Y. Fukuda et al. "Evidence for oscillation of atmospheric neutrinos." In: *Phys. Rev. Lett.* 81 (1998), pp. 1562–1567. arXiv: hep-ex/9807003.

[31] Q. R. Ahmad et al. "Measurement of the rate of $\nu_e + d \to p + p + e^-$ interactions produced by ^{8}B solar neutrinos at the Sudbury Neutrino Observatory." In: *Phys. Rev. Lett.* 87 (2001), p. 071301. arXiv: nucl-ex/0106015.

[32] F. Zwicky. "Die Rotverschiebung von extragalaktischen Nebeln." In: *Helv. Phys. Acta* 6 (1933), pp. 110–127.

[33] A. D. Sakharov. "Violation of CP Invariance, C asymmetry, and baryon asymmetry of the universe." In: *Pisma Zh. Eksp. Teor. Fiz.* 5 (1967), pp. 32–35.

[34] R. Aaij et al. "Test of lepton universality in beauty-quark decays." In: *Nature Phys.* 18.3 (2022), pp. 277–282. arXiv: 2103.11769 [hep-ex].

[35] R. Aaij et al. "Test of lepton universality using $B^+ \to K^+\ell^+\ell^-$ decays." In: *Phys. Rev. Lett.* 113 (2014), p. 151601. arXiv: 1406.6482 [hep-ex].

[36] R. Aaij et al. "Test of lepton universality with $B^0 \to K^{*0}\ell^+\ell^-$ decays." In: *JHEP* 08 (2017), p. 055. arXiv: 1705.05802 [hep-ex].

[37] R. Aaij et al. "Search for lepton-universality violation in $B^+ \to K^+\ell^+\ell^-$ decays." In: *Phys. Rev. Lett.* 122.19 (2019), p. 191801. arXiv: 1903.09252 [hep-ex].

[38] R. Aaij et al. "Differential branching fractions and isospin asymmetries of $B \to K^{(*)}\mu^+\mu^-$ decays." In: *JHEP* 06 (2014), p. 133. arXiv: 1403.8044 [hep-ex].

[39] R. Aaij et al. "Angular analysis and differential branching fraction of the decay $B_s^0 \to \phi\mu^+\mu^-$." In: *JHEP* 09 (2015), p. 179. arXiv: 1506.08777 [hep-ex].

[40] R. Aaij et al. "Measurements of the S-wave fraction in $B^0 \to K^+\pi^-\mu^+\mu^-$ decays and the $B^0 \to K^*(892)^0\mu^+\mu^-$ differential branching fraction." In: *JHEP* 11 (2016). [Erratum: JHEP 04, 142 (2017)], p. 047. arXiv: 1606.04731 [hep-ex].

[41] R. Aaij et al. "Branching Fraction Measurements of the Rare $B_s^0 \to \phi\mu^+\mu^-$ and $B_s^0 \to f_2'(1525)\mu^+\mu^-$- Decays." In: *Phys. Rev. Lett.* 127.15 (2021), p. 151801. arXiv: 2105.14007 [hep-ex].

[42] R. Aaij et al. "Angular analysis of the $B^0 \to K^{*0}\mu^+\mu^-$ decay using 3 fb^{-1} of integrated luminosity." In: *JHEP* 02 (2016), p. 104. arXiv: 1512.04442 [hep-ex].

[43] R. Aaij et al. "Measurement of CP-Averaged Observables in the $B^0 \to K^{*0}\mu^+\mu^-$ Decay." In: *Phys. Rev. Lett.* 125.1 (2020), p. 011802. arXiv: 2003.04831 [hep-ex].

[44] M. Aaboud et al. "Angular analysis of $B_d^0 \to K^*\mu^+\mu^-$ decays in pp collisions at $\sqrt{s} = 8$ TeV with the ATLAS detector." In: *JHEP* 10 (2018), p. 047. arXiv: 1805.04000 [hep-ex].

[45] "Measurement of the P_1 and P_5' angular parameters of the decay $\mathrm{B}^0 \to \mathrm{K}^{*0}\mu^+\mu^-$ in proton-proton collisions at $\sqrt{s} = 8$ TeV." In: (Mar. 2017, CMS-PAS-BPH-15-008.).

[46] V. Khachatryan et al. "Angular analysis of the decay $B^0 \to K^{*0}\mu^+\mu^-$ from pp collisions at $\sqrt{s} = 8$ TeV." In: *Phys. Lett. B* 753 (2016), pp. 424–448. arXiv: 1507.08126 [hep-ex].

[47] R. Aaij et al. "Angular analysis of the rare decay $B_s^0 \to \phi\mu^+\mu^-$." In: *JHEP* 11 (2021), p. 043. arXiv: 2107.13428 [hep-ex].

[48] B. Abi et al. "Measurement of the Positive Muon Anomalous Magnetic Moment to 0.46 ppm." In: *Phys. Rev. Lett.* 126.14 (2021), p. 141801. arXiv: 2104.03281 [hep-ex].

[49] T. Albahri et al. "Magnetic-field measurement and analysis for the Muon $g-2$ Experiment at Fermilab." In: *Phys. Rev. A* 103.4 (2021), p. 042208. arXiv: 2104.03201 [hep-ex].

[50] T. Albahri et al. "Beam dynamics corrections to the Run-1 measurement of the muon anomalous magnetic moment at Fermilab." In: *Phys. Rev. Accel. Beams* 24.4 (2021), p. 044002. arXiv: 2104.03240 [physics.acc-ph].

[51] T. Albahri et al. "Measurement of the anomalous precession frequency of the muon in the Fermilab Muon $g-2$ Experiment." In: *Phys. Rev. D* 103.7 (2021), p. 072002. arXiv: 2104.03247 [hep-ex].

[52] G. W. Bennett et al. "Final Report of the Muon E821 Anomalous Magnetic Moment Measurement at BNL." In: *Phys. Rev. D* 73 (2006), p. 072003. arXiv: hep-ex/0602035.

[53] T. Aoyama et al. "The anomalous magnetic moment of the muon in the Standard Model." In: *Phys. Rept.* 887 (2020), pp. 1–166. arXiv: 2006.04822 [hep-ph].

[54] G. Colangelo et al. "Prospects for precise predictions of a_μ in the Standard Model." In: *2022 Snowmass Summer Study*. Mar. 2022. arXiv: 2203.15810 [hep-ph].

[55] J. Kriewald et al. "Leptoquarks facing flavour tests and $b \to s\ell\ell$ after Moriond 2021." In: *55th Rencontres de Moriond on Electroweak Interactions and Unified Theories*. Mar. 2021. arXiv: 2104.00015 [hep-ph].

[56] G. Aad et al. "Measurements of differential cross-sections in top-quark pair events with a high transverse momentum top quark and limits on beyond the Standard Model contributions to top-quark pair production with the ATLAS detector at $\sqrt{s} = 13$ TeV." In: (Feb. 2022). arXiv: 2202.12134 [hep-ex].

[57] S. Bißmann et al. "Top and Beauty synergies in SMEFT-fits at present and future colliders." In: *JHEP* 06 (2021), p. 010. arXiv: 2012.10456 [hep-ph].

[58] S. Bißmann et al. "Correlating uncertainties in global analyses within SMEFT matters." In: *Phys. Rev. D* 102 (2020), p. 115019. arXiv: 1912.06090 [hep-ph].

[59] S. Bißmann et al. "Constraining top-quark couplings combining top-quark and decay observables." In: *Eur. Phys. J. C* 80.2 (2020), p. 136. arXiv: 1909.13632 [hep-ph].

[60] J. A. Aguilar-Saavedra. "Top flavor-changing neutral interactions: Theoretical expectations and experimental detection." In: *Acta Phys. Polon. B* 35 (2004). Ed. by F. del Aguila et al., pp. 2695–2710. arXiv: hep-ph/0409342.

[61] "Search for flavour-changing neutral-current couplings between the top-quark and the photon with the ATLAS detector at $\sqrt{s} = 13$ TeV." In: (Feb. 2022, ATLAS-CONF-2022-003.).

[62] "Observation of single-top-quark production in association with a photon at the ATLAS detector." In: (Mar. 2022, ATLAS-CONF-2022-013.).

[63] A. Cerri et al. "Report from Working Group 4: Opportunities in Flavour Physics at the HL-LHC and HE-LHC." In: *CERN Yellow Rep. Monogr.* 7 (2019). Ed. by A. Dainese et al., pp. 867–1158. arXiv: 1812.07638 [hep-ph].

[64] W. Altmannshofer et al. "The Belle II Physics Book." In: *PTEP* 2019.12 (2019). Ed. by E. Kou and P. Urquijo. [Erratum: PTEP 2020, 029201 (2020)], p. 123C01. arXiv: 1808.10567 [hep-ex].

[65] M. Ablikim et al. "Future Physics Programme of BESIII." In: *Chin. Phys. C* 44.4 (2020), p. 040001. arXiv: 1912.05983 [hep-ex].

[66] A. E. Bondar et al. "Project of a Super Charm-Tau factory at the Budker Institute of Nuclear Physics in Novosibirsk." In: *Phys. Atom. Nucl.* 76 (2013), pp. 1072–1085.

[67] F. Zimmermann. "LHC/FCC-based muon colliders." In: (2018), MOPMF065.

[68] A. Abada et al. "FCC Physics Opportunities: Future Circular Collider Conceptual Design Report Volume 1." In: *Eur. Phys. J. C* 79.6 (2019), p. 474.

[69] A. Abdesselam et al. "Observation of $D^0 \to \rho^0\gamma$ and search for CP violation in radiative charm decays." In: *Phys. Rev. Lett.* 118.5 (2017), p. 051801. arXiv: 1603.03257 [hep-ex].

[70] R. Aaij et al. "Observation of D^0 meson decays to $\pi^+\pi^-\mu^+\mu^-$ and $K^+K^-\mu^+\mu^-$ final states." In: *Phys. Rev. Lett.* 119.18 (2017), p. 181805. arXiv: 1707.08377 [hep-ex].

[71] R. Aaij et al. "Measurement of Angular and CP Asymmetries in $D^0 \to \pi^+\pi^-\mu^+\mu^-$ and $D^0 \to K^+K^-\mu^+\mu^-$ decays." In: *Phys. Rev. Lett.* 121.9 (2018), p. 091801. arXiv: 1806.10793 [hep-ex].

[72] R. Aaij et al. "Angular analysis of $D^0 \to \pi^+\pi^-\mu^+\mu^-$ and $D^0 \to K^+K^-\mu^+\mu^-$ decays and search for CP violation." In: (Nov. 2021). arXiv: 2111.03327 [hep-ex].

[73] R. Aaij et al. "Search for the rare decay $D^0 \to \mu^+\mu^-$." In: *Phys. Lett. B* 725 (2013), pp. 15–24. arXiv: 1305.5059 [hep-ex].

[74] R. Aaij et al. "Search for the lepton-flavour violating decay $D^0 \to e^\pm\mu^\mp$." In: *Phys. Lett.* B754 (2016), pp. 167–175. arXiv: 1512.00322 [hep-ex].

[75] R. Aaij et al. "Search for D+(s) to pi+ mu+ mu- and D+(s) to pi- mu+ mu+ decays." In: *Phys. Lett.* B724 (2013), pp. 203–212. arXiv: 1304.6365 [hep-ex].

[76] R. Aaij et al. "Searches for 25 rare and forbidden decays of D^+ and D_s^+ mesons." In: *JHEP* 06 (2021), p. 044. arXiv: 2011.00217 [hep-ex].

[77] R. Aaij et al. "Search for the rare decay $\Lambda_c^+ \to p\mu^+\mu^-$." In: *Phys. Rev. D* 97.9 (2018), p. 091101. arXiv: 1712.07938 [hep-ex].

[78] M. Ablikim et al. "Search for the decay $D^0 \to \pi^0\nu\bar{\nu}$." In: (Dec. 2021). arXiv: 2112.14236 [hep-ex].

[79] M. Staric et al. "Evidence for D^0 - $\bar{D}^0$ Mixing." In: *Phys. Rev. Lett.* 98 (2007). Ed. by E. Augé, B. Pietrzyk, and J. Trân Thanh Vân, p. 211803. arXiv: hep-ex/0703036.

[80] B. Aubert et al. "Evidence for $D^0 - \overline{D}^0$ Mixing." In: *Phys. Rev. Lett.* 98 (2007), p. 211802. arXiv: hep-ex/0703020.

[81] T. Aaltonen et al. "Evidence for $D^0 - \bar{D}^0$ mixing using the CDF II Detector." In: *Phys. Rev. Lett.* 100 (2008), p. 121802. arXiv: 0712.1567 [hep-ex].

[82] R. Aaij et al. "Updated determination of D^0-$\overline{D}^0$ mixing and CP violation parameters with $D^0 \to K^+\pi^-$ decays." In: *Phys. Rev. D* 97.3 (2018), p. 031101. arXiv: 1712.03220 [hep-ex].

[83] R. Aaij et al. "Search for time-dependent CP violation in $D^0 \to K^+K^-$ and $D^0 \to \pi^+\pi^-$ decays." In: *Phys. Rev. D* 104.7 (2021), p. 072010. arXiv: 2105.09889 [hep-ex].

[84] R. Aaij et al. "Measurement of the Charm-Mixing Parameter y_{CP}." In: *Phys. Rev. Lett.* 122.1 (2019), p. 011802. arXiv: 1810.06874 [hep-ex].

[85] R. Aaij et al. "Observation of CP Violation in Charm Decays." In: *Phys. Rev. Lett.* 122.21 (2019), p. 211803. arXiv: 1903.08726 [hep-ex].

[86] S. de Boer. "Two loop virtual corrections to $b \to (d,s)\ell^+\ell^-$ and $c \to u\ell^+\ell^-$ for arbitrary momentum transfer." In: *Eur. Phys. J.* C77.11 (2017), p. 801. arXiv: 1707.00988 [hep-ph].

[87] S. de Boer, B. Müller, and D. Seidel. "Higher-order Wilson coefficients for $c \to u$ transitions in the standard model." In: *JHEP* 08 (2016), p. 091. arXiv: 1606.05521 [hep-ph].

[88] S. De Boer and G. Hiller. "Null tests from angular distributions in $D \to P_1P_2l^+l^-$, $l = e, \mu$ decays on and off peak." In: *Phys. Rev.* D98.3 (2018), p. 035041. arXiv: 1805.08516 [hep-ph].

[89] S. de Boer and G. Hiller. "Rare radiative charm decays within the standard model and beyond." In: *JHEP* 08 (2017), p. 091. arXiv: 1701.06392 [hep-ph].

[90] S. de Boer and G. Hiller. "Flavor and new physics opportunities with rare charm decays into leptons." In: *Phys. Rev. D* 93.7 (2016), p. 074001. arXiv: 1510.00311 [hep-ph].

[91] S. Fajfer, N. Kosnik, and S. Prelovsek. "Updated constraints on new physics in rare charm decays." In: *Phys. Rev. D* 76 (2007), p. 074010. arXiv: 0706.1133 [hep-ph].

[92] S. Fajfer and N. Košnik. "Resonance catalyzed CP asymmetries in D→P$\ell^+\ell^-$." In: *Phys. Rev. D* 87.5 (2013), p. 054026. arXiv: 1208.0759 [hep-ph].

[93] S. Fajfer and N. Košnik. "Prospects of discovering new physics in rare charm decays." In: *Eur. Phys. J. C* 75.12 (2015), p. 567. arXiv: 1510.00965 [hep-ph].

[94] S. Fajfer, S. Prelovsek, and P. Singer. "Rare charm meson decays D —> P lepton+ lepton- and c —> u lepton+ lepton- in SM and MSSM." In: *Phys. Rev. D* 64 (2001), p. 114009. arXiv: hep-ph/0106333.

[95] S. Fajfer, P. Singer, and J. Zupan. "The Radiative leptonic decays D0 —> e+ e- gamma, mu+ mu- gamma in the standard model and beyond." In: *Eur. Phys. J.* C27 (2003), pp. 201–218. arXiv: hep-ph/0209250 [hep-ph].

[96] S. Fajfer and S. Prelovsek. "Effects of littlest Higgs model in rare D meson decays." In: *Phys. Rev. D* 73 (2006), p. 054026. arXiv: hep-ph/0511048.

[97] C. Greub et al. "The c —> u gamma contribution to weak radiative charm decay." In: *Phys. Lett. B* 382 (1996), pp. 415–420. arXiv: hep-ph/9603417.

[98] G. Burdman et al. "Rare charm decays in the standard model and beyond." In: *Phys. Rev.* D66 (2002), p. 014009. arXiv: hep-ph/0112235 [hep-ph].

[99] L. Cappiello, O. Cata, and G. D'Ambrosio. "Standard Model prediction and new physics tests for $D^0 \to h^+h^-\ell^+\ell^-(h = \pi, K : \ell = e, \mu)$." In: *JHEP* 04 (2013), p. 135. arXiv: 1209.4235 [hep-ph].

[100] E. Golowich et al. "Relating D0-anti-D0 Mixing and D0 —> l+ l- with New Physics." In: *Phys. Rev.* D79 (2009), p. 114030. arXiv: 0903.2830 [hep-ph].

[101] E. Golowich et al. "Implications of D^0 - $\bar{D}^0$ Mixing for New Physics." In: *Phys. Rev.* D76 (2007), p. 095009. arXiv: 0705.3650 [hep-ph].

[102] T. Feldmann, B. Müller, and D. Seidel. "$D \to \rho\,\ell^+\ell^-$ decays in the QCD factorization approach." In: *JHEP* 08 (2017), p. 105. arXiv: 1705.05891 [hep-ph].

[103] S. Meinel. "$\Lambda_c \to N$ form factors from lattice QCD and phenomenology of $\Lambda_c \to n\ell^+\nu_\ell$ and $\Lambda_c \to p\mu^+\mu^-$ decays." In: *Phys. Rev.* D97.3 (2018), p. 034511. arXiv: 1712.05783 [hep-lat].

[104] A. Bharucha, D. Boito, and C. Méaux. "Disentangling QCD and new physics in $D^+ \to \pi^+\ell^+\ell^-$." In: *JHEP* 04 (2021), p. 158. arXiv: 2011.12856 [hep-ph].

[105] S. Fajfer and A. Novosel. "Colored scalars mediated rare charm meson decays to invisible fermions." In: *Phys. Rev. D* 104.1 (2021), p. 015014. arXiv: 2101.10712 [hep-ph].

[106] P. Colangelo, F. De Fazio, and F. Loparco. "c→u$\nu\nu^-$ transitions of Bc mesons: 331 model facing Standard Model null tests." In: *Phys. Rev. D* 104.11 (2021), p. 115024. arXiv: 2107.07291 [hep-ph].

[107] G. Faisel, J.-Y. Su, and J. Tandean. "Exploring charm decays with missing energy in leptoquark models." In: *JHEP* 04 (2021), p. 246. arXiv: 2012.15847 [hep-ph].

[108] S. de Boer and G. Hiller. "The photon polarization in radiative D decays, phenomenologically." In: *Eur. Phys. J. C* 78.3 (2018), p. 188. arXiv: 1802.02769 [hep-ph].

[109] N. Adolph, G. Hiller, and A. Tayduganov. "Testing the standard model with $D_{(s)} \to K_1(\to K\pi\pi)\gamma$ decays." In: *Phys. Rev. D* 99.7 (2019), p. 075023. arXiv: 1812.04679 [hep-ph].

[110] N. Adolph and G. Hiller. "Probing QCD dynamics and the standard model with $D^+_{(s)} \to P_1^+ P_2^0 \gamma$ decays." In: *JHEP* 06 (2021), p. 155. arXiv: 2104.08287 [hep-ph].

[111] N. Adolph, J. Brod, and G. Hiller. "Radiative three-body D-meson decays in and beyond the standard model." In: *Eur. Phys. J. C* 81.1 (2021), p. 45. arXiv: 2009.14212 [hep-ph].

[112] N. Adolph and G. Hiller. "Rare radiative decays of charm baryons." In: *Phys. Rev. D* 105.11 (2022), p. 116001. arXiv: 2203.14982 [hep-ph].

[113] K. G. Wilson. "Nonlagrangian models of current algebra." In: *Phys. Rev.* 179 (1969), pp. 1499–1512.

[114] J. Ellis. "TikZ-Feynman: Feynman diagrams with TikZ." In: (2016). arXiv: 1601.05437 [hep-ph].

[115] E. O. Lebigot. *Uncertainties: a Python package for calculations with uncertainties*. Version 2.4.6.1.

[116] J. D. Hunter. "Matplotlib: A 2D Graphics Environment." Version 1.4.3. In: *Computing in Science & Engineering* 9.3 (2007), pp. 90–95.

[117] T. E. Oliphant. "NumPy: Python for Scientific Computing." Version 1.9.2. In: *Computing in Science & Engineering* 9.3 (2007), pp. 10–20.

[118] E. Jones, T. E. Oliphant, P. Peterson, et al. *SciPy: Open source scientific tools for Python*. Version 0.16.0.

[119] W. R. Inc. *Mathematica, Version 9*. Champaign, IL, 2012.

[120] M. E. Peskin and D. V. Schroeder. *An Introduction to Quantum Field Theory*. Reading, USA: Addison-Wesley, 1995.

[121] S. Weinberg. *The Quantum Theory of Fields. Vol. 1: Foundations*. Cambridge University Press, June 2005.

[122] S. Weinberg. *The Quantum Theory of Fields. Vol. 2: Modern applications*. Cambridge University Press, Aug. 2013.

[123] M. D. Schwartz. *Quantum Field Theory and the Standard Model*. Cambridge University Press, Mar. 2014.

[124] A. Buras. *Gauge Theory of Weak Decays*. Cambridge University Press, June 2020.

[125] D. J. Gross and F. Wilczek. "Ultraviolet Behavior of Nonabelian Gauge Theories." In: *Phys. Rev. Lett.* 30 (1973). Ed. by J. C. Taylor, pp. 1343–1346.

[126] G. 't Hooft and M. J. G. Veltman. "Regularization and Renormalization of Gauge Fields." In: *Nucl. Phys. B* 44 (1972), pp. 189–213.

[127] H. D. Politzer. "Reliable Perturbative Results for Strong Interactions?" In: *Phys. Rev. Lett.* 30 (1973). Ed. by J. C. Taylor, pp. 1346–1349.

[128] S. Weinberg. "Nonabelian Gauge Theories of the Strong Interactions." In: *Phys. Rev. Lett.* 31 (1973), pp. 494–497.

[129] H. Fritzsch, M. Gell-Mann, and H. Leutwyler. "Advantages of the Color Octet Gluon Picture." In: *Phys. Lett. B* 47 (1973), pp. 365–368.

[130] A. Salam. "Weak and Electromagnetic Interactions." In: *Conf. Proc. C* 680519 (1968), pp. 367–377.

[131] S. L. Glashow. "Partial Symmetries of Weak Interactions." In: *Nucl. Phys.* 22 (1961), pp. 579–588.

[132] S. Weinberg. "A Model of Leptons." In: *Phys. Rev. Lett.* 19 (1967), pp. 1264–1266.

[133] N. Cabibbo. "Unitary Symmetry and Leptonic Decays." In: *Phys. Rev. Lett.* 10 (1963), pp. 531–533.

[134] M. Kobayashi and T. Maskawa. "CP Violation in the Renormalizable Theory of Weak Interaction." In: *Prog. Theor. Phys.* 49 (1973), pp. 652–657.

[135] Y. Nir. "Probing new physics with flavor physics (and probing flavor physics with new physics)." In: *2nd Workshop on Monte Carlo Tools for Beyond the Standard Model Physics*. Aug. 2007. arXiv: 0708.1872 [hep-ph].

[136] A. Ali et al. "A Comparative study of the decays $B \to (K, K^{*)}\ell^+\ell^-$ in standard model and supersymmetric theories." In: *Phys. Rev. D* 61 (2000), p. 074024. arXiv: hep-ph/9910221.

[137] C. D. Froggatt and H. B. Nielsen. "Hierarchy of Quark Masses, Cabibbo Angles and CP Violation." In: *Nucl. Phys. B* 147 (1979), pp. 277–298.

[138] G. Altarelli and F. Feruglio. "Discrete Flavor Symmetries and Models of Neutrino Mixing." In: *Rev. Mod. Phys.* 82 (2010), pp. 2701–2729. arXiv: 1002.0211 [hep-ph].

[139] I. de Medeiros Varzielas and G. Hiller. "Clues for flavor from rare lepton and quark decays." In: *JHEP* 06 (2015), p. 072. arXiv: 1503.01084 [hep-ph].

[140] G. Hiller, D. Loose, and K. Schönwald. "Leptoquark Flavor Patterns & B Decay Anomalies." In: *JHEP* 12 (2016), p. 027. arXiv: 1609.08895 [hep-ph].

[141] A. J. Bevan et al. "The Physics of the B Factories." In: *Eur. Phys. J. C* 74 (2014), p. 3026. arXiv: 1406.6311 [hep-ex].

[142] A. Bharucha, D. M. Straub, and R. Zwicky. "$B \to V\ell^+\ell^-$ in the Standard Model from light-cone sum rules." In: *JHEP* 08 (2016), p. 098. arXiv: 1503.05534 [hep-ph].

[143] R. R. Horgan et al. "Rare B decays using lattice QCD form factors." In: *PoS* LATTICE2014 (2015), p. 372. arXiv: 1501.00367 [hep-lat].

[144] N. Gubernari, A. Kokulu, and D. van Dyk. "$B \to P$ and $B \to V$ Form Factors from B-Meson Light-Cone Sum Rules beyond Leading Twist." In: *JHEP* 01 (2019), p. 150. arXiv: 1811.00983 [hep-ph].

[145] A. Khodjamirian et al. "Charm-loop effect in $B \to K^{(*)}\ell^+\ell^-$ and $B \to K^*\gamma$." In: *JHEP* 09 (2010), p. 089. arXiv: 1006.4945 [hep-ph].

[146] C. Bobeth et al. "Long-distance effects in $B \to K^*\ell\ell$ from analyticity." In: *Eur. Phys. J. C* 78.6 (2018), p. 451. arXiv: 1707.07305 [hep-ph].

[147] M. Bordone, G. Isidori, and A. Pattori. "On the Standard Model predictions for R_K and R_{K^*}." In: *Eur. Phys. J. C* 76.8 (2016), p. 440. arXiv: 1605.07633 [hep-ph].

[148] G. Hiller and F. Kruger. "More model-independent analysis of $b \to s$ processes." In: *Phys. Rev. D* 69 (2004), p. 074020. arXiv: hep-ph/0310219.

[149] J. P. Lees et al. "Evidence for an excess of $\bar{B} \to D^{(*)}\tau^-\bar{\nu}_\tau$ decays." In: *Phys. Rev. Lett.* 109 (2012), p. 101802. arXiv: 1205.5442 [hep-ex].

[150] J. P. Lees et al. "Measurement of an Excess of $\bar{B} \to D^{(*)}\tau^-\bar{\nu}_\tau$ Decays and Implications for Charged Higgs Bosons." In: *Phys. Rev. D* 88.7 (2013), p. 072012. arXiv: 1303.0571 [hep-ex].

[151] M. Huschle et al. "Measurement of the branching ratio of $\bar{B} \to D^{(*)}\tau^-\bar{\nu}_\tau$ relative to $\bar{B} \to D^{(*)}\ell^-\bar{\nu}_\ell$ decays with hadronic tagging at Belle." In: *Phys. Rev. D* 92.7 (2015), p. 072014. arXiv: 1507.03233 [hep-ex].

[152] Y. Sato et al. "Measurement of the branching ratio of $\bar{B}^0 \to D^{*+}\tau^-\bar{\nu}_\tau$ relative to $\bar{B}^0 \to D^{*+}\ell^-\bar{\nu}_\ell$ decays with a semileptonic tagging method." In: *Phys. Rev. D* 94.7 (2016), p. 072007. arXiv: 1607.07923 [hep-ex].

[153] S. Hirose et al. "Measurement of the τ lepton polarization and $R(D^*)$ in the decay $\bar{B} \to D^* \tau^- \bar{\nu}_\tau$." In: *Phys. Rev. Lett.* 118.21 (2017), p. 211801. arXiv: 1612.00529 [hep-ex].

[154] R. Aaij et al. "Measurement of the ratio of branching fractions $\mathcal{B}(\bar{B}^0 \to D^{*+} \tau^- \bar{\nu}_\tau)/\mathcal{B}(\bar{B}^0 \to D^{*+} \mu^- \bar{\nu}_\mu)$." In: *Phys. Rev. Lett.* 115.11 (2015). [Erratum: Phys.Rev.Lett. 115, 159901 (2015)], p. 111803. arXiv: 1506.08614 [hep-ex].

[155] R. Aaij et al. "Measurement of the ratio of the $B^0 \to D^{*-} \tau^+ \nu_\tau$ and $B^0 \to D^{*-} \mu^+ \nu_\mu$ branching fractions using three-prong τ-lepton decays." In: *Phys. Rev. Lett.* 120.17 (2018), p. 171802. arXiv: 1708.08856 [hep-ex].

[156] L. J. Hall et al. "Freeze-In Production of FIMP Dark Matter." In: *JHEP* 03 (2010), p. 080. arXiv: 0911.1120 [hep-ph].

[157] N. Bernal et al. "The Dawn of FIMP Dark Matter: A Review of Models and Constraints." In: *Int. J. Mod. Phys. A* 32.27 (2017), p. 1730023. arXiv: 1706.07442 [hep-ph].

[158] T. Appelquist and J. Carazzone. "Infrared Singularities and Massive Fields." In: *Phys. Rev. D* 11 (1975), p. 2856.

[159] E. Fermi. "An attempt of a theory of beta radiation. 1." In: *Z. Phys.* 88 (1934), pp. 161–177.

[160] A. J. Buras. "Weak Hamiltonian, CP violation and rare decays." In: *Les Houches Summer School in Theoretical Physics, Session 68: Probing the Standard Model of Particle Interactions*. June 1998, pp. 281–539. arXiv: hep-ph/9806471.

[161] G. Buchalla, A. J. Buras, and M. E. Lautenbacher. "Weak decays beyond leading logarithms." In: *Rev. Mod. Phys.* 68 (1996), pp. 1125–1144. arXiv: hep-ph/9512380.

[162] A. Pich. "Effective field theory: Course." In: *Les Houches Summer School in Theoretical Physics, Session 68: Probing the Standard Model of Particle Interactions*. June 1998, pp. 949–1049. arXiv: hep-ph/9806303.

[163] M. Neubert. "Effective field theory and heavy quark physics." In: *Theoretical Advanced Study Institute in Elementary Particle Physics: Physics in $D \geqq 4$*. Dec. 2005, pp. 149–194. arXiv: hep-ph/0512222.

[164] M. Neubert. "Renormalization Theory and Effective Field Theories." In: (Jan. 2019). Ed. by S. Davidson et al. arXiv: 1901.06573 [hep-ph].

[165] A. V. Manohar. "Effective field theories." In: *Lect. Notes Phys.* 479 (1997). Ed. by H. Latal and W. Schweiger, pp. 311–362. arXiv: hep-ph/9606222.

[166] S. de Boer. "Probing the standard model with rare charm decays." https://eldorado.tu-dortmund.de/handle/2003/36043. PhD thesis. TU Dortmund, 2017.

[167] T. Inami and C. S. Lim. "Effects of Superheavy Quarks and Leptons in Low-Energy Weak Processes k(L) —> mu anti-mu, K+ —> pi+ Neutrino anti-neutrino and K0 <—> anti-K0." In: *Prog. Theor. Phys.* 65 (1981). [Erratum: Prog.Theor.Phys. 65, 1772 (1981)], p. 297.

[168] I. Brivio et al. "The complete HEFT Lagrangian after the LHC Run I." In: *Eur. Phys. J. C* 76.7 (2016), p. 416. arXiv: 1604.06801 [hep-ph].

[169] S. Weinberg. "Baryon and Lepton Nonconserving Processes." In: *Phys. Rev. Lett.* 43 (1979), pp. 1566–1570.

[170] C. Degrande et al. "Effective Field Theory: A Modern Approach to Anomalous Couplings." In: *Annals Phys.* 335 (2013), pp. 21–32. arXiv: 1205.4231 [hep-ph].

[171] A. Kobach. "Baryon Number, Lepton Number, and Operator Dimension in the Standard Model." In: *Phys. Lett. B* 758 (2016), pp. 455–457. arXiv: 1604.05726 [hep-ph].

[172] W. Buchmuller and D. Wyler. "Effective Lagrangian Analysis of New Interactions and Flavor Conservation." In: *Nucl. Phys. B* 268 (1986), pp. 621–653.

[173] B. Grzadkowski et al. "Dimension-Six Terms in the Standard Model Lagrangian." In: *JHEP* 10 (2010), p. 085. arXiv: 1008.4884 [hep-ph].

[174] I. Brivio and M. Trott. "The Standard Model as an Effective Field Theory." In: *Phys. Rept.* 793 (2019), pp. 1–98. arXiv: 1706.08945 [hep-ph].

[175] Y. Amhis et al. "Averages of b-hadron, c-hadron, and τ-lepton properties as of summer 2016." In: *Eur. Phys. J.* C77.12 (2017), p. 895. arXiv: 1612.07233 [hep-ex].

[176] Y. S. Amhis et al. "Averages of b-hadron, c-hadron, and τ-lepton properties as of 2018." In: *Eur. Phys. J. C* 81.3 (2021), p. 226. arXiv: 1909.12524 [hep-ex].

[177] C. Bobeth, G. Hiller, and G. Piranishvili. "Angular distributions of $\bar{B} \to \bar{K}\ell^+\ell^-$ decays." In: *JHEP* 12 (2007), p. 040. arXiv: 0709.4174 [hep-ph].

[178] N. K. Nisar et al. "Search for the rare decay $D^0 \to \gamma\gamma$ at Belle." In: *Phys. Rev. D* 93.5 (2016), p. 051102. arXiv: 1512.02992 [hep-ex].

[179] V. Lubicz et al. "Scalar and vector form factors of $D \to \pi(K)\ell\nu$ decays with $N_f = 2+1+1$ twisted fermions." In: *Phys. Rev.* D96.5 (2017). [erratum: Phys. Rev.D99,no.9,099902(2019)], p. 054514. arXiv: 1706.03017 [hep-lat].

[180] V. Lubicz et al. "Tensor form factor of $D \to \pi(K)\ell\nu$ and $D \to \pi(K)\ell\ell$ decays with $N_f = 2+1+1$ twisted-mass fermions." In: *Phys. Rev.* D98.1 (2018), p. 014516. arXiv: 1803.04807 [hep-lat].

[181] J. Koponen, C. T. H. Davies, and G. Donald. "D to K and D to pi semileptonic form factors from Lattice QCD." In: *Proceedings, 5th International Workshop on Charm Physics (Charm 2012): Honolulu, Hawaii, USA, May 14-17, 2012*. 2012. arXiv: 1208.6242 [hep-lat].

[182] P. Lichard. "Are the production and decay of a resonance always independent?" In: *Acta Phys. Slov.* 49 (1999), pp. 215–230. arXiv: hep-ph/9811493.

[183] R.-M. Wang et al. "Decays $D^+_{(s)} \to \pi(K)^+\ell^+\ell^-$ and $D^0 \to \ell^+\ell^-$ in the MSSM with and without R-parity." In: *Int. J. Mod. Phys.* A30.12 (2015), p. 1550063. arXiv: 1409.0181 [hep-ph].

[184] P. Zyla et al. "Review of Particle Physics." In: *PTEP* 2020.8 (2020), p. 083C01.

[185] F. Kruger and L. M. Sehgal. "Lepton polarization in the decays b —> X(s) mu+ mu- and B —> X(s) tau+ tau-." In: *Phys. Lett. B* 380 (1996), pp. 199–204. arXiv: hep-ph/9603237.

[186] K. Kodama et al. "Upper limits of charm hadron decays to two muons plus hadrons." In: *Phys. Lett. B* 345 (1995), pp. 85–92.

[187] S. X. Li et al. "First measurement of the $\Lambda_c^+ \to p\eta'$ decay." In: *JHEP* 03 (2022), p. 090. arXiv: 2112.14276 [hep-ex].

[188] R. N. Faustov and V. O. Galkin. "Rare $\Lambda_c \to p\ell^+\ell^-$ decay in the relativistic quark model." In: *Eur. Phys. J. C* 78.6 (2018), p. 527. arXiv: 1805.02516 [hep-ph].

[189] K. Azizi, Y. Sarac, and H. Sundu. "Light cone QCD sum rules study of the semileptonic heavy Ξ_Q and Ξ'_Q transitions to Ξ and Σ baryons." In: *Eur. Phys. J. A* 48 (2012), p. 2. arXiv: 1107.5925 [hep-ph].

[190] M. Jacob and G. C. Wick. "On the General Theory of Collisions for Particles with Spin." In: *Annals Phys.* 7 (1959), pp. 404–428.

[191] J. D. Richman. "An Experimenter's Guide to the Helicity Formalism." In: (June 1984, CALT-68-1148.).

[192] H. E. Haber. "Spin formalism and applications to new physics searches." In: *Spin structure in high-energy processes: Proceedings, 21st SLAC Summer Institute on Particle Physics, 26 Jul - 6 Aug 1993, Stanford, CA*. 1994, pp. 231–272. arXiv: hep-ph/9405376 [hep-ph].

[193] J. Gratrex, M. Hopfer, and R. Zwicky. "Generalised helicity formalism, higher moments and the $B \to K_{J_K}(\to K\pi)\bar{\ell}_1\ell_2$ angular distributions." In: *Phys. Rev. D* 93.5 (2016), p. 054008. arXiv: 1506.03970 [hep-ph].

[194] D. Das. "Model independent New Physics analysis in $\Lambda_b \to \Lambda\mu^+\mu^-$ decay." In: *Eur. Phys. J. C* 78.3 (2018), p. 230. arXiv: 1802.09404 [hep-ph].

[195] Y. Grossman and P. Tanedo. "Just a Taste: Lectures on Flavor Physics." In: *Theoretical Advanced Study Institute in Elementary Particle Physics: Anticipating the Next Discoveries in Particle Physics*. 2018, pp. 109–295. arXiv: 1711.03624 [hep-ph].

[196] A. Lenz and G. Wilkinson. "Mixing and CP Violation in the Charm System." In: *Ann. Rev. Nucl. Part. Sci.* 71 (2021), pp. 59–85. arXiv: 2011.04443 [hep-ph].

[197] F. Buccella, A. Paul, and P. Santorelli. "$SU(3)_F$ breaking through final state interactions and CP asymmetries in $D \to PP$ decays." In: *Phys. Rev. D* 99.11 (2019), p. 113001. arXiv: 1902.05564 [hep-ph].

[198] Y. Grossman and S. Schacht. "The emergence of the $\Delta U = 0$ rule in charm physics." In: *JHEP* 07 (2019), p. 020. arXiv: 1903.10952 [hep-ph].

[199] H.-N. Li, C.-D. Lü, and F.-S. Yu. "Implications on the first observation of charm CPV at LHCb." In: (Mar. 2019). arXiv: 1903.10638 [hep-ph].

[200] H.-Y. Cheng and C.-W. Chiang. "Revisiting CP violation in $D \to PP$ and VP decays." In: *Phys. Rev. D* 100.9 (2019), p. 093002. arXiv: 1909.03063 [hep-ph].

[201] A. L. Kagan and L. Silvestrini. "Dispersive and absorptive CP violation in $D^0 - \overline{D^0}$ mixing." In: *Phys. Rev. D* 103.5 (2021), p. 053008. arXiv: 2001.07207 [hep-ph].

[202] S. Schacht and A. Soni. "Enhancement of charm CP violation due to nearby resonances." In: *Phys. Lett. B* 825 (2022), p. 136855. arXiv: 2110.07619 [hep-ph].

[203] U. Nierste. "Charm decays." In: *PoS* Beauty2019 (2020), p. 048. arXiv: 2002.06686 [hep-ph].

[204] I. Bediaga, T. Frederico, and P. Magalhaes. "Enhanced charm CP asymmetries from final state interactions." In: (Mar. 2022). arXiv: 2203.04056 [hep-ph].

[205] M. Chala et al. "ΔA_{CP} within the Standard Model and beyond." In: *JHEP* 07 (2019), p. 161. arXiv: 1903.10490 [hep-ph].

[206] A. Khodjamirian and A. A. Petrov. "Direct CP asymmetry in $D \to \pi^-\pi^+$ and $D \to K^-K^+$ in QCD-based approach." In: *Phys. Lett. B* 774 (2017), pp. 235–242. arXiv: 1706.07780 [hep-ph].

[207] A. Soni. "Resonance enhancement of Charm CP." In: (May 2019). arXiv: 1905.00907 [hep-ph].

[208] A. Dery and Y. Nir. "Implications of the LHCb discovery of CP violation in charm decays." In: *JHEP* 12 (2019), p. 104. arXiv: 1909.11242 [hep-ph].

[209] J. Brod et al. "A Consistent Picture for Large Penguins in D -> pi+ pi-, K+ K-." In: *JHEP* 10 (2012), p. 161. arXiv: 1203.6659 [hep-ph].

[210] J. P. Lees et al. "Searches for Rare or Forbidden Semileptonic Charm Decays." In: *Phys. Rev.* D84 (2011), p. 072006. arXiv: 1107.4465 [hep-ex].

[211] M. Petric et al. "Search for leptonic decays of D^0 mesons." In: *Phys. Rev. D* 81 (2010), p. 091102. arXiv: 1003.2345 [hep-ex].

[212] A. Abdesselam et al. "Observation of $D^0 \to \rho^0\gamma$ and search for CP violation in radiative charm decays." In: *Phys. Rev. Lett.* 118.5 (2017), p. 051801. arXiv: 1603.03257 [hep-ex].

[213] A. Angelescu, D. A. Faroughy, and O. Sumensari. "Lepton Flavor Violation and Dilepton Tails at the LHC." In: *Eur. Phys. J. C* 80.7 (2020), p. 641. arXiv: 2002.05684 [hep-ph].

[214] J. Fuentes-Martin et al. "Charm physics confronts high-p_T lepton tails." In: *JHEP* 11 (2020), p. 080. arXiv: 2003.12421 [hep-ph].

[215] L.-F. Lai et al. "Prospects for discovering new physics in charm sector through low-energy scattering processes e-p→e-(μ-)Λc." In: *Phys. Rev. D* 105.3 (2022), p. 035007. arXiv: 2111.01463 [hep-ph].

[216] L.-F. Lai et al. "Searching and identifying leptoquarks through low-energy polarized scattering processes $e^-p \to e^-\Lambda_c$." In: (Mar. 2022). arXiv: 2203.17104 [hep-ph].

[217] W. Buchmuller, R. Ruckl, and D. Wyler. "Leptoquarks in Lepton - Quark Collisions." In: *Phys. Lett.* B191 (1987). [Erratum: Phys. Lett.B448,320(1999)], pp. 442–448.

[218] I. Doršner et al. "Physics of leptoquarks in precision experiments and at particle colliders." In: *Phys. Rept.* 641 (2016), pp. 1–68. arXiv: 1603.04993 [hep-ph].

[219] J. C. Pati and A. Salam. "Is Baryon Number Conserved?" In: *Phys. Rev. Lett.* 31 (1973), pp. 661–664.

[220] J. C. Pati and A. Salam. "Lepton Number as the Fourth Color." In: *Phys. Rev. D* 10 (1974). [Erratum: Phys.Rev.D 11, 703–703 (1975)], pp. 275–289.

[221] J. C. Pati and A. Salam. "Unified Lepton-Hadron Symmetry and a Gauge Theory of the Basic Interactions." In: *Phys. Rev. D* 8 (1973), pp. 1240–1251.

[222] G. Hiller and M. Schmaltz. "R_K and future $b \to s\ell\ell$ physics beyond the standard model opportunities." In: *Phys. Rev. D* 90 (2014), p. 054014. arXiv: 1408.1627 [hep-ph].

[223] S. Fajfer and N. Košnik. "Vector leptoquark resolution of R_K and $R_{D^{(*)}}$ puzzles." In: *Phys. Lett. B* 755 (2016), pp. 270–274. arXiv: 1511.06024 [hep-ph].

[224] D. Ghosh, M. Nardecchia, and S. A. Renner. "Hint of Lepton Flavour Non-Universality in B Meson Decays." In: *JHEP* 12 (2014), p. 131. arXiv: 1408.4097 [hep-ph].

[225] R. Barbieri et al. "Anomalies in B-decays and $U(2)$ flavour symmetry." In: *Eur. Phys. J. C* 76.2 (2016), p. 67. arXiv: 1512.01560 [hep-ph].

[226] C. Cornella, J. Fuentes-Martin, and G. Isidori. "Revisiting the vector leptoquark explanation of the B-physics anomalies." In: *JHEP* 07 (2019), p. 168. arXiv: 1903.11517 [hep-ph].

[227] C. Hati et al. "A nonunitary interpretation for a single vector leptoquark combined explanation to the B-decay anomalies." In: *JHEP* 12 (2019), p. 006. arXiv: 1907.05511 [hep-ph].

[228] C. Hati et al. "The fate of $\mathbf{V_1}$ vector leptoquarks: the impact of future flavour data." In: *Eur. Phys. J. C* 81.12 (2021), p. 1066. arXiv: 2012.05883 [hep-ph].

[229] A. Angelescu et al. "Single leptoquark solutions to the B-physics anomalies." In: *Phys. Rev. D* 104.5 (2021), p. 055017. arXiv: 2103.12504 [hep-ph].

[230] S. Sahoo and R. Mohanta. "New physics effects in charm meson decays involving $c \to ul^+l^-(l_i^\mp l_j^\pm)$ transitions." In: *Eur. Phys. J.* C77.5 (2017), p. 344. arXiv: 1705.02251 [hep-ph].

[231] W. Altmannshofer and D. M. Straub. "New Physics in $B \to K^*\mu\mu$?" In: *Eur. Phys. J. C* 73 (2013), p. 2646. arXiv: 1308.1501 [hep-ph].

[232] A. Crivellin, G. D'Ambrosio, and J. Heeck. "Addressing the LHC flavor anomalies with horizontal gauge symmetries." In: *Phys. Rev. D* 91.7 (2015), p. 075006. arXiv: 1503.03477 [hep-ph].

[233] D. Bhatia, S. Chakraborty, and A. Dighe. "Neutrino mixing and R_K anomaly in $\mathrm{U}(1)_X$ models: a bottom-up approach." In: *JHEP* 03 (2017), p. 117. arXiv: 1701.05825 [hep-ph].

[234] C. Bonilla et al. "$U(1)_{B_3-3L_\mu}$ gauge symmetry as a simple description of $b \to s$ anomalies." In: *Phys. Rev. D* 98.9 (2018), p. 095002. arXiv: 1705.00915 [hep-ph].

[235] L. Bian et al. "A minimal flavored $U(1)'$ for B-meson anomalies." In: *Phys. Rev. D* 96.7 (2017), p. 075038. arXiv: 1707.04811 [hep-ph].

[236] S. F. King. "$R_{K^{(*)}}$ and the origin of Yukawa couplings." In: *JHEP* 09 (2018), p. 069. arXiv: 1806.06780 [hep-ph].

[237] A. Falkowski et al. "Flavourful Z' portal for vector-like neutrino Dark Matter and $R_{K^{(*)}}$." In: *JHEP* 08 (2018), p. 061. arXiv: 1803.04430 [hep-ph].

[238] J. Ellis, M. Fairbairn, and P. Tunney. "Anomaly-Free Models for Flavour Anomalies." In: *Eur. Phys. J.* C78.3 (2018), p. 238. arXiv: 1705.03447 [hep-ph].

[239] B. C. Allanach, J. E. Camargo-Molina, and J. Davighi. "Global fits of third family hypercharge models to neutral current B-anomalies and electroweak precision observables." In: *Eur. Phys. J. C* 81.8 (2021), p. 721. arXiv: 2103.12056 [hep-ph].

[240] B. C. Allanach. "$U(1)_{B_3-L_2}$ explanation of the neutral current B—anomalies." In: *Eur. Phys. J. C* 81.1 (2021). [Erratum: Eur.Phys.J.C 81, 321 (2021)], p. 56. arXiv: 2009.02197 [hep-ph].

[241] J.-Y. Cen et al. "Flavor Specific $U(1)_{B_q-L_\mu}$ Gauge Model for Muon $g-2$ and $b \to s\bar{\mu}\mu$ Anomalies." In: (Apr. 2021). arXiv: 2104.05006 [hep-ph].

[242] A. Greljo, P. Stangl, and A. E. Thomsen. "A model of muon anomalies." In: *Phys. Lett. B* 820 (2021), p. 136554. arXiv: 2103.13991 [hep-ph].

[243] R. Bause et al. "B-anomalies from flavorful U(1)′ extensions, safely." In: *Eur. Phys. J. C* 82.1 (2022), p. 42. arXiv: 2109.06201 [hep-ph].

[244] A. Bilal. "Lectures on Anomalies." In: (2008). arXiv: 0802.0634 [hep-th].

[245] A. J. Buras, F. De Fazio, and J. Girrbach. "The Anatomy of Z' and Z with Flavour Changing Neutral Currents in the Flavour Precision Era." In: *JHEP* 02 (2013), p. 116. arXiv: 1211.1896 [hep-ph].

[246] A. Smolkovič, M. Tammaro, and J. Zupan. "Anomaly free Froggatt-Nielsen models of flavor." In: *JHEP* 10 (2019), p. 188. arXiv: 1907.10063 [hep-ph].

[247] G. Hiller and R. Zwicky. "(A)symmetries of weak decays at and near the kinematic endpoint." In: *JHEP* 03 (2014), p. 042. arXiv: 1312.1923 [hep-ph].

[248] G. Hiller and R. Zwicky. "Endpoint relations for baryons." In: *JHEP* 11 (2021), p. 073. arXiv: 2107.12993 [hep-ph].

[249] T. Blake and M. Kreps. "Angular distribution of polarised Λ_b baryons decaying to $\Lambda\ell^+\ell^-$." In: *JHEP* 11 (2017), p. 138. arXiv: 1710.00746 [hep-ph].

[250] R. Aaij et al. "Search for CP violation in $D_s^+ \to K_S^0\pi^+$, $D^+ \to K_S^0K^+$ and $D^+ \to \phi\pi^+$ decays." In: *Phys. Rev. Lett.* 122.19 (2019), p. 191803. arXiv: 1903.01150 [hep-ex].

[251] A. Paul, I. I. Bigi, and S. Recksiegel. "On $D \to X_u l^+ l^-$ within the Standard Model and Frameworks like the Littlest Higgs Model with T Parity." In: *Phys. Rev.* D83 (2011), p. 114006. arXiv: 1101.6053 [hep-ph].

[252] G. Buchalla, G. Hiller, and G. Isidori. "Phenomenology of nonstandard Z couplings in exclusive semileptonic $b \to s$ transitions." In: *Phys. Rev. D* 63 (2000), p. 014015. arXiv: hep-ph/0006136.

[253] R. Aaij et al. "Observation of the Mass Difference Between Neutral Charm-Meson Eigenstates." In: *Phys. Rev. Lett.* 127.11 (2021), p. 111801. arXiv: 2106.03744 [hep-ex].

[254] Y. Grossman, A. L. Kagan, and J. Zupan. "Testing for new physics in singly Cabibbo suppressed D decays." In: *Phys. Rev. D* 85 (2012), p. 114036. arXiv: 1204.3557 [hep-ph].

[255] R. Aaij et al. "Physics case for an LHCb Upgrade II - Opportunities in flavour physics, and beyond, in the HL-LHC era." In: (Aug. 2018). arXiv: 1808.08865 [hep-ex].

[256] D. Mitzel. private communication.

[257] R. Alonso et al. "Renormalization Group Evolution of the Standard Model Dimension Six Operators III: Gauge Coupling Dependence and Phenomenology." In: *JHEP* 04 (2014), p. 159. arXiv: 1312.2014 [hep-ph].

[258] F. Feruglio, P. Paradisi, and A. Pattori. "On the Importance of Electroweak Corrections for B Anomalies." In: *JHEP* 09 (2017), p. 061. arXiv: 1705.00929 [hep-ph].

[259] A. Efrati, A. Falkowski, and Y. Soreq. "Electroweak constraints on flavorful effective theories." In: *JHEP* 07 (2015), p. 018. arXiv: 1503.07872 [hep-ph].

[260] I. Brivio et al. "O new physics, where art thou? A global search in the top sector." In: *JHEP* 02 (2020), p. 131. arXiv: 1910.03606 [hep-ph].

[261] K. Kowalska, D. Kumar, and E. M. Sessolo. "Implications for new physics in $b \to s\mu\mu$ transitions after recent measurements by Belle and LHCb." In: *Eur. Phys. J. C* 79.10 (2019), p. 840. arXiv: 1903.10932 [hep-ph].

[262] J. Aebischer et al. "B-decay discrepancies after Moriond 2019." In: *Eur. Phys. J. C* 80.3 (2020), p. 252. arXiv: 1903.10434 [hep-ph].

[263] W. Altmannshofer and P. Stangl. "New physics in rare B decays after Moriond 2021." In: *Eur. Phys. J. C* 81.10 (2021), p. 952. arXiv: 2103.13370 [hep-ph].

[264] J. F. Kamenik and C. Smith. "Tree-level contributions to the rare decays B+ —> pi+ nu anti-nu, B+ —> K+ nu anti-nu, and B+ —> K*+ nu anti-nu in the Standard Model." In: *Phys. Lett. B* 680 (2009), pp. 471–475. arXiv: 0908.1174 [hep-ph].

[265] Y. .-T. Lai et al. "Search for D^0 decays to invisible final states at Belle." In: *Phys. Rev. D* 95.1 (2017), p. 011102. arXiv: 1611.09455 [hep-ex].

[266] M. Lisovyi, A. Verbytskyi, and O. Zenaiev. "Combined analysis of charm-quark fragmentation-fraction measurements." In: *Eur. Phys. J. C* 76.7 (2016), p. 397. arXiv: 1509.01061 [hep-ex].

[267] J. Brod, M. Gorbahn, and E. Stamou. "Two-Loop Electroweak Corrections for the $K \to \pi\nu\bar{\nu}$ Decays." In: *Phys. Rev. D* 83 (2011), p. 034030. arXiv: 1009.0947 [hep-ph].

[268] J. Brod, M. Gorbahn, and E. Stamou. "Updated Standard Model Prediction for $K \to \pi\nu\bar{\nu}$ and ϵ_K." In: *PoS* BEAUTY2020 (2021), p. 056. arXiv: 2105.02868 [hep-ph].

[269] M. Misiak and J. Urban. "QCD corrections to FCNC decays mediated by Z penguins and W boxes." In: *Phys. Lett. B* 451 (1999), pp. 161–169. arXiv: hep-ph/9901278.

[270] G. Buchalla and A. J. Buras. "The rare decays $K \to \pi\nu\bar{\nu}$, $B \to X\nu\bar{\nu}$ and $B \to l^+l^-$: An Update." In: *Nucl. Phys. B* 548 (1999), pp. 309–327. arXiv: hep-ph/9901288.

[271] J. Grygier et al. "Search for $B \to h\nu\bar{\nu}$ decays with semileptonic tagging at Belle." In: *Phys. Rev. D* 96.9 (2017). [Addendum: Phys.Rev.D 97, 099902 (2018)], p. 091101. arXiv: 1702.03224 [hep-ex].

[272] J. P. Lees et al. "Search for $B \to K^{(*)}\nu\bar{\nu}$ and invisible quarkonium decays." In: *Phys. Rev. D* 87.11 (2013), p. 112005. arXiv: 1303.7465 [hep-ex].

[273] O. Lutz et al. "Search for $B \to h^{(*)}\nu\bar{\nu}$ with the full Belle $\Upsilon(4S)$ data sample." In: *Phys. Rev. D* 87.11 (2013), p. 111103. arXiv: 1303.3719 [hep-ex].

[274] C. S. Kim and R.-M. Wang. "Studying Exclusive Semi-leptonic b —> (s,d)nu anti-nu Decays in the MSSM without R-parity." In: *Phys. Lett. B* 681 (2009), pp. 44–51. arXiv: 0904.0318 [hep-ph].

[275] W. Adam et al. "Study of rare b decays with the DELPHI detector at LEP." In: *Z. Phys. C* 72 (1996), pp. 207–220.

[276] A. J. Buras et al. "$B \to K^{(*)}\nu\bar{\nu}$ decays in the Standard Model and beyond." In: *JHEP* 02 (2015), p. 184. arXiv: 1409.4557 [hep-ph].

[277] R. Barate et al. "Measurements of BR (b —> tau- anti-nu(tau) X) and BR (b —> tau- anti-nu(tau) D*+- X) and upper limits on BR (B- —> tau- anti-nu(tau)) and BR (b—> s nu anti-nu)." In: *Eur. Phys. J. C* 19 (2001), pp. 213–227. arXiv: hep-ex/0010022.

[278] D. Du et al. "Phenomenology of semileptonic B-meson decays with form factors from lattice QCD." In: *Phys. Rev. D* 93.3 (2016), p. 034005. arXiv: 1510.02349 [hep-ph].

[279] D. M. Straub. "flavio: a Python package for flavour and precision phenomenology in the Standard Model and beyond." In: (2018). arXiv: 1810.08132 [hep-ph].

[280] B. Grinstein and D. Pirjol. "Exclusive rare $B \to K^*\ell^+\ell^-$ decays at low recoil: Controlling the long-distance effects." In: *Phys. Rev. D* 70 (2004), p. 114005. arXiv: hep-ph/0404250.

[281] "Search for charged lepton flavor violation in top quark production and decay in proton-proton collisions at $\sqrt{s} = 13$ TeV." In: (June 2021, CMS-PAS-TOP-19-006.).

[282] "Search for charged lepton-flavour violation in top-quark decays at the LHC with the ATLAS detector." In: (Sept. 2018, ATLAS-CONF-2018-044.).

[283] J. P. Delahaye et al. "Muon Colliders." In: (Jan. 2019). arXiv: 1901.06150 [physics.acc-ph].

[284] C. Aimè et al. "Muon Collider Physics Summary." In: *2022 Snowmass Summer Study*. Mar. 2022. arXiv: 2203.07256 [hep-ph].

[285] A. M. Sirunyan et al. "Search for new physics in top quark production with additional leptons in proton-proton collisions at $\sqrt{s} = 13$ TeV using effective field theory." In: *JHEP* 03 (2021), p. 095. arXiv: 2012.04120 [hep-ex].

[286] B. Schmidt and M. Steinhauser. "CRunDec: a C++ package for running and decoupling of the strong coupling and quark masses." In: *Comput. Phys. Commun.* 183 (2012), pp. 1845–1848. arXiv: 1201.6149 [hep-ph].

[287] J. Charles et al. "CP violation and the CKM matrix: Assessing the impact of the asymmetric B factories." In: *Eur. Phys. J. C* 41.1 (2005), pp. 1–131. arXiv: hep-ph/0406184.

[288] M. Bona et al. "The 2004 UTfit collaboration report on the status of the unitarity triangle in the standard model." In: *JHEP* 07 (2005), p. 028. arXiv: hep-ph/0501199.

[289] N. T. Huong, E. Kou, and B. Viaud. "Novel approach to measure the leptonic $\eta(')\to \mu^+\mu^-$ decays via charmed meson decays." In: *Phys. Rev. D* 94.5 (2016), p. 054040. arXiv: 1606.08195 [hep-ph].

[290] L. G. Landsberg. "Electromagnetic Decays of Light Mesons." In: *Phys. Rept.* 128 (1985), pp. 301–376.

[291] P. Masjuan and P. Sanchez-Puertas. "η and η' decays into lepton pairs." In: *JHEP* 08 (2016), p. 108. arXiv: 1512.09292 [hep-ph].

[292] S. X. Li et al. "Measurement of the branching fraction of $\Lambda_c^+ \to p\omega$ decay at Belle." In: *Phys. Rev. D* 104.7 (2021), p. 072008. arXiv: 2108.11301 [hep-ex].

[293] C. Greub, V. Pilipp, and C. Schupbach. "Analytic calculation of two-loop QCD corrections to $b \to sl^+l^-$ in the high q^2 region." In: *JHEP* 12 (2008), p. 040. arXiv: 0810.4077 [hep-ph].

[294] S. Aoki et al. "FLAG Review 2019: Flavour Lattice Averaging Group (FLAG)." In: *Eur. Phys. J. C* 80.2 (2020), p. 113. arXiv: 1902.08191 [hep-lat].

[295] Y. Aoki et al. "FLAG Review 2021." In: (Nov. 2021). arXiv: 2111.09849 [hep-lat].

[296] T. Gutsche et al. "Rare baryon decays $\Lambda_b \to \Lambda l^+l^-(l = e, \mu, \tau)$ and $\Lambda_b \to \Lambda\gamma$: differential and total rates, lepton- and hadron-side forward-backward asymmetries." In: *Phys. Rev.* D87 (2013), p. 074031. arXiv: 1301.3737 [hep-ph].

[297] A. Dery et al. "$SU(3)_F$ analysis for beauty baryon decays." In: *JHEP* 03 (2020), p. 165. arXiv: 2001.05397 [hep-ph].

[298] R.-M. Wang et al. "Studying $\mathcal{B}_1(\frac{1}{2}^+) \to \mathcal{B}_2(\frac{1}{2}^+)\ell^+\ell^-$ semileptonic weak baryon decays with the SU(3) flavor symmetry." In: *Phys. Rev. D* 103.1 (2021), p. 013007. arXiv: 2101.02421 [hep-ph].

[299] C. L. Y. Lee, M. Lu, and M. B. Wise. "B(l4) and D(l4) decay." In: *Phys. Rev. D* 46 (1992), pp. 5040–5048.

[300] J. P. Lees et al. "Measurement of the $D*(2010)^+$ meson width and the $D*(2010)^+ - D^0$ mass difference." In: *Phys. Rev. Lett.* 111.11 (2013), p. 111801. arXiv: 1304.5657 [hep-ex].

[301] D. Leljak, B. Melić, and D. van Dyk. "The $\overline{B} \to \pi$ form factors from QCD and their impact on $|V_{ub}|$." In: *JHEP* 07 (2021), p. 036. arXiv: 2102.07233 [hep-ph].

[302] A. Abada et al. "Heavy to light vector meson semileptonic decays." In: *Nucl. Phys. B Proc. Suppl.* 119 (2003). Ed. by R. Edwards, J. W. Negele, and D. Richards, pp. 625–628. arXiv: hep-lat/0209116.

[303] K. C. Bowler et al. "B —> rho l nu form-factors in lattice QCD." In: *JHEP* 05 (2004), p. 035. arXiv: hep-lat/0402023.

[304] B. C. Allanach, J. Davighi, and S. Melville. "An Anomaly-free Atlas: charting the space of flavour-dependent gauged $U(1)$ extensions of the Standard Model." In: *JHEP* 02 (2019). [Erratum: JHEP08,064(2019)], p. 082. arXiv: 1812.04602 [hep-ph].

[305] J. Rathsman and F. Tellander. "Anomaly-free Model Building with Algebraic Geometry." In: *Phys. Rev.* D100.5 (2019), p. 055032. arXiv: 1902.08529 [hep-ph].

[306] D. B. Costa, B. A. Dobrescu, and P. J. Fox. "General Solution to the U(1) Anomaly Equations." In: *Phys. Rev. Lett.* 123.15 (2019), p. 151601. arXiv: 1905.13729 [hep-th].

[307] A. Bazavov et al. "Short-distance matrix elements for D^0-meson mixing for $N_f = 2 + 1$ lattice QCD." In: *Phys. Rev.* D97.3 (2018), p. 034513. arXiv: 1706.04622 [hep-lat].

[308] O. Gedalia et al. "Lessons from Recent Measurements of D0 - anti-D0 Mixing." In: *Phys. Rev.* D80 (2009), p. 055024. arXiv: 0906.1879 [hep-ph].

[309] Y. Grossman, A. L. Kagan, and Y. Nir. "New physics and CP violation in singly Cabibbo suppressed D decays." In: *Phys. Rev.* D75 (2007), p. 036008. arXiv: hep-ph/0609178 [hep-ph].

[310] W. Altmannshofer et al. "New Physics Models of Direct CP Violation in Charm Decays." In: *JHEP* 04 (2012), p. 049. arXiv: 1202.2866 [hep-ph].

[311] P. Böer, T. Feldmann, and D. van Dyk. "Angular Analysis of the Decay $\Lambda_b \to \Lambda(\to N\pi)\ell^+\ell^-$." In: *JHEP* 01 (2015), p. 155. arXiv: 1410.2115 [hep-ph].

[312] W. Altmannshofer et al. "New strategies for New Physics search in $B \to K^*\nu\bar{\nu}$, $B \to K\nu\bar{\nu}$ and $B \to X_s\nu\bar{\nu}$ decays." In: *JHEP* 04 (2009), p. 022. arXiv: 0902.0160 [hep-ph].

[313] C. Bobeth et al. "QCD corrections to $\bar{B} \to X_{d,s}\nu\bar{\nu}$, $\bar{B}_{d,s} \to \ell^+\ell^-$, $K \to \pi\nu\bar{\nu}$ and $K_L \to \mu^+\mu^-$ in the MSSM." In: *Nucl. Phys. B* 630 (2002), pp. 87–131. arXiv: hep-ph/0112305.

[314] D. Melikhov, N. Nikitin, and S. Simula. "Right-handed currents in rare exclusive B —> (K, K*) neutrino anti-neutrino decays." In: *Phys. Lett. B* 428 (1998), pp. 171–178. arXiv: hep-ph/9803269.

[315] P. Colangelo et al. "Rare $B \to K^{(*)}$ neutrino anti-neutrino decays at B factories." In: *Phys. Lett. B* 395 (1997), pp. 339–344. arXiv: hep-ph/9610297.

[316] J. J. Sakurai and J. Napolitano. *Modern Quantum Mechanics*. Quantum physics, quantum information and quantum computation. Cambridge University Press, Oct. 2020.

[317] E. D. Commins and P. H. Bucksbaum. *Weak Interactions of Leptons and Quarks*. Cambridge University Press, 1983.

[318] J. Kriewald. "Indirect searches for New Physics via flavour observables." PhD thesis. Clermont-Ferrand U., 2021. arXiv: 2202.14015 [hep-ph].

[319] R. Aaij et al. "Test of lepton universality in beauty-quark decays." In: *Nature Phys.* 18.3 (2022), pp. 277–282. arXiv: 2103.11769 [hep-ex].

[320] R. Bause et al. *Model-independent analysis of $b \to d$ processes.* DO-TH 21/30, in preparation.

[321] A. Ali, A. Y. Parkhomenko, and A. V. Rusov. "Precise Calculation of the Dilepton Invariant-Mass Spectrum and the Decay Rate in $B^{\pm} \to \pi^{\pm}\mu^+\mu^-$ in the SM." In: *Phys. Rev. D* 89.9 (2014), p. 094021. arXiv: 1312.2523 [hep-ph].

[322] A. V. Rusov. "Probing New Physics in $b \to d$ transitions." In: *JHEP* 07 (2020), p. 158. arXiv: 1911.12819 [hep-ph].

[323] R. Aaij et al. "Measurement of the $B_s^0 \to \mu^+\mu^-$ decay properties and search for the $B^0 \to \mu^+\mu^-$ and $B_s^0 \to \mu^+\mu^-\gamma$ decays." In: *Phys. Rev. D* 105.1 (2022), p. 012010. arXiv: 2108.09283 [hep-ex].

[324] R. Aaij et al. "Analysis of Neutral B-Meson Decays into Two Muons." In: *Phys. Rev. Lett.* 128.4 (2022), p. 041801. arXiv: 2108.09284 [hep-ex].

[325] R. Aaij et al. "Evidence for the decay $B_S^0 \to \overline{K}^{*0}\mu^+\mu^-$." In: *JHEP* 07 (2018), p. 020. arXiv: 1804.07167 [hep-ex].

[326] G. Buchalla and G. Isidori. "Nonperturbative effects in $\bar{B} \to X_s l^+ l^-$ for large dilepton invariant mass." In: *Nucl. Phys. B* 525 (1998), pp. 333–349. arXiv: hep-ph/9801456.

Glossary

ADM anomalous dimension matrix. 11

BSM physics beyond the Standard Model. 1–4, 7–10, 14, 17, 18, 20, 21, 23, 34–37, 39, 41, 44, 46, 49, 50, 53, 55, 57, 61, 67, 74–77, 80, 85, 86, 100, 101, 113, 142, 146, 148

C.L. confidence level. 21, 27, 28, 32, 36–38, 77, 85, 87, 92, 93, 95, 96, 98, 99, 102, 115

CKM Cabibbo-Kobayashi-Maskawa. 7–9, 34, 35, 43, 45, 62, 80, 81, 91, 92, 103, 115, 140

cLFC charged lepton flavor conservation. 3, 78, 85–87, 89, 90, 98, 100, 101, 146, 147

EFT Effective Field Theory. 2–4, 10, 12, 17, 86, 91, 92, 95, 96, 119, 133, 146, 148

EOM equations of motion. 19

FCC Future Circular Collider. 2

FCCC flavor changing charged current. 7, 9

FCNC flavor changing neutral current. 1, 2, 7–9, 16, 18, 26, 34, 38, 41, 44, 45, 78–82, 98, 100, 101, 114, 115, 141, 142

FIMP feebly interacting massive particle. 10

GIM Glashow-Iliopolus-Maiani. 1, 8, 13, 15, 16, 26, 34, 65, 77, 78, 85, 97, 100, 146

HEFT Higgs Effective Field Theory. 17

HHχPT heavy hadron chiral perturbation theory. 111

LCSR Light-cone sum rules. 20, 30, 112

LFU lepton flavor universality. 1, 3, 9, 36, 46, 73–75, 77–79, 81, 85–90, 94–96, 98, 100, 101, 142–148

LFV lepton flavor violating. 3, 28, 29, 37, 38, 44, 75–77, 85, 99, 100, 124

LFV lepton flavor violation. 39, 41, 44, 46, 75–77, 98, 126, 143, 144

LH left-handed. 5–7, 10, 16, 36, 41–45, 55, 61, 67, 80, 81, 86, 87, 101, 115, 117, 122, 142, 144

LHC Large Hadron Collider. 9

LHCb Large Hadron Collider beauty. 2, 9, 21, 32, 34, 37, 67, 72, 143, 144

LLO leading logarithmic order. 12

LNV lepton number violating. 86, 88

LO leading order. 10–13, 23, 78, 100, 105, 119

LQ leptoquark. 3, 9, 36, 40, 44, 45, 75, 76, 100

LQCD Lattice QCD. 20, 22, 30, 108, 110, 112

NLLO next-to-leading logarithmic order. 12

NLO next-to-leading order. 13, 105

NNLLO next-to-next-to-leading logarithmic order. 13, 100

NNLO next-to-next-to-leading order. 13, 105, 106

NP new physics. 1, 2, 8–10, 15–18, 20, 25, 34, 35, 39, 41, 46–52, 54–58, 60–62, 67, 73–77, 79, 80, 86, 88, 95, 97, 98, 100, 101, 115, 119, 121, 142, 144

OPE Operator Product Expansion. 3, 10, 19, 94

PDF parton distribution function. 39, 142

PMNS Pontecorvo-Maki-Nakagawa-Sakata. 8, 44, 80, 81, 140

QCD quantum chromodynamics. 4–6, 8, 10, 13, 19–21, 23, 24, 29, 42, 60, 73, 77, 101, 119, 131

QCDF QCD Factorization. 23

QED quantumelectro dynamics. 5, 6, 15, 24, 73, 74

QFT quantum field theory. 4

RG renormalization group. 13, 114, 119, 122

RH right-handed. 5, 6, 8, 15, 16, 36, 40–45, 55, 61, 67, 68, 75, 80, 81, 86–88, 93, 95, 113–115, 117, 142

SM Standard Model of particle physics. 1–21, 23, 25–28, 30–37, 40–42, 46–48, 50–57, 60–62, 65, 67, 71, 73–75, 77, 78, 80, 81, 85, 91–101, 105, 106, 108, 113–115, 118, 121, 142, 144, 146, 148

SMEFT Standard Model Effective Field Theory. 2–4, 17, 18, 78–80, 99, 100, 140

UV ultraviolet. 1, 36, 40, 41, 114

vev vacuum expectation value. 5, 6

VMD vector meson dominance. 23, 24

WET Weak Effective Theory. 2–4, 17, 18, 79–81, 100

WIMP weakly interacting massive particle. 10